This is to certify that the
dissertation entitled

A MINIMALLY INVASIVE SYSTEM FOR THE EVALUATION OF PROSTHETIC HEART VALVES

presented by

Shiu Chuen Chan

has been accepted towards fulfillment
of the requirements for the

Doctoral degree in Electrical and Computer Engineering

Satish Udpa
Major Professor's Signature

May 1, 2008
Date

A MINIMALLY INVASIVE SYSTEM FOR THE EVALUATION OF PROSTHETIC HEART VALVES

By

Shiu Chuen Chan

A DISSERTATION

Submitted to
Michigan State University
in partial fulfillment of the requirements
for the degree of

DOCTOR OF PHILOSOPHY

Department of Electrical and Computer Engineering

2008

ABSTRACT

A MINIMALLY INVASIVE SYSTEM FOR THE EVALUATION OF PROSTHETIC HEART VALVES

By

Shiu Chuen Chan

The Björk-Shiley Convexo-Concave (BSCC) heart valve employs a pyrolytic carbon disc, held in place by two struts, as an occluder to prevent retrograde flow of blood in the heart. The strut on the inlet side is integral to the suture ring while the strut on the outlet side is welded to the suture ring. In some cases, for reasons yet unclear, the weld at one of the two sites fractures after several years of use. This results in a single-leg separation (SLS) of the strut. The fracture causes the load on the weld at the other end of the strut to increase, thereby setting the stage for it to fail eventually. A complete fracture of the outlet strut would cause the disc to escape resulting in mortality. This thesis describes a minimally invasive electromagnetic approach, called the gradiometer-based method, for detecting SLS failures. The feasibility of the method is investigated using three dimensional finite element analysis techniques. A clinical scale gradiometer-based examination system is constructed and *in vitro* studies of the system have shown 100% accuracy in detecting SLS cases.

To my wife, Suzanne, and our extended families.

ACKNOWLEDGEMENTS

I am grateful to the Bowling-Pfizer Settlement Funds Supervisory Panel for generously supporting of this work. Their support has provided accesses to invaluable resources and opportunities that have helped made this project a success.

I would like to thank the members of my Guidance Committee: Dr. Christina Chan, Dr. Pradeep Ramuhalli, Dr. Lalita Udpa, and my Major Professor, Dr. Satish Udpa for their willingness and time spent serving on my committee, and the many intellectual discussions on this and other subjects.

I am also deeply indebted to Drs. Lalita and Satish Udpa who had critically reviewed this thesis despite their overwhelming schedules.

A project of this magnitude cannot be accomplished by one person alone. I am very thankful for my colleagues and friends, past and present, in the "Heart Valve Project," all of whom I have the pleasure to work, brain-storm, and, at times, constructively disagree with. In particular, I wish to thank Dr. Tian Yong for the many discussions on induction heating modeling, Dr. Lalita Udpa and Dr. Zhiwei Zeng for the discussions on probability of detection models, and Mr. Robert Clifford for the construction of the various mechanical components of the system.

A very special thank you goes to Dr. Mohachiro Oka of the Oita National College of Technology (Oita, Japan), whose collaboration was instrumental in the development of the first gradiometer prototype that had since evolved into the current designs.

I would like to express my appreciation to all the world-class faculty, staff, members, and visiting scholars of the Nondestructive Evaluation Laboratory at the Department of Electrical and Computer Engineering at Michigan State University for all the opportunities and support over the years.

A very special thanks goes to my mother, late father, brother and his family, as well as my wife's family for their unconditional support and care.

Last but not least, I wish to extend my deepest gratitude to my wife, Suzanne, who is an Angel from Heaven sent by God. Her endless love, patience, care, and encouragement have accompanied me over many challenges of this project as well as the completion of this thesis.

TABLE OF CONTENTS

LIST OF TABLES

LIST OF FIGURES

KEY TO ABBREVIATIONS

BSCC	Björk-Shiley convexo-concave
EM	Electromagnetic
EMF	Electromotive force
IOS	Intact outlet strut
OSF	Outlet strut fracture
RF	Radio frequency
SAR	Specific absorption rate
SLS	Single-leg separation
WBA	Whole-body-average

CHAPTER 1. INTRODUCTION

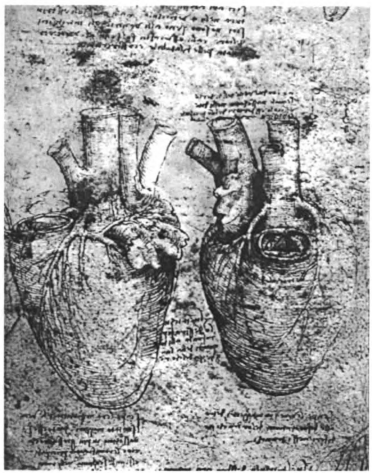

Drawing of the Heart and its Blood Vessels, from the Anatomical Notebooks
Leonardo da Vinci (1452-1519)
(Image courtesy of *The Arts Renewal Center*, www.artrenewal.org)

It is known that the heart, in every-day conversation, is synonymous with love and life, but it also has many other associations. For example `have a heart' means to be merciful, and `have your heart in the right place' means to be kind, while 'heavy heart' refers to sadness. No other bodily organ elicits this kind of response. After all, when was the last time you had a heavy pancreas?

Adapted from
David Henry Pinney (http://www.pinney.co.uk)
and http://www.howstuffworks.com/heart.htm

The Björk-Shiley Convexo-Concave (BSCC) prosthetic heart valve was one of the commonly implanted prosthetic heart valves[1] until its withdrawal from the market in 1986. Between 1979 and 1986, about 86,000 BSCC valves were implanted worldwide. The valve employs a pyrolytic carbon disc as an occluder to ensure unidirectional blood flow from the atrium to the ventricle of the heart, as well as from the ventricle into the aorta. The disc is held in place by two struts. The strut on the inlet side is integral to the flange ring while the strut on the outlet side is tungsten inert gas welded to the ring. Occasionally, after years of use, the weld at one of the two sites fractures, resulting in a single-leg separation (SLS) of the strut [16]. This single-leg separation causes the load on the weld at the other end of the strut to increase, thereby setting the stage for it to fail eventually. If the outlet strut is severed from the flange ring, the disc can escape, leading to loss of blood flow control and fatality in most cases. There is, therefore, a considerable amount of interest and a sense of urgency in developing techniques to detect SLS failures.

This thesis describes a minimally invasive approach, called the gradiometer-based method, for detecting SLS failures in BSCC heart valves. The method employs two large excitation coils placed on either side of the valve to generate a uniform, time varying magnetic field in the neighborhood of the heart valve. The coils are oriented in a manner to ensure the current induced in the flange ring is a minimum, while maximizing the current induced in the outlet strut. The field generated by the induced eddy currents in the outlet strut perturbs the uniform field established by the external excitation coils. The perturbation in the applied field, or more specifically the perturbation in the gradient of the field, in the vicinity of the

[1] See Appendix A for a survey on the heart, heart valve diseases and types of treatments.

strut is measured using a catheter-mounted gradiometer. An SLS failure causes a reduction in the current and hence the perturbation in the magnetic field. The gradiometer signal can, therefore, be analyzed to indicate SLS failures.

Finite element simulation models have been used to demonstrate the feasibility of the gradiometer-base detection method as well as to determine the system parameters. Proof-of-concept experiments have been conducted to validate the models findings as well as to validate the gradiometer design. Finally, a clinical-scale system that is suitable for animal and human subject studies has been fabricated. *In Vitro* double-blind tests of this system has achieved 100% accuracy in detecting SLS failures.

1.1 Organization of the Thesis

This thesis is organized as follows: Chapter 2 introduces the history of the BSCC prosthetic heart valve, the outlet strut failure problem, and a number of proposed techniques by other research groups for detecting single-leg fractures of the valves. Chapter 3 describes the gradiometer-based method for SLS detection. The mathematical formulations describing the principles of the examination approach are shown in Chapter 4. Chapter 5 discusses the finite element analysis results of the gradiometer-based method, including the generation of the excitation magnetic field and the interaction of the heart valve and the outlet strut with this field. Chapter 6 describes the hardware components and specifications of an examination system based on the gradiometer-based method, and Chapter 7 presents two gradiometer designs that are suitable for clinical use. Chapter 8 discusses the system performance characteristics and presents the *in vitro* test results. Chapter 9 presents a

technique for developing the probability of detection model for the system. Chapter 10 examines the effects of inductive heating on both the patient and the heart valve due to the magnetic field of the system. Issues with patient and operator safety, as well as compliance with applicable international health standards are discussed in Chapter 11. Chapter 12 presents a few concluding remarks and ideas for future works.

For background and supplemental information, Appendix A gives a physiological description of the heart and the cardiac functions, the nature of heart valve diseases and their typical treatment, and a brief survey on the kinds of prosthetic heart valves. Lastly, Appendix B recommends a procedure for conducting animal study with the gradiometer-based examination system.

1.2 Benefits of Work

Successful development of the gradiometer-based detection method will provide patients and physicians with a highly reliable tool for diagnosing single-leg separation (SLS) in Björk-Shiley Convexo-Concave (BSCC) prosthetic heart valves. Knowledge of an intact valve will provide immense comfort to the patient and his or her family. Patients whose heart valve has a single-leg separated outlet strut can evaluate their options more objectively with their physicians, as well as to better prepare for emergency responses in case if a complete outlet strut fracture occurs.

CHAPTER 2. THE GRADIOMETER-BASED METHOD

The gradiometer-based method is a minimally invasive catheter-based method. In this approach, two large excitation coils are placed on each side of the heart valve outside the patient's body to generate a uniform time-varying magnetic field around the valve as shown in Figure 2.1. Eddy currents are induced in the various parts of the valve according to *Faraday's Law*. The field produced by the external coils is oriented in a fashion that is parallel to the valve flange ring. This orientation ensures that a minimum amount of eddy current is induced in the ring, and that the current induced in the outlet strut is dominant. The field generated by the induced eddy currents in the outlet strut perturbs the uniform field established by the external excitation coils. The perturbation in the field (or rather, the gradient of the field) in the vicinity of the strut is measured using a catheter-mounted gradiometer. The presence of an SLS reduces the induced current and the perturbation of the applied uniform field. The gradiometer signal, therefore, can be used as a basis to determine the condition of the outlet strut.

2.1 Faraday's Law and Maxwell's Equations

In the gradiometer approach, the operating principle of the gradiometer as well as the eddy currents induced in the heart valve are both described by the *Faraday's Law of Induction*. Faraday's Law states that a time-varying magnetic field will produce an induced voltage, called the electromotive force (EMF), in a closed circuit, which causes current to flow. The

induced EMF, V_{EMF} (in volts), is related to the time rate of change of the magnetic flux linkage by the circuit. This relation is expressed as

$$V_{EMF} = -\frac{d\lambda}{dt} = -N\frac{d\phi}{dt} \tag{2.1}$$

where λ is the magnetic flux linkage, N is the number of turns in the circuit and ϕ is the flux through each turn. The induced voltage acts to oppose the effect of the applied magnetic field as indicated by the negative sign in equation (2.1). This is known as *Lenz's Law*: the induced current in the circuit flows in the direction such that the induced magnetic field produced by the induced current opposes the original magnetic field.

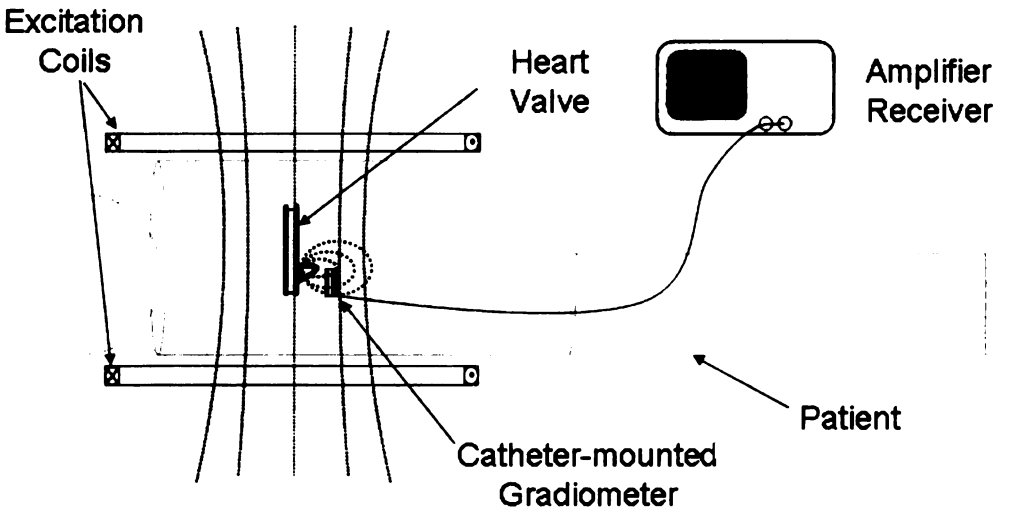

Figure 2.1 Illustration of the gradiometer-based approach for BSCC heart valve SLS detection (components not drawn to scale)

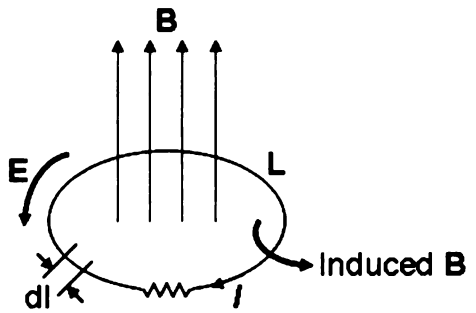

Figure 2.2 Induced EMF due to a time-varying magnetic field, **B**. After [2]

In Figure 2.2, the amount of magnetic flux linking the circuit (the circular loop) is given by

$$\phi = \int_S \mathbf{B} \cdot d\mathbf{S} \tag{2.2}$$

where **B** is a time-varying magnetic field and S is the surface area of the circuit bounded by the closed path L. For a single-loop circuit (i.e., $N = 1$), (2.1) can be written as

$$V_{EMF} = -\frac{d}{dt}\int_S \mathbf{B} \cdot d\mathbf{S} = -\int_S \frac{\partial \mathbf{B}}{\partial t} \cdot d\mathbf{S} \tag{2.3}$$

From Figure 2.2, the V_{EMF} is also given by

$$V_{EMF} = \oint_L \mathbf{E} \cdot d\mathbf{l} \tag{2.4}$$

where **E** is a time-varying electric field and $d\mathbf{l}$ is the incremental path length. Applying Stokes's theorem to (2.4) and equating to (2.3) gives

$$\int_S (\nabla \times \mathbf{E}) \cdot d\mathbf{S} = -\int_S \frac{\partial \mathbf{B}}{\partial t} \cdot d\mathbf{S} \tag{2.5}$$

Comparing the integrands yields

$$\nabla \times \mathbf{E} = -\frac{\partial \mathbf{B}}{\partial t} \tag{2.6}$$

which is one of Maxwell's equations for time-varying fields. Equation (2.6) describes the relationship between the induced electric field in the circuit and the applied magnetic field.

A detailed discussion on the Maxwell's equations is beyond the scope of this thesis. The reader is referred to references such as [1]-[3] for a comprehensive treatment of the subject.

In the gradiometer approach, the heart valve is submerged in a time-varying uniform magnetic field. The valve is oriented such that the flange ring is parallel to the applied field. In this manner, the flange intercepts the least amount of the applied field as shown in Figure 2.1. Meanwhile, the outlet strut protrudes away from the plane of the heart valve and forms a closed loop with the flange. This outlet strut loop intercepts the applied magnetic field and an EMF is induced in the loop according to (2.1). The induced EMF causes a current to flow in the outlet strut, which in turn creates a magnetic field that perturbs the applied excitation field as illustrated in Figure 2.2. The net perturbation in the vicinity of the outlet strut is measured using a gradiometer. The gradiometer consists of a pair of sensor coils separated by a known distance. When subjected to a time-varying magnetic field, a current is induced in each coil, again, according to *Faraday's Law*. The difference of the coil signals provides a measurement of the gradient of the field in the vicinity of the outlet strut. In the case of an IOS, the loop formed by outlet strut and the flange is complete and the amount of induced current is large. The perturbation of the uniform field is correspondingly large and the gradiometer output signal is strong. In the presence of a SLS, the loop formed by the strut and the flange is either partially or completely opened, resulting in little or no current flow. Consequently, the perturbation on the applied field is small. The gradiometer output signal level in this case will be very weak or non-existent. The gradiometer signal can, therefore, be analyzed to indicate a SLS failure.

2.2 Implementing the Gradiometer-Based Method

The implementation of the gradiometer-based method begins with the development of a mathematical model for the approach. Finite element analysis is also performed to demonstrate system feasibility before construction commences. The components of the clinical scale prototype—the gradiometer-based examination system—are then identified and their operating parameters specified. Gradiometer prototypes will be evaluated in the clinical scale system. Component designs and parameters are refined until the system is optimized. *In vitro* tests will then commence with actual heart valve specimens. The *in vitro* test results will be used to demonstrate the accuracy of the gradiometer-based method.

The development of the gradiometer-based examination system and the system test results are described in the following chapters.

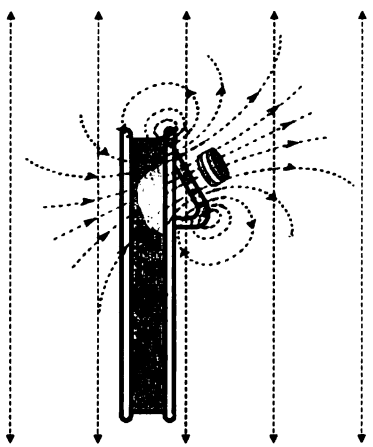

Figure 2.3 Induced current in the outlet strut by the excitation field in turn creates a magnetic field which perturbs the original excitation field (magnetic flux lines simplified for clarity; components not drawn to scale)

CHAPTER 3. BJÖRK-SHILEY CONVEXO-CONCAVE PROSTHETIC HEART VALVE

The original Björk-Shiley tilting disc valve was co-developed by Dr. Viking O. Björk of Sweden and Shiley, Incorporated in USA [4]. It was first introduced clinically in 1969. This original model was reliable, durable, and had good hemodynamics and a low rate of thromboembolism [5], [6]. This model was then modified to further decrease the thromboembolism risk by further improving the hemodynamics of the valve [5], [6]. The end result was the introduction of the convexo-concave models ([7]-[9]) with the tilting disc occluder opening at 60° and 70° angles, respectively. Figure 3.1 shows a Björk-Shiley Convexo-Concave (BSCC) 60° valve. The 70° valve had a similar design with the exception that the disc opened at a 70° angle. Figure 3.3 shows drawings of a BSCC valve with the occluder disc in the open (top figure) and closed (bottom figure) positions. The opening angle is labeled θ in this figure. The implantation of the BSCC 60° heart valve started in 1976 with the commencement of the clinical trials. The valve was eventually approved by the United States Food and Drug Administration (FDA) in April 1979, and was implanted world-wide until 1986 when the manufacturer withdrew it from the market [10]-[16]. The 70° valve was sold only outside of the U.S. between 1980 and 1983. Since only the 60° valve models were implanted in the U.S., the discussions in this thesis will be centered primarily on this model, which will be referred to simply as the BSCC valve in the remaining chapters. It is important to note that although the discussions are focused on the 60° convexo-concave valve, the work described in this thesis is nevertheless equally applicable to the 70° valve.

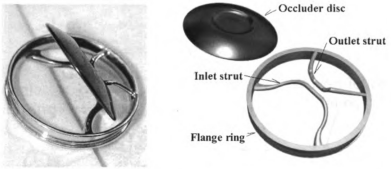

Figure 3.1 Björk-Shiley Convexo-Concave (BSCC) 60° heart valve. The 70° valve has a similar design except the occluder disc opens at a 70° angle

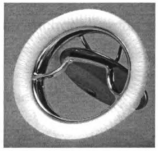

Figure 3.2 A BSCC heart valve with the woven Teflon fabric sewing ring

3.1 Outlet Strut Fracture of the BSCC Valve

The BSCC valve consists of a flange (orifice) ring, an inlet strut, an outlet strut, an occluder disc (Figure 3.1, Figure 3.2) and a fabric sewing ring (Figure 3.2, Figure 3.3). The inlet strut and the flange are manufactured as an integral unit from a cobalt-based Haynes-25 alloy bar stock. The outlet strut is fabricated from a wire of the same alloy and is tungsten inert gas (TIG) welded[1] to the ring. This welding method melts the ends of the outlet strut legs and the neighboring flange material to form solid welds without using any filler material [29]. The sewing ring is made from woven Teflon fabric.

[1] Tungsten Inert Gas welding (TIG-welding) is also known as Gas Tungsten Arc Welding (GTAW).

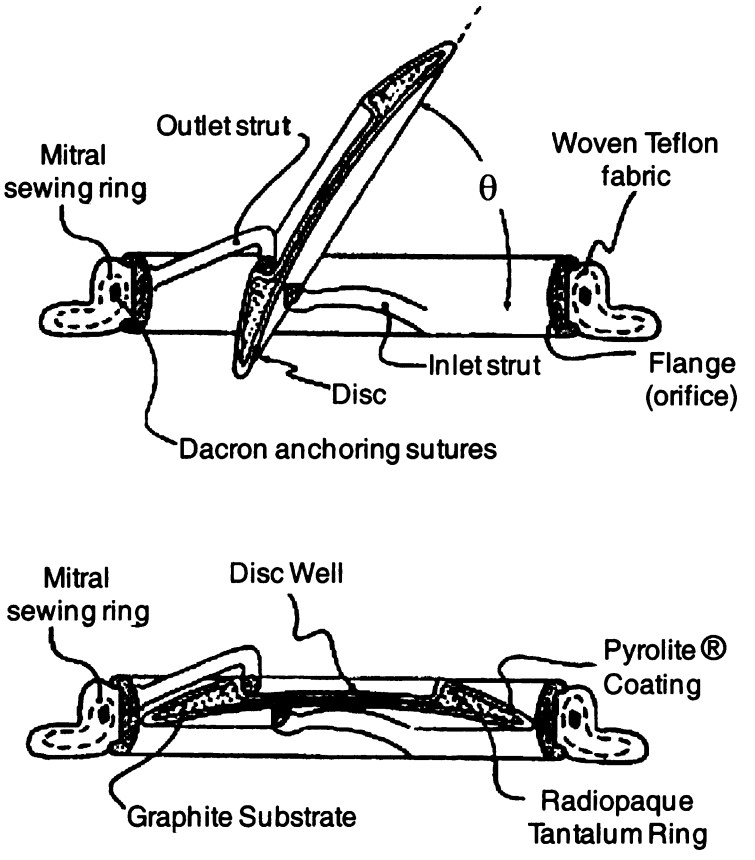

Figure 3.3 Drawings of a BSCC heart valve showing the disc in the open (top) and closed positions (bottom). The disc opening angle θ is either 60° or 70°. Adapted from [17]

The occluder disc, made by CarboMedics, Incorporated (Austin, Texas), has a graphite core covered with a Pyrolite® coating. The disc is held in place by the inlet and outlet struts. The occluder disc has an embedded tantalum ring to provide radiopacity [17]. This marker ring has a gap to allow for thermal expansion during the Pyrolite coating process. The disc is inserted into position between the struts by manually bending the outlet strut and setting the hook-to-well gap distance on the convex surface of the disc. The valve is then checked to ensure proper clearance around the perimeter of the disc

when opened and closed. The opening translation and rotation of the disc are limited by the hook-shaped central tip of the inlet strut. On closing, pressure gradient across the valve causes the disc to return to and rest on the inlet strut's convex surface, thus preventing backflow into the inlet orifice. This ensures unidirectional blood flow through the valve. The valve was manufactured in odd millimeter sizes from 17 mm to 33 mm. The two smallest sizes (17 and 19 mm) valves were only available in the 70° design. The three largest size (29, 31 and 33 mm) models all had the same 29-mm flange ring and disc size. They were labeled according to the outside diameter of the fabric sewing rings.

3.1.1 Loading of the Outlet Strut

The human heart beats an average of 37.8 million times a year. During each cardiac cycle, the occluder disc impacts the arresting struts and the flange ring with a force as much as 2200-2600 grams [17], [19]-[22], [70]. Stress loading and other factors sometimes result in fatigue fracture [24]-[27] of one of the two outlet strut legs, a condition known as a single-leg separation (SLS) of the strut. Figure 3.4 and Figure 3.5 show two scanning electron microscope (SEM) images of a fractured outlet strut as view from the outlet and inlet side, respectively. This single-leg separation causes the impact load on the other leg of the strut to increase, thereby setting the stage for it to fail eventually. When both legs of the outlet strut break, the occluder disc escapes. This leads to a sudden massive valvular incompetence—a loss of blood flow control and pressure to maintain circulation by the heart—as well as embolization by the occluder disc [30]-[36]. The result is acute heart failure which requires immediate surgical intervention [37], [38]. Figure 3.6 shows a chest radiograph of a patient whose heart

valve has fractured. In this figure, the outlet strut is floating near the valve flange, and the occluder disc has embolized the aortic arch. The mean time between the onset of symptoms and fatality depends on the location of the valve—a few minutes in the case of an aortic valve, and one to two hours for a mitral valve [10]. Approximately 86,000 valves were implanted worldwide between 1976 and 1986, with about 4000 of the 70° model. By the end of 2005, there have been a total of 656 outlet strut fractures reported to the manufacturer [39]. Meanwhile, Shiley, Inc. has reported 272 cases of confirmed fatalities[1] related to outlet strut fractures, with an additional 167 alleged fracture-related deaths [39]. The total alleged and confirmed fatalities constitute approximately 66%, or two-third, of all the outlet strut fracture cases reported. This number is believed to be underestimated as many cases may have gone unreported or misdiagnosed. Misdiagnoses of outlet strut fractures (OSFs) are mostly due to the fact that the symptoms of a valve failure resemble closely to other forms of acute heart failures. A valve failure-related fatality can only be determined by performing an autopsy. As of July 2004, there is an estimated 22,200 surviving BSCC patients [39] world-wide. There is, therefore, a considerable amount of interest and a sense of urgency in developing patient care strategies to prevent future valve-related fatalities.

[1] This is the total number of alleged and actual events reported to Shiley as death related to the valve.

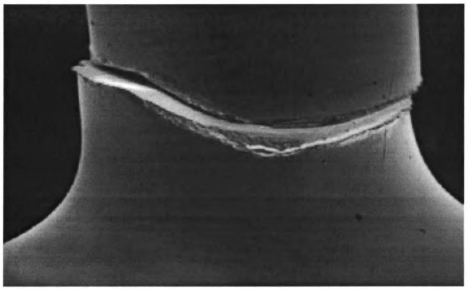

Figure 3.4 Scanning electron microscope (SEM) image of a fractured outlet strut viewed from the outlet side. Adapted from [81]

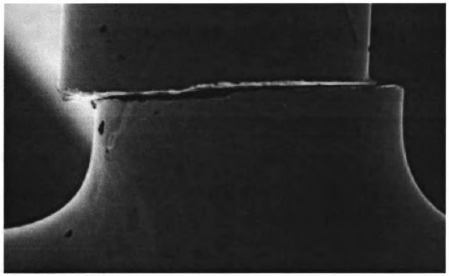

Figure 3.5 Inlet side view SEM image of the fractured outlet strut shown in Figure 3.4. Adapted from [81]

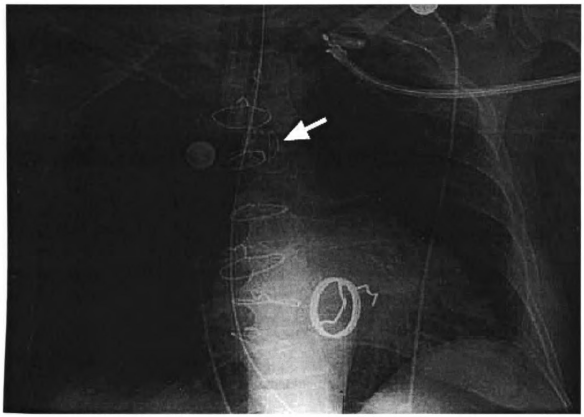

Figure 3.6 Chest radiograph of a patient with outlet strut fracture. The outlet strut has separated and is floating near the flange. The occluder disc (arrow) has embolized the aortic arch. Adapted from [81]

3.2 Care for the BSCC Heart Valve Patients

Collective efforts have been focused on three areas to reduce the number of fatalities due to outlet strut fracture in BSCC heart valve patients. The first is to understand the mechanics of OSFs in BSCC heart valves, [24]-[82]. The second is to identify factors that may increase the risk of OSFs [47]-[68] and to recommend courses of actions [64]-[68] to both BSCC heart valve patients and attending physicians. The third effort is to develop screening techniques to detect single-leg separations (SLSs) ([71]-[118]) *in situ* before they evolve into complete outlet strut structures.

3.2.1 BSCC Heart Valve Outlet Strut Fracture Mechanisms

Early investigations of outlet strut fractures focused on the opening events of the valve. As the occluder disc opens, the central hook of the outlet strut is designed to limit the opening rotation and translation of the disc. The outlet strut arrests the opening disc and sustains an impact force in excess of 2200 grams. The force also exerts a bending moment on the strut. Meanwhile, high-speed photographs and accelerated wear tests showed [17] that the disc closing impact loads are largely transferred to the inlet strut. Consequently, the valve opening forces were the focus of investigations in the early 1980's.

Studies of outlet strut loading suggested that increasing the opening angle from 60° to 70° would reduce the strut opening load by almost 50% [17]. This fact, along with hemodynamic advantages, prompted the introduction of the 70° valves by Shiley. Ironically, the 70° valve models turned out to be more susceptible to OSF than the 60° models of the same sizes [47], [59]. Meanwhile, as outlet strut fractures continued to occur, more valve specimens became available from clinical explants. Data collected from examinations of the explanted clinical valves, along with the fact that the 70° valves were more prone to fracture, had shifted the focus of investigation to searching for and studying the previously unanticipated transient and irregularly occurring closing events. Metallurgical analyses [25]-[29] of the unused valve inventory, *in vitro* studies in pulse duplicators ([19], [20], [22], [74], [97] and [104]) and *in vivo* studies with sheep under both sedentary and exercising conditions had led to a better understanding of the valve closing dynamics and the outlet strut fracture mechanics [21], [86].

3.2.2 The Mechanics of Valve Closure

Examination of explanted BSCC valves showed, in some cases, multiple wear marks on the outlet strut tip and leg bases and on the inner surface of the flange ring. This suggested that the occluder disc potentially has more than one closing position. To understand and observe any transient closing events, Structural Acoustics, Incorporated[1] (SAI) had mounted miniature strain gages on the leg bases of the struts to measure dynamic loading. Figure 3.7 shows the position of the disc in relation to the outlet strut loading at the instance of closure measured in a pulse duplicator. During closure, the disc initially rotates beyond its mean stable closed position. The over-rotated disc then comes into contact with and loads the outlet strut. The impact loading of the outlet strut continues as the disc damps out to a final closed position, coming to rest on the inlet strut.

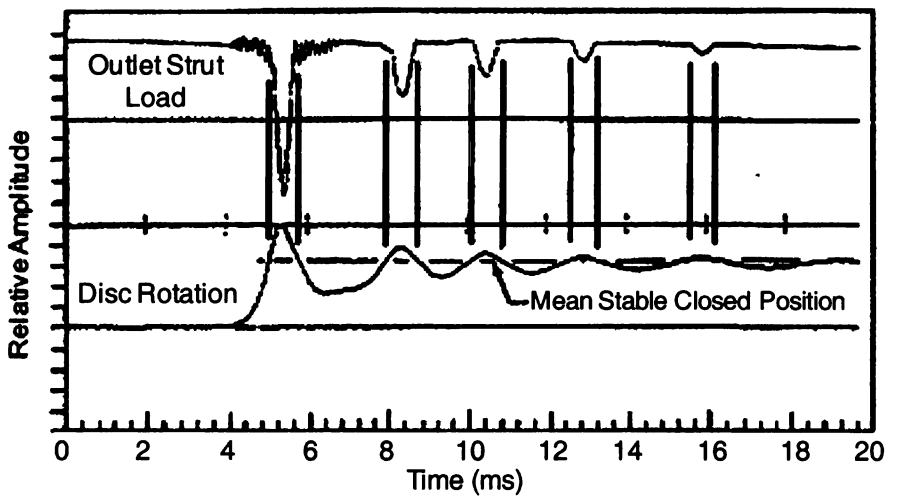

Figure 3.7 Relationship between outlet strut loading and disc rotation during valve closure measured in a pulse duplicator. Adapted from [17].

[1] Structural Acoustics, Incorporated, Raleigh, North Carolina, USA.

One cause of the outlet strut loading may be attributed to the manufacturing tolerance standard. During valve assembly, the outlet strut was manually bent into place after it was welded to the flange ring. The metallic parts of the heart valve were then polished and checked for tolerance compliance. Prior to 1984, the outlet strut was adjusted such that there were gaps (Figure 3.8) between the disc and the base of the strut as well as between the hook and the well of the disc (hook-to-well gap, Figure 3.9). An example of outlet strut loading is shown in Figure 3.10. In this case, when the occluder disc over-rotates, the inlet strut tip acts as a fulcrum for the disc to impact the outlet strut tip with a vertical force Fc for less than 2 ms. This impact force creates a bending moment on the outlet strut. This scenario was observed by SAI in their *in vitro* study. Figure 3.11 shows the load experienced by the inlet and outlet struts during a closure event with disc over-rotation. In this figure, the inlet strut load begins to rise approximately 1 ms before over-rotation occurs. The inlet strut load then drops dramatically as the disc over-rotates and the outlet strut tip becomes loaded. After approximately 1.5 ms, the disc rebounds from the outlet strut and in turn impacts the inlet strut. The oscillation of the disc continues as it comes to rest at its final closed position, striking the inlet and outlet struts alternately in the process.

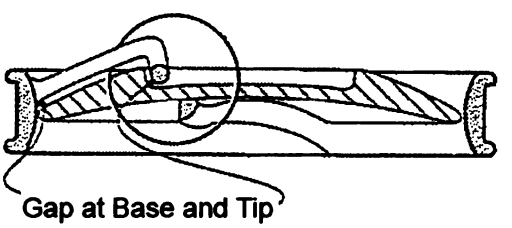

Figure 3.8 Prior to April 1984, the manufacturing tolerance specified gaps at the base and tip of the outlet strut. Adapted from [17].

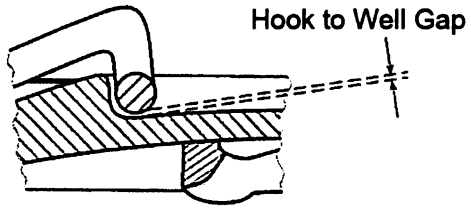

Figure 3.9 Hook-to-well gap between the outlet strut tip and the ocluder disc well. Adapted from [17].

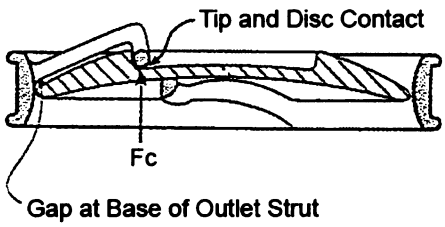

Figure 3.10 A simulated case of disc over-rotation. Fc is the vertical implact force on the outlet strut. Adapted from [17].

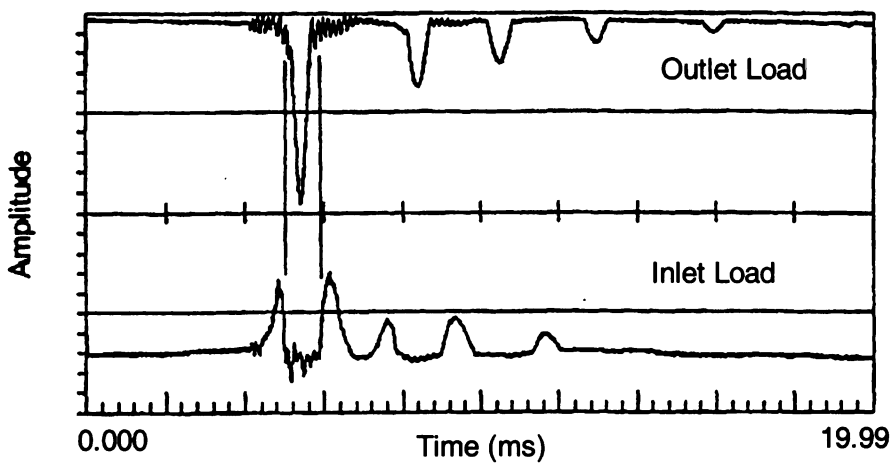

Figure 3.11 Loading of the inlet and outlet struts during the occluder disc over-rotation. Adapted from [104].

In April, 1984, Shiley changed the tolerance specifications and modified the procedures for setting and verifying the hook-to-well gap. The new specifications eliminated the gap between the disc and the strut base, allowing the rim of the disc to remain in contact with the base of the outlet strut when the disc was at rest (Figure 3.12). With this new configuration, a disc over-rotation would cause it to impact the outlet strut leg bases rather than the strut tip, thus eliminating the vertical force, Fc, in Figure 3.10 and the subsequent bending moment exerted on the outlet strut. These modifications appear to be effective as no outlet strut fracture has been reported in a BSCC valve manufactured after April 1984.

Although the effect of the hook-to-well gap is a candidate for the cause of outlet strut failures, the effect of the gap on valve closure dynamics is not yet completely understood. Investigations are on-going [46] to evaluate the effect of hook-to-well separation on tip loading of the outlet strut.

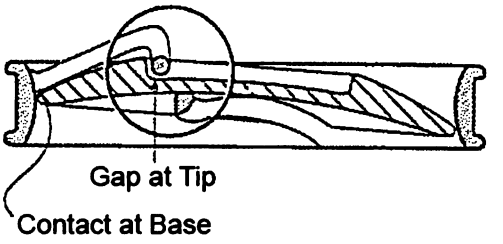

Figure 3.12 After April 1984, the new manufacturing specifications ensured that the disc remained in contact with the base of the outlet strut when at rest. Adapted from [17].

3.2.3 Dynamics of the BSCC Valve

With an unmodified hook-to-well closure clearance, finite element analyses performed by SAI [17] showed maximum stress concentration on the inlet side near the base of the outlet strut during tip loading as shown in Figure 3.13. Although this stress is experienced for less than 0.5 ms, the loading force can reach between 2200 g to 2500 g under sedentary conditions. This amount of loading exceeds the outlet strut's endurance limit of approximately 430×10^3 kPa (~62000 p.s.i). If critical loading were kept continuous, valve fracture could occur in as few as three months (10^7 cardiac cycles) [17].

The dynamics of BSCC heart valves in the mitral position had been studied extensively in pulse duplicators [18], [20], [22], [23] and in sheep [19], [21] to determine the impact forces on the outlet strut during valve closure, and to investigate the physiological factors that affect these forces. Of particular interest were the valve responses under sedentary and exercise conditions. Impact forces were measured using miniature strain gages mounted on the bases of the outlet strut legs, and the left ventricular pressure was measured using a catheter-mounted manometer positioned in the left ventricle of the sheep or pulse duplicator chamber. In the sheep study, an ECG was also recorded for both synchronization and determination of the instantaneous heart rate.

In the heart valve dynamics studies, the systolic left ventricle (LV) pressure signal, LVP, was low-pass filtered and differentiated to give the *LV pressure rise*, dP/dt (where P is the pressure measured in mmHg, and t is time in seconds). $\dot{\text{L}}$V dP/dt was used as an

indicator of the level of physiological activity: at the time of valve closure, an anesthetized subject typically has a dP/dt of 450-750 mmHg/s; under sedentary conditions, dP/dt ~ 750-1300 mmHg/s; and, in exercise conditions the dP/dt may range from 2500-5200 mmHg/s. Note that these dP/dt valves are rough estimates—they are highly dependent on the subject and its general physiological condition.

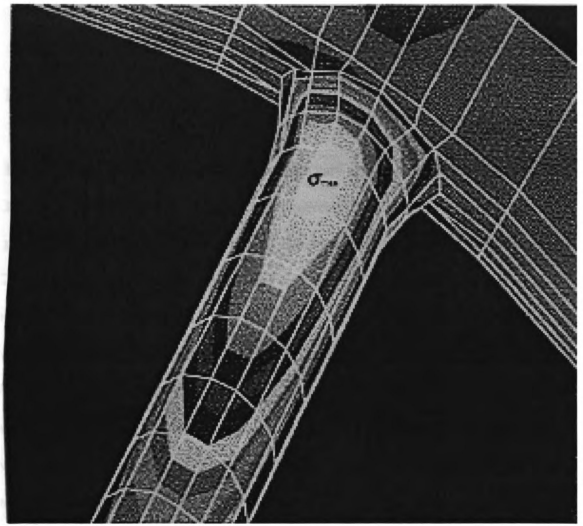

Figure 3.13 Finite element analysis of the outlet strut leg showing the stress distribution due to tip loading by the occluder disc during over-rotation (σ-max denotes the region of maximum stress). Adapted from [17].

From pulse duplicator studies, Rau et al. [20] observed that the impact forces on the outlet strut legs vary linearly with the disc closing velocities. Meanwhile, Guo et al. [18] derived an equation for the leaflet closing velocity in a bileaflet valve. Based on these results, Schreck et al. [21] suggested that

$$(\text{impact force})^{1/3} \sim \text{LV } dP/dt_{\text{closure}}. \tag{3.1}$$

and

$$(\text{impact force})^{2} \sim \text{LVP}_{\text{closure}}. \tag{3.2}$$

Equations (3.1) and (3.2) had been verified by *in situ* data collected from sheep studies.

In general, impact forces on the outlet strut legs vary greatly with cardiac activities. Impact forces are significantly higher under exercise conditions than those at rest. In pulse duplicator studies, Chandran et al. [22] reported an impact force of approximately 2000 grams (~ 4.4 lbs) with a disc closing velocity of ~ 2 m/s (~ 6.56 ft/s). Rau et al. reported impact loads reaching 2800 grams at a LV dP/dt of 4000 mmHg/s, with closing velocities up to 2.0 m/s. In animal studies, Schreck et al. reported impact forces ranging from 1780 grams (anesthetized) to 3250 grams (exercising) in sheep. These results suggest that a higher level of physical activity increases the loading of the outlet strut, which may increase the likelihood of strut fracture. Younger heart valve patients tend to assume more active lifestyles, and their hearts are more likely to function at higher maximum heart rates, increased stroke volumes, and more rapid pressure changes (dP/dt)

than those of older patients. These factors collectively subject a heart valve to more frequent heavy loading, thus increasing the chances for an outlet strut failure.

3.2.4 Valve Closure Delay

As the differential pressure between the atrium and ventricle reverses during the start of systole, the higher pressure in the ventricle causes a reverse flow of fluid through the prosthetic heart valve. In a tilting disc valve such as the BSCC valve, the valve does not close immediately to stop the back-flow. Rather, the valve is closed sometime after the onset of the reverse flow when the disc is pushed by the current to the closed position. As a result, the instant of valve closure varies as much as 20 ms comparing to a stationary cardiac cycle, both at rest and under exercise [19]. Rau et al. [20] observed that the maximum amplitude of the disc over-rotation was larger with increased closure delay. The arresting forces for the disc on the outlet strut legs was also larger with increased delay—with a 20 ms closure delay approximately doubling the impact forces on the outlet strut. This suggests that valve closure delay is highly correlated with the disc closing velocity, left ventricle pressure during closure, and the impact loads on the outlet strut legs. Incidentally, when one strut leg is separated, the disc may be arrested from contact with the base, rather than the tip, of the outlet strut. This condition results in small impact loads on the strut that are due to the acceleration forces of the disc and are not correlated to the pressure at closure [20].

In 1995, Rau et al. reported that the outlet strut loading was symmetrical for both strut legs in their studies. In the following year, Chandran et al. [21] reported that the impact

loads on the outlet struts were asymmetric, with the loading on one leg up to 25% larger than that on the other. This result may explain the single-leg separation preceding a complete outlet strut fracture.

Based on the relationships between component loads, closure delay, disc velocity, and pressure peaks, non-invasive approaches may be developed to evaluate the condition of the heart valve. One class of such approaches to determine the state of the outlet strut is by examining the closing sounds of the valve. These acoustic approaches are described later in this chapter.

3.3 Metallurgical Analyses of the Heart Valve and the Outlet Strut Weld Sites

The high impact loading of the outlet strut raised suspicions on the integrity of the strut legs and their welding sites to the flange ring. Metallurgical analyses of the alloy and the weld sites suggested that valve failures were due to material fatigue [24]-[29]. Wenzel et al. [29] reported that in their study, 22% of first-to-fail leg separations and 17% of all fractures initiated outside of the weld. Fatigue striations were also observed in all the fractured valves in the specimen collection, with evidence indicating that every fracture originated from the inflow side. In all the complete OSF cases, the fracture surface on one leg was heavily faceted and showed branching cracks while the facture surface on the other leg appeared rounded and burnished. This suggested that one leg of the outlet strut had failed before the other [25]. Welding metallurgy study concluded that no metallurgical feature of any weld investigated could be identified as contributor to the fracturing of the outlet struts [29].

Meanwhile, Xiao et al. [28] suggested an electrochemical failure mechanism of the valve in which the strut leg fractures at the less noble weld area (which includes the welding point and the surrounding heat-affected zone on the strut leg and the flange) due to stress corrosion cracking and erosion corrosion in the oxygen-rich, chloride-containing arterial blood. He suggested that the pyrolytic carbon occluder disc and Haynes 25 alloy valve material formed a bimetallic couple, essentially a dynamic electrochemical device. During the opening and closing of the valve, a current on the order of 10^{-6}A flows through the metallic parts of the valve. This current and the potential difference between the disc and the ring lower the pH of the fluid immediately surrounding the less noble weld region and break down the oxide film that covers and protects the alloy. In this slightly acidic environment, material from the weld region erodes away, resulting in reduced strength of the weld region and renders it susceptible to mechanical cracking.

Although Xiao et al. presented a highly plausible explanation into the failure of the BSCC valve, their conclusions disagree with findings from other researchers in one key area: by Xiao's electrochemical model, the downstream part of the less-noble weld area should be most affected due to its proximity to the rapidly-flowing blood electrolyte. This implies fractures should originate from the outlet side of the welds. Nevertheless, as mentioned earlier, Wenzel et al. [29] presented evidence indicating that every fracture in their study originated from the inflow side.

3.3.1 Risk Factor Analysis and Prophylactic Valve Replacement

Identification of the BSCC heart valve failure risk factors can raise the awareness of the high risk patients and potentially increase their survival chances in case of an outlet strut fracture. Epidemiological studies in Europe with selected cohorts had provided some estimates for the strut fracture risk. Results of these studies were reported from: Sweden, 1989 [55]; the Netherlands, 1992 [47]; the Netherlands follow-up report, 1996 [40]; the United Kingdom, 2001 [53], and a UK follow-up study from 2002-2003 [54], of which the results have not been published. Meanwhile, Walker et al. [41] had also conducted a United States and Canada case study on the nature of the valve fractures in relation to the manufacturing characteristics and patient physiological conditions.

Results of applying actuarial methods to the epidemiological data have shown that large valves ($\geq$ 29 mm) have consistently been found at greater risks [47]-[53]. Mitral valve implants are at least 4 times higher in fracture incidents than aortic implants [41], [47], [55]. Valves with 70° openings are 6 times more likely to fracture than 60° valves, and patients with 60° valves have a better survival rate than those with 70° valves in case of a strut failure [47]. Valves manufactured between 1981 and 1984 also have an elevated failure risk [40], [41], [59], with those manufactured between 1981 and June 1982 having the highest failure rate [50], [65]. In a United States and Canadian cohort study of 150 outlet strut fracture cases, Walker et al. [41] suggested that the hook deflection test and load deflection test used in the manufacturing quality control process might have indirectly indicated the risk of outlet strut fracture in certain valves. The hook deflection test was used from May, 1980 to January, 1982. In this test, a 7.0 kg weight was

suspended from the outlet strut and the movement of the strut was measured. In February, 1982, the load deflection test replaced the hook deflection test for manufacturing tolerance control. In the load deflection test, a 5.0 kg load was gradually applied (loading), removed (unloading), and reapplied. The amount of deflection was recorded against the applied load for two cycles of loading and unloading. The intent of this test was to verify that there was no yield of the outlet strut at 4.0 kg of loading, or less. However, Walker et al. observed an increased risk associated with increased cumulative deflection and the amount of permanent deformation of the outlet strut resulting from the testing procedures. They suggested the increased outlet strut flexibility, as indicated by the deflection test results, as a risk factor for failure.

In general, younger patients tend to be of higher risk as they are more likely to be active. In fact, patients under age 50 at the time of implant typically encounter a higher rate of outlet strut fractures and a higher cumulative risk of fatality than those above 50 years of age [47], [50].

For a BSCC heart valve patient, it is sometimes difficult to weigh the benefits and risks of an elective valve replacement surgery since an outlet strut fracture is not a guaranteed event for all BSCC heart valves. Although a SLS is a frequent precursor to OSF, not every SLS case evolves into an OSF. The development duration from a SLS to an OSF, if it indeed occurs, may last for two or more years [17], and is highly case dependent. In cases where the patient is older or is suffering from chronic diseases, increased surgical morbidity risk may prohibit a valve replacement surgery. On the other hand, for a

younger and otherwise healthy patient, a prophylactic valve replacement operation may increase his life expectancy as well as quality of life. Many researchers have attempted to develop guidelines for prophylactic replacement of the BSCC valves [55]-[63], while others have suggested patient care recommendations [64], [65]. Van Gorp et al. [62] devised a clinical prediction rule for the 30-day mortality in BSCC valve replacement surgeries. In 1997, the Bowling-Pfizer Supervisory Panel issued a set of guidelines for assessing patients with Björk-Shiley convexo-concave heart valves for elective explantation [66]. The guidelines were revised in 2002 [67] and again in 2003 [68]. The Supervisory Panel document provided guidelines for comparing the risk of valve fracture with the risk of reoperation to replace the valve. The risk of fracture is estimated based on factors such as valve size, implant position, specific manufacturing characteristics, patient gender and current age. This risk is estimated differently between the 60° and 70° valves. The risk of reoperation, on the other hand, was derived from the published cohort studies data and actual BSCC valve reoperation experiences.

Along with the guidelines, the Supervisory Panel also recommends that all BSCC heart valve patients should regularly consult their physicians. A patient and his relatives and close friends should have a good understanding of the symptoms related to an OSF, as well as knowledge of the nearest medical facility with significant experience in cardiovascular surgery in case if an emergency valve replacement is needed. The best preventive measure for the patient is early SLS detection and subsequent aggressive monitoring. This thesis presents a minimally invasive electromagnetic approach that is

best suited for diagnosing SLS conditions. In case of an OSF, prompt recognition and surgical intervention can be lifesaving.

3.4 Previous Approaches in BSCC Heart Valve SLS Detection

Since an outlet strut fracture of a BSCC heart valve is typically preceded by the separation of one of the two outlet strut legs, there have been world-wide efforts [71]-[124], with a sense of urgency, to develop reliable *in vivo* techniques to detect SLS failures in BSCC valves. Such techniques all aim to provide improved patient-level data to facilitate informed diagnostic and therapeutic decisions. At present, cineradiography is the only clinical diagnostic tool for detecting SLS in BSCC heart valve patients despite the method's less than satisfactory success rate [75]-[84]. Other approaches under development are based on modalities such as echocardiography, acoustics, ultrasound, electromagnetic acoustic transduction, and several electromagnetic methods based on eddy current phenomenon.

3.4.1 Radiographic Detection Approach

High-resolution, high energy (80-125 kVp) cineradiography has been used to evaluate the outlet strut condition of the BSCC heart valve [75]-[88]. Radiographs from two imaging profiles are obtained for each valve: a tunnel or *en face* view (the valve inclined 30° from the horizontal plane of the flange) as shown in Figure 3.14, and the left or right 60° oblique view as shown in Figure 3.15. If necessary, radiographs from the complementary 60° oblique view may also be used. The cineangiographic images are captured at approximately 30 frames per second for 3 to 4 seconds. The images are then visually

evaluated by an expert review panel for SLS cues: gap and offset on the outlet strut. Gap refers to the opening when the outlet strut leg separates from the flange, and offset refers to the deviation of the strut leg from its central axis of insertion (e.g., see Figure 3.5). The expert reviewers rate each radiograph on a 0 to 5 grade according to Table 3.1. Although the review panel typically consists of board-certified experts in cardiology, cardiothoracic surgery, and radiology, the assessment of radiographs tend to be both reviewer and valve specific. In one phantom model study [84] of 6 manufactured SLS and 3 IOS valves, 3 of the fractured valves were either not detected or rarely detected. The study also reported a high false positive rate and increased human fatigue errors after viewing more than 120 radiographs.

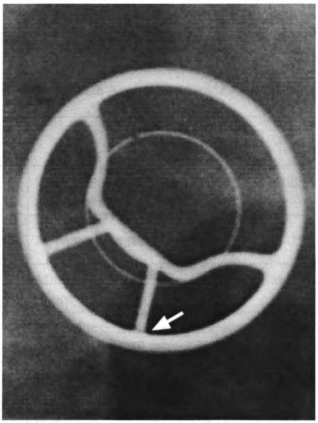

Figure 3.14 Cineradiographic tunnel view of a BSCC heart valve showing a case of "definite SLS" assessment (arrow). Adapted from [81].

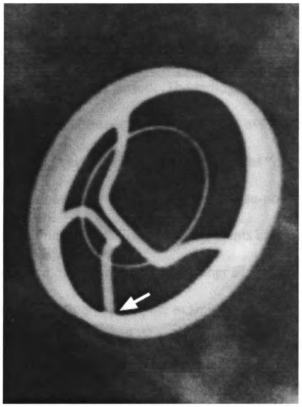

Figure 3.15 Cineradiographic oblique view of a BSCC heart valve showing a case of "definite SLS" assessment (arrow). Adapted from [81].

Table 3.1 Definition of Image Assessment Grades for Visual Interpretation of Cineangiographs

Image Assessment Grade	Description
0	Suboptimal examination: insufficient image contrast or strut base display
1	Apparently normal
2	Minimally suspect: fractured appearance in 1 or 2 frames in one view only
3	Suspicious: fractured appearance in several frames in one view, or in 1 or 2 frames in two views
4	Probable fracture: fracture appearance in multiple frames in 1 view, or several frames in 2 views
5	Definite fracture: fractured appearance in multiple frames in more than 1 view

In a clinical study [81] at the William Beaumont Hospital at Royal Oak, Michigan, 315 BSCC heart valve patients were examined with a cineradiograph system. Each patient is examined 2 or 3 times over a 9-month period. The radiographic assessments were later confirmed in 21 cases by physical inspection of the valves, available due to explantation or autopsy. Ten of the eleven valves radiographically rated as "probable" or "definite SLS" were confirmed, with one "probable" case being a false-positive. On the other hand, two patients who had negative radiograph assessments experienced strut fractures—both patients died. It was not known whether SLS conditions existed in either or both of the cases during the cineradiographic examinations

In a follow-up study [82], the trials at William Beaumont Hospital were expanded to the Stanford University Medical Center and the Western Infirmary in Glasgow, Scotland. From both studies, a total of 964 BSCC valves were imaged (828 mitral valves, 136 aortic valves). Twenty-six SLS valves were correctly identified. In addition, there were 4 false-positive and 1 false-negative assessments.

In order to reduce reviewer-dependency and inter-reviewer variability, many quantitative approaches ([77], [80], [83], and [85]) have been developed for the automatic objective and reproducible assessment of BSCC heart valve outlet strut cineradiographs. These approaches employ image processing techniques such as temporal registration, object translation and rotation correction [77], segmentation and principal axis transformation [80], with quantitative metrics such as decrease in pixel intensity (DIPI) ratio, gap half-width [83], normalized pit depth (NPD) and the depth-sigma ratio (DSR) [85]. In [83],

logistic regression was used to identify a statistical model for the prediction of SLS in the post-processing of radiographic images. This approach has accuracy equal to that of a panel of expert subjective reviewers. Meanwhile, Vrooman, et al. [85] developed a software package for processing BSCC heart valve cineradiographic images. This package had a reported accuracy of 100% with limited phantom studies. The complete performance data of this package in clinical tests were not provided in the report [85].

The results from the phantom model studies and clinical trials suggest that although the feasibility of SLS detection by cineradiography has been demonstrated, the accuracy of the method has yet to be defined [82]. The resolution and capacity of present x-ray technology maybe inadequate for guaranteed strut fracture detectability [84]. Current clinical cineradiographic systems may detect as little as 25% of the single-leg separated BSCC valves [86]. Visual radiograph assessment also has high inter-observer variability. Extensive training in radiograph interpretation is, therefore, required for accurately identifying SLS conditions [81], [86]. Although automatic quantitative assessment algorithms and software packages appear promising, further development and verifications are needed before such algorithms may be applied clinically.

At present, the Penn State Milton S. Hershey Medical Center in Hershey, Pennsylvania, USA is the only cineradiographic imaging center for BSCC heart valve patients. This screening program is sponsored by the Bowling-Pfizer Supervisory Panel [89].

3.4.2 Echocardiography, Acoustics, Ultrasound and Electromagnetic Acoustic Transduction Based Approaches

3.4.2.1 Echocardiographic Detection Approach

Two-dimensional echocardiography had been demonstrated in diagnosing complete BSCC heart valve outlet strut fractures [71], [72]. In such cases, the dislodged echo-dense occluder disc is often seen moving rapidly and chaotically in the left ventricle. Beyond a diagnostic tool for OSFs, efforts to use echophonocardiography to detect outlet strut single-leg separations had not achieved much success [73], [74]. The most recent reported project involving the application of echocardiography on BSCC heart valves was the work conducted by the Cleveland Clinic [89] to characterize three-dimensional motion of the valve by computed tomography and echocardiography. This work was supported by the Bowling-Pfizer Supervisory Panel.

3.4.2.2 Acoustic Detection Approaches

In a mechanical heart valve prosthesis such as the BSCC heart valve, the periodic opening and closing of the occluder disc generates a clicking sound that is audible over a distance external to the patient. It has been postulated [90]-[122] that a significant alteration of valve properties such as obstruction of the occluder or fracture of the valve would change the frequency content and intensity of the opening and closing sounds. Based on this assumption, much work has been focused on acquiring and analyzing the transthoracic prosthetic heart valve sounds for the non-invasive diagnosis of the functioning and structural integrity of the valve. For instance, Nygaard et al. [95] investigated the optimal position for recording *in situ* heart valve sounds and determined

that the precordial area of the fourth and fifth left intercostal space on the chest near the sternum would allow the transmission of prosthetic heart valve sounds from the heart to the chest surface with the lowest attenuation and a minimum interference from respiration. Others [106] had also used the second intercostal space adjacent to the right sternal border for recording aortic valve sounds. These recording locations and the immediate surrounding areas on the chest have been commonly used for acquiring *in situ* heart valve sounds described in the literature. Several of these reports are described in the following sections.

The acoustic approaches for detecting SLS in BSCC valves may be divided into three categories: the low frequency, resonant frequency, and acoustical data recognition approaches. The low frequency approaches ([90]-[93], [96], [105] and [103]) examine the frequency response of the heart valve from zero to approximately 1.5 kHz to identify the condition of the outlet strut. The resonant frequency approaches ([94], [97], [98], [99], [106] and [107]) determine the condition of the outlet strut by detecting its first natural resonant frequency. The acoustical recognition approaches apply signal processing and pattern recognition techniques to process and classify a heart valve sound recording as from either an IOS valve or one with SLS.

Stein et al. [90] developed a low frequency approach by examining the opening sounds of two BSCC heart valves in a pulse duplicator and suggested that the dominant frequency of the intact valve was 234 Hz and that for the fractured valve (with a through-and-through cut) was 78 Hz. Durand et al. [96] demonstrated a low frequency (0-500 Hz)

analysis approach combined with a pattern classifier such as the K-means or Bayesian classifier for classifying the opening sounds both in a pulse duplicator (6 IOS, 6 SLS valves) and in sheep (11 IOS, 16 SLS valves). They achieved 83% correct classification for the *in vitro* tests and 82% accuracy in a sheep study. In a separate report [105], Durand et al. demonstrated anther low frequency outlet strut condition diagnosis approach based on the ratio of the high frequency area to the low frequency area of the averaged and amplitude-normalized opening sound spectrum. A cut-off frequency of 500 Hz was shown to generate ratios that provided the most robust separation of the two classes of valves. They tested 4 SLS and 24 IOS valves and achieved 96.4% correct classifications, with one SLS valve incorrectly classified. Meanwhile, Walker and Scotten [92], [93] reported the feasibility of identifying fractured valves from their closing sounds, and Sava et al. [103] reported that the main part of the energy in the *in vivo* closing sounds was located below 2 kHz.

Eberhardt et al. [69] and Chia [70] had separately performed finite element analyses of BSCC heart valves with different outlet strut conditions. Their work suggested that the fundamental resonance mode for an intact outlet strut was between 7000-8000 Hz. They had also reported that the fundamental vibration frequency of a fractured minor strut with a hinged joint was approximately 4000 Hz, while a strut with a non-contacting fracture had a resonant frequency between 2000-2700 Hz. It is, therefore, feasible to determine the condition of the outlet strut by detecting its fundamental vibration frequency.

With knowledge of the estimated resonant frequency ranges, Plemons et al. [94] demonstrated a technique for identifying IOS valves in time-windowed signals by examining the area after the 1st 95% of the energy spectrum. In another report [98], Plemons and colleagues concluded from observations of sheep experiments that the IOS resonant frequency remained constant under changing physiological conditions (e.g., exercise versus resting) and observation times, whereas the occluder disc tonals showed significant variations. They suggested that this feature of the IOS valve maybe used to distinguish its resonant frequency from interfering disc tonals. In a companion report [99], Plemons et al. analyzed the closing sounds recordings from 24 confirmed clinical cases using spectral techniques. They selected six characteristic features of the first resonant peak of the intact valve in the time-windowed, ensemble averaged spectrum of the recordings. Their technique correctly classified 13 of 14 intact valves, and 10 of 10 fractured valves.

Dow et al. [106] extended Plemons' work and developed a time-frequency representation (TFR) technique for detecting the presence or absence of the intact outlet strut tonal component around the 7-8 kHz band. The technique applies overlapping time-windows of approximately 5.5 ms to each closing event and calculates the spectral density function for each of these signals. These calculations are then repeated for all qualifying events in a recording session and an ensemble average is obtained. The peak density within the target frequency band is then selected as the TFR for this valve. In a test of 32 valve recordings (16 intact, 16 SLS valves), Dow's technique correctly identified all SLS

valves, and 11 of 16 IOS valves (accuracy = 84.4%). Dow suggested the technique as a prescreening tool for radiographic diagnosis.

Without restricting the frequency range of interest, the acoustical recognition approach applies signal processing and pattern recognition techniques in classifying the heart valve sound recordings. For example, Eberhardt et al. [96], [104] examined transthoracic recordings of BSCC heart valve closing sounds from patients and applied statistical techniques to process the recordings. They applied the Volterra expansion to the coefficients of the processed data to identify characteristic features of the data, and used an artificial neural network to classify the features as belonging to either an IOS or SLS valve. In blinded and leave-one-out[1] tests, Eberhardt's technique classified 33 SLS and IOS "gold standard" valves correctly [104].

Scarbrough et al. [100], on the other hand, applied a short-time Fourier Transform-based approach to classify the closing sounds from the phonocardiograms of 22 BSCC (12 IOS, 10 SLS) valves. The approach was shown to classify all but two of the processed signals correctly. The misclassified signals belonged to an IOS and SLS valve, respectively.

Candy et al. [101], [102] suggested two elaborate acoustic signal processing systems for classifying heart valve opening sounds recordings. The first technique represented the data in terms of spectrograms that displayed the individual sounds as a function of heart beat number and temporal frequency. This spectral technique extracted potentially

[1] In a leave-one-out test, the valve being tested is not used in the training data set.

discriminatory features of each signal that were subsequently processed by a statistical classifier for valve condition identification. The second technique was a parametric approach in which a heart valve sound generation model was constructed. Heart valve closing sounds were synthesized and collected into a database. The data were then used to develop both an optimal classifier and an adaptive classifier implemented with a probabilistic neural network. In a test with 7 IOS and 10 SLS valves, the optimal detector was able to correctly classify 15 of 17 valves (88.2%), misidentifying one IOS and one SLS valve. The adaptive probabilistic neural network was able to classify 14 of 17 valves correctly (82.4%), misidentifying 3 SLS valves.

Acoustic diagnosis approaches generally suffer from the following practical issues. First, the heart valve sound is influenced by its surrounding biological structures which exhibit frequency dependent sound transmission and resonance properties. Second, respiration induces variance in transthoracic sound propagations from the valve to the chest surface. Third, optimal sensor locations need to be determined. And finally, the time or frequency domain processing windows used in the algorithms need to be defined.

Although acoustic approaches present potentials in diagnosing SLS failures in BSCC heart valve patients, the overall accuracy must be improved before they can be adopted clinically as the implications for a patient with ether a false-positive or false-negative diagnosis can be serious or even life-threatening.

3.4.2.3 Ultrasonic Detection Techniques

Active acoustic methods, including ultrasonic and electromagnetic acoustic transduction techniques [108]-[122], have been proposed to improve the reliability of detecting BSCC heart valve outlet strut fractures. Shawkat et al. [108] devised a technique to assess the condition of the heart valve by analyzing its ultrasonic "clicks," or signatures, of the detected signal. Rambod et al. [109]-[111] proposed an Ultrasound Burst-Spectrography (UBS) system in which bursts of two ultrasonic pressure waves at approximately 3.1 MHz were focused onto the outlet strut. The pressure waves exert forces on the strut and cause it to vibrate. The frequency of one of the ultrasonic waves is swept from 3.101–3.110 MHz such that the vibration frequency of the outlet strut varies from 1–10 kHz. The responses are measured by a hydrophone positioned in the vicinity of the heart valve. When the vibration frequency coincides with the fundamental resonance frequency of the outlet strut, a strong response is detected. The frequency of this response may then be used to infer the condition of the outlet strut based on the results of Chia [70] and Eberhardt [69]. The UBS approach had demonstrated 100% classification accuracy in aortic-model pulse duplicator studies of 11 IOS, 6 explanted SLS and 2 manufactured SLS valves.

Although these results appear to merit further development, Rambod's approach is, at the time of this writing, experimental and has yet to be developed into a clinical system. The most important obstacle of this approach is the *in vivo* focusing of the ultrasonic waves onto the outlet strut. The movement of the heart within the thoracic cavity during cardiac cycles and the hemodynamics inside the ventricle pose the challenging tasks of targeting

and tracking the outlet strut by the ultrasound waves, as well as maintaining the proper focal distance between the transducer and the outlet strut.

Van Neer, et al. [112] proposed another ultrasonic fracture detection approach based on the assumption that a broken outlet strut leg will have increased movement compared to either the intact leg or the flange. *In vitro* studies of this approach were conducted in a pulse duplicator using a 10 MHz ultrasonic transducer. Focused ultrasound waves were directed at a particular leg of the valve. The movement of the outlet strut was obtained by correlating the received signals with the excitation signal to produce the time delays of the echoes. These time-of-flight differences of the received echoes were then used to indicate the amount of movement of the target strut leg. Van Neer reported that the amplitude of movement between both legs of an IOS valve was approximately 9.2 μm ± 0.1 μm. In the case of an SLS valve, the amplitude of movement of the fractured leg was 12 μm ± 1.6 μm while that for the intact leg was 8.6 μm ± 0.1 μm. These results showed that although there was a difference in movement amplitudes between an intact and a fractured outlet strut leg, the difference was so small such that a definitive determination on the outlet strut condition is difficult. The damping of the fractured leg's movement also decreased the accuracy of the approach. Also, it is generally challenging to focus the ultrasonic wave onto a specific location on the valve. There are also potentially high levels of movements from other sources within the body that manifest themselves as noise in the received signal.

3.4.2.4 Electromagnetic Acoustic Transduction Based Approach

Udpa et al. [119]-[123] proposed a beat frequency electromagnetic acoustic transduction (EMAT) based technique to actively excite the outlet strut for determining its fundamental resonance frequency. The technique uses two pairs of excitation coils (coil A and B) each excited by an alternating current source. The coils are placed around a patient and oriented in the manner shown in Figure 3.16 (the patient is not shown in this figure for clarity). Coil pair A, excited at frequency f_1, induces currents in the heart valve with the same frequency. Coil pair B, excited at frequency f_2, generates a magnetic field in the vicinity of the valve that interacts with the induced current in the heart valve. A Lorentz force is produced and acts on the heart valve. The amplitude of the force is proportional to the flux densities of coils A and B and the frequency f_1. The force has two frequency components at $f_1 + f_2$ and $f_1 - f_2$, respectively. The frequencies f_1 and f_2 are chosen in a manner such that $f_1 + f_2$ is significantly above the dominant resonant modes of any of the valve components, while the beat frequency $f_1 - f_2$ is close to the resonant mode of an intact or fractured outlet strut. In practice, coil A is operated in a tone burst mode, while the frequency f_2 is swept such that the beat frequency varies over a range of approximately 10 kHz, coinciding with the range of expected outlet strut modal frequencies for IOS and SLS valves. Transthoracic vibration recordings are made during a short period soon after the excitation tone burst is switched off. Signal processing algorithms are then applied to the recordings to extract the dominant frequency and determine the condition of the outlet strut.

In a prototype unit, the beat frequency EMAT based approach demonstrated 100% accuracy in classifying 34 BSCC heart valves (14 IOS, 11 explanted SLS and 10 manufactured SLS valves). Although these results appear promising, the approach has yet to be developed into a clinical-scale system. Successful completion of the clinical unit may lead to a noninvasive alternative to the current prescreening and diagnostic systems for SLS failures in BSCC heart valves.

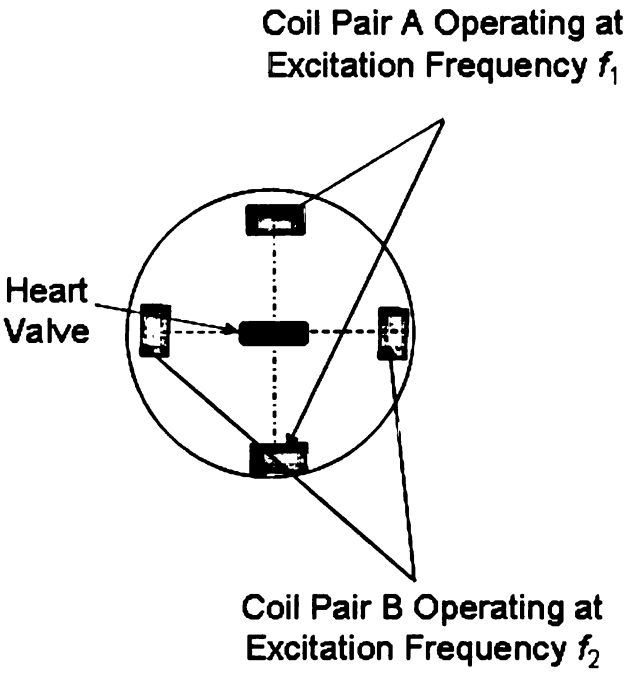

Figure 3.16 Orientation of the EMAT excitation system. Patient not shown for clarity. Adapted from [121].

3.4.3 Electromagnetic Approaches

Evaluation techniques ([113]-[119], [122]-[124]) exploiting the electromagnetic behavior of a BSCC heart valve have emerged as potential tools for detecting a single-leg separated outlet strut. Two of the techniques, proposed by Amin [118] and Lepelaars et

al. [113]-[117], respectively, are described in the following sections. The remaining chapters of this thesis describe the third and the most promising method called the gradiometer-based examination approach.

3.4.4 Differential Eddy Current Approach

Amin [117] applied differential eddy current testing techniques to evaluate the condition of the outlet strut in a BSCC heart valve. (A detailed treatment of differential eddy current testing is beyond the scope of this dissertation. Readers are referred to references such as [125] and [126] for more information.) In this approach, a differential eddy current probe (Figure 3.17) is positioned in the vicinity of the outlet strut as shown in Figure 3.18. Figure 3.19 shows the electrical circuit diagram of a differential eddy current probe, which functions as both the excitation source and the sensor. Figure 3.20 shows signal examples from an IOS valve and one with SLS, respectively, when the probe is positioned and aligned properly as shown in Figure 3.18. The condition of the outlet strut is inferred from the signal amplitude from the probe. In a laboratory test, the differential eddy current probe approach achieved 100% classification accuracy with 5 IOS and 10 SLS valves.

One disadvantage of the differential eddy current probe approach is that it is highly sensitive to the position and orientation of the sensor in relation to the outlet strut. As is typical with eddy current testing, this approach is affected by the distance and the alignment angle between the probe and the outlet strut. The effects of probe movement

inside the heart and the constantly varying distance between the probe and the heart valve due to the cardiac cycle must be addressed before this approach can be applied clinically.

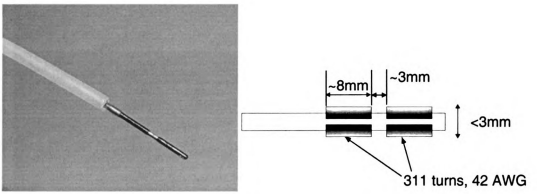

Figure 3.17 A differential eddy current probe for detecting the outlet strut condition of a BSCC heart valve. Adapted from [118].

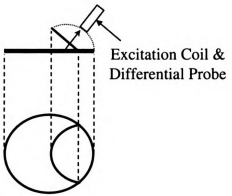

Figure 3.18 Differential eddy current probe detection approach. Adapted from [118].

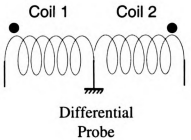

Figure 3.19 Circuit diagram of the differential eddy current probe. Adapted from [118].

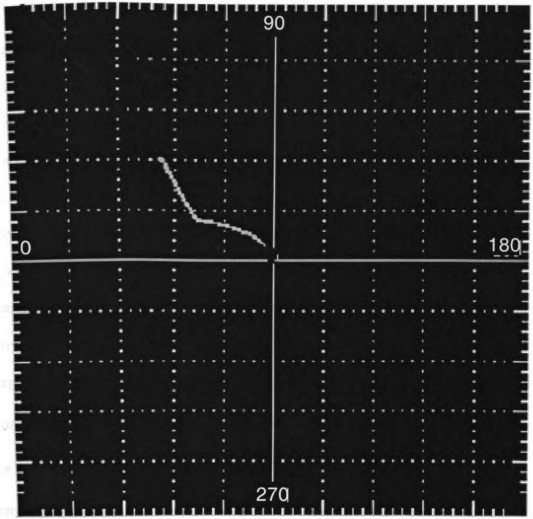

Figure 3.20 Examples of differential eddy current probe signals from an *in vitro* test. The large amplitude signal is from an IOS valve and the small amplitude signal is from a SLS case. Adapted from [118].

3.4.5 Catheter-Based Antenna Approach

Lepelaars et al. [113] proposed a catheter-based antenna for detecting complete and partial fractures in BSCC heart valves. In this approach, a pulsed current is injected into a small transmitting antenna placed in front of the heart valve. The magnetic field generated by this antenna induces a current in the flange ring as well as in the loops formed between the inlet and outlet struts with the ring. The transmitting antenna is then used as the receiving antenna to detect these currents. When the valve is intact, the

receiving antenna signal shows a stationary behavior at late times (the time period after the initial over-shoot and oscillations due to the pulsed excitation). When the valve is fractured, the antenna output signal is small as there is no continuous current flow in the valve, and that the transient current is terminated after the initial oscillations. A partial valve fracture will result in an exponential decay superimposed on a constant current, with the decay rate proportional to the severity of the fracture. Lepelarrs et al. had performed detailed analytical and numerical studies [113]-[116] on simplified models that use thin-wire loops to represent the heart valve and the transmitting-receiving antenna. In these models, electrical impedances are inserted into the wire-loops representing the heart valve to simulate various flaw depths in the valve. An intact valve is represented by an impedance of 0 Ω, while a completely broken valve is represented by an impedance of 10^6 Ω. Figure 3.21 shows the analytical modeling results with various flaw depths (impedance valves). Figure 3.22 shows the results from Figure 3.21 normalized with respect to the $Z_1=10^6$ Ω reference signal.

Although the initial results from Figure 3.21 and Figure 3.22 appear promising, the catheter-based antenna approach is still in early development stage. Some of the key issues that must be addressed include:

1. The impedance representation of fractures in a BSCC valve must be verified;
2. More realistic models must be developed to replace the thin-wire models used;
3. The sizes of the thin-wire models should match those of actual BSCC heart valve components (the flange ring and the inlet and outlet struts);

4. The performance of the approach taking into consideration the overlapping natural of the flange ring and inlet and outlet strut loops;
5. The specific indication of a single-leg separation in the outlet strut;
6. The optimal location of the antenna must be determined;
7. Clinical aspects of the system such as the size versus sensitivity of the antenna, and the effect of the heart's motion on the detection system must be examined.

Until these issues are addressed satisfactorily, the catheter-based antenna approach is not ready for clinical applications.

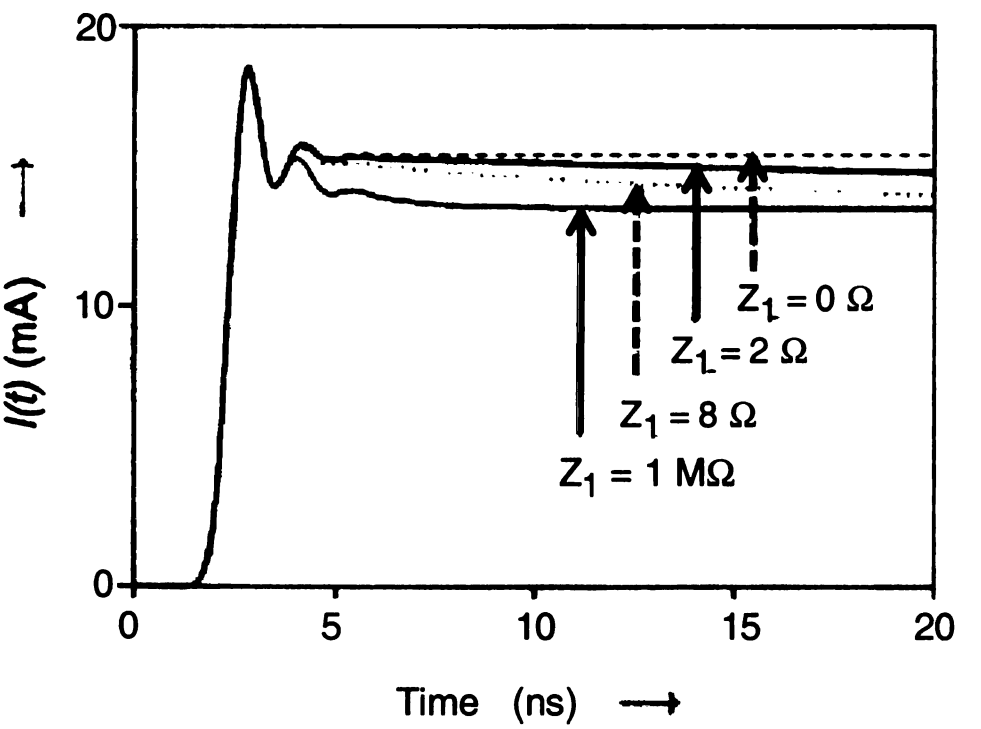

Figure 3.21 Induced current along a wire-loop model of a heart valve. The different impedance valves (Z_1's) represent various flaw depths. Adapted from [116].

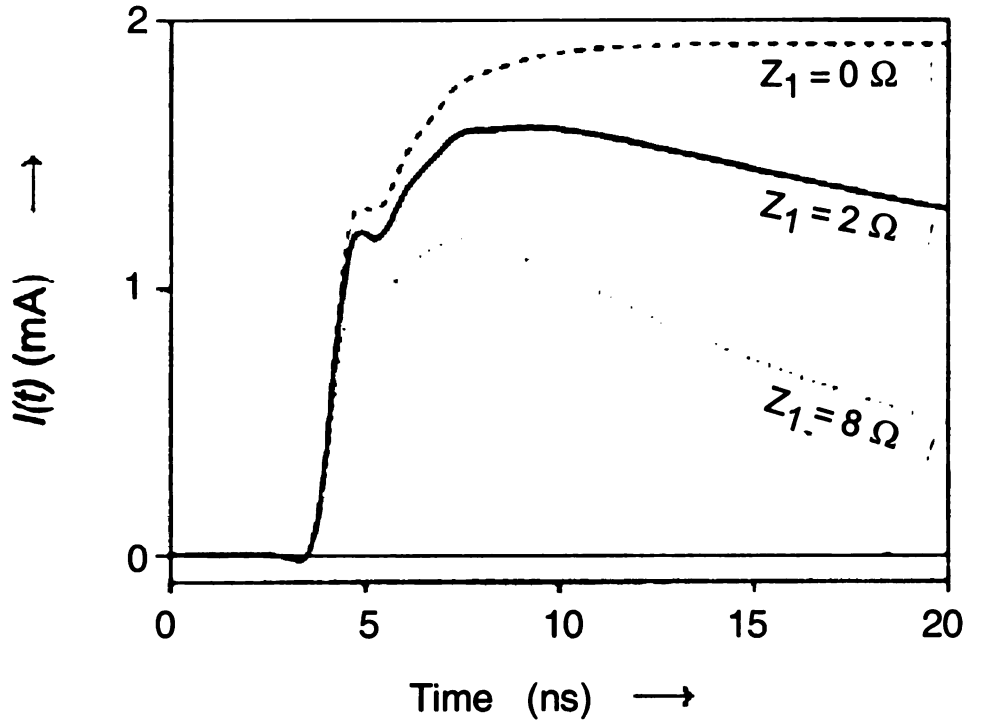

Figure 3.22 Results in Figure 3.21 normalized with respect to the $Z_1=10^6\ \Omega$ signal. Adapted from [116].

3.5 A Novel Approach for SLS Detection in BSCC Heart Valves

The radiographic, acoustic and electromagnetic approaches described above all suffered from a lack of accuracy, with cardiac motions frequently introduce additional errors. The following chapters of this thesis describe a novel electromagnetic approach, called the gradiometer-based method, for detecting single-leg separations in BSCC heart valves. This approach is highly accurate and is not affected by the movement of the heart (and the heart valve).

CHAPTER 4. MATHEMATICAL MODEL

A mathematical model for the gradiometer-based method has been developed to facilitate the design and characterization of system components and to provide deeper insights into the examination technique. The model expresses the output of the gradiometer as a function of physical parameters such as the characteristics of the excitation magnetic field and the location and orientation of the heart valve in relation to both the excitation field and the gradiometer. The model also relates the gradiometer output signal to the condition of the outlet strut. In the following discussions, a general case is first developed for the scenario when the gradiometer is positioned arbitrarily in front of the outlet strut loop. Then, the results are presented for the special case when the gradiometer is located on the axis of the outlet strut loop and the sensor coils are positioned parallel to the plane of the loop. This special case and the underlying orientation and positional assumptions simplify the problem and permit the development of a closed-form solution for the gradiometer signal. The simplified model is used in Chapter 7 to provide a starting point for designing the gradiometer and understanding how the various physical parameters affect system performance. The mathematical model shows the gradiometer output as a function of the outlet strut condition, and thus demonstrates the feasibility of the gradiometer-based method for characterizing the outlet strut integrity.

4.1 Induced Current in the Outlet Strut

In the gradiometer-based method, the heart valve is submerged in a time-varying uniform magnetic field, $\mathbf{B}_H$, created by a Helmholtz coil. The valve is oriented such that the flange ring is parallel to the applied field as shown in Figure 4.1. In this fashion, the flange intercepts the least amount of the magnetic field and minimal eddy current is induced in the ring. Meanwhile, the outlet strut forms a closed loop with the flange and protrudes away from the plane of the heart valve at a 42° [151] angle[1]. This outlet strut loop intercepts the applied magnetic field and an electromotive force (EMF), v_S, is induced in the loop according to *Faraday's Law*:

$$\begin{aligned} v_S(t) &= -\frac{d}{dt} N_S \psi_S \\ &= -\frac{d}{dt} \int_{S_S} \mathbf{B}_H \cdot d\bar{\mathbf{S}}_S \quad \text{V} \end{aligned} \tag{4.1}$$

In (4.1), the number of turns, N_S, is equal to 1 for the strut loop. ψ_S is the magnetic flux linking the loop, and $\mathbf{S}_S$ is the projected or effective area of the strut loop that intercepts the applied field. The orientation of this field is shown in Figure 4.1. In Figure 4.2, the component of $\mathbf{B}_H$ that is normal to the plane of the strut loop is

[1] This angle is for a 60° BSCC valve. The outlet strut angle is different between a 60° and 70° valve. Although the discussions in this thesis focus on the 60° valves, the design, results and conclusions presented for the gradiometer-based detection system herein are equally applicable for the 70° valves.

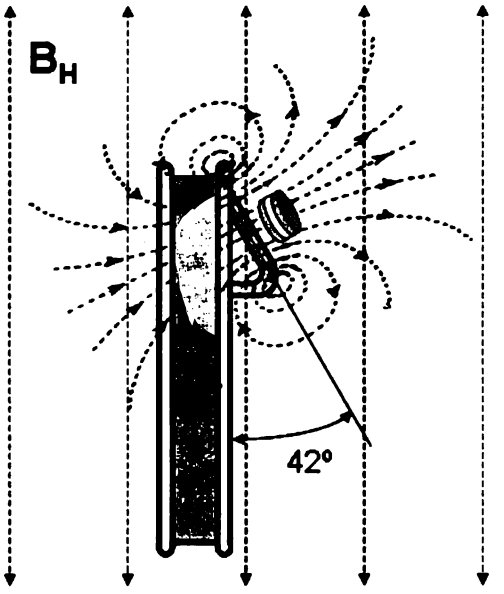

Figure 4.1 The heart valve is submerged in a uniform magnetic field and oriented in a fashion such that the flange ring intercepts the least amount of the applied field, while the outlet strut loop intercepts the maximum amount of the field.

$$\mathbf{B}'_{\mathrm{H}} = |\mathbf{B}_{\mathrm{H}}|\sin(\alpha)\hat{\mathbf{a}}_{\mathrm{H}} \tag{4.2}$$

Substituting (4.2) into (4.1) and integrating the contributions from the incremental regions $d\vec{\mathbf{S}}_{\mathrm{S}}$ over the effective strut loop area $\mathbf{S}_{\mathrm{S}}$ yields:

$$\begin{aligned} v_{\mathrm{S}}(t) &= -\frac{d\mathbf{B}'_{\mathrm{H}}}{dt}|\mathbf{S}_{\mathrm{S}}| \\ &= -\frac{d}{dt}|\mathbf{B}_{\mathrm{H}}||\mathbf{S}_{\mathrm{S}}|\sin(\alpha) \\ &= -\frac{d}{dt}B_{\mathrm{H}}S_{\mathrm{S}}\sin(\alpha) \end{aligned} \tag{4.3}$$

where $B_{\mathrm{H}} = |\mathbf{B}_{\mathrm{H}}|$ is the amplitude of the applied magnetic field at the outlet strut, $S_{\mathrm{S}} = |\mathbf{S}_{\mathrm{S}}|$ is the effective area of the strut loop, and α is the angle between the outlet strut plane and the direction of the applied magnetic field. Equation (4.3) is valid when the heart valve is oriented as shown in Figure 4.1. In this manner, the outlet strut loop

presents the maximum effective area for intercepting the applied magnetic field. If the outlet strut is rotated β degrees with respect to the applied field as depicted in Figure 4.3, the effective area will decrease and the induced EMF in the strut loop will subsequently be reduced by a factor of cos(β) such that

$$v_s(t) = -\frac{d}{dt} B_H S_S \sin(\alpha)\cos(\beta) \tag{4.4}$$

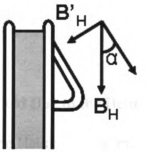

Figure 4.2 Current is induced in the outlet strut loop due to the component of the applied magnetic field that is normal to the plane of the loop

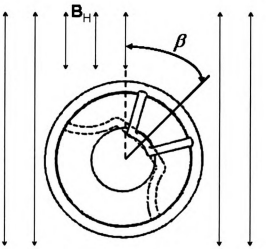

Figure 4.3 If the heart valve is rotated β degrees with respect to the applied magnetic field, the effective area of the outlet strut loop for intercepting the applied field will be reduced.

The current, i_S, in the strut loop due to the induced EMF is given by *Ohm's Law*:

$$i_S(t) = \frac{v_S(t)}{R_S} \tag{4.5}$$

$$i_S(t) = -\frac{d}{dt}\frac{B_H S_S \sin(\alpha)\cos(\beta)}{R_S} \tag{4.6}$$

where R_S is the resistance of the outlet strut loop. This resistance is a function of the conditions and material characteristics of the closed-loop formed by outlet strut and the flange. The relation between the outlet strut condition and the strut loop resistance will be discussed later in this chapter.

4.2 Magnetic Field Due to the Helmholtz Coil System

To obtain B_H (the magnitude of the Helmholtz coil magnetic field, $\mathbf{B}_H$), let the excitation current be a sinusoidal signal, i_H, with amplitude I_H and frequency f_H Hz, such that

$$i_H(t) = I_H \sin(\omega_H t) \quad \text{A} \tag{4.7}$$

where $\omega_H = 2\pi f_H$. With a radius r_H and N_H turns in each coil, the magnitude of the magnetic field at the center of the excitation coil system is given by the Helmholtz coil equation [129]:

$$B_H = \frac{8\mu_0 N_H}{5\sqrt{5} r_H} i_H$$

$$B_H(t) = \frac{8\mu_0 N_H}{5\sqrt{5} r_H} I_H \sin(\omega_H t) \tag{4.8}$$

The direction of this field is parallel to the axis of the coils. Substituting (4.8) into (4.6) yields

$$i_S(t) = -\frac{d}{dt}\left(\frac{8\mu_0 N_H I_H}{5\sqrt{5} r_H}\frac{S_S}{R_S}\sin(\omega_H t)\sin(\alpha)\cos(\beta)\right) \tag{4.9}$$

In practice, the angles α and β are functions of time synchronized with the cardiac cycle. In which case, (4.9) can be expressed as

$$i_S(t) = -\frac{d}{dt}\left(\frac{8\mu_0 N_H I_H}{5\sqrt{5} r_H}\frac{S_S}{R_S}\sin(\omega_H t)\sin(\alpha(t))\cos(\beta(t))\right) \tag{4.10}$$

On the other hand, *in situ* movement study[1] reveals that the heart valve motion due to the cardiac activity involves primarily translational movements that are orthogonal to the applied magnetic field. In this case, α and β may be assumed stationary and (4.9) may be simplified to:

$$i_S(t) = -\frac{8\mu_0 N_H I_H}{5\sqrt{5} r_H}\frac{S_S}{R_S}\omega_H \sin(\alpha)\cos(\beta)\cos(\omega_H t) \tag{4.11}$$

4.3 Magnetic Field Due to the Outlet Strut Loop Current

The induced current in the strut loop creates a magnetic field, $\mathbf{B}_S$. To describe this field, the outlet strut loop is approximated as a single-wire circular coil. The radius r_S of the circular coil is selected such that the area enclosed by the coil is equal to the projected area of the outlet strut loop:

---

[1]Results of the *in situ* heart valve movement study from cinegrams are discussed in Chapter 9.

$$S_S = \pi \cdot r_S^2 \tag{4.12}$$

With the circular coil approximation, the magnetic field observed at an off-axis point P (Figure 4.4) may be obtained by determining the vector potential of the loop. Since $\nabla \cdot \mathbf{B}_S = 0$, the magnetic flux density may be expressed as the curl of the magnetic vector potential, $\mathbf{A}_S$, such that

$$\mathbf{B}_S = \nabla \times \mathbf{A}_S \tag{4.13}$$

From *Biot-Savart's Law*, the vector potential due to a differential current element, $d\mathbf{i}$, on the circular loop L_S is [184]

$$\mathbf{A}_S(r', z') = \frac{\mu_0 i_S}{4\pi} \int_{L_S} \frac{d\mathbf{i}}{W} = \frac{\mu_0 i_S}{4\pi} \int_{L_S} \frac{r_S \mathbf{u}_{\varphi'}}{W} d\varphi' \tag{4.14}$$

In (4.14), the variables r' and z' belong to a local coordinate system in which the z' axis is normal to the plane of the outlet strut loop and the x'-y' plane coincides with the strut loop plane. The length W is the distance between the wire loop and point P. The cylindrical coordinate variables (r', φ', z') are given by $r' = \sqrt{x'^2 + y'^2}$, $\varphi' = \tan^{-1} \frac{y'}{x'}$ and $z' = z'$. The origin of this local coordinate system is located at the center of the strut loop as shown in Figure 4.4. In this figure, the vector potential due to the differential current at point m is largely cancelled by the contributions from the differential current at point n due to symmetry about the $\varphi' = 0$ (x'-z') plane. The resulting net potential at P is perpendicular to that plane, or more generally, in the direction of $\hat{\mathbf{a}}_{\varphi'}$. Considering the contributions from all the symmetric differential-current pairs on the loop, the resulting

magnetic vector potential, $\mathbf{A}_S$, of the loop will also be in the $\hat{\mathbf{a}}_{\varphi'}$ direction, with a magnitude, A_S, given by

$$A_S(r',z') = \frac{\mu_0 i_S}{4\pi} \int_0^{\pi} \frac{2r_S \cos\varphi'}{\left(r_S^2 + r'^2 + z'^2 - 2r_S r' \cos\varphi'\right)^{\frac{1}{2}}} d\varphi' \tag{4.15}$$

Equation (4.15) can be rewritten as [184]-[187]

$$A_S(r',z') = \frac{\mu_0 i_S}{k\pi} \left(\frac{r_S}{r'}\right)^{\frac{1}{2}} \left[\left(1 - \frac{k^2}{2}\right) K(k) - E(k)\right] \tag{4.16}$$

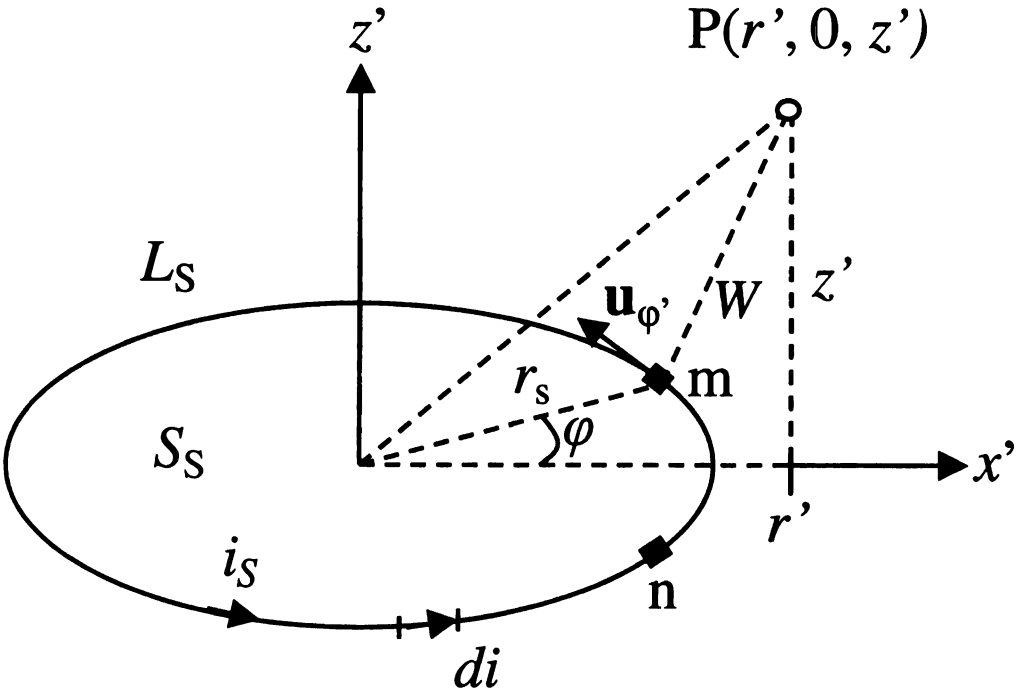

Figure 4.4 Off-axis magnetic field due to the outlet strut (approximated by a circular current loop).

where

$$k = \left(\frac{4 r_S r'}{(r_S + r')^2 + z'^2} \right)^{\frac{1}{2}} \tag{4.17}$$

and $K(k)$ and $E(k)$ are the complete elliptic integrals [188], [189] of the first and second kind, respectively. The two integrals are defined as

$$K(k) = \int_0^{\frac{\pi}{2}} \frac{1}{\left(1 - k^2 \sin^2 \theta\right)^{\frac{1}{2}}} d\theta \tag{4.18}$$

$$E(k) = \int_0^{\frac{\pi}{2}} \left(1 - k^2 \sin^2 \theta\right)^{\frac{1}{2}} d\theta \tag{4.19}$$

From the expression of A_S and equations (4.17)-(4.19), the components of the magnetic field, $\mathbf{B}_S$, due to the outlet strut current (as approximated by a circular current loop of radius r_S) are given by [184], [185]

$$B_{Sr'} = \frac{\mu_0 i_S}{2\pi} \frac{z'}{r' \left[(r_S + r')^2 + z'^2\right]^{\frac{1}{2}}} \left[\frac{r_S^2 + r'^2 + z'^2}{(r_S - r')^2 + z'^2} E(k) - K(k) \right] \tag{4.20}$$

$$B_{Sz'} = \frac{\mu_0 i_S}{2\pi} \frac{1}{\left[(r_S + r')^2 + z'^2\right]^{\frac{1}{2}}} \left[\frac{r_S^2 - r'^2 - z'^2}{(r_S - r')^2 + z'^2} E(k) + K(k) \right] \tag{4.21}$$

Equations (4.20) and (4.21) describe the magnetic field due to the induced current i_S in the outlet strut for a location off-axis from the strut loop as shown in Figure 4.5. For a gradiometer placed at this position, the total magnetic field experienced by each of the

two gradiometer sensor coils is the sum of the magnet fields due to the Helmholtz coil and the outlet strut current:

$$\mathbf{B}_{total} = \mathbf{B}_{\mathrm{H}} + \mathbf{B}_{\mathrm{S}} \tag{4.22}$$

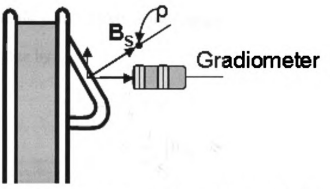

Figure 4.5 A gradiometer placed off-axis from the outlet strut loop

4.4 Induced EMF in the Gradiometer Coils

The gradiometer consists of two bobbin coils aligned co-axially and separated by a fixed distance. Let the coil closest to the outlet strut loop be coil 1, with N_1 number of turns, radius r_1 and a cross sectional area S_1 such that $S_1 = \pi \cdot r_1^2$. Similarly, denote the coil farther away from the strut loop as coil 2, with N_2 number of turns, radius r_2, and a cross sectional area S_2. In practice, the two gradiometer coils are identical in construction and geometry. The two coils are also electrically connected in opposition such that the output of the gradiometer, v_g, is the difference of two coil outputs, v_1 and v_2, respectively.

The magnetic flux lines linking the outlet strut and the gradiometer coils are

$$\psi_1 = \int_{S_1} \mathbf{B}_{S_1} \cdot d\vec{\mathbf{S}}_1 \tag{4.23}$$

$$\psi_2 = \int_{S_2} \mathbf{B}_{S_2} \cdot d\vec{\mathbf{S}}_2 \tag{4.24}$$

From *Faraday's Law*, the induced EMF in the first gradiometer coil due to the linkage flux from (4.23) is given by:

$$\begin{aligned} v_1(t) &= -\frac{d}{dt} N_1 \psi_1 \\ &= -N_1 \frac{d}{dt} \int_{S_1} \mathbf{B}_{S_1} \cdot d\vec{\mathbf{S}}_1 \end{aligned} \tag{4.25}$$

Similarly, the induced EMF in the second gradiometer coil due to the linkage flux in (4.24) is

$$\begin{aligned} v_2(t) &= -\frac{d}{dt} N_2 \psi_2 \\ &= -N_2 \frac{d}{dt} \int_{S_2} \mathbf{B}_{S_2} \cdot d\vec{\mathbf{S}}_2 \end{aligned} \tag{4.26}$$

The gradiometer output is, therefore, given by

$$v_g(t) = v_1(t) - v_2(t) \tag{4.27}$$

These matching EMFs terms are canceled upon the subtraction in (4.27) and consequently do not contribute to the output of the gradiometer.

To obtain the output, v_g, for this non-trivial case, the location and geometry of each gradiometer sensor coil must be known. Equations (4.20) and (4.21) are then solved for every point that lies on the plane of the area, S_1 or S_2, enclosed by the respective sensor coil. The linkage fluxes are then obtained from (4.23) and (4.24), and the corresponding induced electromotive forces are obtained from (4.25) and (4.26). Finally, the gradiometer output signal is obtained from (4.27).

4.5 Special Case: Gradiometer on Axis of Outlet Strut Loop

From Section 4.3, if a gradiometer is placed at a point (r', φ', z') in front of the outlet strut loop, the magnetic field experienced by the gradiometer coils due to the current in the strut loop is given by (4.20) and (4.21). For the special case when the gradiometer is placed on the z'-axis of the outlet strut loop as shown in Figure 4.6, and assuming the sensor coil areas, S_1 and S_2 are small comparing to the strut loop, the equations may be combined and simplified as

$$\mathbf{B}_S\big|_{r'=0} = \frac{\mu_0 i_S r_S^2}{2\left(r_S^2 + z'^2\right)^{\frac{3}{2}}}\hat{\mathbf{a}}_{z'} \tag{4.28}$$

If the gradiometer is advanced to the center of the strut loop, z' also becomes zero and the field experienced by the gradiometer is given by

$$\mathbf{B}_S\big|_{r'=0,z'=0} = \frac{\mu_0 i_S}{2r_S}\hat{\mathbf{a}}_{z'} \tag{4.29}$$

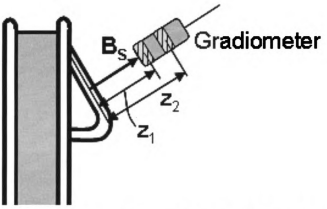

Figure 4.6 A gradiometer placed on the axis of the outlet strut loop

In practice, the gradiometer is positioned by a cardiologist during the prosthetic heart valve inspection. The cardiologist will adjust the orientation and alignment of the gradiometer as close to that shown in Figure 4.6 as possible.

4.6 Induced EMF in the Gradiometer Coils

For the case when the gradiometer is positioned on the axis of the outlet strut loop as shown in Figure 4.6, (4.25) and (4.26) may be simplified as

$$v_1(t) = -N_1 \frac{d}{dt} B_{S_1} S_1 \tag{4.30}$$

and

$$v_2(t) = -N_2 \frac{d}{dt} B_{S_2} S_2 \tag{4.31}$$

The magnitude of the outlet strut's magnetic field experienced by each of the two gradiometers coils located at z_1 and z_2, respectively, is

$$B_{S_1} = \frac{\mu_0 r_S^2 i_S}{2\left(r_S^2 + z_1{}^2\right)^{\frac{3}{2}}} \tag{4.32}$$

and

$$B_{S_2} = \frac{\mu_0 r_S^2 i_S}{2\left(r_S^2 + z_2{}^2\right)^{\frac{3}{2}}} \tag{4.33}$$

The induced EMF in each gradiometer coil is, therefore,

$$v_1(t) = -N_1 \frac{\pi\mu_0 r_S^2 r_1^2}{2\left(r_S^2 + z_1{}^2\right)^{\frac{3}{2}}} \frac{di_S(t)}{dt} \tag{4.34}$$

and

$$v_2(t) = -N_2 \frac{\pi\mu_0 r_S^2 r_2^2}{2\left(r_S^2 + z_2{}^2\right)^{\frac{3}{2}}} \frac{di_S(t)}{dt} \tag{4.35}$$

Since the two gradiometer coils are identical, substituting (4.34) and (4.35) into (4.27) yields

$$v_g(t) = \frac{N_g \pi\mu_0 r_S^2 r_g^2}{2} \frac{di_S(t)}{dt} \left[-\frac{1}{\left(r_S^2 + z_1{}^2\right)^{\frac{3}{2}}} + \frac{1}{\left(r_S^2 + z_2{}^2\right)^{\frac{3}{2}}} \right] \tag{4.36}$$

where $N_g = N_1 = N_2$ is the number turns in each gradiometer coil and $r_g = r_1 = r_2$ is the radius of the gradiometer coil. The current in the outlet strut, i_S, is given by (4.9). For this on-axis case, if the angles α and β and the resistance R_S of the strut loop remain constant over time, carrying out the differentiation in (4.9) gives

$$
\begin{aligned}
i_S(t) &= -\frac{8\mu_0 N_H I_H}{5\sqrt{5} r_H} \frac{S_S}{R_S} \sin(\alpha)\cos(\beta)\frac{d}{dt}\sin(\omega_H t) \\
&= -\frac{\omega_H}{R_S}\frac{8\mu_0 N_H I_H S_S}{5\sqrt{5} r_H}\sin(\alpha)\cos(\beta)\cos(\omega_H t)
\end{aligned}
\tag{4.37}
$$

Substituting (4.37) into (4.36) yields

$$
v_g(t) =
$$

$$
\frac{N_g \pi \mu_0 r_S^2 r_g^2}{2}\left[\frac{1}{\left(r_S^2 + {z_2}^2\right)^{\frac{3}{2}}} + \frac{1}{\left(r_S^2 + {z_1}^2\right)^{\frac{3}{2}}}\right]\frac{\omega_H}{R_S}\frac{8\mu_0 N_H I_H S_S}{5\sqrt{5} r_H}\sin(\alpha)\cos(\beta)\frac{d}{dt}\cos(\omega_H t)
\tag{4.38}
$$

Rearranging and simplifying this equation gives the gradiometer output for the on-axis case as

$$
v_g(t) = \frac{\omega_H^2}{R_S}\frac{4\pi\mu_0^2 N_H I_H N_g r_g^2 r_S^2 S_S}{5\sqrt{5} r_H}\sin(\alpha)\cos(\beta)\left[\frac{1}{\left(r_S^2 + {z_1}^2\right)^{\frac{3}{2}}} - \frac{1}{\left(r_S^2 + {z_2}^2\right)^{\frac{3}{2}}}\right]\sin(\omega_H t)
\tag{4.39}
$$

Let the separation between the two gradiometer coils be Δz. The distance z_2 can then be expressed in terms of z_1 as:

$$
z_2 = z_1 + \Delta z \tag{4.40}
$$

Substituting (4.12) and (4.40) into (4.39) yields

$$v_g(t) =$$

$$\frac{\omega_H^2}{R_S}\frac{4\pi\mu_0^2 N_H I_H N_g r_g^2 r_S^2 S_S}{5\sqrt{5} r_H}\sin(\alpha)\cos(\beta)\left[\frac{1}{\left(r_S^2 + z_1^2\right)^{\frac{3}{2}}} - \frac{1}{\left(r_S^2 + (z_1 + \Delta z)^2\right)^{\frac{3}{2}}}\right]\sin(\omega_H t) \tag{4.41}$$

Equation (4.41) gives the output of the gradiometer located on the axis of the outlet strut loop. Note that in (4.37) and (4.41) the angles α and β, the effective areas S_S and $S_g\left(=\pi \cdot r_g^2\right)$, and the strut loop resistance R_S are assumed to be non-varying over time. These equations show that the outlet strut current and the gradiometer output voltage are both sinusoidal signals at the excitation frequency.

4.7 Outlet Strut Condition and Strut Loop Resistance

In equation (4.5), the resistance R_S of the outlet strut loop is a function of the material characteristics and condition of the loop. Assuming that the conductance of the strut loop is homogeneous throughout the flange ring and the outlet strut, the resistance of an intact outlet strut loop may be represented by a lumped resistance, R_0. For an outlet strut that is either completely or partially fractured, the separation may be represented by an electrical resistance, R_L, corresponding to the degree of discontinuity at the location of the fracture [113]-[117]. The outlet strut loop resistance R_S for a general case can then be expressed as

$$R_S = R_0 + R_L \tag{4.42}$$

The current induced in the outlet strut loop becomes a function of the load resistance (which in terms is a function of the condition of the outlet strut):

$$i_S(t) = -\frac{d}{dt}\left(\frac{8\mu_0 N_H I_H}{5\sqrt{5}r_H}\frac{S_S}{(R_0+R_L)}\sin(\omega_H t)\sin(\alpha)\cos(\beta)\right)$$
$$= -\frac{8\mu_0 N_H I_H}{5\sqrt{5}r_H}\frac{S_S}{(R_0+R_L)}\omega_H \cos(\omega_H t)\sin(\alpha)\cos(\beta) \qquad (4.43)$$

In (4.43), the condition of the outlet strut is modeled by the load resistance R_L. For a complete fracture (i.e., a SLS case), $R_L = \infty$. This effectively creates an open circuit and no current may flow in the outlet strut loop. For an intact outlet strut, $R_L = 0$, $R_S = R_0$, and (4.43) becomes (4.9).

The development of a comprehensive model between R_L and the degree of discontinuity in a fractured outlet strut is described in [113]-[117]. For the development of the gradiometer-based examination system, only the cases where $R_L = 0$ and $R_L = \infty$ will be considered.

4.8 An Alternative Approach: Mutual Inductance Consideration

A conceptual representation of the gradiometer-based examination method is shown in Figure 4.7. In this figure, the gradiometer output, v_g, is the difference between the two gradiometer sensor signals, v_1 and v_2, respectively. The output of each gradiometer coil is the result of flux linkages among a system of four coils: the top and bottom coils of the Helmholtz system, the outlet strut loop and the gradiometer sensor coil itself. Figure 4.8

shows a circuit element representation of the coil systems with the first gradiometer sensor coil. In this figure, the various coils and current loops are represented as inductors (L). The time domain output signal, v_1, is obtained from the frequency domain expression

$$V_1 = -j\omega_H M_{1,S} I_S + j\omega_H M_{1,H1} I_H + j\omega_H M_{1,H2} I_H \tag{4.44}$$

where I_S and I_H are the frequency domain representations of the outlet strut current and excitation coil current, respectively. The output, V_1, is the frequency domain representation of v_1, and ω is the excitation frequency. The mutual inductance, $M_{1,S}$, is defined as the flux linkage $\lambda_{1,S} = N_1 \psi_{1,S}$ on the first gradiometer sensor coil due to the outlet strut loop current, I_S:

$$M_{1,S} = \frac{\lambda_{1,S}}{I_S} = \frac{N_1 \psi_{1,S}}{I_S} \tag{4.45}$$

Similarly, the mutual inductance $M_{1,H1}$ is defined as the flux linkages of the first gradiometer sensor coil per unit I_H such that

$$M_{1,H1} = \frac{\lambda_{1,H1}}{I_H} = \frac{N_1 \psi_{1,H1}}{I_H} \tag{4.46}$$

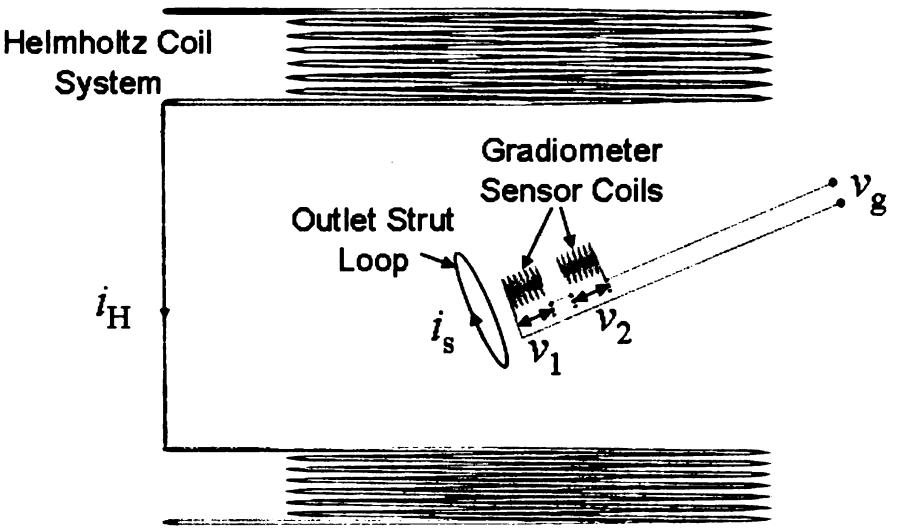

Figure 4.7 A conceptual representation of the gradiometer-based inspection system (components not drawn to scale)

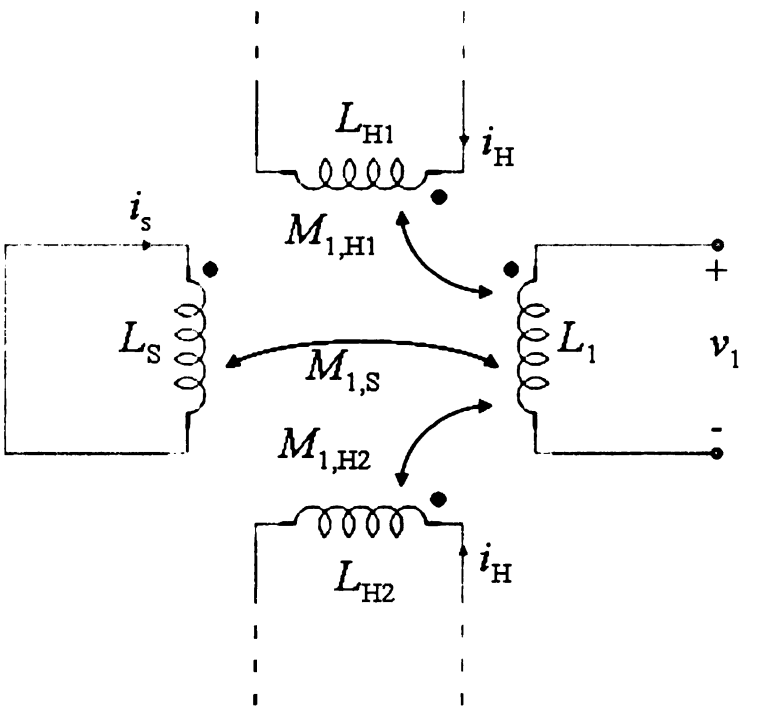

Figure 4.8 A circuit element representation of the gradiometer-based inspection system components (shown with the first gradiometer sensor coil only) in Figure 4.7.

Similar to (4.44), the frequency domain expression for v_2 is

$$V_2 = -j\omega_H M_{2,S} I_S + j\omega_H M_{2,H1} I_H + j\omega_H M_{2,H2} I_H \tag{4.47}$$

where $M_{2,S}$, $M_{2,H1}$ and $M_{2,H2}$ are the mutual inductances due to the flux linkages to the second sensor coil from the outlet strut loop and the top and bottom coils of the Helmholtz system, respectively. Since the gradiometer is submerged in a uniform field created by the Helmholtz coil, the flux linkages from the top and bottom coils to the gradiometer sensor coils are equal. As a result, the gradiometer output may be written as:

$$\begin{aligned} V_g &= V_1 - V_2 = -j\omega_H M_{1,S} I_S + j\omega_H M_{2,S} I_S \\ &= (M_{2,S} - M_{1,S}) j\omega_H I_S \end{aligned} \tag{4.48}$$

The corresponding time domain signal is

$$v_g(t) = (M_{2,S} - M_{1,S}) \frac{di_S(t)}{dt} \tag{4.49}$$

To determine $M_{1,S}$, the definition of mutual inductance may be used:

$$M_{1,S} = \frac{N_1 \psi_1}{I_S} \tag{4.50}$$

The flux ψ_1 passing through the first gradiometer sensor coil due to the current in the outlet strut loop is given by (4.23). For the case when the gradiometer is positioned on the axis of the outlet strut loop (as shown in Figure 4.6), the magnitude of the outlet strut magnetic field experienced by the first gradiometer sensor coil is given by (4.32). The magnetic flux linking the outlet strut loop and the sensor coil is

$$\begin{aligned}\psi_1 &= \int_{S_1} \mathbf{B}_{S_1} \cdot d\bar{\mathbf{S}}_1 \\ &= \frac{\mu_0 r_S^2 i_S}{2\left(r_S^2 + z_1^2\right)^{\frac{3}{2}}}\left(\pi r_1^2\right) \\ &= \frac{M_{1,S} i_S}{N_1}\end{aligned} \tag{4.51}$$

Comparing (4.50) and (4.51), the mutual inductance $M_{1,S}$ is given by

$$M_{1,S} = \frac{\mu_0 r_S^2 N_1}{2\left(r_S^2 + z_1^2\right)^{\frac{3}{2}}}\left(\pi r_1^2\right) \tag{4.52}$$

Similarly, the mutual inductance between the outlet strut loop and the second sensor coil of the gradiometer is given by

$$M_{2,S} = \frac{\mu_0 r_S^2 N_2}{2\left(r_S^2 + z_2^2\right)^{\frac{3}{2}}}\left(\pi r_2^2\right) \tag{4.53}$$

Using equations (4.52) and (4.53) and recalling the gradiometer specifications $N_g = N_1 = N_2$ and $r_g = r_1 = r_2$, (4.49) can be written as

$$v_g(t) = \frac{N_g \pi \mu_0 r_S^2 r_g^2}{2}\left(\frac{1}{\left(r_S^2 + z_2^2\right)^{\frac{3}{2}}} - \frac{1}{\left(r_S^2 + z_1^2\right)^{\frac{3}{2}}}\right)\frac{di_S(t)}{dt} \tag{4.54}$$

The current i_S in the outlet strut loop is given by (4.37). The time derivative of this current is

$$\frac{di_S(t)}{dt} = -\frac{\omega_H^2}{R_S}\frac{8\mu_0 N_H I_H S_S}{5\sqrt{5}r_H}\sin(\alpha)\cos(\beta)\sin(\omega_H t) \tag{4.55}$$

Substituting (4.55) into (4.54) yields

$$v_g(t) = \frac{\omega_H^2}{R_S}\frac{4\pi\mu_0^2 N_g N_H I_H r_S^2 r_g^2 S_S}{5\sqrt{5}r_H}\sin(\alpha)\cos(\beta)\left(\frac{1}{\left(r_S^2 + z_1^2\right)^{\frac{3}{2}}} - \frac{1}{\left(r_S^2 + z_2^2\right)^{\frac{3}{2}}}\right)\sin(\omega_H t) \tag{4.56}$$

Equation (4.56) is identical to (4.39). This result is expected since, by definition, the mutual inductance is the flux linkage of the sensor coil due to the outlet strut loop current. As this linkage flux is also used in the derivation of (4.39), both developments are expected to arrive at the same result. Essentially, the mutual inductance approach amounts to an alternative presentation of the same physical phenomenon as described by the *Faraday's Law* in (4.25) and (4.26).

4.9 Factors Affecting the Gradiometer Signal Output

Equation (4.37) shows that the amplitude of the strut current is proportional to the excitation frequency, ω_H, and inversely proportional to the resistance, R_S, of the strut loop. From (4.41), the amplitude of the gradiometer output signal is:

- proportional to the square of the excitation frequency, ω_H^2;
- inversely proportional to the strut loop resistance, R_S;
- proportional to the number of turns, N_g, in each gradiometer sensor coil;
- proportional to the effective area of each gradiometer sensor coil, $S_g = \pi r_g^2$;

- related to the strength of the applied uniform excitation magnetic field, B_H, from the Helmholtz coil system. This field is in turn
    - a function of the number of turns, N_H, in each excitation coil;
    - proportional to the amplitude of the current (I_H) through the coils;
    - inversely proportional to the radius, r_H, and separation of the coils.

4.10 Spatial Dependency of the Gradiometer Output Signal

The gradiometer output signal is also a function of its distance, z_1, from the outlet strut as well as the separation, Δz, between the two gradiometer sensor coils. To visualize these dependencies, Equation (4.41) is expressed as a product of a time-dependent function $W(t)$ and a position-dependent function $U(z_1, \Delta z)$ such that

$$v_g = W(t) \cdot U(z_1, \Delta z) \tag{4.57}$$

where

$$W(t) = \frac{\omega_H^2}{R_S} \frac{4\pi\mu_0^2 N_H I_H N_g r_g^2 r_S^2 S_S}{5\sqrt{5} r_H} \sin(\alpha)\cos(\beta)\sin(\omega_H t) \tag{4.58}$$

and

$$U(z_1, \Delta z) = \left(r_S^2 + {z_1}^2\right)^{-\frac{3}{2}} - \left(r_S^2 + (z_1 + \Delta z)^2\right)^{-\frac{3}{2}} \tag{4.59}$$

Equation (4.59) describes the scaled gradiometer output signal, $U(z_1, \Delta z)$, as a function of both z_1 and Δz. Figure 4.9 and Figure 4.10 show $U(z_1, \Delta z)$ as a function of z_1 and Δz, respectively. Experimental results showing the examination system output as a

function of z_1 are shown in Chapter 8, and the development of a probability of detection model with respect to variations in z_1 is presented in Chapter 9.

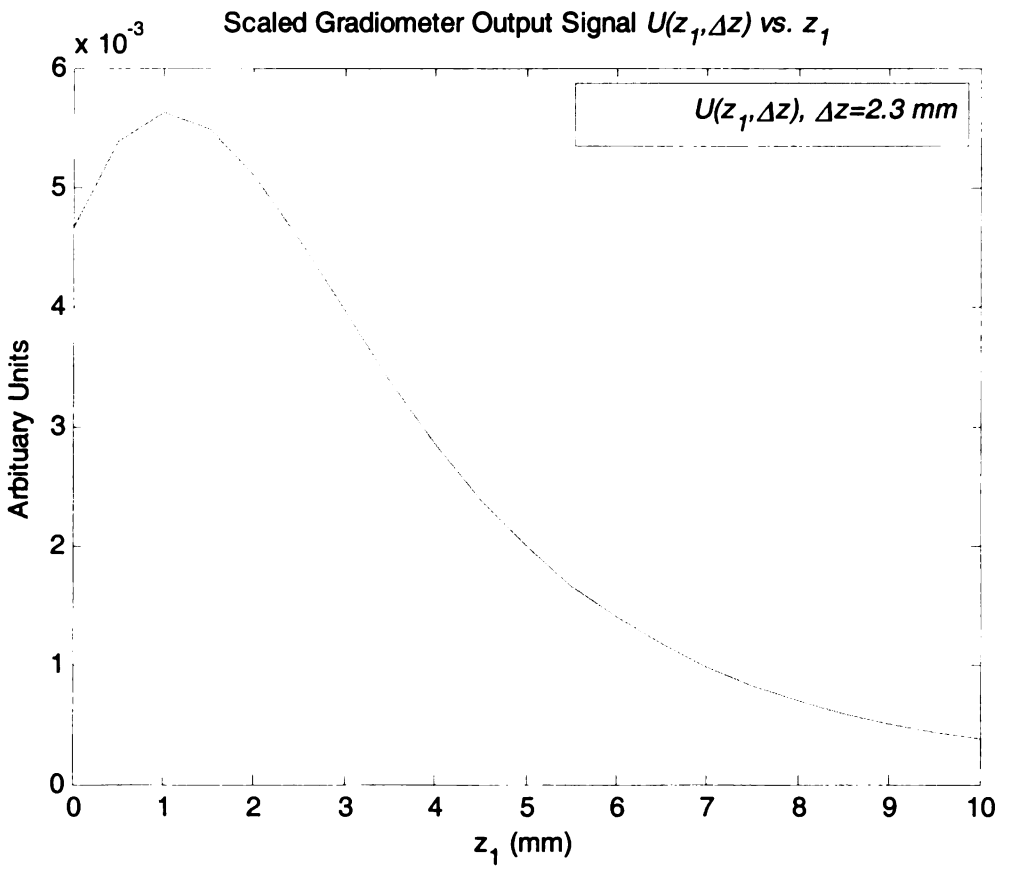

Figure 4.9 Scaled gradiometer output signal as a function of the distance, z_1, between the gradiometer and the outlet strut loop

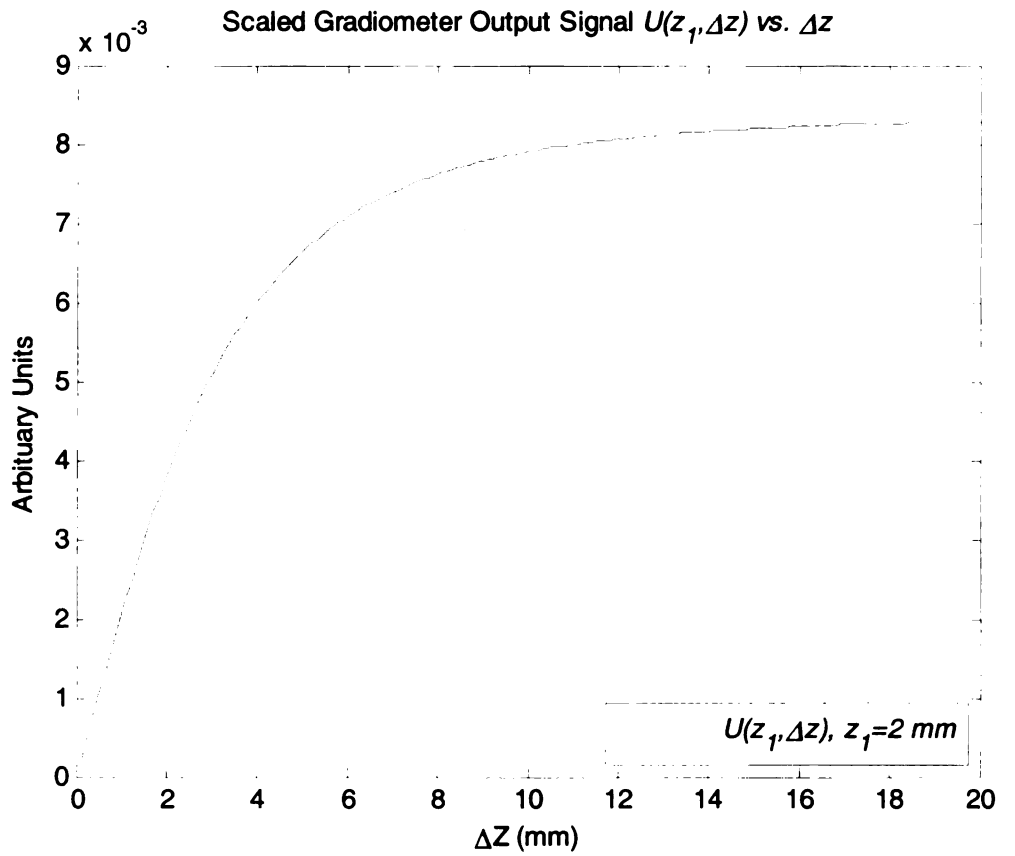

Figure 4.10 Scaled gradiometer output signal as a function of the separation, Δz, between the two sensor coils

In Figure 4.9, the output signal, $U(z_1,\Delta z)$ (Δz=2.3 mm), increases in the first 1-2 mm when the distance between the gradiometer and the outlet strut is increased. The signal subsequently decreases with distance, and is reduced by 3 dB from its maximum value when the gradiometer is approximately 3 mm from the outlet strut loop. These results suggest that the gradiometer should be placed within 5 mm of the outlet strut (i.e., $z_1 \leq 5$ mm) during an examination. Finite element analysis of the gradiometer output with respect to its distance from the outlet strut is presented in Chapter 5, and the experimental results are given in Chapter 8. A probability of detection model that takes variabilities in z_1 into consideration is presented in Chapter 9.

Figure 4.10 shows the scaled gradiometer output signal as a function of Δz (with $z_1 = 2$ mm). The results from this figure show that if the first sensor coil is placed in the vicinity of the outlet strut loop, the gradiometer output signal will increase as the second sensor coil is moved away from the first. This is because when the second coil is near to the first, the induced signals in both coils are very similar and, therefore, the difference signal is small. As the separation between the coils, Δz, increases, the induced signal in the second coil decreases and the difference signal subsequently increases until it levels off towards a valve that is a function of the first sensor coil signal. The gradiometer output as functions of the distance, z_1, from the outlet strut, and the separation, Δz, between the two sensor coils, is examined further in Chapter 7 for designing the gradiometer.

It is important to recall that when simplifying (4.20) and (4.21) into (4.28), the area of the sensor coils was assumed to be small comparing to the outlet strut loop. If this assumption is not satisfied, (4.20) and (4.21) must be evaluated and applied in (4.30) and (4.31) to obtain the output of the sensor coils. Nevertheless, equation (4.41) and the simplified mathematical model developed in this chapter provide a valid and convenient starting point for designing the gradiometer. Equation (4.41) also provides insights into the effects of various physical parameters on the gradiometer output as described in Section 4.9. For example, Equation (4.41) shows that, with all other parameters kept constant, the amplitude of the gradiometer output signal, $|v_g|$, is a quadratic function of the excitation frequency, ω_H (i.e., $|v_g| \propto \omega_H^2$). This quadratic dependency can be

observed from Figure 4.11, which shows the scaled amplitude of the gradiometer signal from f_H = 10-100 kHz ($\omega_H = 2\pi f_H$). The results in this figure suggest that the excitation frequency should be set as high as possible within the limits of the equipment. The experimental results for the gradiometer output as a function of excitation frequency are presented in Chapter 8.

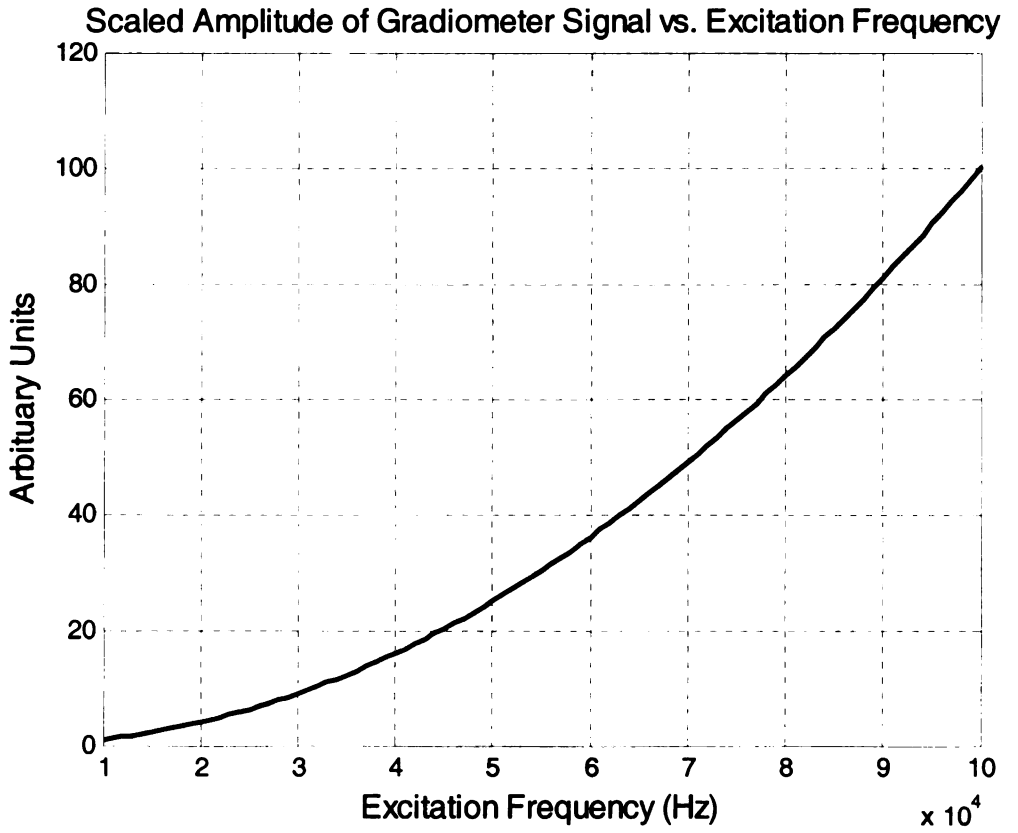

Figure 4.11 Scaled amplitude of the gradiometer output signal as a function of the excitation frequency

Equation (4.43) shows that, if the outlet strut fracture is modeled as an electrical resistance and the valve is subjected to an externally applied uniform magnetic field, the induced current in the strut is directly related to the outlet strut condition. This outlet

strut current manifests itself as perturbation in the applied magnetic field. When a gradiometer is used to measure this perturbation, the results from (4.25)-(4.27) can be used to indicate the condition of the outlet strut.

Equation (4.41), though developed for the special case when the gradiometer is positioned on the axis of the outlet strut loop, expresses the gradiometer output signal as a function of the applied excitation field, the geometry of the gradiometer coils, the orientation of the gradiometer in relation to the outlet strut, and the condition of the outlet strut. These results are all taken into considerations when designing the gradiometer assembly.

CHAPTER 5. NUMERICAL MODELING

A three-dimensional finite element analysis has been performed on the gradiometer-based heart valve examination system to investigate the feasibility of the approach and for optimizing system parameters. The analysis results show the magnetic field perturbations in the vicinity of the heart valve when subjected to an applied excitation field. The results also show that the amount of perturbation due to an intact heart valve is large when compared to that due to a single-leg separated valve. These results demonstrate that the gradiometer-based method is a promising approach for detecting SLS in BSCC heart valves.

5.1 The Finite Element Model

The finite element model is based on a quasi-static vector-scalar ($\overline{A}$-V) potential formulation [129], [130]. Figure 5.1 shows the configuration for a typical eddy current problem. The solution domain is divided into a conducting region, Ω_1, and a non-conducting region, Ω_2. In Ω_1, the magnetic vector potential $\overline{A}$ and electric scalar potential V are used to represent the electromagnetic field. In Ω_2, only $\overline{A}$ is used. The excitation current is represented in the form of a current density, $\overline{J}_S$, and is assumed to exist in the non-conducting region only. The governing equations are derived from the Maxwell's equations:

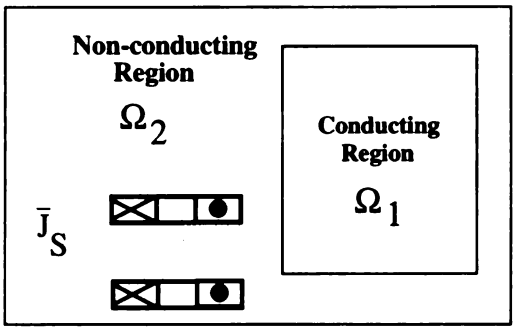

Figure 5.1 A typical configuration for eddy current problems

$$\nabla \times \bar{E} = -\frac{\partial \bar{B}}{\partial t} \tag{5.1}$$

$$\nabla \times \bar{H} = \bar{J} + \frac{\partial \bar{D}}{\partial t} \tag{5.2}$$

$$\nabla \cdot \bar{B} = 0 \tag{5.3}$$

$$\nabla \cdot \bar{D} = \rho_V \tag{5.4}$$

where

$\bar{E}$ = electric field intensity (V/m)
$\bar{D}$ = electric flux density (C/m^2)
$\bar{H}$ = magnetic field intensity (A/m)
$\bar{B}$ = magnetic flux density (T)
$\bar{J}$ = current density (A/m^2)
ρ_V = volume charge density (C/m^3)

Under quasi-static conditions, the displacement current, $\bar{D}$, is assumed to be negligible:

$$\frac{\partial \bar{D}}{\partial t} = 0. \tag{5.5}$$

Applying the magnetic vector potential formulation

$$\bar{B} = \nabla \times \bar{A}. \tag{5.6}$$

with the Columb gauge ([131])

$$\nabla \cdot \overline{\mathrm{A}} = 0 \tag{5.7}$$

and a sinusoidal excitation of frequency ω

$$-\frac{\partial \overline{\mathrm{B}}}{\partial t} = -j\omega \overline{\mathrm{B}} \tag{5.8}$$

allows substituting (5.6) and (5.8) into (5.2) to give

$$\nabla \times \overline{\mathrm{E}} = -j\omega \overline{\mathrm{B}} = -j\omega\left(\nabla \times \overline{\mathrm{A}}\right) \tag{5.9}$$

from which

$$\nabla \times \left(\overline{\mathrm{E}} + j\omega \overline{\mathrm{A}}\right) = 0. \tag{5.10}$$

Hence,

$$\overline{\mathrm{E}} = -j\omega \overline{\mathrm{A}} - \nabla \mathrm{V} \tag{5.11}$$

where V is the electric scalar potential function.

Also, from the constitutive equations we have

$$\begin{aligned} \overline{\mathrm{H}} &= \frac{1}{\mu} \overline{\mathrm{B}} \\ &= \frac{1}{\mu}\left(\nabla \times \overline{\mathrm{A}}\right) \end{aligned} \tag{5.12}$$

and

$$\overline{\mathrm{J}} = \sigma \overline{\mathrm{E}} \tag{5.13}$$

where σ is the conductivity and μ the permeability of the material in the region.

Substituting (5.5) and (5.11)-(5.13) into (5.2) yields

$$\nabla \times \frac{1}{\mu}\left(\nabla \times \overline{\mathrm{A}}\right) = \sigma\left(-j\omega \overline{\mathrm{A}} - \nabla \mathrm{V}\right) \tag{5.14}$$

The problem is therefore defined by the following governing equations:

In Ω_1:

$$\nabla \times \frac{1}{\mu} \nabla \times \bar{A} + j\omega\sigma\bar{A} + \sigma\nabla V = 0 \tag{5.15}$$

$$\nabla \cdot \sigma\left(j\omega\bar{A} + \nabla V\right) = 0 \tag{5.16}$$

In Ω_2:

$$\nabla \times \frac{1}{\mu} \nabla \times \bar{A} = \bar{J}_S \tag{5.17}$$

In these equations, ω is the angular frequency of the excitation signal. At the interface Γ_{12} between the conducting and non-conducting regions, the boundary condition

$$\bar{J} \cdot \hat{n} = \sigma\left(- j\omega\bar{A} - \nabla V\right) \cdot \hat{n} = 0 \tag{5.18}$$

is imposed.

Solving equations (5.15)-(5.17) yields the magnetic vector potential function, $\bar{A}$, and electric scalar potential function, V, from which the magnetic flux density, $\bar{B}$, can be obtained.

The finite element method does not solve these partial differential equations directly. Rather, the method seeks the weak form solution. Using Galerkin's rule, the discretized weak form representation is [122]:

$$\begin{aligned} &\sum_j \iiint \left\{ \left[\left(\nabla \times \bar{N}_i\right) \frac{1}{\mu} \left(\nabla \times \bar{N}_j\right) + \left(\nabla \bar{N}_i\right) \frac{1}{\mu} \left(\nabla \bar{N}_j\right) + j\omega\sigma \bar{N}_i \bar{N}_j \right] d\Omega \right\} A_j \\ &+ \sum_j \left[\iiint N_i \nabla N_j \, d\Omega \right] V_j \\ &= \iiint \bar{N}_i \bar{J}_S \, d\Omega \end{aligned} \tag{5.19}$$

and

$$\sum_j \left[\left(j\omega\sigma \iiint \nabla \overline{N}_i \overline{N}_j d\Omega \right) A_j \right] + \left[\iiint \nabla \overline{N}_i \sigma \nabla \overline{N}_j d\Omega \right] V_j = 0 \tag{5.20}$$

where $\overline{N}_j$ represents the basis function associated with the nodes of the elements. This discretized weak form representation is a linear system.

The finite element analysis of the system involves the following steps:

- discretize the solution domain into finite elements,
- evaluate the elemental equations,
- assemble the global linear system,
- solve the linear system of equations,
- process the nodal values to obtain the physically measurable quantities.

Figure 5.2 shows the finite element mesh of a BSCC heart valve generated using the COMSOL Multiphysics[1] software package. In this model, first order tetrahedron elements are used. Solving the linear system given in (5.19) and (5.20) produces a solution for $\overline{A}$ and V at the finite element nodes. The values of the potential functions and fields at any arbitrary point in the solution domain can then be obtained through interpolation.

[1] Formerly known as FEMLAB, by COMSOL, Inc. of Burlington, MA (www.COMSOL.com).

5.2 Simulation Results

At the center of the gradiometer-based inspection system is a uniform magnetic field encompassing the heart valve under test. To maximize the volume of this uniform field, a Helmholtz excitation coil system is used. In a clinical-scale setup, the excitation coils are separated by 1 m in order to accommodate the patient and the examination table. Each excitation coil also has a 1-meter radius following the Helmholtz configuration. When constructing the finite element model for the system, the element size has to be sufficiently small particularly within the ring and its vicinity. Unfortunately, this requires the use of a large number of elements, making the computational effort prohibitively large.

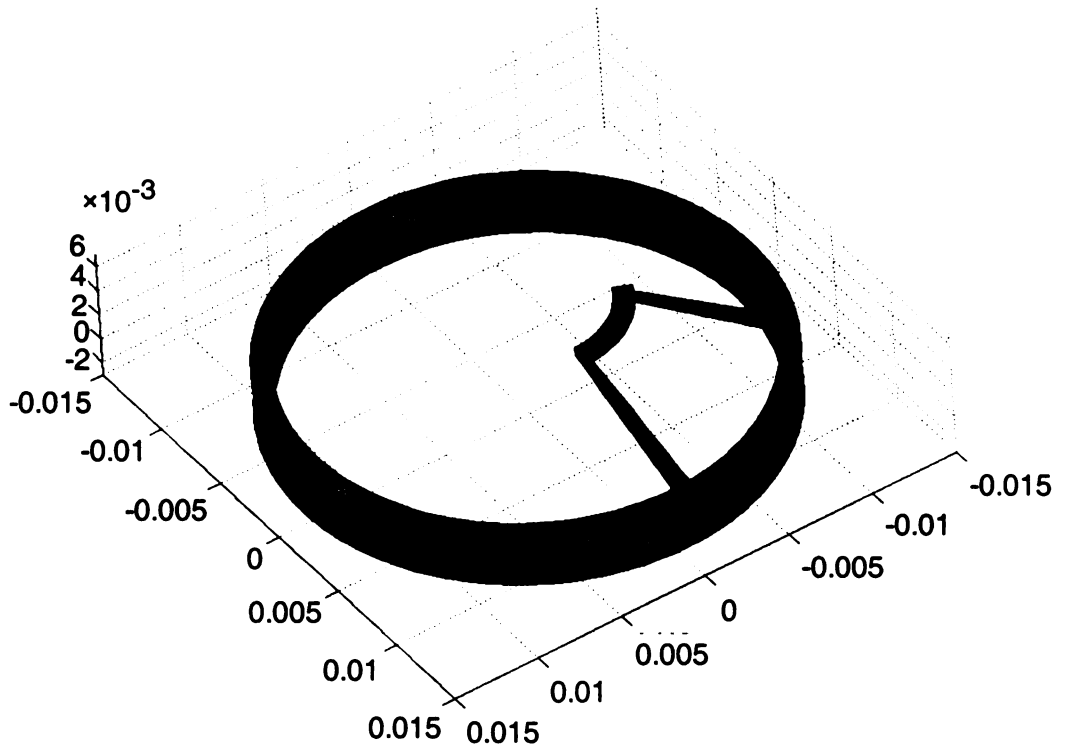

Figure 5.2 Finite element mesh of a BSCC heart valve (the inlet strut and occluder disc are omitted for clarity without loss of model accuracy)

In order to reduce the computational requirements, the analysis of the gradiometer-based method is performed in two steps. First, the excitation coils are modeled to obtain the field distribution at the center region. This provides estimates of the field strength and the size of the uniform magnetic field volume. Next, a second analysis is performed to model the heart valve centered in the uniform magnetic field. The field distribution obtained from the first finite element analysis is applied as the source to the second model to excite the heart valve. The perturbation of the applied magnetic field is then calculated for various outlet strut conditions.

5.2.1 The Excitation Coils

A 3-D finite element model has been constructed for the Helmholtz coil system. In this model, each excitation coil consists of 9 turns (3 layers of 3 turns each) of a 1/0 AWG[1] wire (Figure 5.3). The diameter of the wire is 11 mm and the mean radius of each excitation coil is 1 m. The two excitation coils are separated by 1 m. The two coils are also electrically connected in series, and oriented such that the current flows through both coils in the same direction. From Figure 5.3, the cross-sectional area of the 3×3 winding stack is approximately 1.52×10^{-3} m^2 (39 mm × 39 mm). The empty spaces between the wires in the winding stack and the insulation jacket thickness (~ 1 mm) make the fill-factor[2] of each excitation coil less than 0.57. The empty spaces and the wire insulation also complicate the 3-D finite element model. To simplify the model and reduce the

---

[1] American wire gauge

[2] Fill factor = conductor area / window area used = $\frac{9\pi(0.0055)^2}{(0.039)^2} = 0.56$

mesh size without loss of accuracy, each excitation coil is modeled as a square-shaped wire (Figure 5.4) with a cross-sectional area equivalent to the total conductor area of the 3×3 winding stack. With a total winding cross-sectional conductor area of $9\pi(0.0055)^2 = 8.553 \times 10^{-4}$ m^2, the cross-sectional width and height of the square wire are both 29.245 mm.

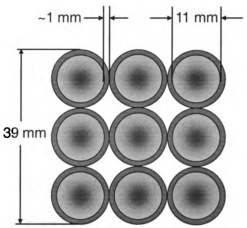

Figure 5.3 Each excitation coil consists of nine turns of a 1/0 AWG wire. Due to the inter-wire spacing and jacket thickness, the fill-factor of this coil less than 0.57.

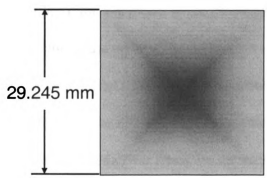

Figure 5.4 Excitation coil windings are modeled as a wire with a square cross-sectional area

The magnetic flux density and field distribution predicted by the 3-D finite element analysis of the Helmholtz coil system is shown in Figure 5.5. Figure 5.6 shows the magnetic flux density profile along the x axis at the center of the coils, and Figure 5.7 shows the magnetic flux density profile along the z axis. With a sinusoidal input current of 11 A (peak-to-peak) and a frequency of 62.5 kHz, the simulation results show a peak-to-peak magnetic flux density of 1.47×10^{-4} T (1.47 gauss) at the center of the coils. The simulation results also show a less than 0.5% variation in the magnetic flux density within a cylindrical volume 0.5 meters tall and a radius of 0.25 m centered between the coils. The experimental confirmation of these simulation results are presented in Chapter 8.

5.2.2 Field Perturbations Due to Outlet Strut Conditions

The finite element model of a heart valve submerged in a cylindrical volume of uniform magnetic field is shown in Figure 5.8. The magnetic field distribution was obtained previously from the Helmholtz coil simulation. In this model, the center of the valve flange ring is located at the origin of the x-y plane, while the positive z-axis extends from the flange plane into the outlet side of the valve. The outlet strut is positioned in the "+y" direction. Figure 5.9 shows the real part of the y and z components of the magnetic flux density in the x = 0 mm plane for both the IOS and SLS cases (the vertical axis is the y-axis). In these cases, the real components of the fields are unperturbed. The perturbations become obvious in the imaginary parts, as shown in Figure 5.10 and Figure 5.11. From these two figures, the level of perturbations due to an IOS valve is higher than that from a SLS case. Figure 5.12 shows the real and imaginary parts of the x and y

components of the flux density in the z = -5 mm plane for an IOS valve, while Figure 5.13 shows those from a SLS case. The results show that, in the vicinity of the valve (5 mm in front of the flange plane in this case), the degree of perturbation in the magnetic field is higher for an IOS valve than that for a single-leg separated valve. This demonstrates the feasibility of outlet strut SLS detection by measuring the magnetic field perturbations in the vicinity of the heart valve. The following chapters describe a gradiometer-based examination system utilizing this principle for SLS detection.

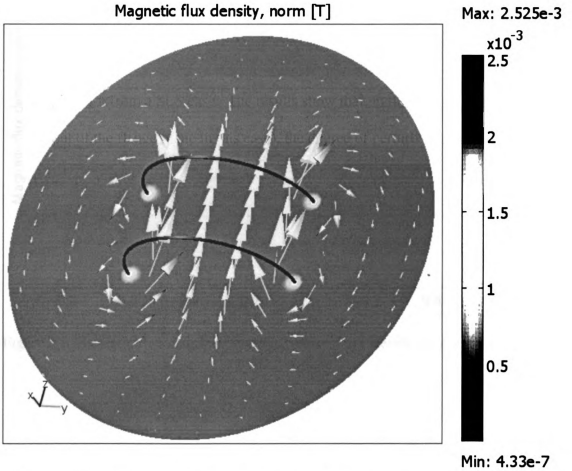

Figure 5.5 Finite element analysis of the Helmholtz coil showing the magnetic flux density and field (arrows) distribution

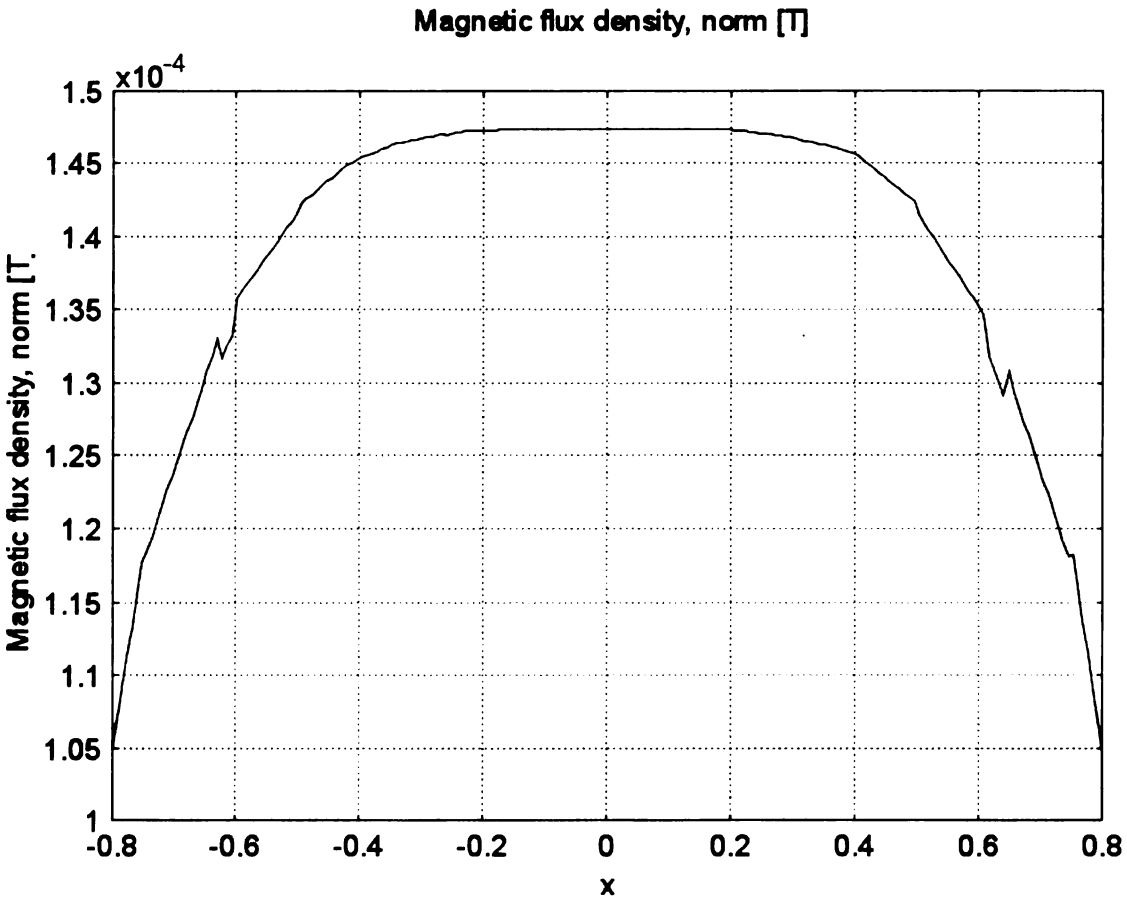

Figure 5.6 Magnetic flux distribution at the center of the Helmholtz coil along the x axis on the y=z=0 line

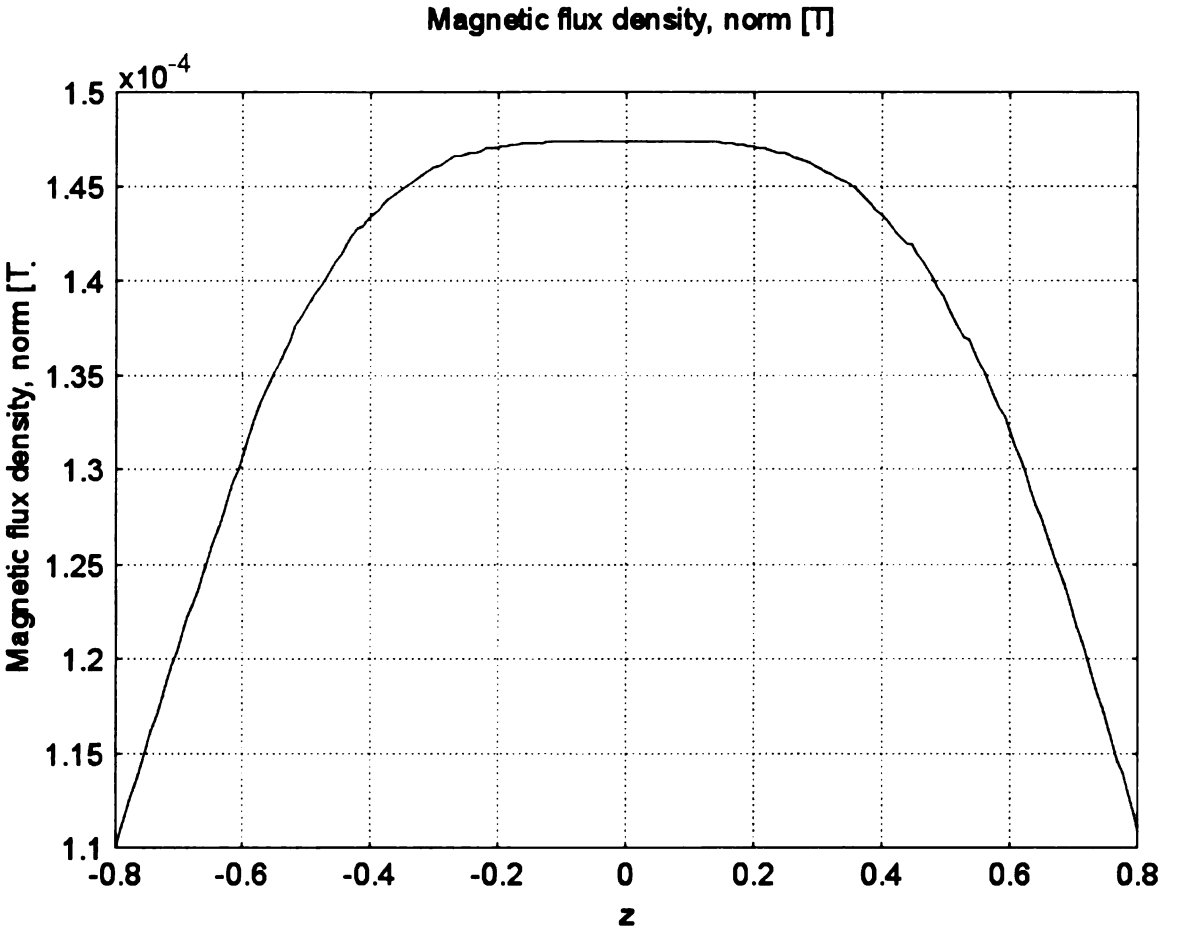

Figure 5.7 Magnetic flux density at the center of the Helmholtz coil along the Z axis on the x=y=0 line

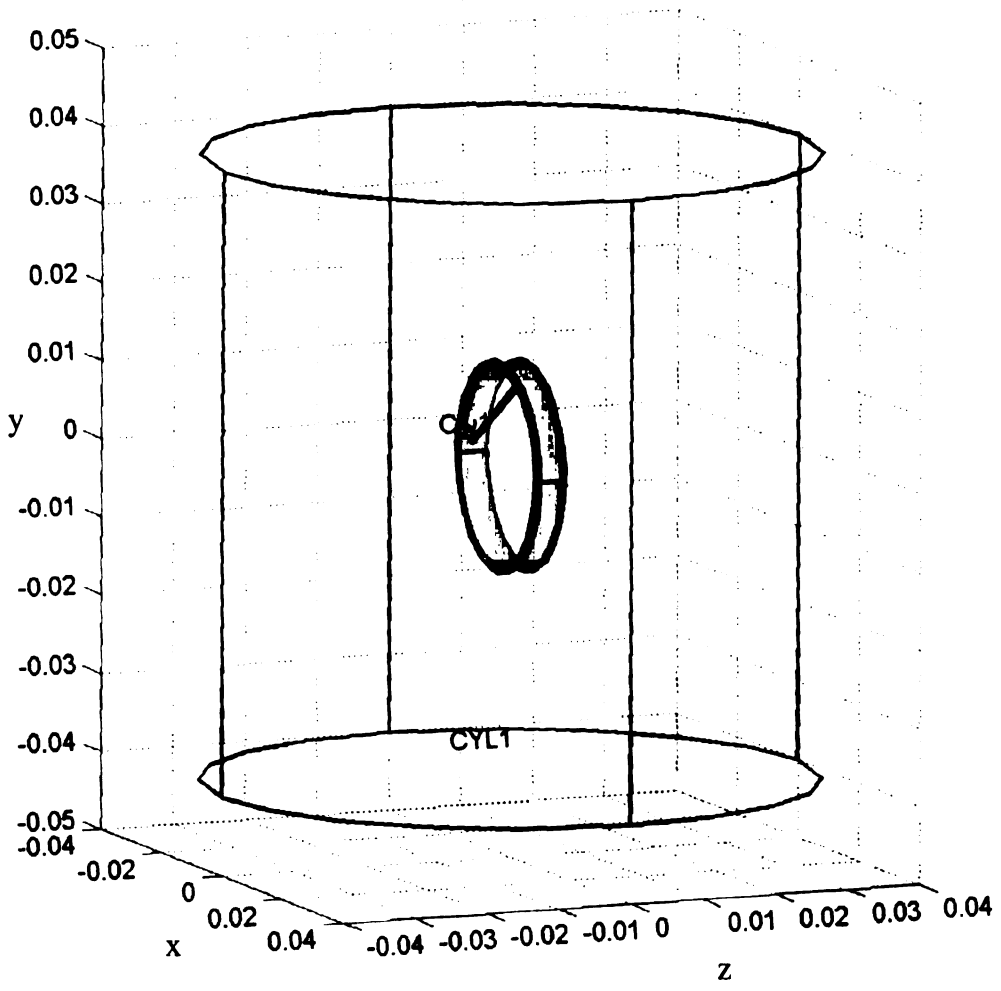

Figure 5.8 Finite element model of a BSCC heart valve submerged in a volume of uniform magnetic field

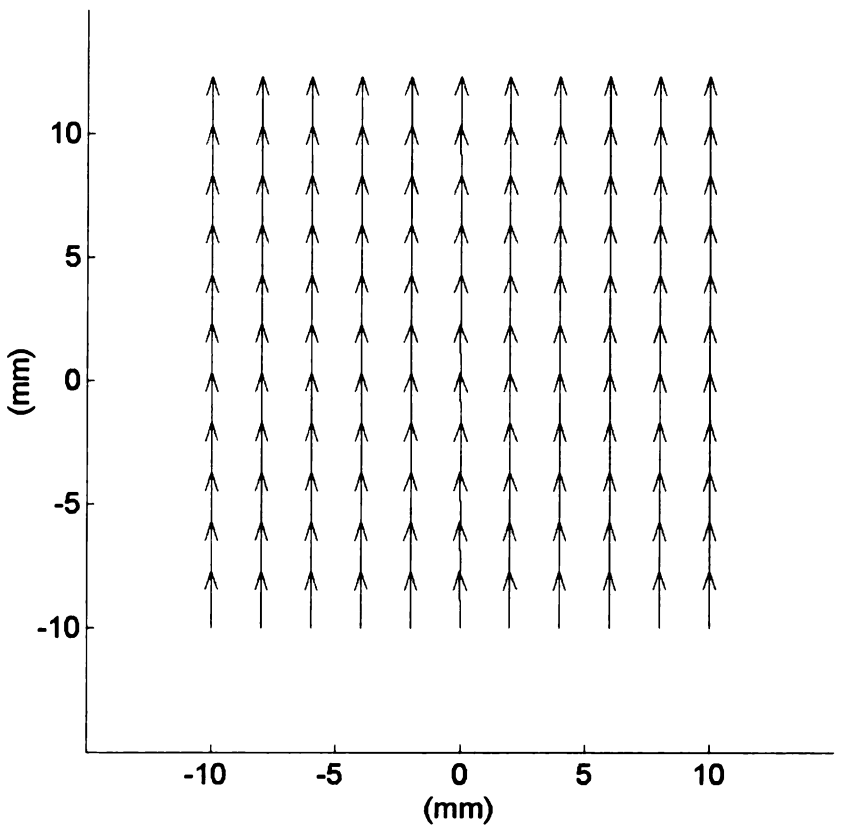

Figure 5.9 Real part of the (By, Bz) components in the x = 0 mm plane for both IOS and SLS cases. The vertical axis is the y-axis. In these cases, the real components of the fields are unperturbed.

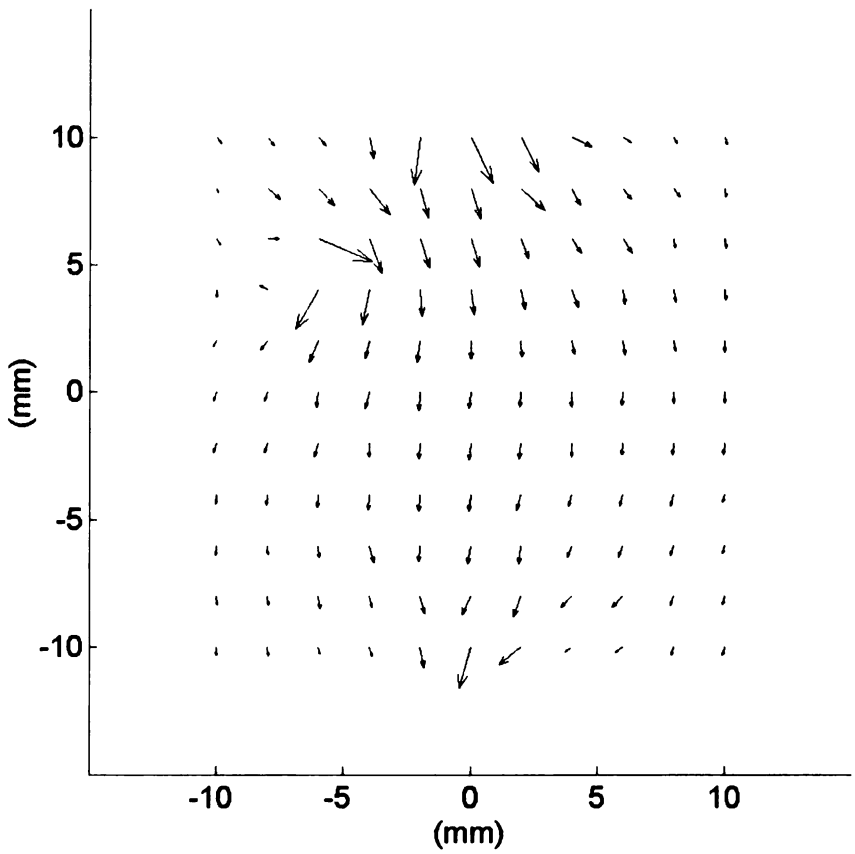

Figure 5.10 Imaginary part of the (By, Bz) components in the x = 0 mm plane for an IOS valve. The vertical axis is the y-axis.

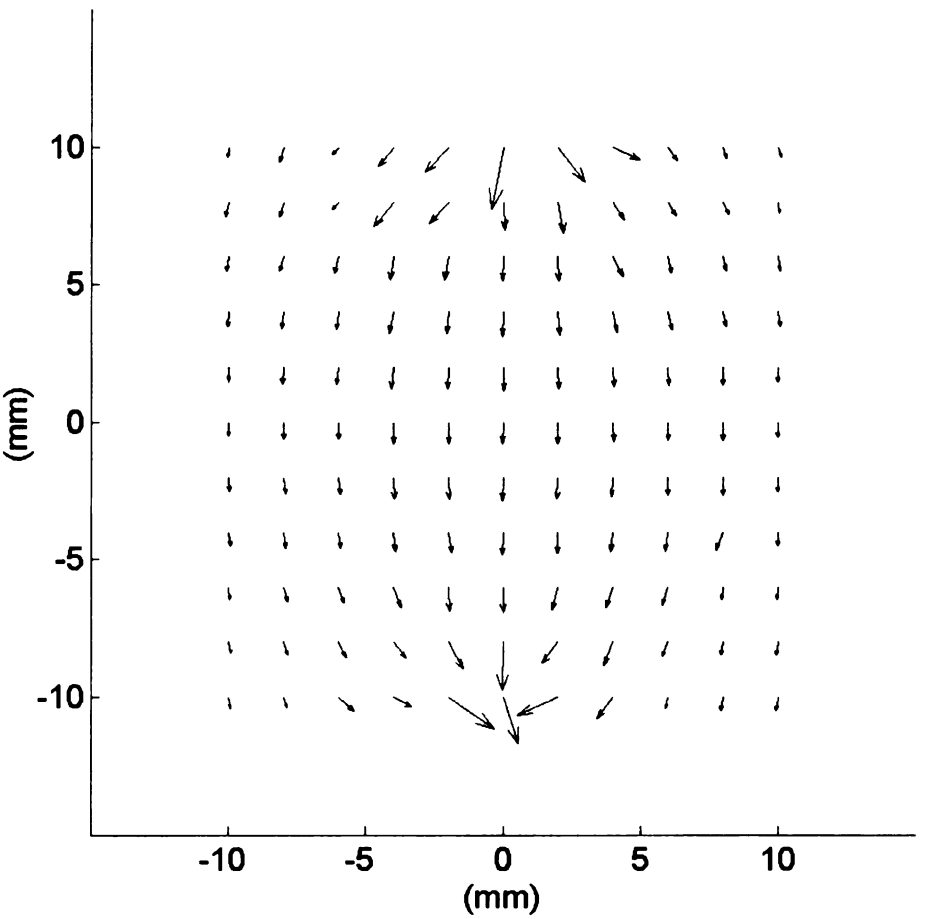

Figure 5.11 Imaginary part of the (By, Bz) components in the x = 0 mm plane for a SLS valve. The vertical axis is the y-axis.

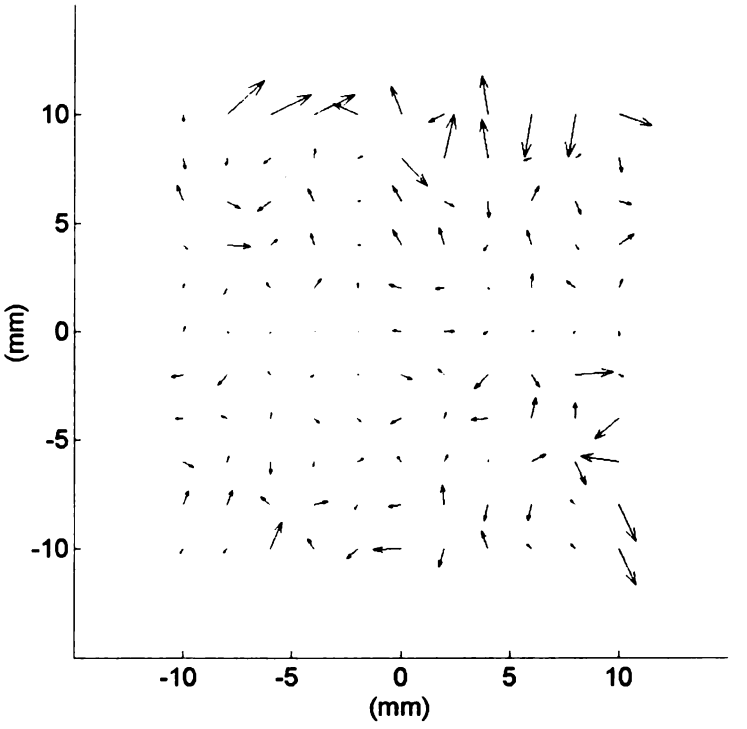

(a)

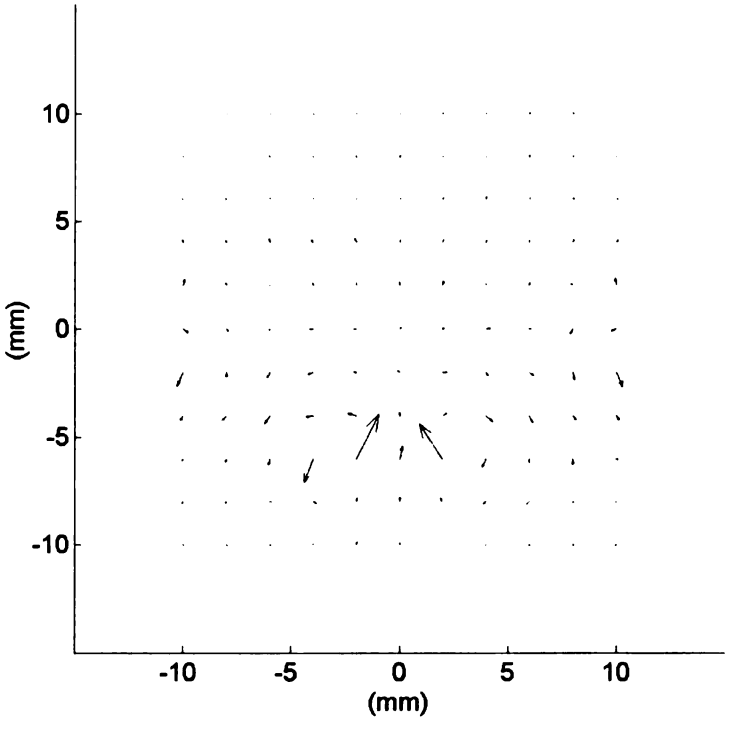

(b)

Figure 5.12 Real (a) and imaginary (b) parts of the (Bx, By) components in the z = -5 mm plane for an IOS valve. The vertical axis is the y-axis.

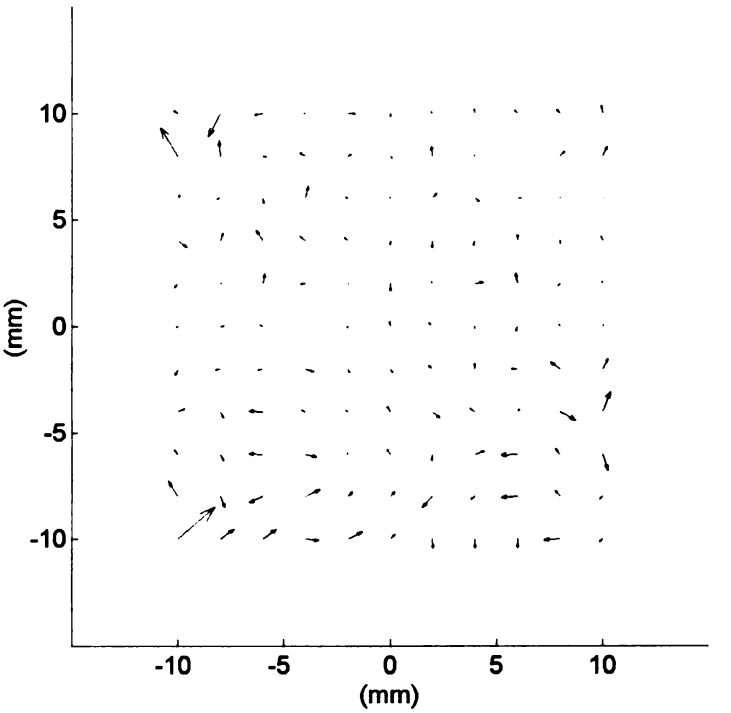

(a)

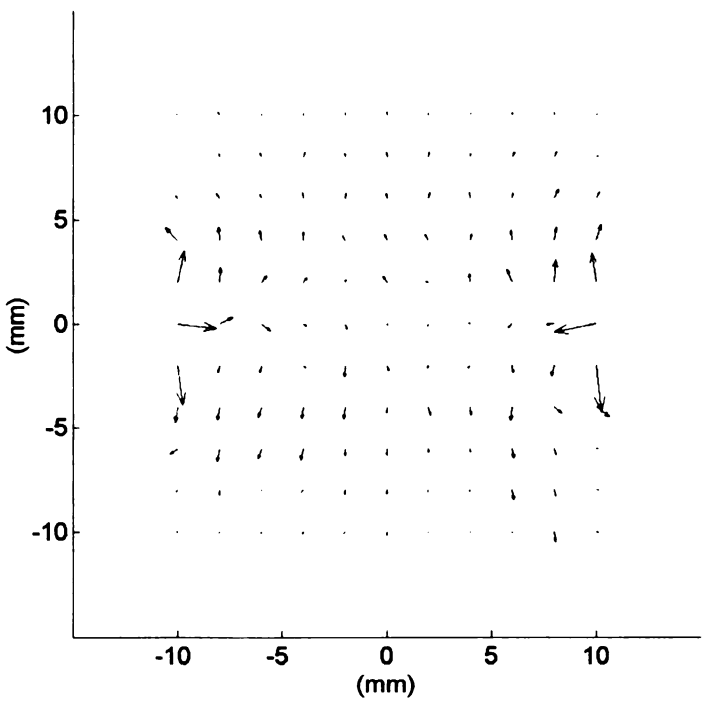

(b)

Figure 5.13 Real (a) and imaginary (b) parts of the (Bx, By) components in the z = -5 mm plane for a SLS valve. The vertical axis is the y-axis.

CHAPTER 6. SYSTEM COMPONENTS

The gradiometer-based prosthetic heart valve examination system consists of two subsystems, the excitation and measurement subsystem, both controlled by a personal computer (PC). Figure 6.1 shows the block diagram of the examination system. The excitation coils, part of the excitation subsystem, are used to establish a region of uniform magnetic field. A heart valve is placed in this region and the gradiometer, part of the measurement subsystem, measures the gradient of the perturbations in the uniform field. The measurement subsystem then processes the gradiometer signal and provides an indication relating to the condition of the outlet strut of the valve.

During the examination, the gradiometer-based evaluation system uses a custom-built mobile frame to support the excitation coils, and a modified surgery table to support the patient. The support frame adds mobility to the excitation coils with minimal inconvenience to the patient. The modified surgery table provides multiple degrees of freedom for positioning the patient to align the heart valve with the applied magnetic field. Since the table top is inserted between the excitation coils during the examination, the top is made with no metallic parts to ensure that it does not interfere or distort the applied field.

This chapter describes the components of the gradiometer-based evaluation system. The characteristics and performance of this system are presented in Chapter 8.

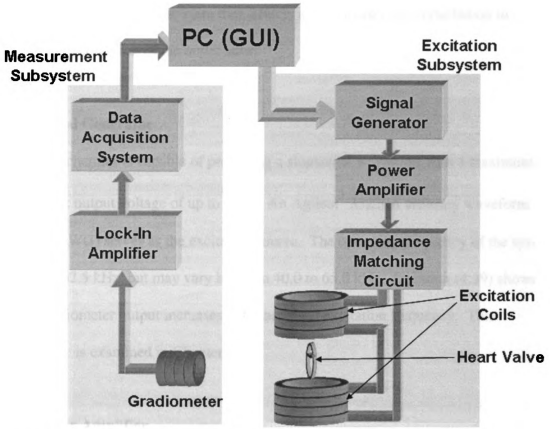

Figure 6.1 System block diagram of the gradiometer-based prosthetic heart valve examination system (components not drawn to scale)

6.1 The Excitation Subsystem

The excitation subsystem consists of a signal generator, power amplifier, an impedance matching circuit and a pair of excitation coils. The signal generator creates a sinusoidal excitation signal that is amplified by the power amplifier. The output of the amplifier is applied to the excitation coils through an impedance matching circuit. The impedance matching circuit ensures that the maximum power is transferred from the amplifier to the excitation coils. The excitation coils establish an alternating magnetic field with a uniform region at the center. The heart valve is placed in this region and the applied magnetic field induces eddy currents in the outlet strut that in turn perturb the applied

field. The measurement subsystem then detects and processes the perturbation to determine the condition of the outlet strut.

6.1.1 Signal Generator

The signal generator is capable of producing a sinusoidal waveform with a maximum peak-to-peak output voltage of up to 20 V. An Agilent[1] 33220A arbitrary waveform generator (AWG) serves as the excitation source. The operating frequency of the system is typically 62.5 kHz, but may vary between 40.0 to 65.0 kHz. Equation (4.39) shows that the gradiometer output increases with increased excitation frequency. This characteristic is examined in Chapter 8.

6.1.2 Power Amplifier

The power amplifier must supply a minimum of 1050 watts to the impedance matching circuit and the excitation coils at an equivalent impedance between 2.0-8.0 Ω. The amplifier must have a bandwidth of at least 80.0 kHz, and capable of supplying an output current of 15.0 A_{rms} or larger, with a maximum output voltage of 70.0 V_{rms} or higher.

The amplifier[2] in the gradiometer-based examination system is constructed from two Crown M-600 power amplifiers interlocked serially into a master-slave (push-pull) configuration known by the manufacturer as the M-2000 setup. The M-2000 can provide

---

[1] Agilent Technologies, Incorporated, Palo Alto, CA.

[2] Alternate power amplifier suggestions: (1) AE Techron 8604 gradient amplifier, AE Techron, Incorporated, Elkart, IN; (2) QSC PL 236a power amplifier, QSC Audio, Incorporated, Costa Mesa, CA.

up to 140 V_{rms} at over 2000 W output power (into a 4-Ω load) and a bandwidth of up to 100.0 kHz. The M-2000's line voltage (110V AC) power requirement makes the amplifier system portable and suitable for use in any examination facility.

6.1.3 Impedance Matching Circuit

An impedance matching circuit (Figure 6.2) is used to ensure that the total load impedance of the circuit and the excitation coils is matched to the output impedance of the amplifier at the excitation frequency. The circuit consists of a power resistor bank, R_T, and a bank of power capacitors, C_T. The resistor bank consists of five 300W 1 Ω power resistors[1] connected in parallel, providing an equivalent resistance of 0.2 Ω. The resistor bank is crucial in maintaining the stability of the excitation circuit by minimizing power oscillation between the capacitors and the excitation coils when their impedances are matched at the excitation frequency. The power capacitor bank consists of thirty five 2000 VAC 250.0 nF capacitors[2], providing a capacitance of approximately 7.143 nF when connected in series. The exact number of capacitors used is a function of both the excitation frequency and the inductance of the excitation coils. For a given operating frequency, *f*, the number of capacitors required is such that the impedance of the

---

[1] Part number 18-136-1AR/WBRKT, 300W, Milwaukee Resistor Corporation, Milwaukee, WI.

[2] Part number SCRN246R, 2000 VAC, 250 nF, Cornell Dubilier Electronics, Incorporated, Liberty, SC.

capacitor bank, X_{Cr}, is matched to that of the excitation coils, X_L, according to Equation (6.1):

$$2\pi f X_L = \frac{1}{2\pi f X_{Cr}}$$

$$X_{Cr} = \frac{1}{(2\pi f)^2 X_L} \tag{6.1}$$

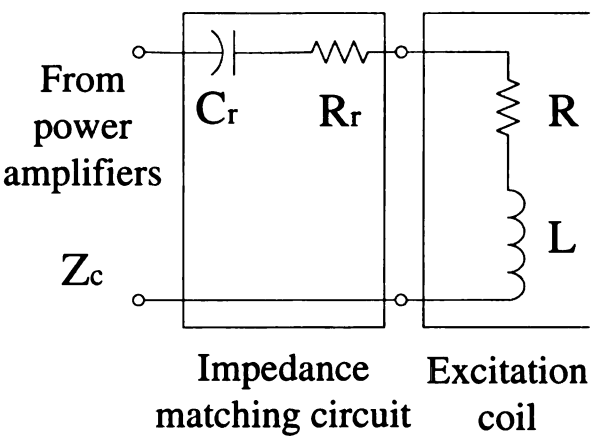

Figure 6.2 Impedance matching circuit. R_r denotes a bank of power resistors, and C_r denotes a bank of power capacitors.

6.1.4 Excitation Coils

A large Helmholtz coil is employed to generate the uniform magnetic field for the gradiometer-based examination system. Each excitation coil has a mean radius of 1 m. The two coils of the Helmholtz system are electrically connected in series and spaced 1 m apart. The input excitation signal causes an alternating current to flow in the coils which in turn generates an alternating magnetic field with a uniform volume at the center.

Two sets of excitation coils have been constructed, one with a 4/0 AWG wire and the other with 1/0 AWG wire. Each excitation coil consists of 9 turns of the respective wire. Both sets of excitation coils have the same Helmholtz configuration and similar electromagnetic properties. The excitation coils constructed with the 1/0 AWG wire has a lower DC resistance, which amounts to a lower overall load impedance when connected to the impedance matching circuit. For example, at an excitation frequency of 60.5 kHz, the overall impedance[1] of the excitation circuit with the 4 AWG wire excitation coils is 9.54 Ω, while that for the circuit with the 1/0 AWG wire coils is 5.52 Ω. A smaller load impedance allows for a closer match to the amplifier output impedance, resulting in a more efficient power transfer from the amplifier to the excitation circuit. The following discussions pertain to both sets of excitation coils.

6.1.5 Helmholtz Coil

The Helmholtz configuration produces a spatially uniform magnetic field in a cylindrical region extending between the centers of the two coils and approximately 1/4 to 1/2 of their diameter as illustrated in Figure 6.3 and obtained numerically in Figure 5.5. For a pair of N-turn coils each of radius R and a current I, the magnetic field at any point on the axis of an ideal Helmholtz coil may be calculated by assuming each coil of the Helmholtz pair is a simple current loop made from a wire of infinitesimal diameter and applying the *Biot-Savart Law* to obtain the magnetic field along the centerline of each loop. The total magnetic field is then obtained by superimposing the fields from the two loops. Hence, the on-axis magnetic field of the Helmholtz coil is given by [129], [185]

---

[1] The overall impedance includes contributions from the connection terminals, wires, and connectors.

$$B = \frac{\mu_0 I}{2R}\left[\frac{1}{\left(\gamma^2+\gamma+\frac{5}{4}\right)^{\frac{3}{2}}} + \frac{1}{\left(\gamma^2-\gamma+\frac{5}{4}\right)^{\frac{3}{2}}}\right] \tag{6.2}$$

where $\gamma = \frac{z}{R}$, z is the distance on the axis from the center of the two coils , and B is the magnetic field in Tesla (T). The direction of the magnetic field is along the axis of the two coils. The constant $\mu_0 = 4\pi$ x 10^{-7} Wb A^{-1} m^{-1} (or H/m) is the permeability of free space. For the special case when z = 0, the magnetic field at the center of the coils may be estimated by the Helmholtz coil equation [129]

$$B = \frac{8\mu_0 NI}{5\sqrt{5}R} \tag{6.3}$$

Although Equation (6.3) may be used to predict the magnetic flux density, the equation does not provide any dimensional information on the uniform magnetic field volume between the coils. To obtain this information, more sophisticated treatments such as the finite element analysis described in Chapter 5 and the methodologies given in [176] and [177] may be used. Chapter 8 presents the volume of the uniform magnetic field obtained by physical measurements.

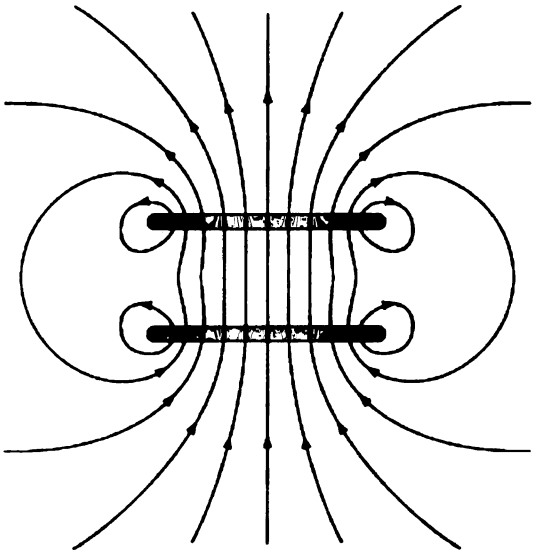

Figure 6.3 Illustration of the magnetic flux lines generated from a Helmholtz coil. After [129].

The gradiometer-based examination system employs two 9-turn excitation coils each with a mean radius of 1 m. The input is an 11-A peak-to-peak sinusoidal current. With these parameter values, Equation (6.3) predicts a magnetic field of approximate 0.89×10^{-4} T (0.89 gauss). This value is smaller than that obtained from the finite element analysis results shown in Figure 5.5-Figure 5.7. The disagreement between the two values is due to the fact Equation (6.3) was derived with the assumption that the excitation current was carried in a wire of infinitesimal diameter. In reality, the excitation coil wire has a finite cross-sectional area as shown in Figure 5.3. The contribution to the overall magnetic field from the current flowing in the finite-thickness wire must be accounted for. This had been done in the finite element analysis and the results were reported in Chapter 5. Physical measurement of the magnetic flux density in the Helmholtz coil with an input current of 11 A (peak-to-peak) has also confirmed a center flux density of approximately

1.45 gauss as predicted by the finite element model. This and other experimental results for the gradiometer-based examination system are described in details in Chapter 8.

The excitation coils are each wound on a 2-meter diameter mounting ring. The mounting rings are separated by 1 m with support beams as shown in Figure 6.4 (the cross and radial beams shown mounted inside the excitation coils in this figure are used for specimen testing. Details and results of these tests are reported in Chapter 8). The entire coil mount structure is modular and can be easily disassembled and transported in parts no larger than 4' by 2'. When assembled, the coil mount is capable of supporting more than 150 lbs of wire.

6.2 Excitation Coils Mobile Custom Support System

The excitation coils are supported on a mobile custom support frame. During the examination, the excitation coils are mounted on a 45° inclination (see Figure 6.5) to facilitate the alignment of the magnetic field with the flange plane of the heart valve. This orientation minimizes the amount of eddy current induced in the flange ring and ensures that the current induced in the outlet strut is dominant. The dimensions of the coil support framework are shown in Figure 6.6. Fine tuning of the alignment may be made by adjusting the roll and tilt of the custom examination table described later in this chapter.

The excitation coils support system is designed to accommodate both the patient and the custom examination table (Figure 6.7). The support system is constructed on a mobile

platform (Figure 6.8) to allow movements of the excitation coils while minimizing the disturbance to the patient. The platform casters each has a leveling pad (Figure 6.9) that can be raised and lowered using a telescoping ratchet handle for securing the support structure in place once it is properly positioned.

6.3 The Measurement Subsystem

The measurement subsystem consists of the gradiometer, lock-in amplifier and a data acquisition system (DAQ). The signal from the gradiometer is amplified and processed by the lock-in amplifier. The outputs of the lock-in amplifier are then digitized by the DAQ and transmitted to the PC where the system software displays, processes and analyzes the gradiometer signal to determine the outlet strut condition of the heart valve. Two gradiometers have been prepared for use with the gradiometer-based examination system. The designs of the gradiometers are described in the next chapter. The remaining Measurement Subsystem components are described in the following sections.

6.3.1 Lock-in Amplifier

The signal from the gradiometer is processed by a 100 kHz bandwidth dual phase lock-in amplifier (LIA). Lock-in detection[1] is a phase-sensitive demodulation technique. The dual phase amplifier uses two phase sensitive detectors to detect and process the gradiometer signal with reference to the input excitation signal. The principle of lock-in detection is described below.

---

[1] Lock-in detection is also commonly known as quadrature detection, quadrature demodulation, phase quadrature technique, or phase quadrature heterodyne demodulation

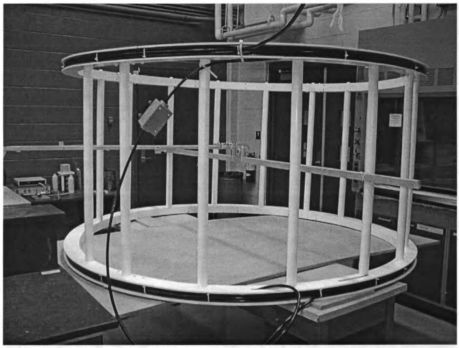

(a)

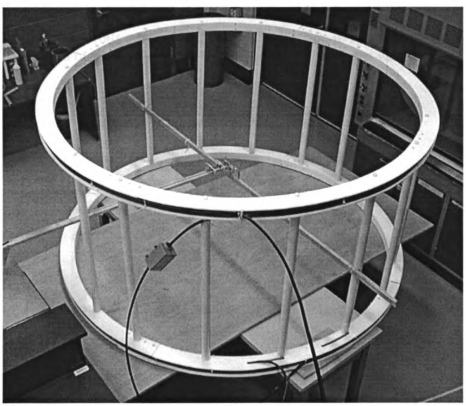

(b)

Figure 6.4 Side (a) and top (b) views of the excitation coils. The excitation coils are mounted on a modular wooden structure arranged in a Helmholtz configuration.

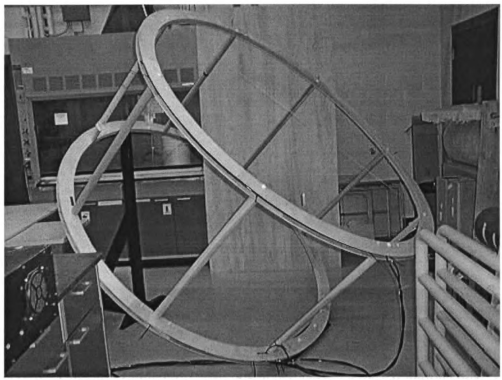

Figure 6.5 Excitation coils are mounted with an inclination to facilitate the alignment of the magnetic field with the flange ring of the heart valve.

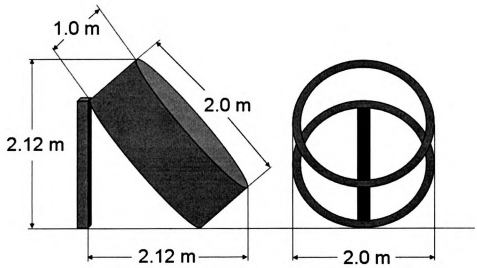

Figure 6.6 Dimensions of the excitation coils and the mobile custom coil support system

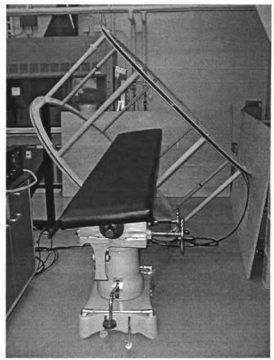

Figure 6.7 Custom examination table positioned between the excitation coils. The excitation coils system is designed to accommodate both the patient and the custom examination table.

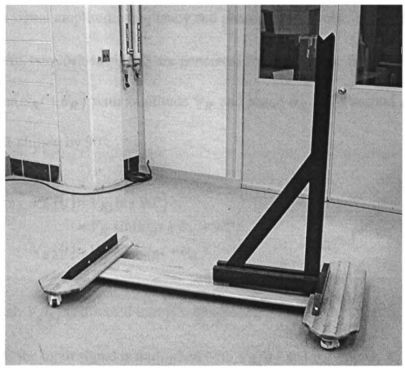

Figure 6.8 A mobile support frame allows the positioning of the coils around the patient and the custom examination table with no disturbance to the patient.

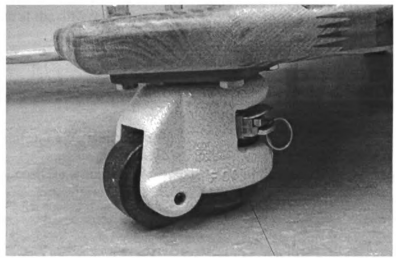

Figure 6.9 Each platform caster has a leveling pad that can be raised and lowered by a telescoping ratchet handle for parking the support structure.

6.3.1.1 Principle of Lock-In Detection

Lock-in detection is performed with respect to a reference frequency, ω_R, which is the excitation signal in this case. Let the input signal be $V_S(t) = P\sin(\omega_S t + \theta_S)$ where P, ω_S and θ_S are the signal amplitude, frequency and phase, respectively. In a lock-in detection system, two lock-in signals are generated from ω_R. The first signal is $V_{R1}(t) = V_R \sin(\omega_R t + \theta_R)$ with amplitude V_R and phase θ_R. The second signal $V_{R2}(t)$ is $V_{R1}(t)$ phase shifted by 90°:

$$\begin{aligned} V_{R2}(t) &= V_{R1}(t + 90°) \\ &= V_R \sin(\omega_R t + \theta_R + 90°) \\ V_{R2}(t) &= V_R \cos(\omega_R t + \theta_R) \end{aligned} \tag{6.4}$$

The input signal, $V_S(t)$ is directed into two quadrature multipliers, A and B, respectively. In multiplier A, the input signal is multiplied with $V_{R1}(t)$ and the output, X, is the sum of

two signals, one at the difference frequency $(\omega_S - \omega_R)$ and the other at the sum frequency $(\omega_S + \omega_R)$:

$$\begin{aligned} X &= PV_{R1}\sin(\omega_S t + \theta_S)\sin(\omega_R t + \theta_R) \\ &= \frac{1}{2}PV_{R1}\cos((\omega_S - \omega_R)t) + \theta_S - \theta_R) - \frac{1}{2}PV_{R1}\cos((\omega_S + \omega_R)t) + \theta_S + \theta_R) \end{aligned} \quad (6.5)$$

A low-pass filter is then applied to X to remove the high frequency component. If the reference frequency is the same as the signal frequency, i.e., $\omega_R = \omega_S$, the component at the difference frequency will be a DC valve. In the case if the input contains signals of other frequencies as well as noise, the low-pass filtering will remove all but the signal at ω_R. Also, setting the reference signal amplitude, V_{R1}, to 2, leads to the filtered multiplier output

$$X = P\cos(\theta_S - \theta_R) \quad (6.6)$$

which is a DC value proportional to the signal amplitude, P.

In multiplier B, the input signal is multiplied with $V_{R2}(t)$. A subsequent low-pass filter produces the output

$$Y = P\sin(\theta_S - \theta_R) \quad (6.7)$$

The two multiplier outputs, X and Y, represent the signal as a vector relative to the lock-in reference signal. The output X is known as the "in-phase" component while Y is the "quadrature" component. Let the phase difference between the input and the lock-in reference signal be θ, i.e., $\theta = \theta_S - \theta_R$. (When $\theta = 0$, the in-phase component measures

the signal while the quadrature component is zero.) To remove the phase dependency, the magnitude, R, can be used:

$$R = \left(X^2 + Y^2\right)^{1/2} \tag{6.8}$$

Substituting (6.6) and (6.7) into (6.8) shows that R is:

$$R = P \tag{6.9}$$

which is the amplitude of the gradiometer signal. Also, the phase, θ, between the input and the lock-in reference signal is given by

$$\theta = \tan^{-1}(Y / X) \tag{6.10}$$

6.3.1.2 Lock-in Detection of the Gradiometer Signal

From the previous section, the relationship between the input and output signals of the LIA is summarized as follows. Let the LIA input signal, $V_S(t)$, be the signal from the gradiometer. Using the excitation signal from the signal generator as the reference, the LIA outputs from (6.6) and (6.7) can be written as

$$X = R\cos(\theta) \tag{6.11}$$

$$Y = R\sin(\theta) \tag{6.12}$$

where θ is the phase angle between $V_S(t)$ and the reference signal, and R is given by Equation (6.8). The outputs of the LIA, X and Y, are then digitized and analyzed to determine the condition of the heart valve. When the gradiometer is placed directly in front[1] of the outlet strut, "large" values of X and Y indicate an IOS valve while "small"

[1] In reality, the gradiometer will not be stationary in front of the outlet strut. Instead, the relative distance between the two will be time-varying in a cyclic manner due to the cardiac cycle. More discussions on the effect of the varying distance between the gradiometer and the outlet strut are given in Chapters 4 and 8.

values indicate a SLS case. (The relative magnitudes of the "large" and "small" signals are system- and gradiometer-dependent, and are obtained by pre-calibrating the examination system with an IOS and a SLS valve, respectively, during system setup. A detailed discussion of the signal level in relationship to the strut condition is given in Chapter 8.) Large LIA outputs are results of a strong gradiometer signal at the excitation frequency. This strong signal indicates a significant perturbation in the gradient of the uniform excitation field, which is indicative of an IOS valve. On the other hand, small and rapidly fluctuating LIA outputs indicate a weak gradiometer output signal at the excitation frequency. This implies a minimal perturbation in the applied magnetic field, which in turn indicates little or no eddy current is circulating in the outlet strut—a result indicative of a single-leg separation in the outlet strut. Chapter 8 explains how to interpret the outlet strut condition based on the LIA outputs. The gradiometer-base system uses an ITHACO, Incorporated, Model 3961 lock-in amplifier[1].

6.3.2 Data Acquisition System

The Data Acquisition System consists of a digital oscilloscope for real-time signal monitoring and a PC-based data acquisition card. The digital oscilloscope displays the X and Y output signals from the lock-in amplifier, and can optionally store these signals. Two channels from a 14-bit, 2 MS/s, 4-channel simultaneous sampling data acquisition card is used to digitize the X and Y output signals from the lock-in amplifier. The third DAQ channel monitors the current passing through the excitation circuit by sampling the

[1] Alternative lock-in amplifier selection: Stanford Research Systems SR 830 DSP dual phase lock-in amplifier, Stanford Research Systems, Incorporated, Sunnyvale, CA 94089, www.thinksrs.com.

output of a current probe. The fourth channel records the electrocardiogram (ECG) signal of the patient during the examination for future reference. The Gradiometer-based examination system uses a HP 54710A/54713A digital oscilloscope by Agilent Technologies, Incorporated[1] (formerly Hewlett-Packard, Incorporated), the NuDAQ DAQ-2010 PC-based data acquisition card by ADLINK Technology, Incorporated[2], and the Agilent 1146A AC/DC current probe also by Agilent Technologies for data monitoring and recording.

6.4 Custom Examination Table

A vintage surgery table had been modified into a custom examination table for patient support during the heart valve examination. The original table had a metallic top that would interfere with the excitation field when inserted between the excitation coils. The tabletop and other metallic sections of the table that would affect the examination results were stripped off and a new top has been fabricated using non-conducting composite materials. The new top contains high density foam and Luan set lengthwise at approximately 6" intervals and wrapped around by fiberglass and resin. This creates a lightweight and yet strong and non-conducting bed that is slightly thicker than 5 cm. Figure 6.10 shows the modified vintage surgery table with the composite table top. The table top is 2.48 m (97.5 in) long and 0.52 m (20.5 in) wide as shown in Figure 6.11. The finished examination table is shown in Figure 6.12. In this figure, a custom tailored black vinyl cover is fitted to provide the table with an even and smooth surface and to allow for easy cleaning and maintenance.

---

[1] Agilent Technologies, Incorporated, Palo Alto, CA 94306, www.agilent.com

[2] ADLINK Technology, Incorporated, Irvine, CA 92618, www.adlinktech.com

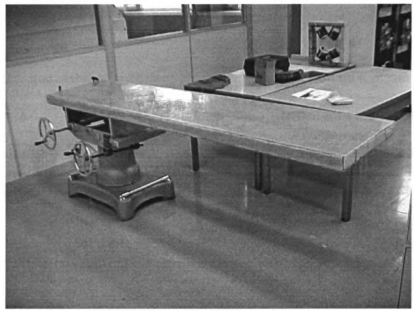

Figure 6.10 Custom examination table with a nonmetallic composite top that does not interfere with the applied magnetic field

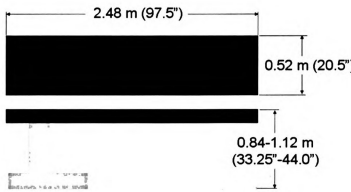

Figure 6.11 Tabletop dimensions and height adjustment range for the custom surgery bed

The examination table can be raised and lowered from 0.84 m (33.25 in) to 1.12 m (44 in) relative to the ground by a hydraulic mechanism. The top can also be tilted in the head-to-toe fashion (pitch). Additional modifications have been made to provide a 10-degree side-to-side tilting (roll) freedom in either direction. Two large wheel handles on the side of the bed are used to adjust the pitch and roll of the tabletop. This positioning flexibility

allows precision positioning of the patient to align the flange plane of the heart valve with the applied magnetic field during examination.

To ensure safety and stability, a custom bracket has been welded underneath the base of the table (Figure 6.13). This bracket accommodates a wooden forward T-shape extension (Figure 6.14) that provides additional support and stability for the table when in use. The extension is 1.85 m (73 in) long and 1.22 m (48 in) wide. Figure 6.15 shows the custom surgery table with the T-shape wooden extension in place. During positioning and transportation of the table, the arm extension maybe removed for mobility.

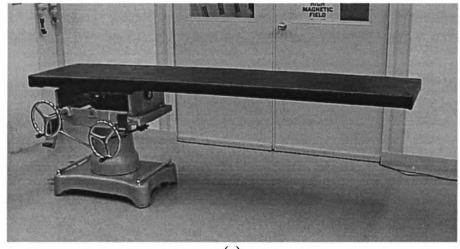

(a)

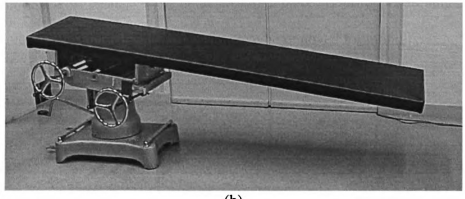

(b)

Figure 6.12 Two views of the finished custom surgery table. Two large wheel handles on

the side are for adjusting the pitch and roll of the tabletop

Figure 6.13 A bracket is welded underneath the base of the custom examination table for accommodating a wooden extension arm that provides additional support and stability.

Figure 6.14 A T-shape wooden extension is used to increase the stability of the custom surgery table when in use

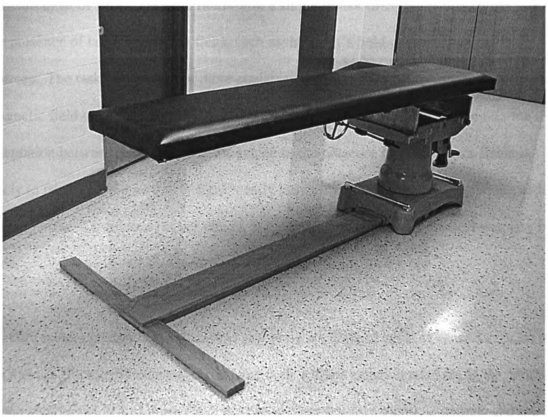

Figure 6.15 Custom surgery table with a T-shape wooden extension for increased stability

A clinical-scale prototype of the gradiometer-based examination system has been constructed from the components described in this chapter. The design of the gradiometer is presented in the next chapter. The operating parameters and settings of these components are described in Chapter 8.

CHAPTER 7. GRADIOMETER DESIGNS

Measurement of small magnetic fields with a single sensor often poses difficulties due to the presence of large interfering fields such as the earth's field or other man-made sources. The task becomes even more challenging if either the source of the small magnetic field or the senor, or both, is non-stationary. A small change in the relative orientation between the source and the sensor in the presence of interference fields is likely to produce a signal that is significantly larger than the actual field variations under investigation. To circumvent the effects of the interference fields, a gradiometer may be used.

A gradiometer consists of two identical and perfectly aligned coils, or sensors. These two sensors are electrically connected such that their outputs are subtracted from one another. When submerged in a uniform field, the two sensors produce identical outputs and the gradiometer output will be zero, effectively removing the influence of the uniform field. If the positional relation between the two sensors remains fixed, the gradiometer may be rotated and translated within the uniform field without producing any orientation-dependent output.

In the gradiometer-based prosthetic heart valve inspection system, the heart valve is submerged in a uniform magnetic field and a gradiometer is placed in the vicinity of the outlet strut. A current is induced in the outlet strut and this current in turn creates a magnetic field. The induced magnetic field perturbs the applied uniform field and the gradiometer measures the gradient of resulting field in the vicinity of the strut. Since the

induced current is a function of the outlet strut integrity, the gradiometer output signal, therefore, can be used to characterize the condition of the outlet strut.

7.1 Gradiometer Output Signal

The mathematical model of the gradiometer-based system described in Chapter 4 provides a starting point for designing the gradiometer. The design goal is to maximize the gradiometer's signal level. Although the gradiometer output is a function of many physical and system parameters, the gradiometer design begins with the factors in Equation (4.41) that are related to the geometry, position and separation of the sensor coils.

From Equation (4.39), the physical qualities of the gradiometer that affect its output signal are the number of turns in each sensor coil, the area of each coil, and the separation between the two coils. By keeping all other factors constant, Equation (4.57) expresses the gradiometer output v_g as a scaled signal $U(z_1, \Delta z)$ that is a function of both its distance, z_1, from the outlet strut and the separation, Δz, between the two sensor coils. For values of z_1 from 0–10 mm, Equation (4.57) is evaluated for Δz from 0–20 mm. The results are shown in Figure 7.1. Figure 7.2 displays the same results in the 2D plane. From this figure, the strongest output signal (the brightest region in the figure) occurs when the gradiometer is 4 mm or less away from the outlet strut and the separation between the sensor coils is approximately 3 mm or more. These results, in conjunction with other physical constraints, are taken into consideration when designing the gradiometer.

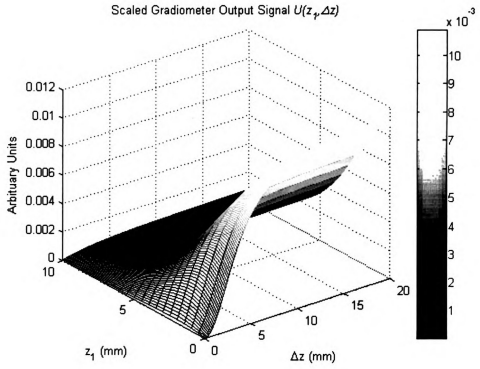

Figure 7.1 Scaled gradiometer output $U(z_1, \Delta z)$ as a function of Δz at values of z_1

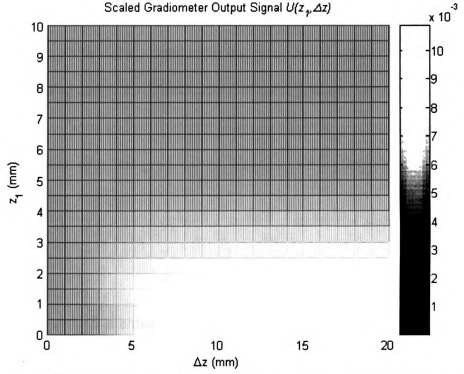

Figure 7.2 A 2D view of the data from Figure 7.1 showing the strongest output signal occurring when $z_1 < 4$ mm and $\Delta z \geq 3$ mm

7.2 Physical Constraints

Besides the signal level and quality, there are three primary physical constraints that affect the design of the gradiometer. First, as the gradiometer is placed in the mitral annulus (in the vicinity of the outlet strut) during the prosthetic heart valve examination, the gradiometer sensor coils and signal leads must be sufficiently small so that they can be delivered and positioned inside the left ventricle of the heart via conventional cardiac catherization procedures. Second, the lead wires of the sensor coils must be shielded from the excitation field to minimize interference. Third, the gradiometer assembly must be of proper stiffness—neither too soft nor rigid—to aid the delivery and positioning of the sensor coils. Based on these constraints, two gradiometer assemblies have been constructed that are suitable for clinical use. In the first assembly, the gradiometer sensor coils, the lead wires and a thin layer of electromagnetic shielding material are encased and sealed inside a 9 F[1] pre-curved guide catheter[2]. The second assembly delivers a 6 F gradiometer with a shielded specialty cable into position via a pre-curved 6 F cardiac guide catheter. The design and specifications of these gradiometer assemblies are given below. Characterization and performance tests results of the gradiometer-based examination system with both gradiometers are presented in Chapter 8.

---

1 "French," abbreviated as either "F" or "Fr," is a unit of length measure typically used in the medical community (e.g., in catheter sizes). 3 F = 1 mm.

2 Size for a catheter is both manufacturer and type dependent. For a conventional catheter the size often refers to the outer diameter while that for a guide catheter refers to the lumen (inner) diameter.

7.3 Delivery Approaches

To satisfy the physical design constraints, the gradiometer size and the delivery and positioning approaches are first determined. For precise positioning of the gradiometer in the left ventricle, conventional cardiac catherization techniques from interventional cardiology are employed. The gradiometer is delivered either intraluminally or via a guide catheter into the ventricle. Circulatory access is obtained via either a femoral or carotid cutdown followed by cannulation. Due to the limited arterial lumen clearance, the outer diameter of the gradiometer assembly is limited to approximately 9 F, which limits the catheter lumen size to less than 8 F. The gradiometer assembly is advanced inferiorly into the left ventricle via the aorta and through the aortic valve until it reaches the apex of the heart (Figure 7.3). The distal end of the assembly is then turned to follow the inner walls of the ventricle and advances superiorly towards the mitral annulus. Figure 7.4 and Figure 7.5 show two approaches for delivering and positioning the gradiometer assembly. In Figure 7.4, a sealed catheter-encased gradiometer assembly is advanced intraluminally into the ventricle and positioned into the mitral annulus. In Figure 7.5, a guide catheter is pre-positioned in the left ventricle using conventional catherization technique. A gradiometer is then advanced through the guide catheter and positioned into the mitral annulus. The designs and benefits of these two gradiometer assemblies are discussed below.

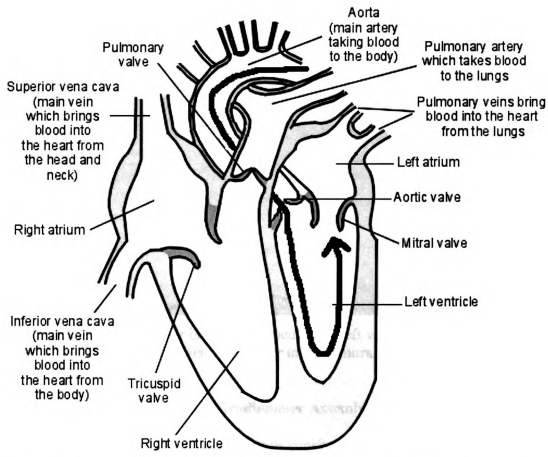

Figure 7.3 Advancement of the gradiometer assembly inside the heart (black arrow)

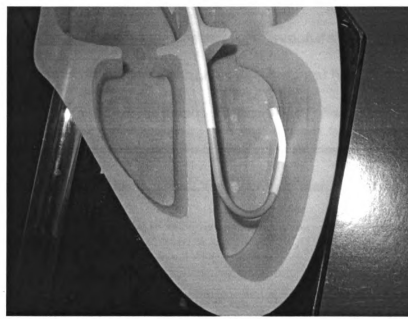

Figure 7.4 A sealed catheter-encased gradiometer assembly is delivered intraluminally and positioned in the mitral annulus. After [195]

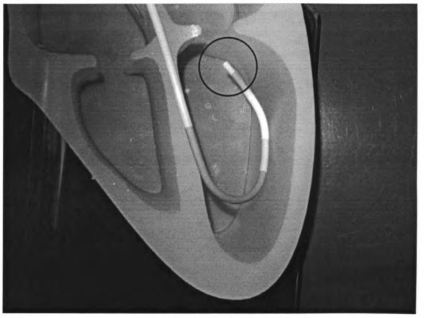

Figure 7.5 A guide catheter is pre-positioned in the left ventricle and the gradiometer (circled) is advanced via the catheter into the mitral annulus. After [195]

7.4 Gradiometer Assemblies

In a gradiometer, each of the two sensor coils consists of a length of wire wound in a multi-layer helical manner around the length of a cylindrical epoxy former. When subjected to a time-varying magnetic field, an EMF is induced in each coil according to *Faraday's Law*. The output of the gradiometer is proportional to the number of turns and the area of each sensor coil at a given excitation frequency and field strength. The design goals are, therefore, to maximize the number of turns and the diameter of the coils while satisfying the physical size constraints. To allow for proper maneuvering and to avoid damages to the blood vessels and the heart, the size (outer diameter) of the gradiometer assemblies are limited to 9 F [150] or less.

During the examination, the gradiometer signal cable is also subjected to the applied excitation magnetic field. To minimize the coupling of the applied field into the signal

cable, two small-diameter specialty cables each containing a pair of shielded twisted signal wires are used. Two gradiometer assemblies, each using one of these cables, have been designed. The first is a 9 F assembly with the gradiometer sealed inside a catheter. The second is a 6 F two-piece assembly consisting of a cardiac guide catheter and a 6 F (standalone) gradiometer. Details of these two catheter assemblies are given below.

7.4.1 The 9 F Gradiometer Assembly

Figure 7.6 shows the schematic diagram and Figure 7.7 shows a picture of the 9 F gradiometer assembly. In this system, a gradiometer is encased and sealed in a 9 F guide catheter to form an integral unit. Figure 7.8 shows the schematic diagram of the gradiometer sensor head. The sensor head is 3.0 mm long and consists of two sensor coils each made from 88 turns of a 44 AWG wire. The gradiometer output is the difference signal from the two sensor coils. The typical[1] resistance and inductance of the sensor coils are given in Table 7.1. Each sensor is approximately 2.5 mm in diameter and 0.35 mm tall, and the two coils are separated by 1.62 mm. The epoxy cylinder (the sensor head) embedding the coils are made from Ultem 1000 polymer. Ultem 1000 is a thermoplastic polyetherimide high heat polymer designed by General Electric[2], Inc. for injection molding applications. The polymer is inert to bio-chemicals and suitable for biological applications. It can also withstand medical sterilization processes.

---

[1] Due to manufacturing variations such as the density and fill-factor of the turns, the inductance of each coil varies slightly. The data given in Table 7.1 are typical valves.

[2] GE Plastics, Incorporated, Pittsfield, MA, www.geplastics.com

Table 7.1Typical resistance and inductance of the 9 F gradiometer sensor coils (Measured at 1 MHz)

Sensor Coil	Resistance (Ω)	Inductance (μH)
Distal	10.375	7.775
Proximal	10.414	7.793

The 9 F gradiometer has been fabricated by Xactex, Corporation[1] and assigned the part number POT-9075 (Figure 7.9). In this gradiometer, the sensor signal cable is made from a pair of 36 AWG wires, twisted and shielded inside an aluminum foil. The signal leads are approximately 1 cm long. The first 25.4 mm of this cable from the sensor head is covered with a heat-shrink tube as shown in Figure 7.8. This section of wires has a maximum diameter of 2 mm, which allows it to fit inside a 9 F guide catheter that has a typical lumen size of approximately 2.6 mm. The signal cable is followed by 512 cm of an Alpha Wire Company[2] number 58401 cable as shown in Figure 7.6. This cable contains a foil-shielded twisted pair of 24 AWG wires. The catheter is a Medtronic, Incorporated3, Zuma™ 9 F, 100 cm, JCL 4.5 SH guiding catheter (catalog number ZM9JCL45SH). This catheter has an outer diameter of 3.02 mm (9.06 F) and an inner diameter of 2.62 mm (7.86 F). The gradiometer is sealed inside the guide catheter using

[1] Xactex, Corporation, Pasco, WA 99301, www.xactex.com

[2] Alpha Wire Company, Elizabeth, NJ 07207-0711, www.alphawire.com

[3] Medtronic, Incorporated, Minneapolis, MN 55432-5604, www.medtronic.com

a small amount of Aron Alpha[1] series 232 medical-grade adhesive. The tip of the gradiometer is also coated with this adhesive to protect the sensor coil. Figure 7.10 shows a close-up view of the 9 F gradiometer-in-catheter assembly. Table 7.2 summarizes the components for the 9 F gradiometer assembly.

Table 7.2 Components of the 9 F (POT-9075) gradiometer assembly

Component	Manufacturer and Part Number
Gradiometer	Xactex, Corporation, Part No: POT-9075
Data Cable	Alpha Wire Company, Part No.: 58401
Catheter	Medtronic, Incorporated, Zuma™ 9 F Guiding Catheter JCL 4.5 SH (Cat. no.: ZM9JCL45SH)
Adhesive	Aron Alpha, Series 232

[1] Aron Alpha, a division of Elmer's Products, Incorporated, Columbus, OH 43215, http://www.krazyglue.com/industrial/industrial.asp

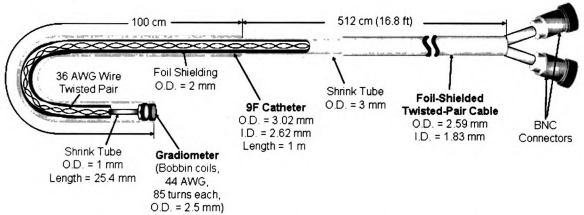

Figure 7.6 Schematic diagram of the 9 F gradiometer assembly

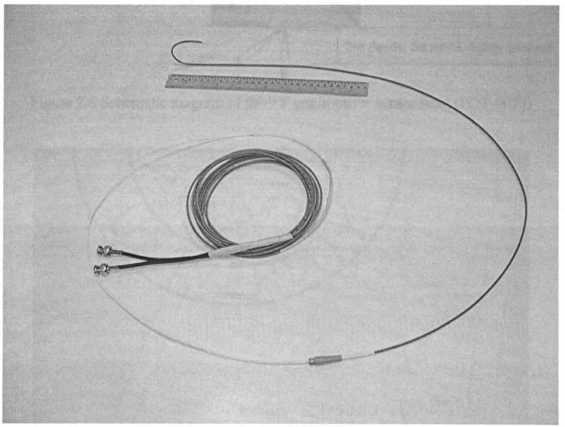

Figure 7.7 9 F gradiometer assembly

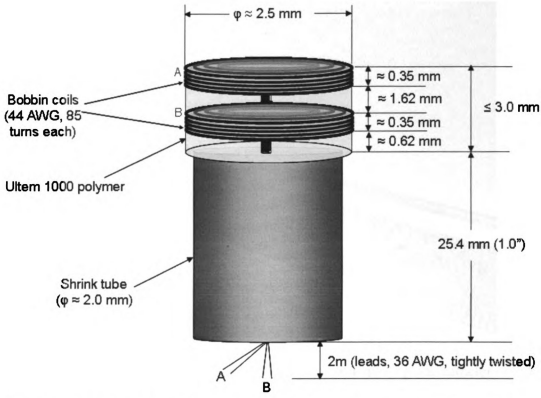

Figure 7.8 Schematic diagram of the 9 F gradiometer sensor head (POT-9075)

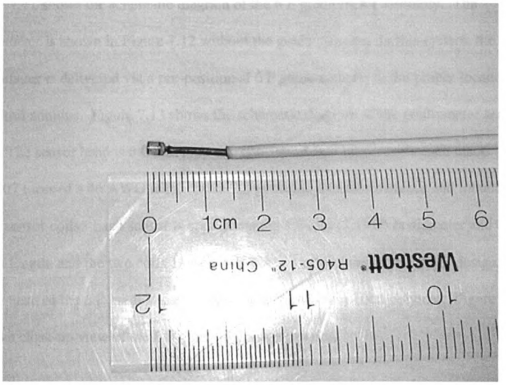

Figure 7.9 Close-up view of the 9 F gradiometer (POT-9075) sensor head

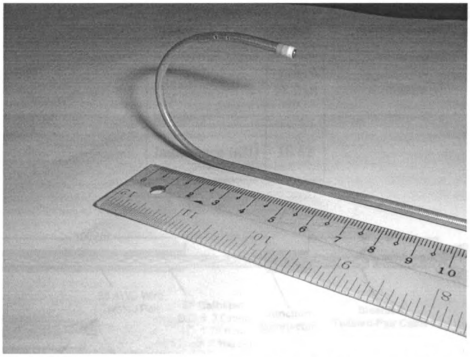

Figure 7.10 9 F gradiometer encased and sealed inside a guide catheter

7.4.2 The 6 F Gradiometer Assembly

Figure 7.11 shows the schematic diagram of the 6 F gradiometer assembly. The gradiometer is shown in Figure 7.12 without the guide catheter. In this system, the gradiometer is delivered via a pre-positioned 6 F guide catheter to the proper location in the mitral annulus. Figure 7.13 shows the schematic diagram of the gradiometer sensor head. The sensor head is 6.0 mm long and consists of two sensor coils each made from107 turns of a 46 AWG wire. Table 7.3 gives the overall resistance and inductance of the sensor coils. Each sensor is approximately 1.7 mm (5.19 F) in diameter and 0.5 mm in length, and the two coils are separated by 1.8 mm. Similar to the 9 F design, the sensor head of the 6 F gradiometer is also made from Ultem 1000 polymer. Figure 7.14 shows a close-up view of the 6 F gradiometer sensor coils.

Table 7.3 Total resistance and inductance of the 6 F gradiometer sensor coils (Measured at 100 kHz)

Resistance (Ω)	18.038
Inductance (μH)	18.62

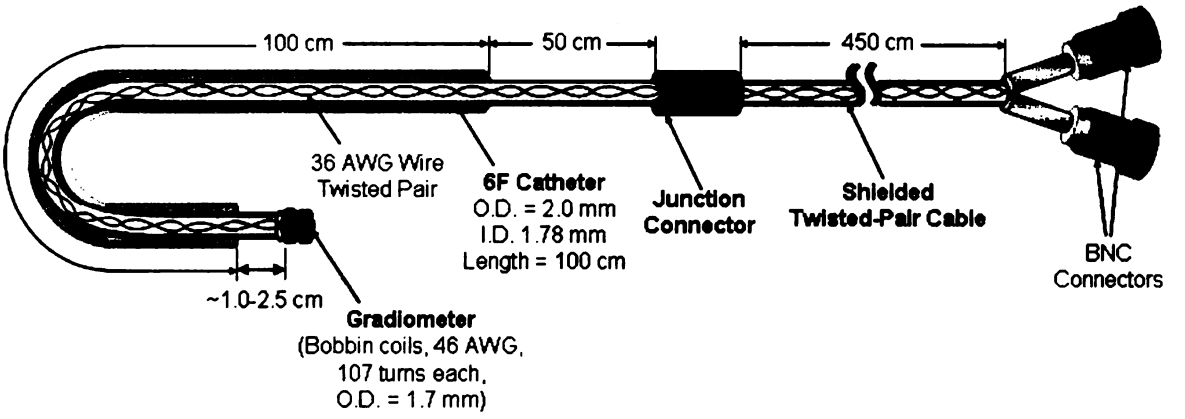

Figure 7.11 Schematic diagram of the 6 F gradiometer assembly

The 6 F gradiometer signal cable is made from a 150 cm long Cooner Wire[1] CZ1215-2F[2] wire, followed by 450 cm of a custom cable as shown in Figure 7.11. The CZ1215-2F cable consists a braid-shielded twisted pair of 36 AWG wires coated with a clear PVC jacket. The custom cable is made from shielding a Cooner Wire CW3735 cable with a 92166 S/S braid and covering the final cable with a white 3520 SPC shrink tube. The CZ1215-2F cable has a maximum outer diameter of 1.35 mm (4.04 F), and can pass through a 6 F guide catheter (lumen size ≈ 1.73 mm) easily. The 6 F gradiometer has

[1] Cooner Wire, Chatsworth, CA 91311, www.coonerwire.com

[2] As of Fall, 2005, the revised part number for CZ1215-2F is AS633-2SSF

been fabricated by Xactex, Corporation and assigned the part number POT-9083 (Figure 7.12).

Figure 7.15 shows an enhanced 6 F gradiometer sensor head with a tapered anchor to the lead cable. The taper provides a smooth transition from the lead cable to the sensor head to facilitate the retraction of the gradiometer into the guide catheter should it becomes necessary (e.g., a gradiometer replacement during the examination).

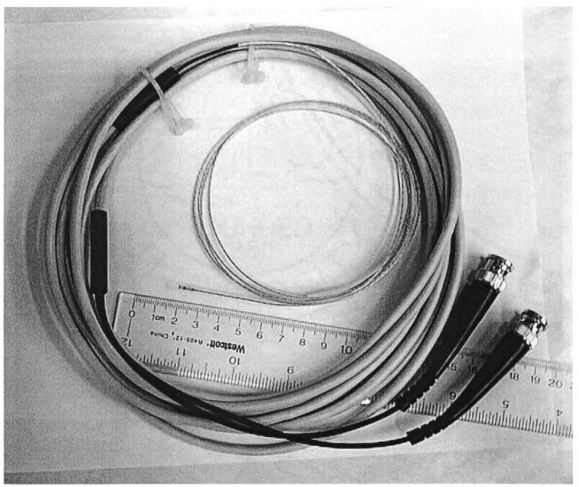

Figure 7.12 6 F gradiometer, POT-9083

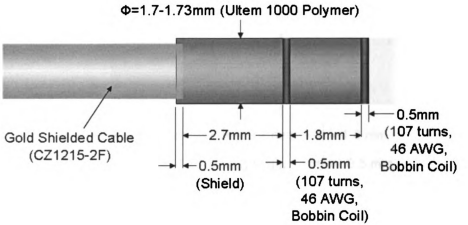

Figure 7.13 Schematic diagram of the 6 F gradiometer sensor head (POT-9083)

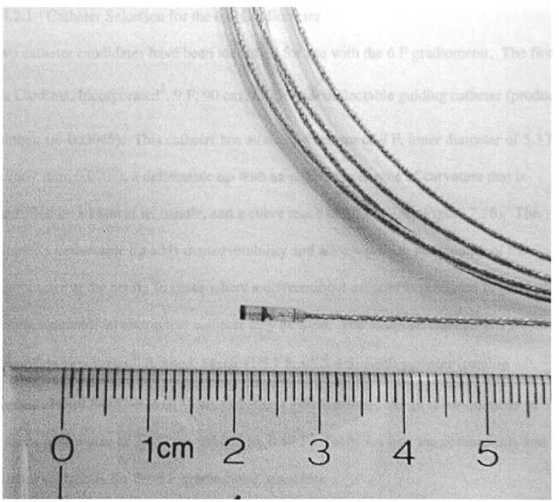

Figure 7.14 Sensor head of the 6 F gradiometer (POT-9083)

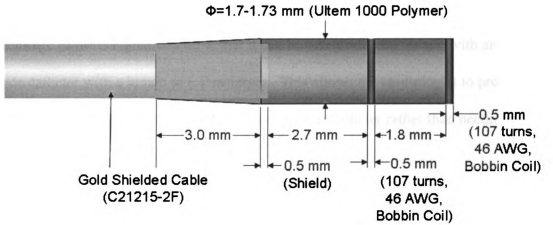

Figure 7.15 Schematic diagram of a modified 6 F gradiometer sensor head with a tapered cable anchor

7.4.2.1 Catheter Selection for the 6 F Gradiometer

Two catheter candidates have been identified for use with the 6 F gradiometer. The first is a Cardima, Incorporated[1], 9 F, 90 cm *Naviport*® deflectable guiding catheter (product number: 08-003045). This catheter has an outer diameter of 9 F, inner diameter of 5.3 F (1.7667 mm, 0.070"), a deflectable tip with an adjustable degree of curvature that is controlled by a knob at its handle, and a curve reach of 10 mm (see Figure 7.16). The catheter's deflectable tip adds maneuverability and allows precise positioning of the gradiometer in the heart. In cases where a conventional catheter is preferred (e.g., by the cardiac surgeon), an alternative catheter may be used. The alternate catheter is a Boston Scientific Corporation[2], Scimed, Mach 1™ 7 F, CLS 4.5, guide catheter (catalog number: H749 34357-576 0). This catheter is 100 mm long, has an outer diameter of 7.0 F, and a lumen size of 2.057 mm (0.081 in, 6.17 F). Table 7.4 lists the components and catheter selections for the 6 F gradiometer assembly.

[1] Cardima, Incorporated, Fremont, CA 94538-7330, www.cardima.com

[2] Boston Scientific Corporation, Natick, MA 01760-1537, www.bostonscientific.com

In practice, a cardiologist may have his or her own cardiac catheter preferences. One advantage of the 6 F gradiometer is that it can be easily adapted for use with any cardiac guide catheter with a lumen of 6 F or larger. This allows the cardiologist to precisely delivery and position the gradiometer with a familiar catheter rather than needing to adjust to a new catheter system.

7.5 Gradiometer Selection

The 6 F and 9 F gradiometer assembly each has its advantages when used in the examination system. The selection of a particular gradiometer is both case- and patient-dependent. The following discussions present several considerations to facilitate the selection process.

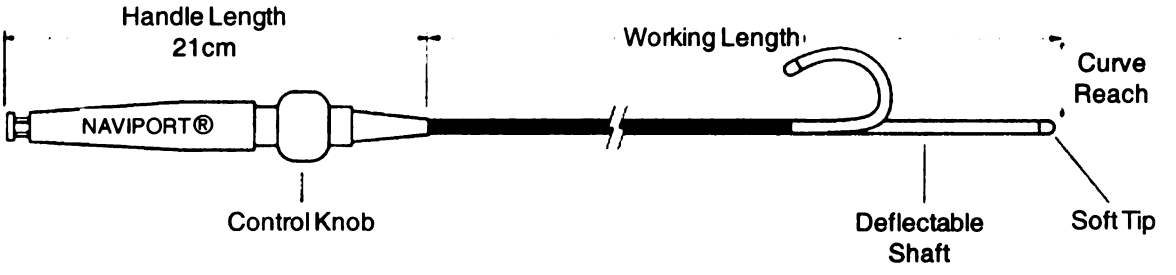

Figure 7.16 Cardima, Incorporated, *Naviport*® guide catheter. After [154]

Table 7.4 Component list for the 6 F (POT-9083) gradiometer assembly

Component	Maunfacturer
Gradiometer	Xactex, Corp., POT-9083
Data Cable (distal)	Cooner Wire, AS633-2SSF (formerly CZ1215-2F)
Data Cable (proximal)	Cooner Wire, CW 3735 with a 92166 S/S braid and a white type 3520 SPC shrink tube
Catheter	Boston Scientific Corporation, Scimed, Mach 1™ 7 F CLS4.5 guide catheter (catalog no. H749 34357-576 0) Cardima, Inc., 9F, 90cm, *Naviport*® 10 mm deflectable guiding catheter (product no. 08-003045)
Alternative Catheters	Boston Scientific Corporation, Scimed, Wiseguide™ 7 F CLS4.5 guide catheter (catalog no. H749 19500-576 0) Boston Scientific Corporation, Scimed, Mach 1™ 8 F CLS4.5 guide catheter (catalog no. H749 34358-576 0) Boston Scientific Corporation, Scimed, Mach 1™ 6 F CLS4.5 guide catheter (catalog no. H749 34356-576 0) (Any guide catheter with a 6 F or larger lumen)

7.5.1 Practical Considerations

The 6 F and 9 F gradiometers each has physical characteristics that may affect its performance in a particular examination. Specifically, the 9 F gradiometer assembly has a larger outer diameter that makes the unit more rigid and less affected by blood turbulence, especially when the gradiometer assembly is positioned downstream from the mitral annulus. The 9 F assembly is also suitable for use with a larger heart, in which the catheter assembly can anchor more securely in the left ventricle (see Figure 7.4). One drawback of the 9 F assembly is that it is a sealed unit. If the encasing catheter or the

sensor coil is damaged from either usage or sterilization, the entire assembly must be replaced.

The 6 F gradiometer assembly is smaller and more pliant. The maneuverability and ease of positioning of the assembly is determined by the choice of the guide catheter, which may be selected on a case-by-case basis. The 6 F assembly is suitable for use with all heart sizes as the guiding catheter may be chosen to match the particular patient. Although the gradiometer is more pliant than the 9 F assembly and consequently more susceptible to effects of hemodynamics, the guiding catheter can serve to stiffen the assembly, especially if a deflectable catheter such as the *Cardima Naviport*® is used. The 6 F gradiometer is generally more durable under repeated use as the gradiometer is protected by the guide catheter, which is discarded after each examination. As the gradiometer is advanced into position only after the catheter is positioned, the sensor head assembly is not subjected to the same physical manipulation as experienced by the catheter during its insertion. Even so, the gradiometer is re-sterilized and thoroughly inspected for damages after each examination.

The 6 F and 9 F gradiometer assemblies have been tested and characterized in a clinical-scale *in vitro* test system and the results are presented in the next chapter.

CHAPTER 8. SYSTEM CHARACTERIZATION AND TEST RESULTS

A clinical-scale prototype has been constructed to study the performance of the gradiometer-based BSCC heart valve examination system. The system components are described in Chapter 6 while details of the gradiometer are presented in Chapter 7. The prototype is used to characterize the system performance as different parameters associated with the system are varied. These parameters include the strength and frequency of the excitation field, placement of the gradiometer in relation to the valve's outlet strut, and the output signal level as a function of the excitation frequency. Based on these results, an *in vitro* test system has been constructed. Double-blind tests of 34 BSCC heart valves with various outlet strut conditions using the system has achieved 100% classification accuracy. These results demonstrate the feasibility and reliability of the gradiometer-based examination system in detecting BSCC outlet strut fractures.

8.1 The Helmholtz Excitation Coil System

The finite element (FE) analysis of the Helmholtz excitation coil system (Chapter 5) predicts a uniform magnetic field at the center of the coils with a cylindrical volume of 0.5 meters tall and a radius of 0.25 m as shown in Figure 8.1. To verify this result, physical measurements of the magnetic field have been taken between the excitation coils with an input of a 6 A peak-to-peak, 1 kHz sinusoidal excitation signal. The measured field distribution, shown in Figure 8.2, confirms the FE analysis results. In this figure, the average flux density is 1.28×10^{-7} T (1.28×10^{-3} gauss) with a variation of 0.74 %.

With an input signal of 10.62 A (peak-to-peak) and 62.77 kHz, the magnetic flux density at the center of the coils is approximately 1.5×10^{-4} T (1.5 gauss). This result agrees reasonably well with the FE model prediction of 1.47×10^{-4} T (1.47 gauss) shown in Figure 5.6 and Figure 5.7. Table 8.1 summaries the parameters and results for the FE analysis and physical measurement. The physical measurement results agree favorably with those from the FE analysis.

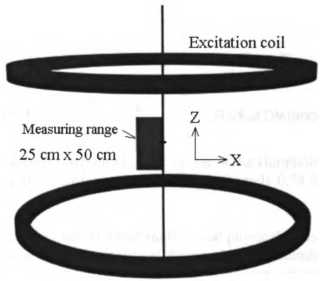

Figure 8.1 The Helmholtz excitation coil system has a uniform magnetic at its center within a cylindrical volume of radius 0.25 m and 0.5 m in height

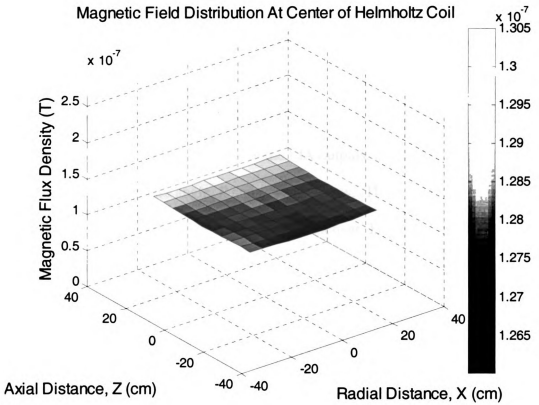

Figure 8.2 Magnetic field distribution at the center of the Helmholtz coil. The results show a volume of uniform field with approximately 0.74 % variation

Table 8.1 Summary of the finite element analysis and physical measurement parameters and results for the magnetic flux density at the center of the Helmholtz excitation coil

	FE Analysis Results	Physical Measurements
Excitation Frequency	62.5 kHz	62.77 kHz
Input Current (peak-to-peak)	11 A	10.62 A
Magnetic Flux Density	1.47×10^{-4} T	1.5×10^{-4} T
Uniform Volume	≈ 0.5 m tall, 0.25 m radius	≈ 0.5 m tall, 0.25 m radius
Uniformity	< 0.5 % variation	≈ 0.74 % variation

8.2 Lock-In Measurement of the Gradiometer Signal

The gradiometer signal is processed by a lock-in amplifier (LIA)(Chapter 6) to increase the signal-to-noise ratio. The LIA performs a phase-sensitive demodulation of the gradiometer output with reference to the excitation signal. Equations (6.6), (6.7), (6.11), and (6.12) describe the relations between the LIA outputs, X and Y, and the gradiometer signal amplitude and phase angle, P and θ, respectively. The in-phase component, X, corresponds to $P\cos(\theta)$ while the quadrature component, Y, is $P\sin(\theta)$. To remove the phase-dependency of the gradiometer output, the magnitude, R, of the signal pair (X, Y) may be used (Equation (6.8)). If the reference signal is rotated such that its phase matches that of the gradiometer signal, θ becomes zero. In this case, $R = X = P$ and $\theta = Y = 0$. By zeroing the phase angle prior to taking measurements, a smaller dynamic range may be used for measuring the quadrature signal Y, effectively increasing the system's sensitivity to small changes in Y and the phase angle, θ. The outputs of the LIA are digitized, recorded and analyzed to determine the condition of the outlet strut. The signal pairs (R, θ) and (X, Y) are used interchangeably in the following sections when the LIA outputs are referenced.

8.3 Clinical-Scale Prototype System

Figure 8.3 shows the clinical-scale prototype of the gradiometer-base examination system. In this figure, the heart valve is mounted at the centre of the diagonal crossbeam while the gradiometer is mounted at the end of the radial beam. The radial beam is connected to a two-dimensional programmable motorized stage for positional control. Figure 8.4 shows the test fixture. In this setup, the heart valve is mounted in an

elastromer ring with a compliance comparable to the myocardium. The gradiometer is encased in, and protrudes from, a guide catheter. The relative position between the gradiometer and the outlet strut is preciously controlled by the motorized stage. The clinical-scale prototype has been used for system verification and heart valves examinations. The test results are presented in the following sections.

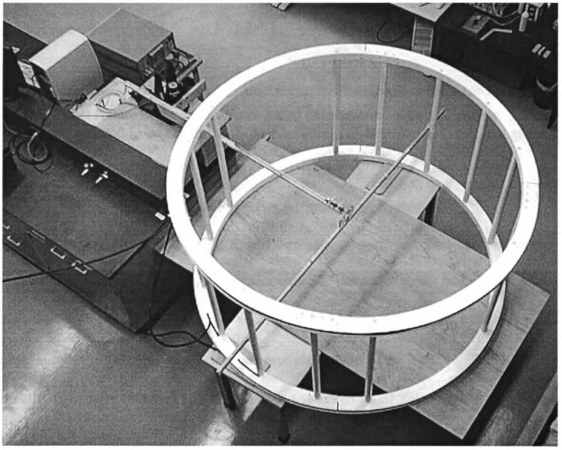

Figure 8.3 Clinical-scale prototype for the gradiometer-based examination system

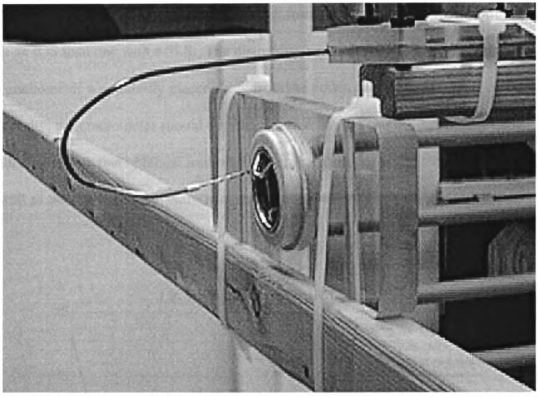

Figure 8.4 Test fixture of the gradiometer-based examination system prototype. The heart valve is mounted in an elastromer holder and the gradiometer is encased in a guide catheter

8.4 Output Signal as a Function of Distance

Figure 8.5-Figure 8.8 show the X, Y, R, and θ signals, respectively, from the LIA as a function of the distance between the gradiometer and the outlet strut. In each figure, the results for three cases are shown: a XSLS (explanted SLS), IOS, and no heart valve. The flange number[1] of each valve specimen is provided in the figure legends. The measurements were obtained with an excitation signal of 60.21 kHz, applied magnetic field of 1.304 gauss, and the 9 F gradiometer. These figures show that, if the gradiometer is initially positioned on the outlet strut plane, the relative change in amplitude for the

[1] The flange number is an unique identifier number edged onto the flange of each BSCC heart valve.

LIA outputs as the gradiometer is moved away from the strut is larger for a heart valve with an IOS than one with a SLS. The distinction between the two signals diminishes if the gradiometer was initially placed away from the outlet strut. Therefore, for optimal sensitivity, the gradiometer should be placed within 5 mm from the outlet strut. This result agrees with that obtained from the mathematical model presented in Section 4.10, as well as the finite element analysis of the system presented in Section 5.2.2.

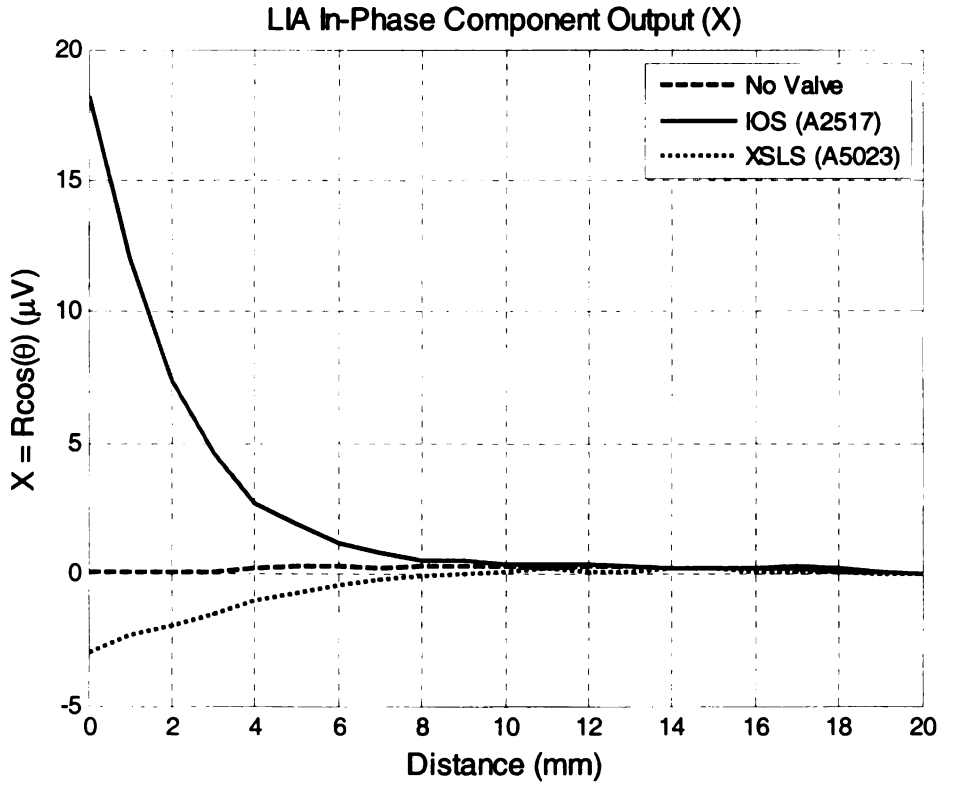

Figure 8.5 In-phase component output, *X*, from the LIA as a function from the outlet strut for the IOS, SLS, and no valve cases

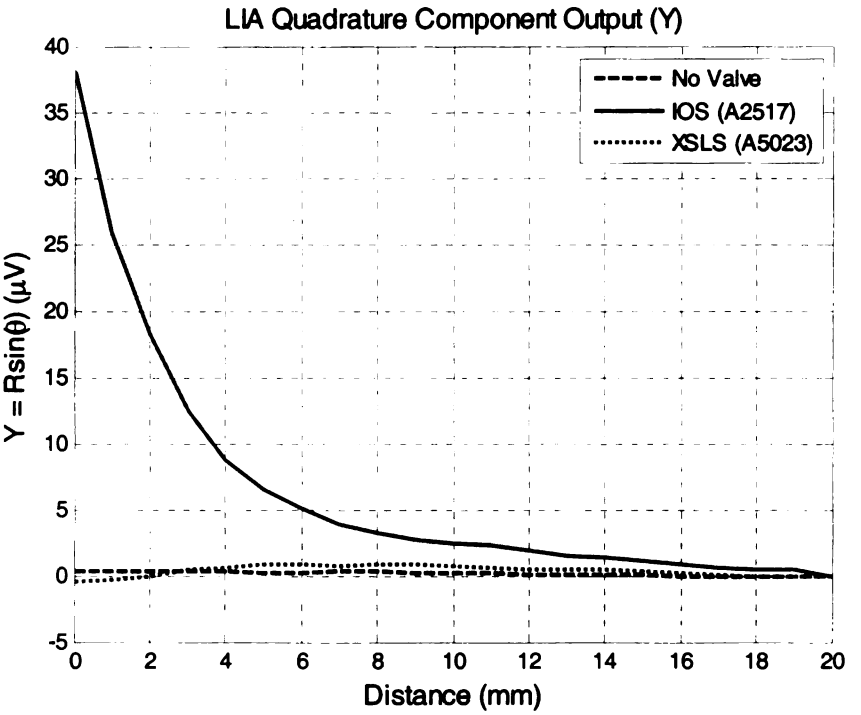

Figure 8.6 Quadrature output, *Y*, from the LIA as a function of the distance between the gradiometer and the outlet strut for the IOS, SLS, and no valve cases

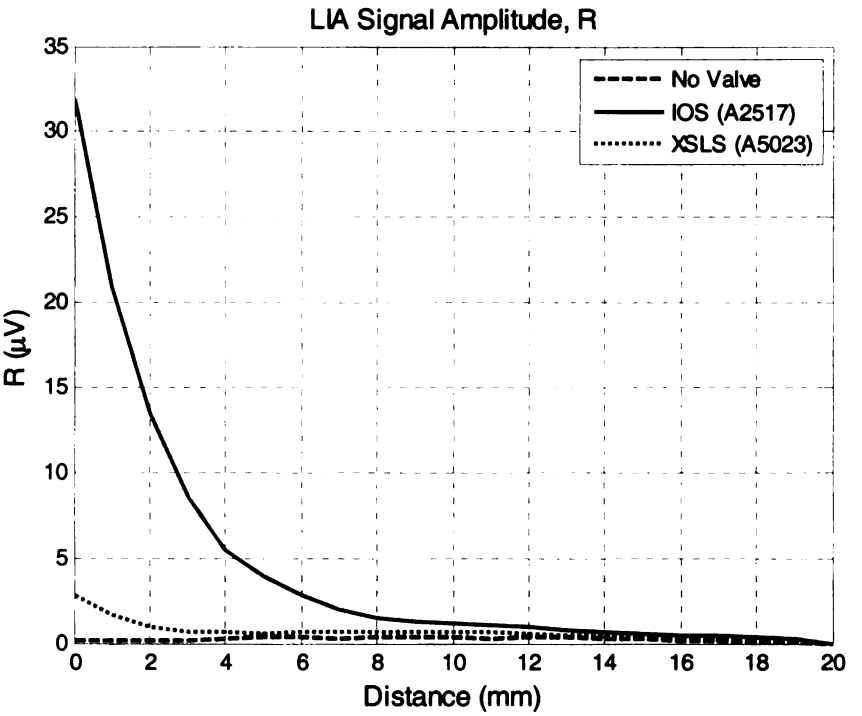

Figure 8.7 Magnitude, *R*, of the gradiometer output as a function of distance from the outlet strut for the IOS, SLS, and no valve cases

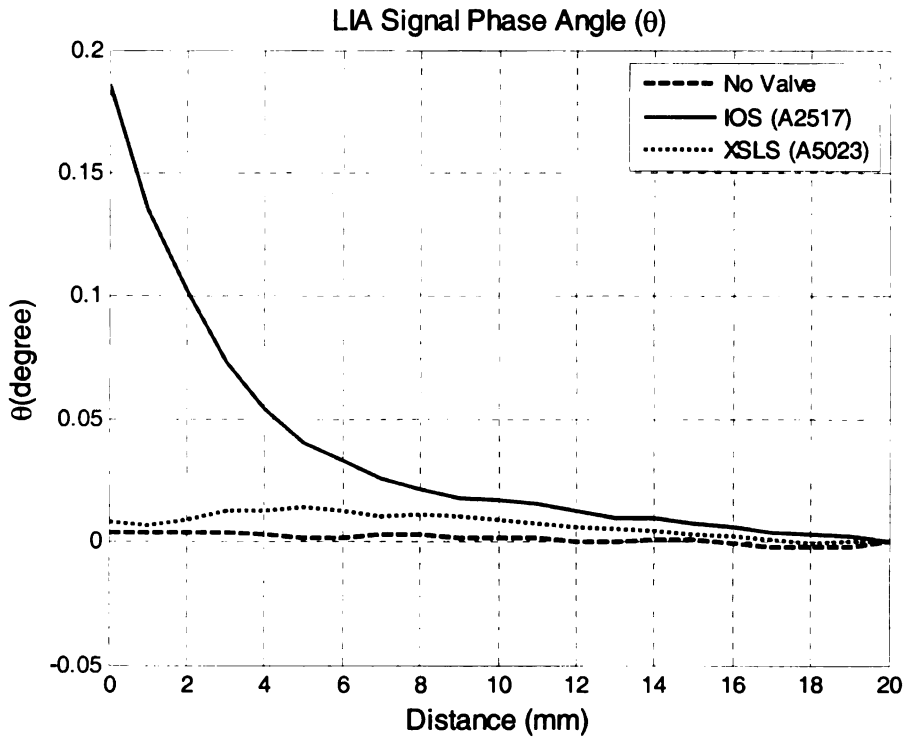

Figure 8.8 Phase angle, θ, output as a function of distance from the outlet strut for the IOS, SLS, and no valve cases

8.4.1 Movement Model

During the heart valve examination, the gradiometer is encased in a guide catheter and the assembly is inserted into the heart and positioned close to the outlet strut. The position of the catheter is affected by the hemodynamics inside the heart, and is continually oscillating about a mean position during the ventricular systole and diastole. The movement of the gradiometer may be modelled by fitting polynomials, $f_X(z)$ and $f_Y(z)$, to the X and Y values in Figure 8.9 and Figure 8.10, respectively. The resulting polynomials express the X and Y outputs as functions of the distance, z, from the outlet strut. For the data from Figure 8.9 and Figure 8.10, the resulting polynomials are:

$$f_X(z) = 0.0001z^5 - 0.0041z^4 + 0.1031z^3 - 1.248z^2 + 7.4479z - 145.8305 \quad (8.1)$$

and

$$f_Y(z) = -0.0001z^5 + 0.0069z^4 - 0.1751z^3 + 2.1706z^2 - 13.5815z + 79.1808 \quad (8.2)$$

The output of the gradiometer can then be expressed as a function of time by assuming an oscillatory gradiometer movement with a frequency of f = 1.2 Hz (corresponding to a heart rate of 72 beats/min). The maximum swing of the gradiometer (i.e., the largest amplitude of the oscillation), L, is a function of the turbulence in the ventricle and the rigidity of the catheter assembly. The oscillatory motion can be modelled as

$$z(t) = \frac{1}{2} L[\sin(2\pi f t) + 1] \quad \text{mm} \quad (8.3)$$

In (8.3), the neutral, or resting, position of the gradiometer is assumed to be $L/2$ mm away from the outlet strut. Substituting (8.3) into (8.1) and (8.2) and removing the mean value from each result yields the X and Y outputs as a function of the gradiometer position over time. Figure 8.9 and Figure 8.10 show the estimated relative changes in X and Y as functions of time for the IOS, SLS and no valve cases with L = 10 mm. The same procedure has been applied for R and θ and the results are shown in Figure 8.11 and Figure 8.12. These figures suggest that large X and Y (or, R and θ) signal variations over time correspond to an IOS valve whereas small signal variations are related to a valve with SLS.

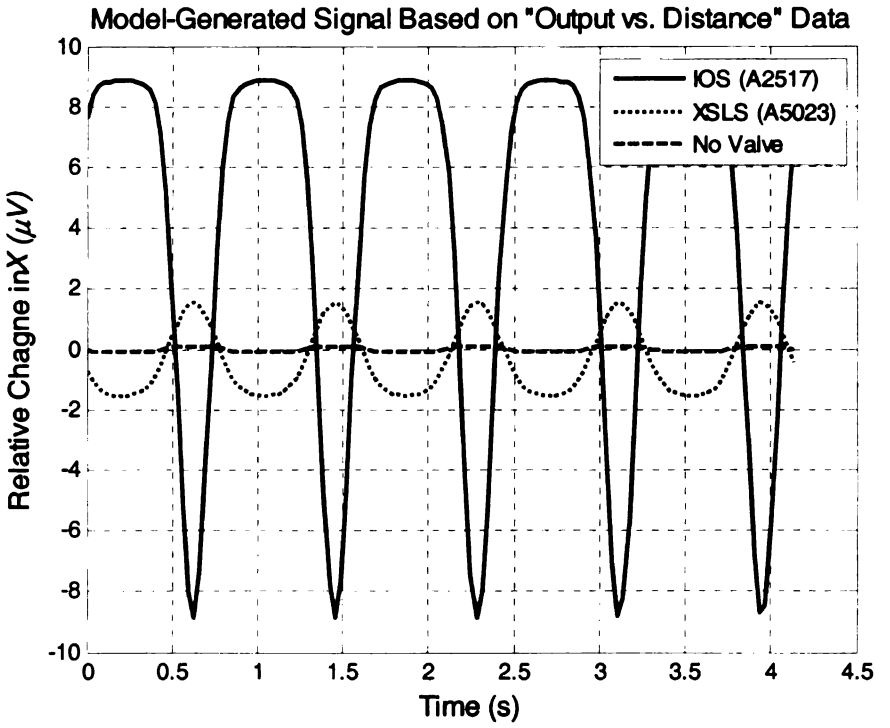

Figure 8.9 Model-generated X signal with respect to the changing distance between the gradiometer and outlet strut for the IOS, XSLS and no heart valve cases. L = 10 mm.

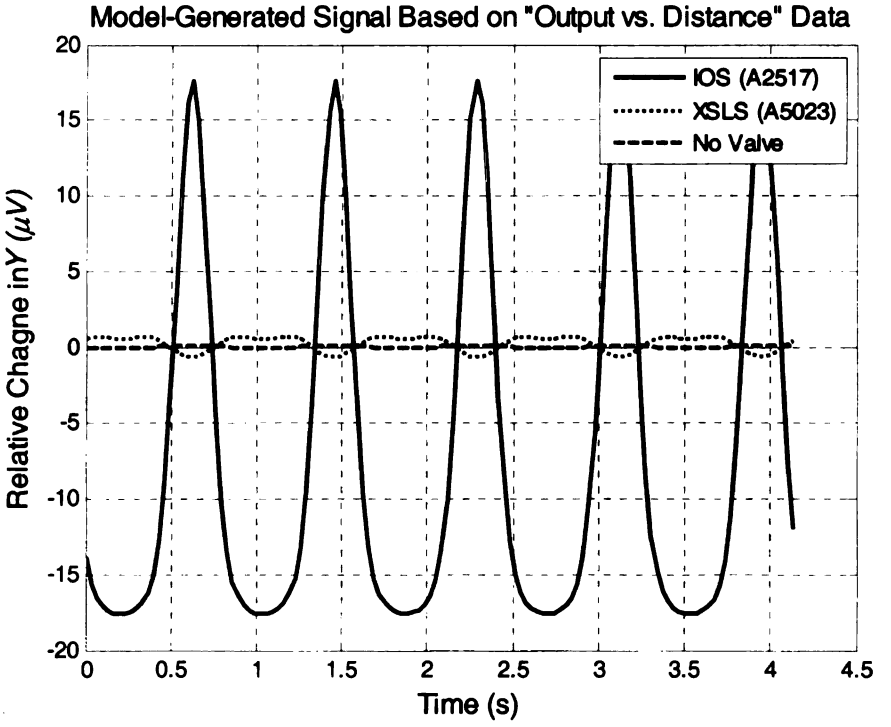

Figure 8.10 Estimated Y signal over time with respect to the changing distance between the gradiometer and outlet strut for the IOS, XSLS and no heart valve cases. L = 10 mm.

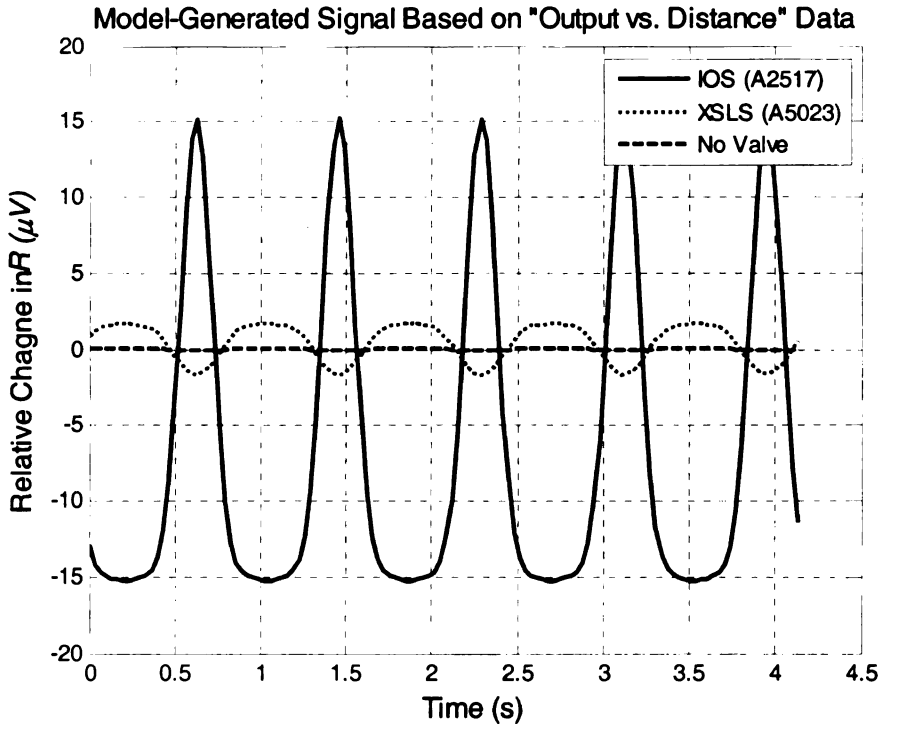

Figure 8.11 Estimated R signal over time with respect to the changing distance between the gradiometer and outlet strut for the IOS, XSLS and no heart valve cases. L = 10 mm.

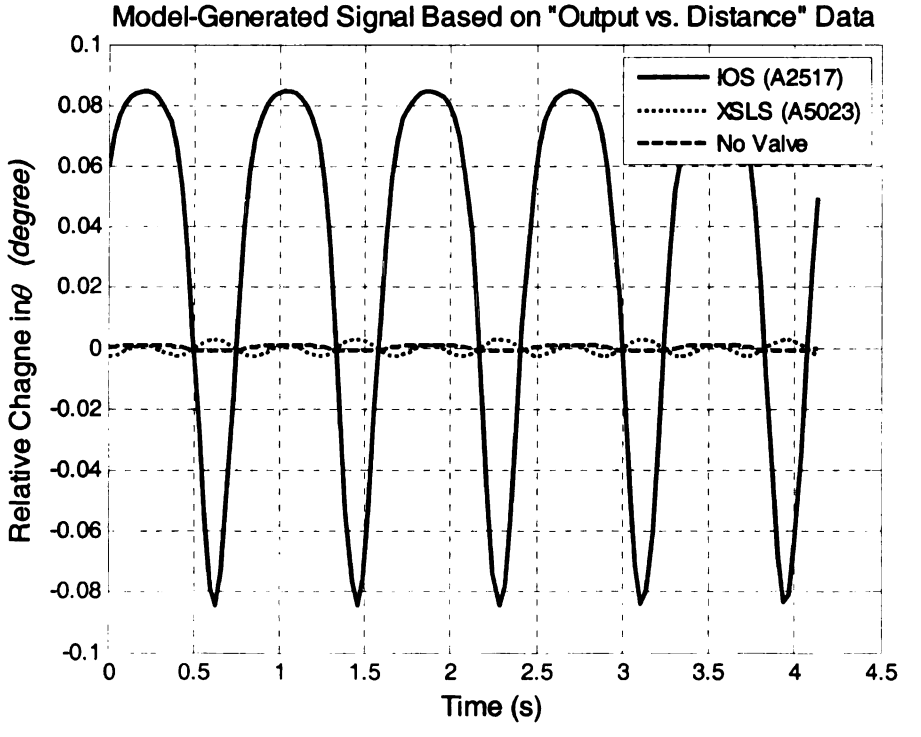

Figure 8.12 Estimated θ signal over time with respect to the changing distance between the gradiometer and outlet strut for the IOS, XSLS and no heart valve cases. L = 10 mm.

8.5 Gradiometer Output as a Function of Excitation Frequency

The gradiometer output at different excitation frequencies has been examined. Prior to each test, the examination system was calibrated by submerging the gradiometer in the uniform excitation field but away from the heart valve. The phase angle, θ, was set to zero to remove the phase difference between the reference and baseline gradiometer signals. The gradiometer was then positioned on the strut loop plane and LIA outputs were recorded as the gradiometer was moved away from the strut loop. Polynomials were fitted to the LIA data to form mathematical models according to the procedure described in the previous section, and the X, Y, R, and θ outputs were generated from the models for an oscillatory motion with L=10 mm. Figure 8.13-Figure 8.16 show the model-generated outputs, X, Y, R, and θ, at various excitation frequencies for an IOS (A2517) and SLS (A5023) valve. The excitation frequencies were 41.15, 45.58, 51.57, 54.85, and 60.45 kHz and the data were collected using a 9 F gradiometer. The magnetic flux density was 1.03×10^{-4} T (1.03 gauss).

8.5.1 In-Phase Signal, X

Figure 8.13 shows the in-phase component, X, of the gradiometer output. In this figure, the signal amplitude for the IOS valve increases with increasing excitation frequency while the signal amplitude for the SLS case remains relatively uniform across the test frequencies. Table 8.2 lists the peak-to-peak X signal for both the IOS and SLS case at the excitation frequencies. For the IOS case, the X signal at 60.45 kHz is 34.169 μV. This is nearly twice the value of that at 41.15 kHz (17.873 μV). Meanwhile, the X signal for the SLS case remains relatively small and does not exhibit any remarkable changes

over frequency. Table 8.2 also lists the ratios of the X signals between the IOS and SLS cases at each excitation frequency. For example, at 41.15 kHz, the ratio between the IOS and SLS signal is 6.6233, while at 60.45 kHz, the ratio is 10.2669. These results suggest that a higher excitation frequency should be used, and that the LIA in-phase output, X, may be used to estimate the condition of the outlet strut.

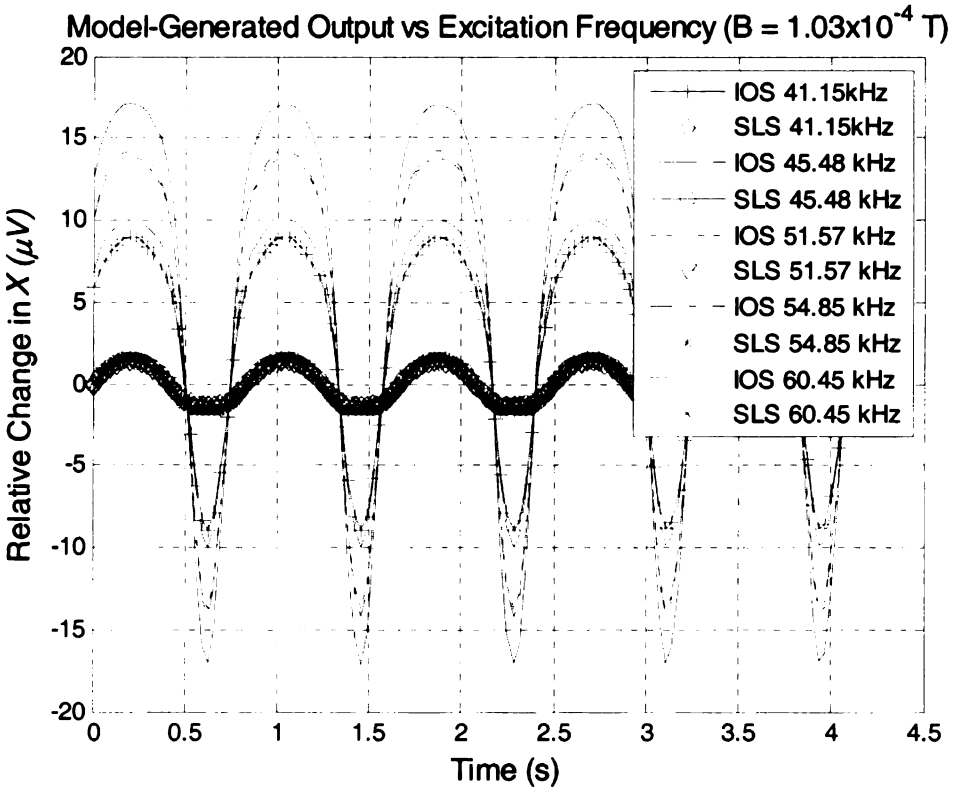

Figure 8.13 Estimated relative changes in X for the IOS and SLS cases at 41.15, 45.58, 51.57, 54.85, and 60.45 kHz. L = 10 mm

Table 8.2 Comparison of the peak-to-peak X signal voltages between the IOS and SLS cases at various excitation frequencies

Excitation Frequency (kHz)	IOS Case Peak-to-Peak Signal (μV)	SLS Case Peak-to-Peak Signal (μV)	Ratio
41.15	17.8728	2.6985	6.6233
45.58	19.9623	2.9964	6.6621
51.57	27.5486	2.7037	10.1893
54.85	28.3733	3.2161	8.8222
60.45	34.1692	3.3281	10.2669

8.5.2 Quadrature, Y, and Amplitude, R, Signals

Figure 8.14 and Figure 8.15 show the model-generated quadrature, *Y*, and amplitude, *R*, signals and Table 8.4 and Table 8.5 summarize the peak-to-peak output voltages for these two figures at the excitation frequencies listed in the previous section. From these results, no definitive frequency-dependent behavior is observed for the IOS case. Meanwhile, signal from the SLS valve show only a moderate increase with increasing frequency. The *Y* and *R* signals are, therefore, not strong indicators of the heart valve outlet strut condition in this case.

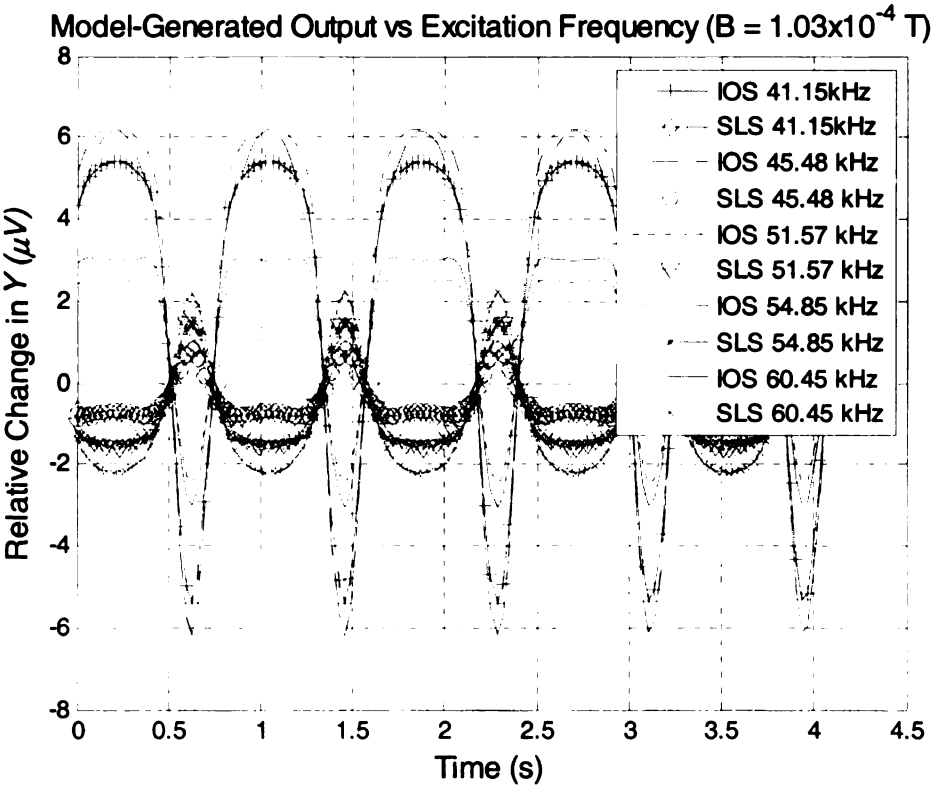

Figure 8.14 Estimated relative changes in *Y* for the IOS and SLS cases at 41.15, 45.58, 51.57, 54.85, and 60.45 kHz. L = 10 mm

Table 8.3 Comparison of the peak-to-peak *Y* signal voltages between the IOS and SLS cases at various excitation frequencies

Excitation Frequency (kHz)	IOS Case Peak-to-Peak Angle (°)	SLS Case Peak-to-Peak Angle (°)	Ratio
41.15	10.7875	1.6192	6.6622
45.58	12.2927	1.6184	7.5956
51.57	5.0313	3.2072	1.5688
54.85	12.4253	2.9070	4.2743
60.45	6.0914	4.4050	1.3828

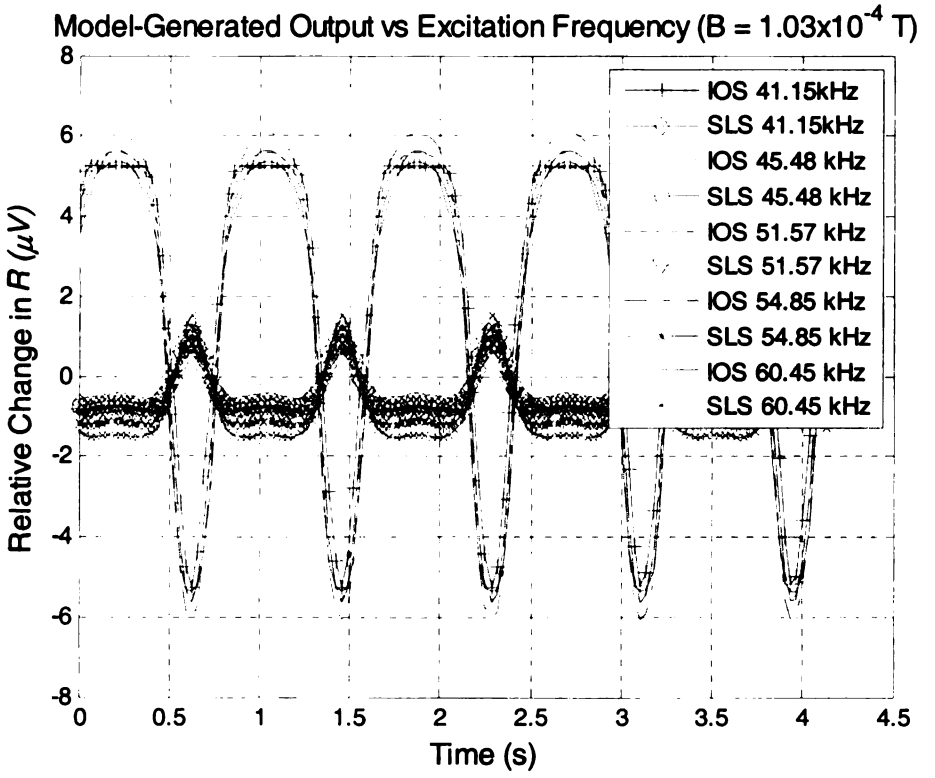

Figure 8.15 Estimated relative changes in *R* for the IOS and SLS cases at 41.15, 45.58, 51.57, 54.85, and 60.45 kHz. $L = 10$ mm

Table 8.4 Comparison of the peak-to-peak *R* signal voltages between the IOS and SLS cases at various excitation frequencies

Excitation Frequency (kHz)	IOS Case Peak-to-Peak Angle (°)	SLS Case Peak-to-Peak Angle (°)	Ratio
41.15	10.5265	1.6351	6.4379
45.58	11.3158	1.5341	7.3762
51.57	11.1909	2.0135	5.5578
54.85	12.1431	2.5230	4.8130
60.45	10.7192	3.0259	3.5424

8.5.3 Output Signal Phase Angle, θ

Figure 8.16 shows the model-generated output phase angle, θ, for the IOS and SLS cases at the test frequencies mentioned in the last sections. Table 8.5 summarizes the phase angles and their ratios as the excitation frequency is increased. The results in this table show that the phase angle increases with frequency. The ratio of the phase angles for the IOS and SLS cases increases from 6.822 to 9.741 as the excitation frequency is increased from 41.15 kHz to 60.45 kHz. These results suggest that the phase angle, θ, may be used to indicate the condition of the outlet strut.

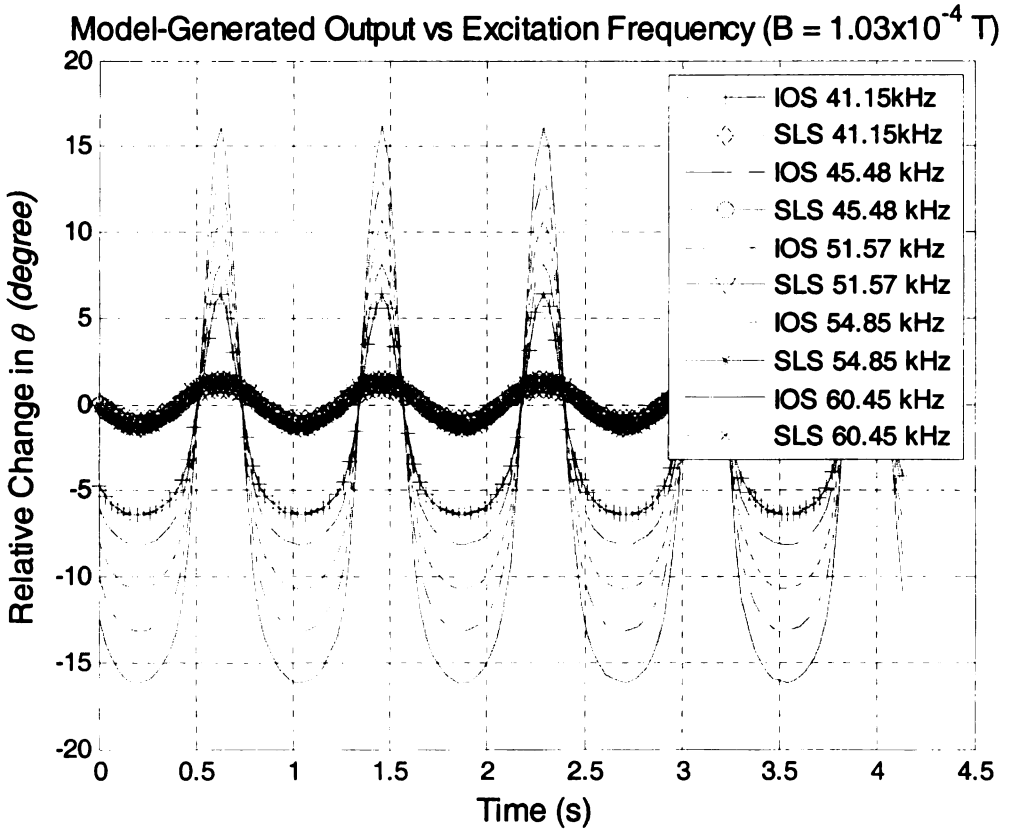

Figure 8.16 Estimated relative changes in θ for the IOS and SLS cases at 41.15, 45.58, 51.57, 54.85, and 60.45 kHz. L = 10 mm

Table 8.5 Comparison of the peak-to-peak θ value between the IOS and SLS cases at various excitation frequencies

Excitation Frequency (kHz)	IOS Case Peak-to-Peak Angle (°)	SLS Case Peak-to-Peak Angle (°)	Ratio
41.15	12.7342	1.8665	6.8223
45.58	16.2826	2.1362	7.6222
51.57	21.3592	2.5015	8.5386
54.85	26.3412	2.6941	9.7775
60.45	32.3120	3.3171	9.7411

8.5.4 Outlet Strut Condition Indicator and Excitation Frequency Specification

The results from Figure 8.13, Figure 8.16, Table 8.2, and Table 8.5 suggest that

1. Either the X or θ signal may be examined to provide an indication for the outlet strut condition.
2. The excitation frequency should be set as high as possible within the limits of the power amplifier and the bandwidth of the impedance matching circuit.

The excitation frequency for the gradiometer-based examination system is approximately 62.5 kHz.

8.6 *In Vitro* Test System

As discussed earlier, the position of the gradiometer inside the heart is affected by the hemodynamics and movement of the heart due to the cardiac cycle. In order to investigate the effect of this movement on the performance of the gradiometer-based examination approach, an *in vitro* test system has been constructed. The test system uses the clinical-scale prototype in Figure 8.3 to simulate the gradiometer movement in relation to the heart valve. A cinegram of an unidentified BSCC heart valve patient is obtained [194] and the *in situ* movement of the heart valve is traced from a series of fluoroscopic images (Figure 8.17). The trace result describes the movement of the heart

valve relative to a stationary observation point. Figure 8.18 shows the heart valve travel path. This travel path is programmed into motorized stages connected to the gradiometer. The result is a motorized simulation of the relative movement between the gradiometer and the outlet strut as shown in Figure 8.19. The motorized test system transverses the travel path every 0.833 seconds (frequency = 1.2 Hz), corresponding to a heart rate of 72 beats per minutes.

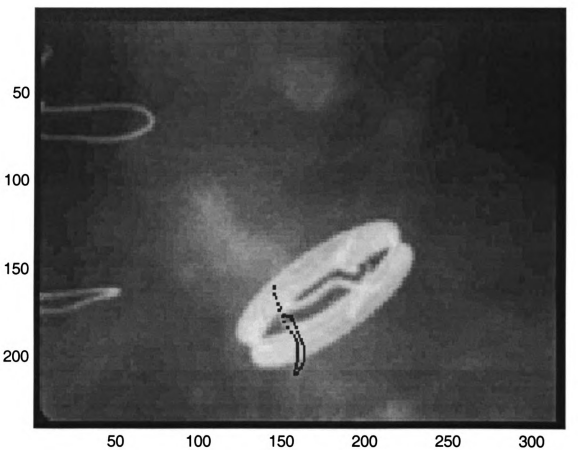

Figure 8.17 *In situ* movement of a BSCC heart valve obtained from a series of fluoroscopic images

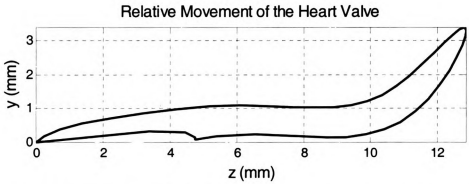

Figure 8.18 Movement of the heart valve in relation to a stationary observation point

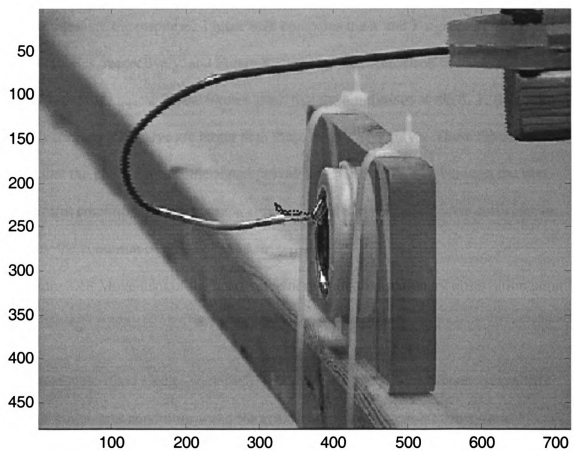

Figure 8.19 Motorized stages programmed to simulate the relative movement between the gradiometer and the outlet strut

8.6.1 *In Vitro* Test System Outputs and Classifications

Figure 8.20-Figure 8.23 show the LIA outputs, X, Y, R and θ, respectively, for an explanted BSCC heart valve with SLS (XSLS, A5023). Figures 8.24 through 8.27 show the same set of signals for an IOS valve (87384). The top graph in each figure shows the raw signal and the bottom graph shows the results after the signal is filtered by a 5th-order Butterworth low-pass filter. The filter cutoff frequency was 5 Hz and the sampling rate was 250 samples/seconds. The system excitation frequency was 60.27 kHz, magnetic field was 1.173×10^{-4} T (1.17 gauss), and a 9 F gradiometer (POT-9075) was used to measure the response. Figure 8.28 compares the X and Y signals for the XSLS and IOS cases, respectively, and Figure 8.29 shows the comparison of the R and θ signals for the two valve cases. These figures show that the amplitudes of the X, Y, R and, θ signals from an IOS valve are larger than those from a SLS valve. These figures also show that the phase angle of the signal provides the best distinction between the two outlet strut conditions. In this case, a simple thresholding of the signal is sufficient to classify the condition of the two outlet struts.

8.7 In Vitro Study Results

In vitro double-blind studies were performed on BSCC 60° 29[1] mm heart valves with various outlet strut conditions using the gradiometer-based examination system prototype. The test samples included valves with IOS as well as SLS cases that were

[1] The three largest size (29, 31 and 33 mm) BSCC heart valves all had the same flange ring (29 mm) and disc sizes. The different sizing referred to the outside diameter of the fabric sewing rings.

either manufactured[1] (MSLS) or naturally occurring (explanted, XSLS). During each study, heart valves were selected randomly from a pool of samples and tested in the gradiometer-based system. The output signals from each valve were interpreted by two operators, one experienced and the other with minimal training. Each operator independently assessed the outlet strut condition of the valve based on the output signals. The signals were also analyzed using a computer software. At the conclusion of the test, the decisions from the operations and the computer system were compared against the true conditions of the valves. The following sections describe the test system parameters, gradiometer selection, and the test results.

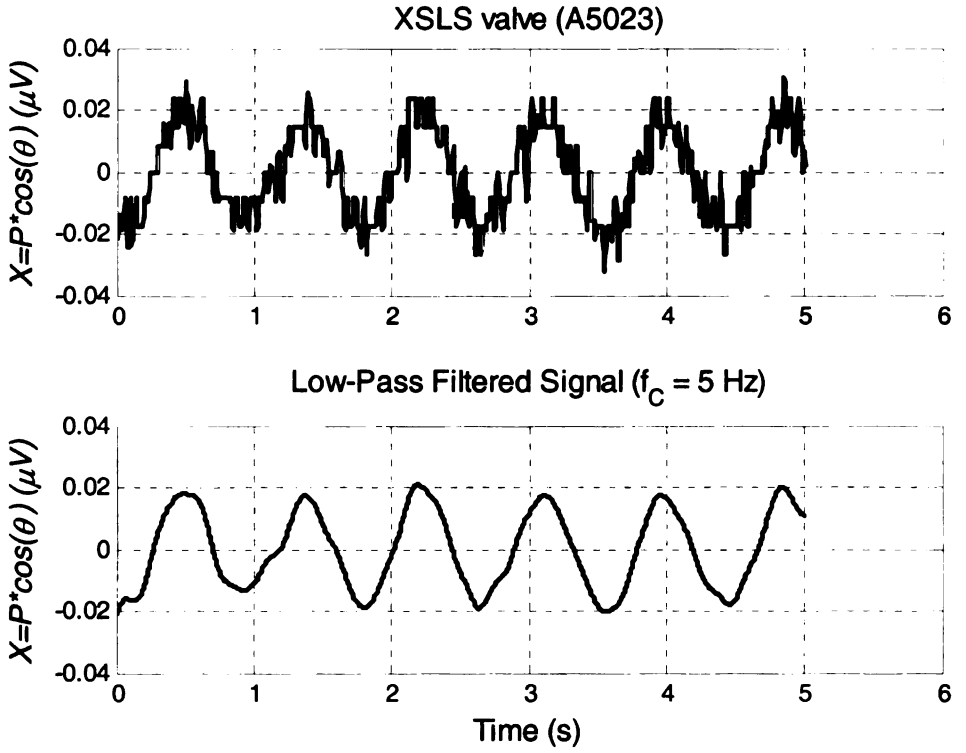

Figure 8.20 Output signal X for a BSCC heart valve with SLS (A5023)

[1] A manufactured SLS (MSLS) was typically created by using either a laser or diamond cutter to sever one of outlet strut legs

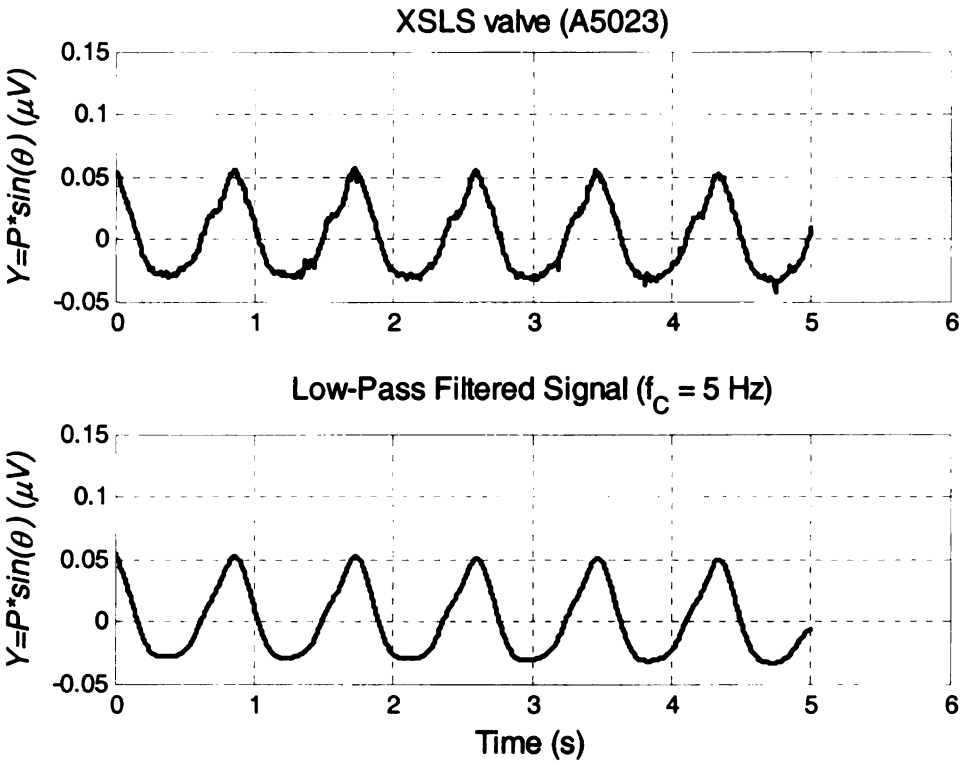

Figure 8.21 Output signal *Y* for a BSCC heart valve with SLS (A5023)

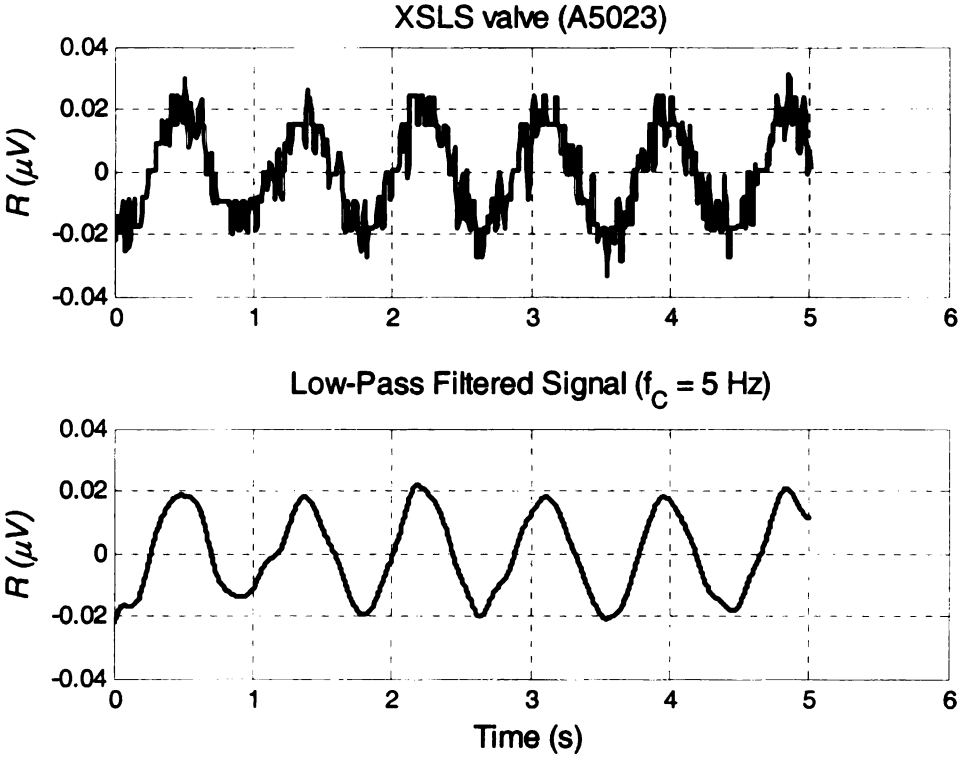

Figure 8.22 Output signal *R* for a BSCC heart valve with SLS (A5023)

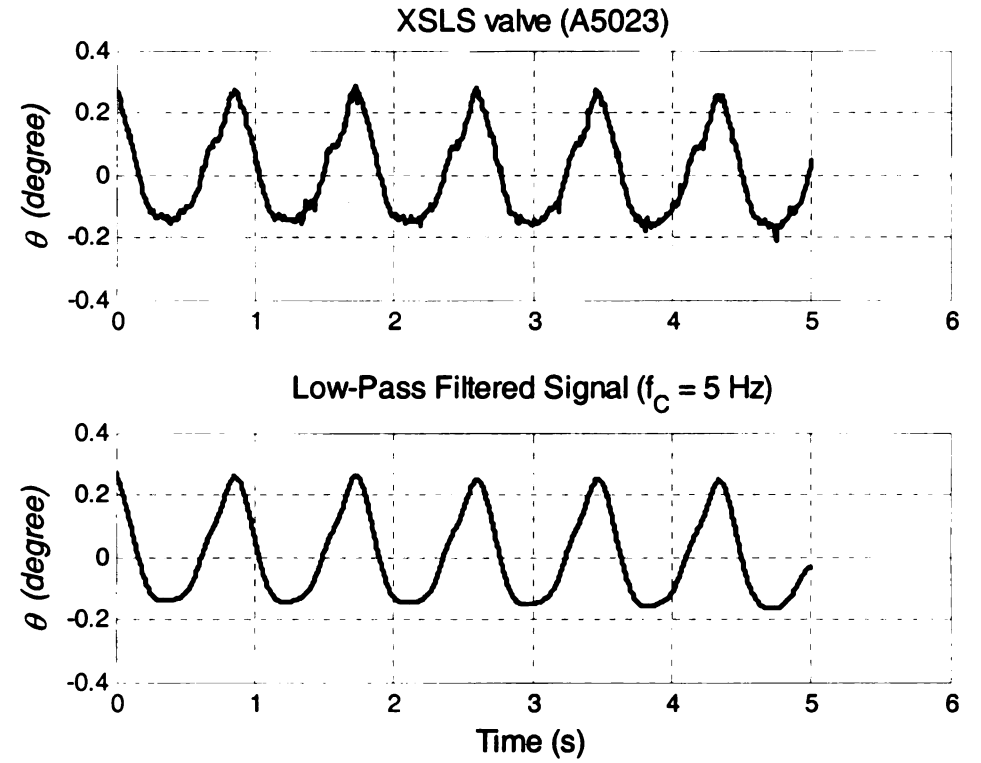

Figure 8.23 Output signal θ for a BSCC heart valve with SLS (A5023)

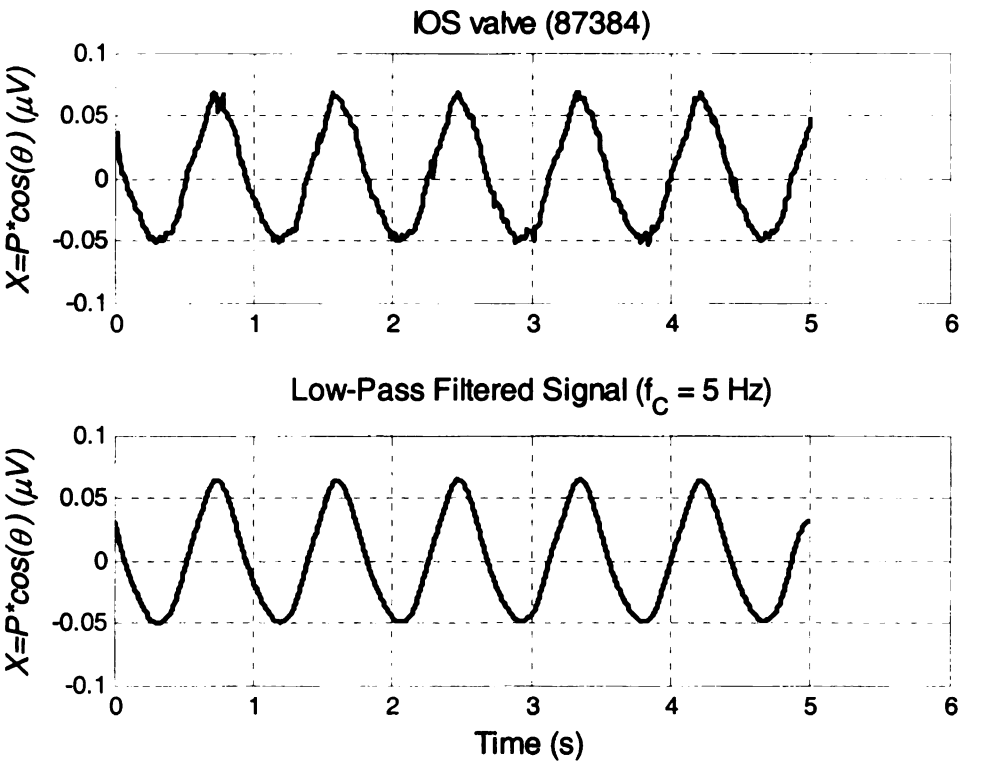

Figure 8.24 Output signal X for a BSCC heart valve with an IOS (87384)

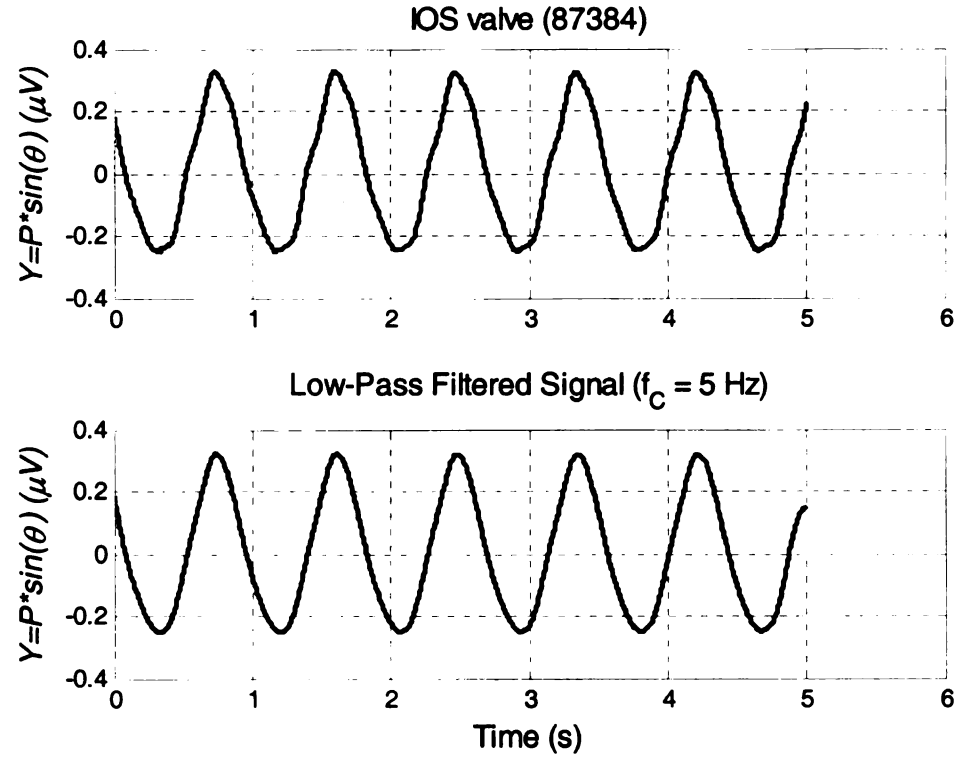

Figure 8.25 Output signal *Y* for a BSCC heart valve with an IOS (87384)

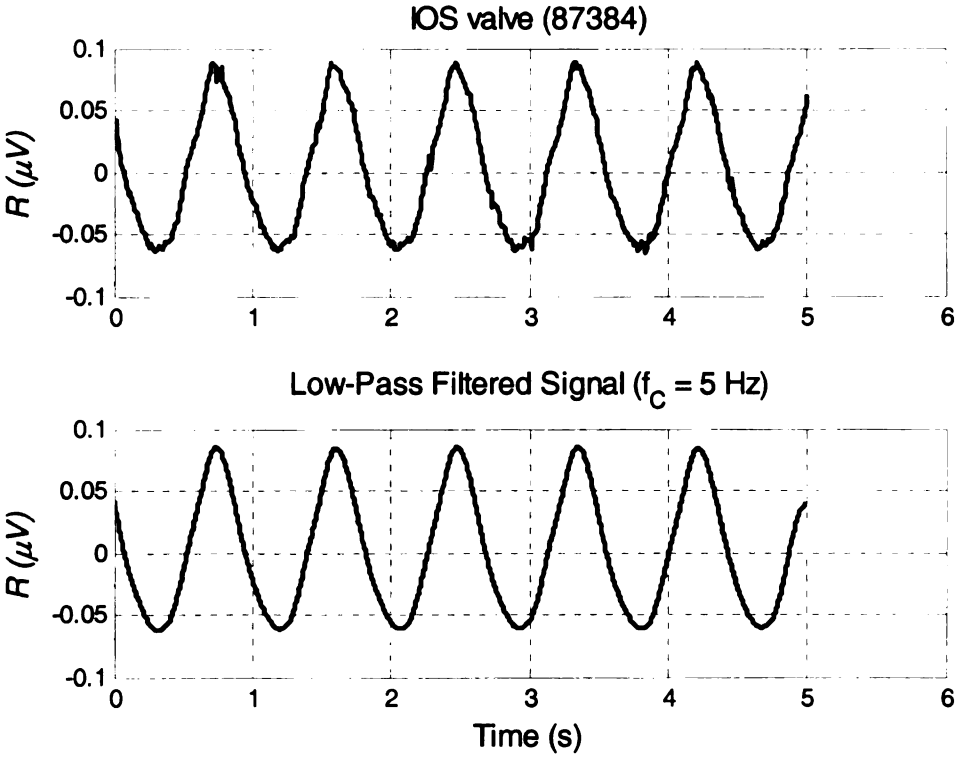

Figure 8.26 Output signal *R* for a BSCC heart valve with an IOS (87384)

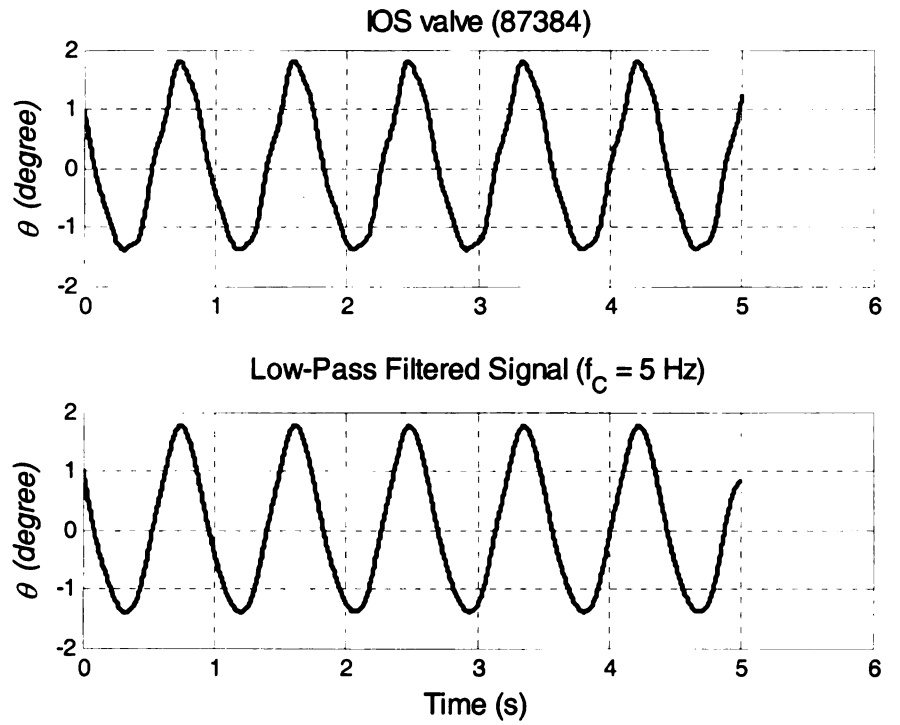

Figure 8.27 Output signal θ for a BSCC heart valve with an IOS (87384)

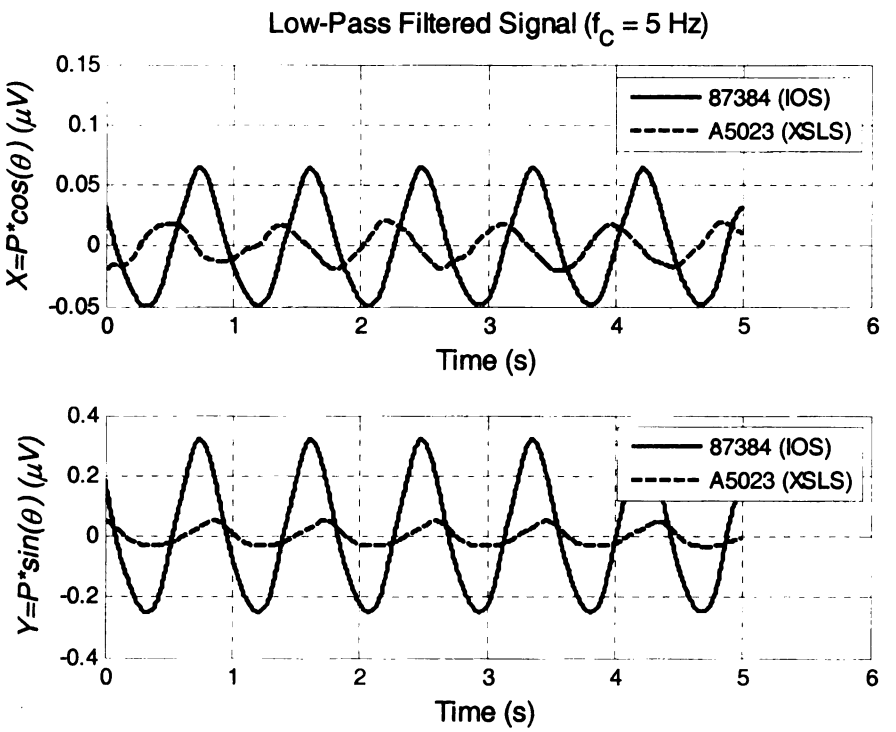

Figure 8.28 Comparison of the LIA X and Y signals for the IOS (solid line) and XSLS (dashed line) cases.

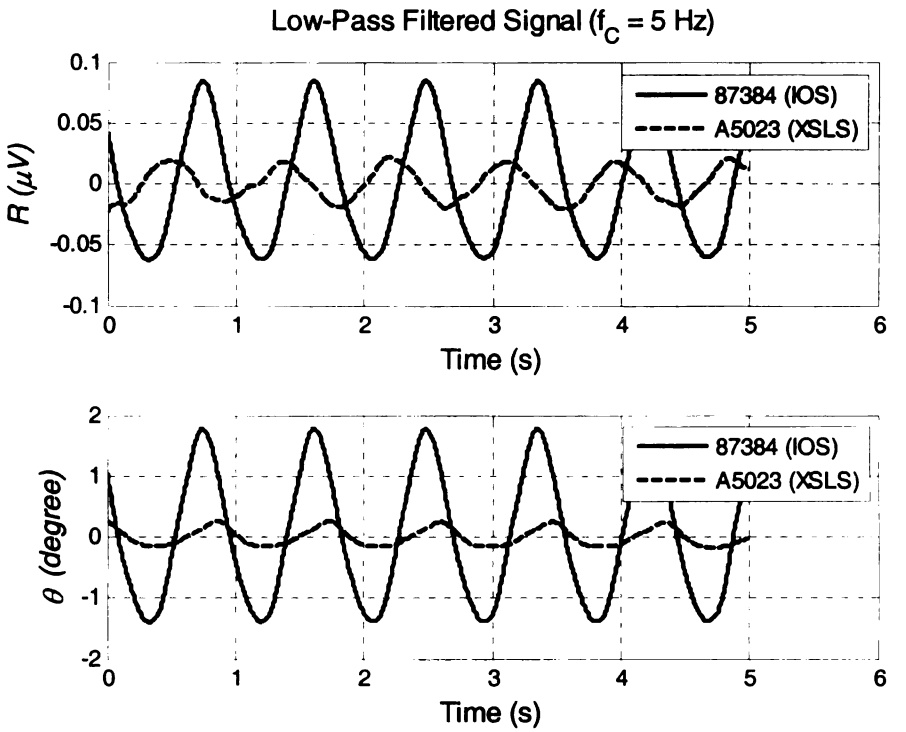

Figure 8.29 Comparison of the LIA R and θ signals for an IOS (solid line) and XSLS (dashed line) cases.

8.7.1 *In Vitro* Study: Trial A, 19 BSCC Heart Valves, 9 F Gradiometer

In a double-blind *in vitro* study with 2 operators, 19 BSCC heart valves were tested in the gradiometer-based examination system with a 9 F (POT-9075) gradiometer. The test samples included 7 IOS valves, 6 with XSLS and 6 with MSLS. The excitation frequency was 60.27 kHz and the applied magnetic field was 1.1726×10^{-4} T (1.173 gauss). Figure 8.30-Figure 8.33 show the phase angle, θ, signals from the tests. The flange number for the test samples are provided in the legends of the respective figures. The computer classification results and the true condition of the heart valves are listed in the format: (computer classification result / true valve condition). For each valve, the computer software processed the LIA output signals by low-pass filtering and removing their DC offsets. The software then applied a predetermined threshold of 0.85 to the

processed signal. (The selection of the software decision threshold is discussed later in this chapter.) An outlet strut with a signal amplitude above the threshold was classified as intact. Otherwise, the strut was classified as fractured. Table 8.6 summarizes the test results. The indications from the operators and the computer software all achieved 100% accuracy in determining the outlet strut condition of the BSCC heart valves. Note that two valves, flange numbers 73234 and 83740, were originally labeled as IOS valves on their shipping containers. Test results from the gradiometer-based examination system indicated a SLS condition for both valves. Visual inspections verified a MSLS on each of these valves.

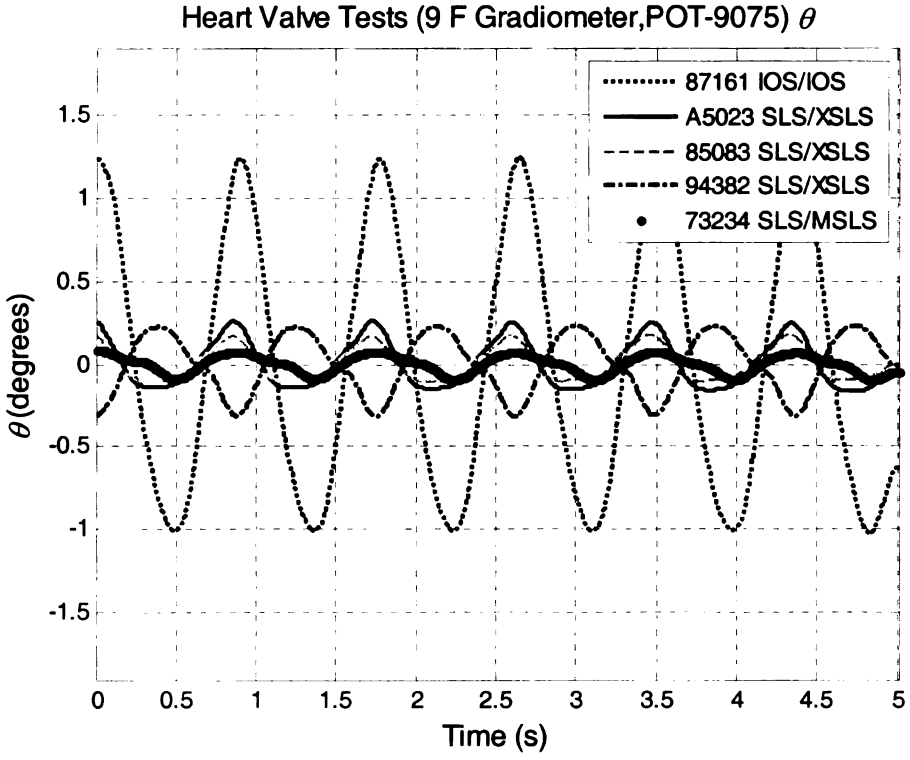

Figure 8.30 Output θ signals from the BSCC heart valve study (Trial A), part I

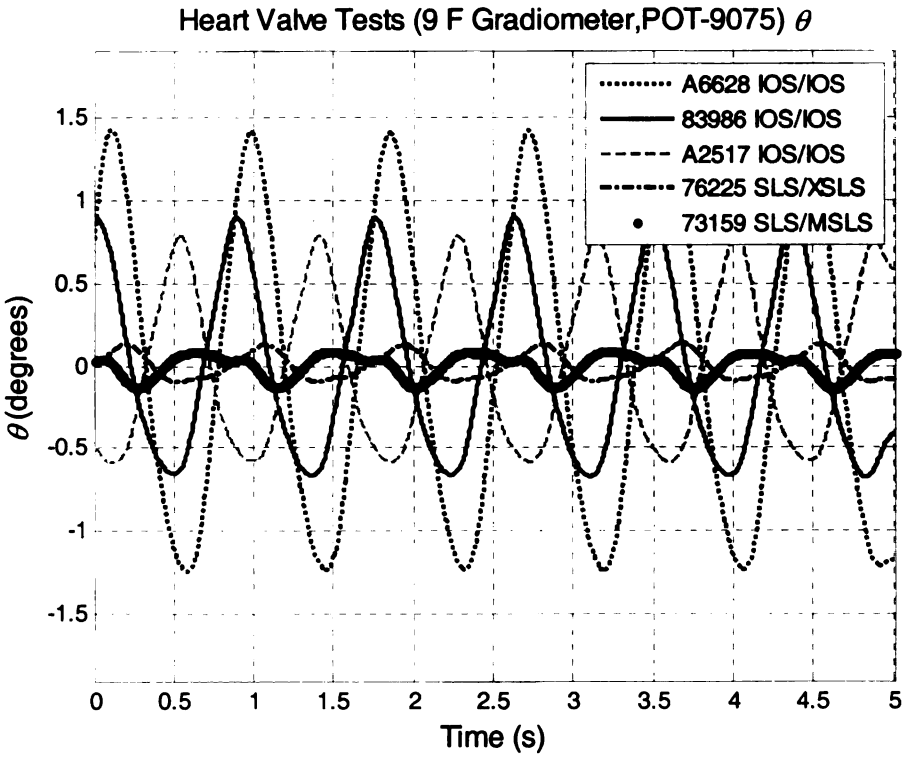

Figure 8.31 Output θ signals from the BSCC heart valve study (Trial A), part II

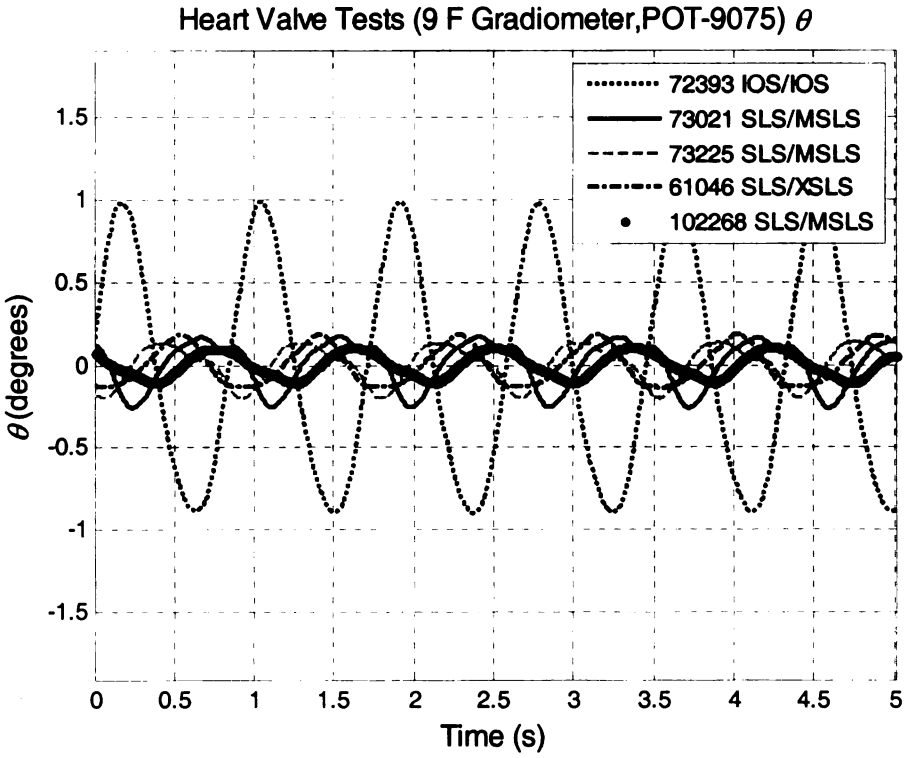

Figure 8.32 Output θ signals from the BSCC heart valve study (Trial A), part III

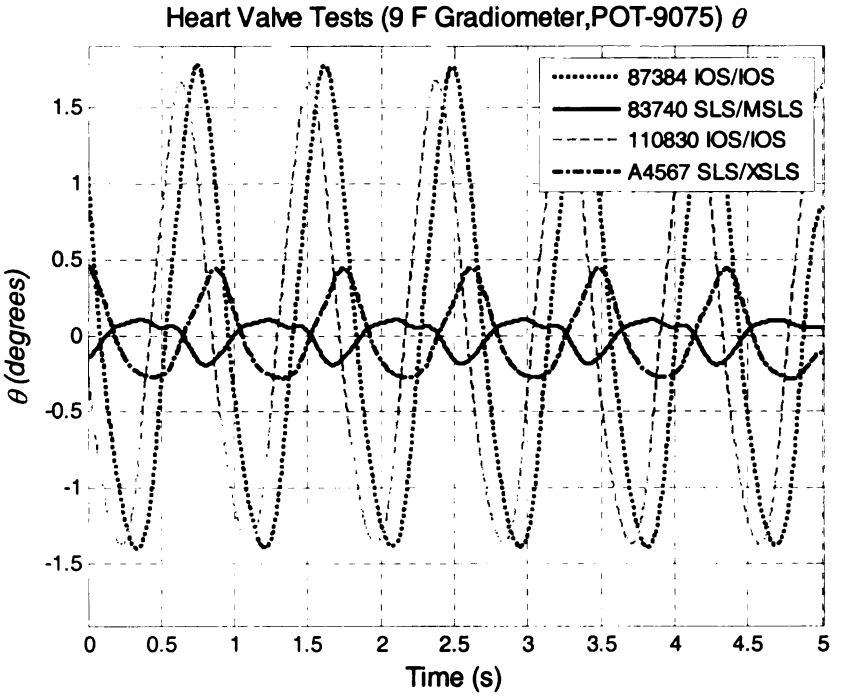

Figure 8.33 Output θ signals from the BSCC heart valve study (Trial A), part IV

Table 8.6 Summary of *In Vitro* Double-Blinded Test Results of 19 BSCC Heart Valves with a 9 F gradiometer (Trial A)

Sample No	Serial No	Flange No	Operator 1 Indication	Operator 2 Indication	Computer Indication	Known Condition
1	29MBRC14924	87161	IOS	IOS	IOS	IOS
2	31MBRC61089	A5023	SLS	SLS	SLS	XSLS
3	31MBRC10029	85083	SLS	SLS	SLS	XSLS
4	31MBRC10177	94382	SLS	SLS	SLS	XSLS
5	29ABC10937	73234	SLS	SLS	SLS	MSLS*
6	29MBC60029	A6628	IOS	IOS	IOS	IOS
7	29ABC11608	83986	IOS	IOS	IOS	IOS
8	31MBRC60112	A2517	IOS	IOS	IOS	IOS
9	31MBRC12926	76225	SLS	SLS	SLS	XSLS
10	29ABC10925	73159	SLS	SLS	SLS	MSLS
11	29ABC40035	72393	IOS	IOS	IOS	IOS
12	31ABC10467	73021	SLS	SLS	SLS	MSLS
13	31MBRC12282	73225	SLS	SLS	SLS	MSLS
14	29MBRC10776	61046	SLS	SLS	SLS	XSLS
15	29MBRC16797	102268	SLS	SLS	SLS	MSLS
16	29MBRC15110	87384	IOS	IOS	IOS	IOS
17	29ABC11607	83740	SLS	SLS	SLS	MSLS*
18	29ABC12556	110830	IOS	IOS	IOS	IOS
19	31MBRC60939	A4567	SLS	SLS	SLS	XSLS

* - MSLS valves originally mislabeled as IOS valves on their shipping containers

8.7.2 *In Vitro* Study: Trial B, 19 BSCC Heart Valves, 9 F Gradiometer

In a second double-blind *in vitro* study with 2 operators, the 19 BSCC heart valves from Trial A were tested again in the gradiometer-based examination system with a 9 F (POT-9075) gradiometer. The excitation frequency was 60.27 kHz and the applied magnetic field was 1.123×10^{-4} T (1.12 gauss). Figure 8.34-Figure 8.37 show the θ output signals from the tests. The software classification threshold was again set at 0.85. Table 8.7 summarizes the test results. As before, the indications from the operators and the computer software all achieved 100% accuracy in determining the outlet strut condition of the BSCC heart valves.

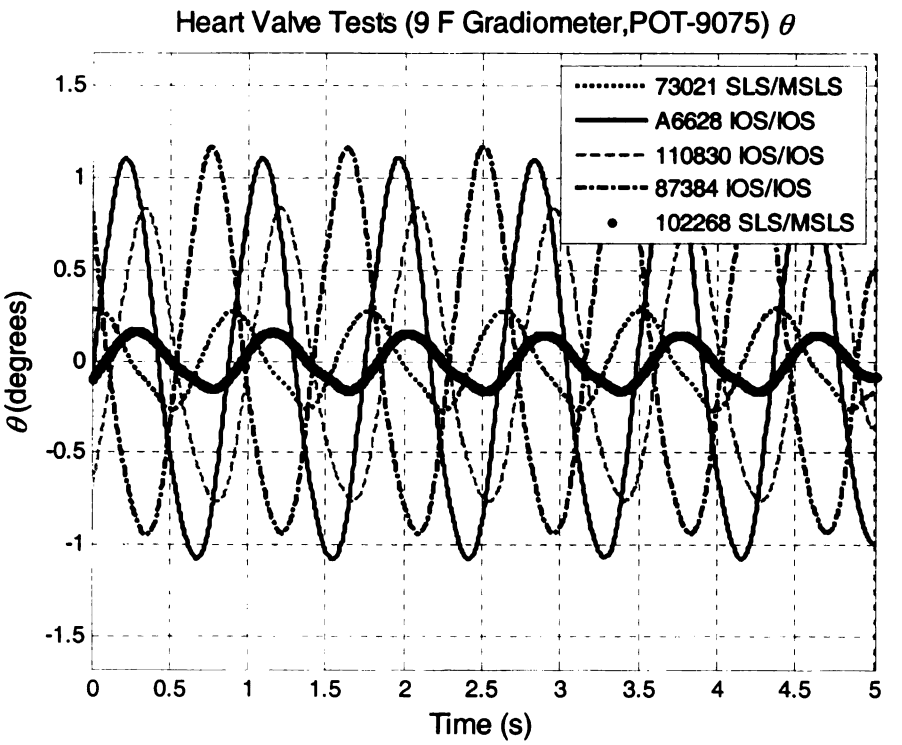

Figure 8.34 Output θ signals from the BSCC heart valve study (Trial B), part I

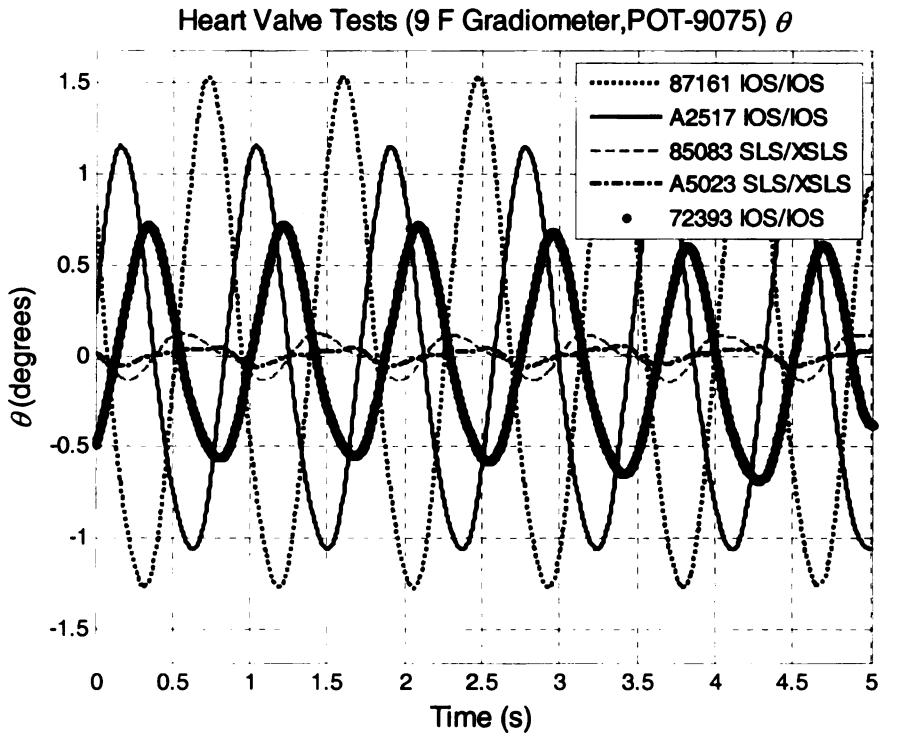

Figure 8.35 Output θ signals from the BSCC heart valve study (Trial B), part II

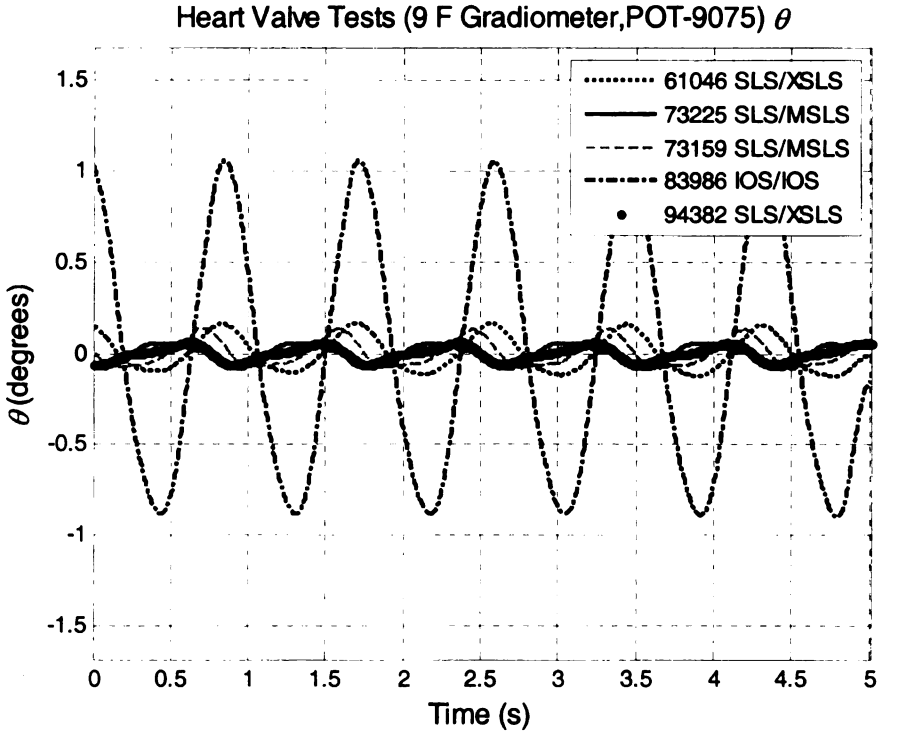

Figure 8.36 Output θ signals from the BSCC heart valve study (Trial B), part III

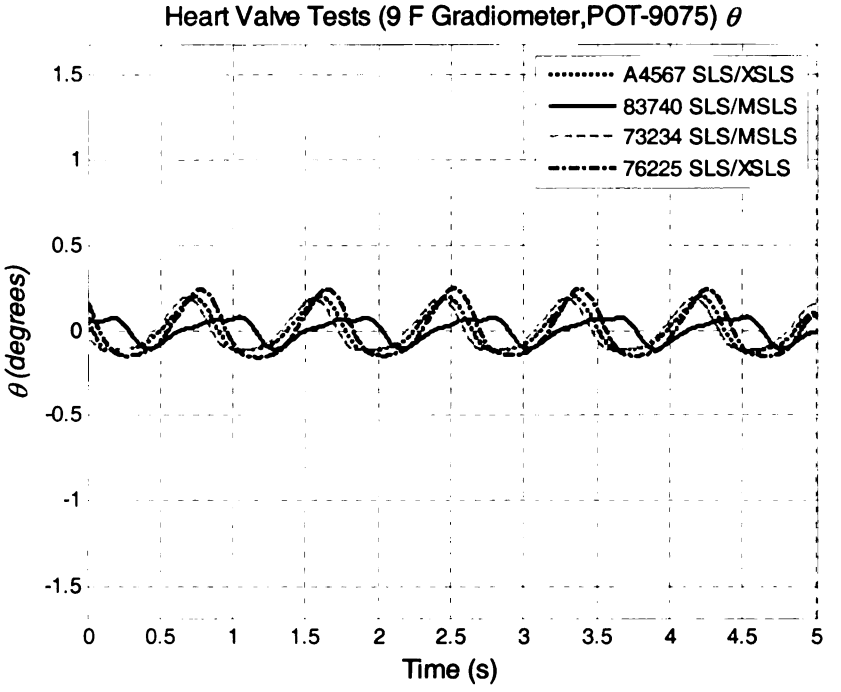

Figure 8.37 Output θ signals from the BSCC heart valve study (Trial B), part IV

Table 8.7 Summary of *In Vitro* Double-Blinded Test Results of 19 BSCC Heart Valves with the 9 F gradiometer (Trial B)

Sample No	Serial No	Flange No	Operator 1 Indication	Operator 2 Indication	Computer Indication	Known Condition
1	31ABC10467	73021	SLS	SLS	SLS	MSLS
2	29MBC60029	A6628	IOS	IOS	IOS	IOS
3	29ABC12556	110830	IOS	IOS	IOS	IOS
4	29MBRC15110	87384	IOS	IOS	IOS	IOS
5	29MBRC16797	102268	SLS	SLS	SLS	MSLS
6	29MBRC14924	87161	IOS	IOS	IOS	IOS
7	31MBRC60112	A2517	IOS	IOS	IOS	IOS
8	31MBRC10029	85083	SLS	SLS	SLS	XSLS
9	31MBRC61089	A5023	SLS	SLS	SLS	XSLS
10	29ABC40035	72393	IOS	IOS	IOS	IOS
11	29MBRC10776	61046	SLS	SLS	SLS	XSLS
12	31MBRC12282	73225	SLS	SLS	SLS	MSLS
13	29ABC10925	73159	SLS	SLS	SLS	MSLS
14	29ABC11608	83986	IOS	IOS	IOS	IOS
15	31MBRC10177	94382	SLS	SLS	SLS	XSLS
16	31MBRC60939	A4567	SLS	SLS	SLS	XSLS
17	29ABC11607	83740	SLS	SLS	SLS	MSLS*
18	29ABC10937	73234	SLS	SLS	SLS	MSLS*
19	31MBRC12926	76225	SLS	SLS	SLS	XSLS

*-Valves with MSLS mislabeled as IOS valves on shipping containers

8.7.3 *In Vitro* Study: Trial C, 34 BSCC Heart Valves, 6 F Gradiometer

A double-blind *in vitro* study was conducted on 34 BSCC heart valves (10 XSLS, 10 MSLS, and 14 IOS cases). Additionally, the control case with no heart valve was also examined. In this study, a 6 F gradiometer (POT-9085, #2) was used. The excitation frequency was 63.32 kHz and the applied magnetic field was 1.161×10^{-4} T (1.161 gauss). The software decision threshold was at 6.081°. (The selection of this threshold is discussed in the following section.) All other test conditions were similar to those in the previous trials. Figure 8.38-Figure 8.44 show the output θ signals from the study. For each valve, the flange number, computer decision, and the true valve condition are displayed in the respective graph legend. Table 8.8 summarizes the study results. The assessments from the operators and the computer software all achieved 100% accuracy in determining the outlet strut condition of the 34 BSCC heart valves. Because of the low signal output level, the "no valve" control case was classified as a SLS condition.

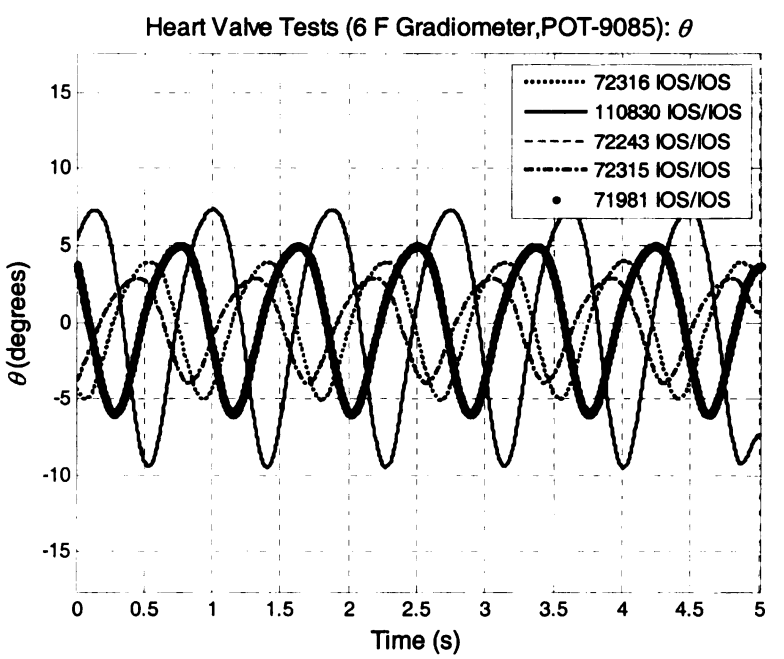

Figure 8.38 Output θ signals from the BSCC heart valve study (Trial C), part I

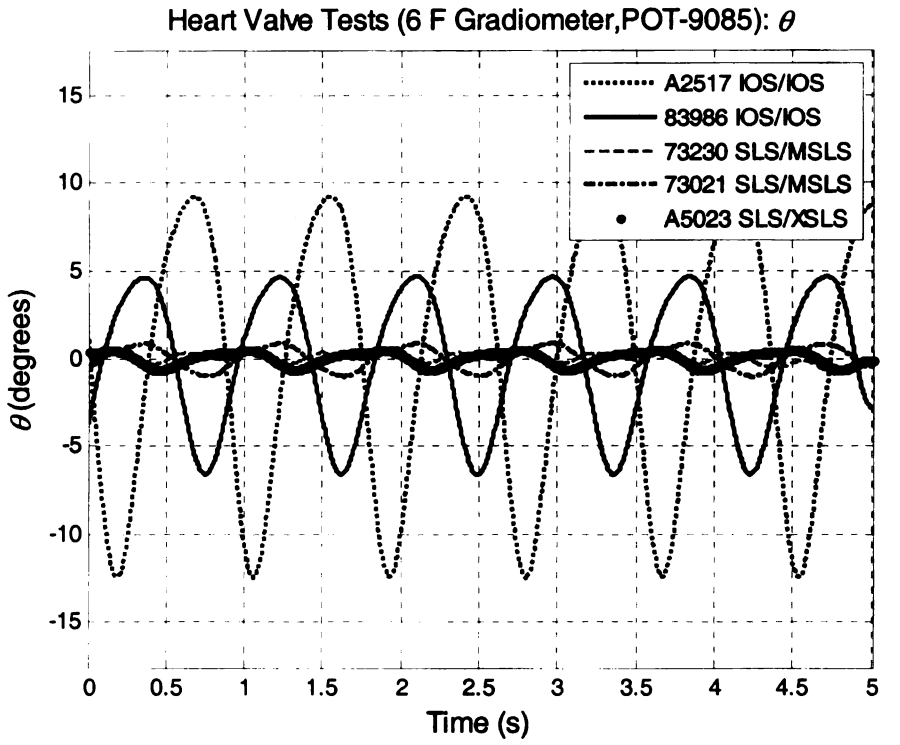

Figure 8.39 Output θ signals from the BSCC heart valve study (Trial C), part II

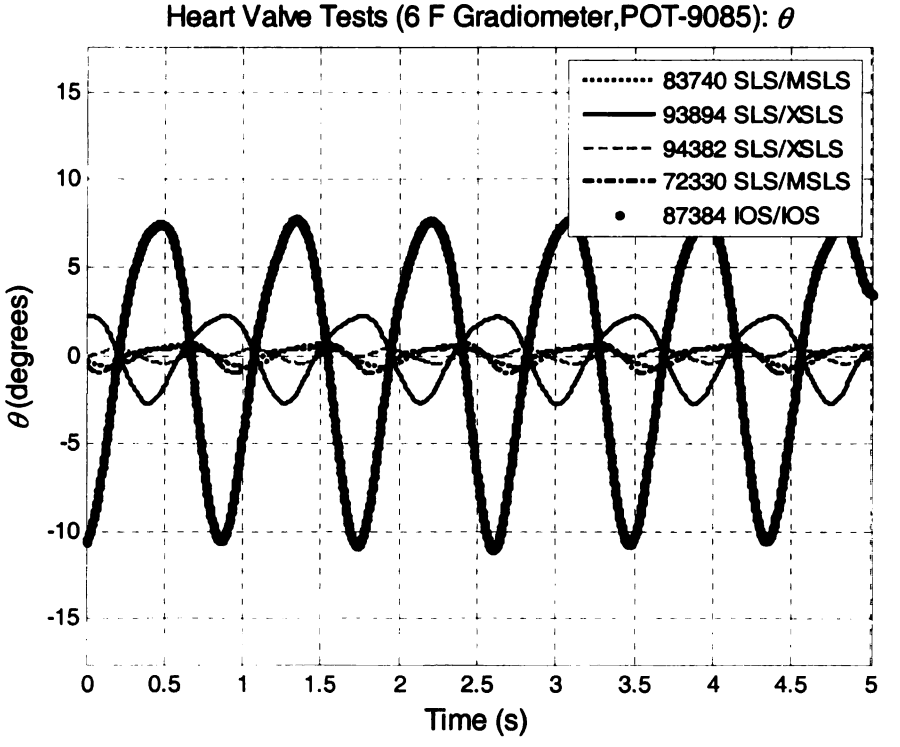

Figure 8.40 Output θ signals from the BSCC heart valve study (Trial C), part III

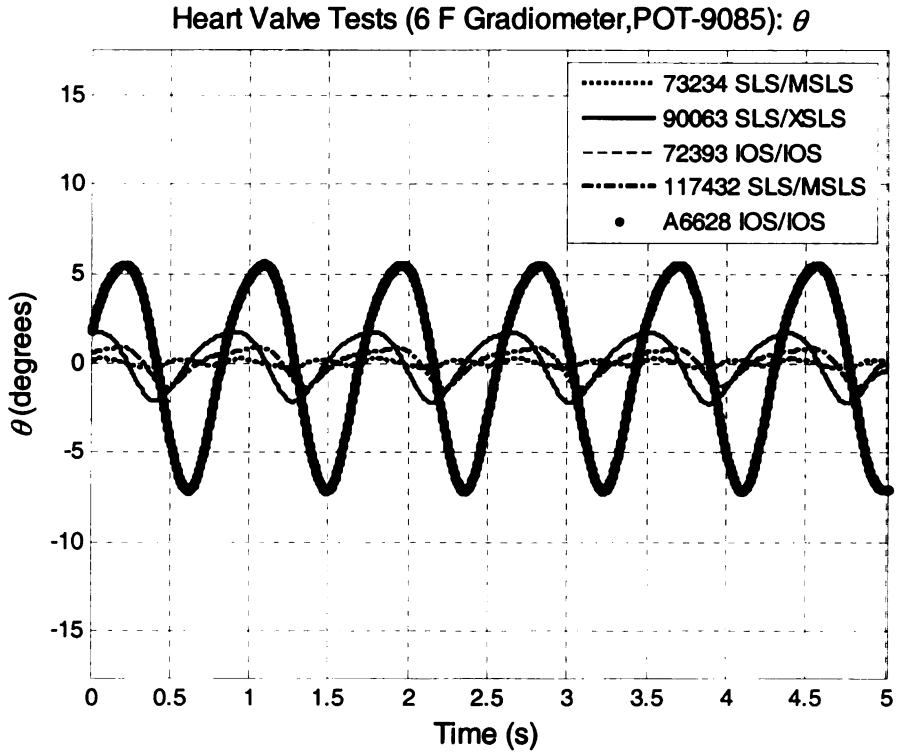

Figure 8.41 Output θ signals from the BSCC heart valve study (Trial C), part IV

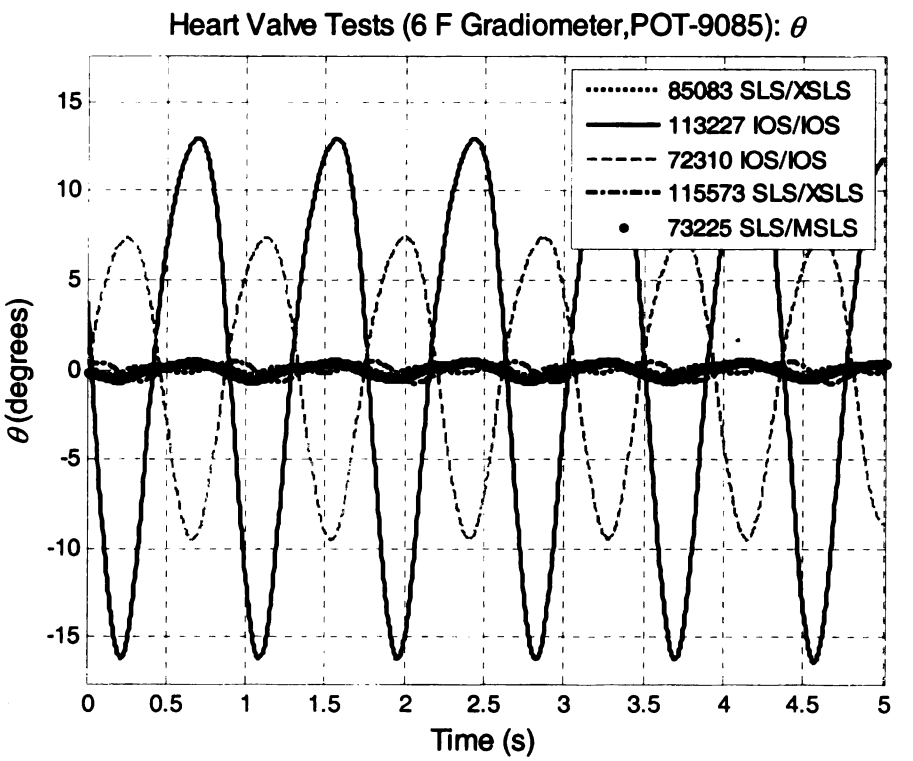

Figure 8.42 Output θ signals from the BSCC heart valve study (Trial C), part V

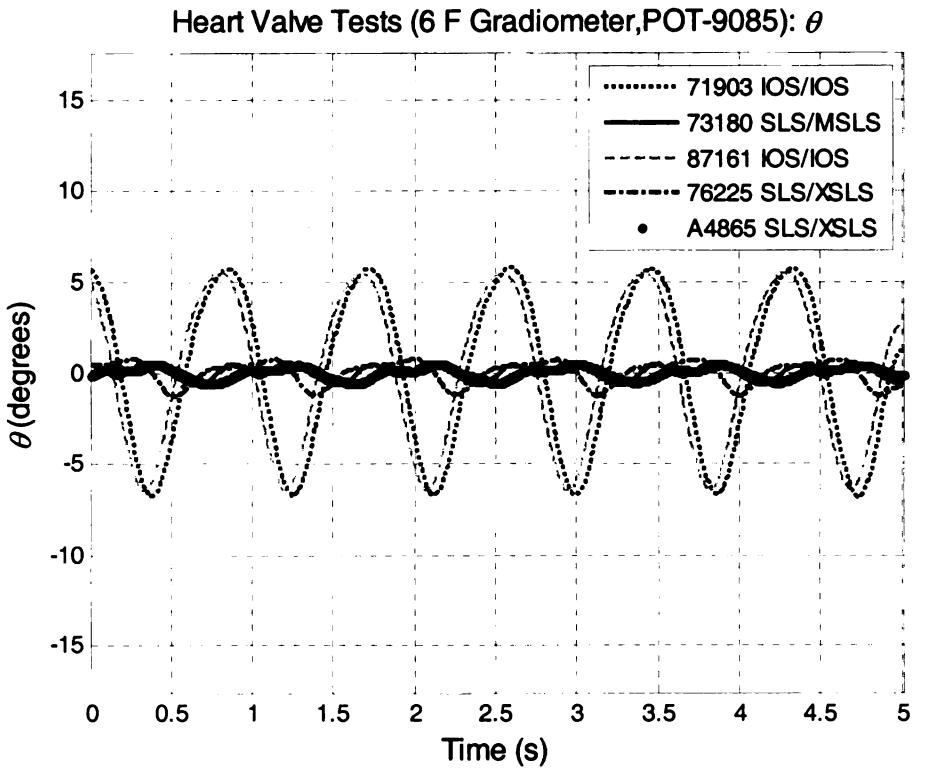

Figure 8.43 Output θ signals from the BSCC heart valve study (Trial C), part VI

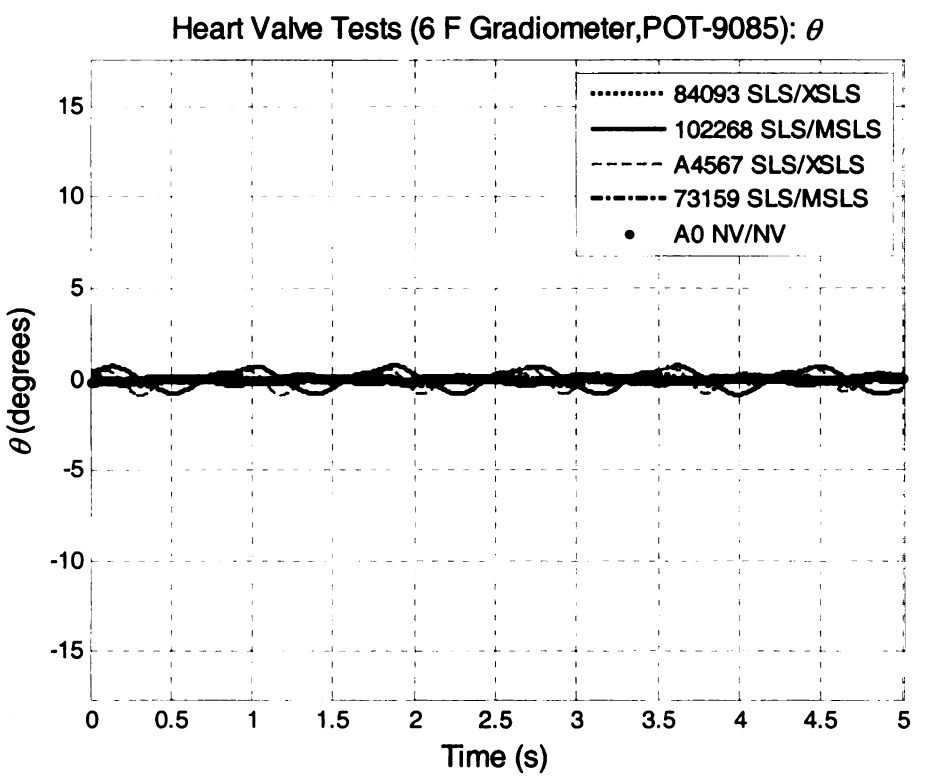

Figure 8.44 Output θ signals from the BSCC heart valve study (Trial C), part VII

Table 8.8 Summary of *In Vitro* Double-Blinded Test Results of 34 BSCC Heart Valves with the 6 F gradiometer (Trial C)

Sample No	Serial No	Flange No	Operator1 Indication	Operator2 Indication	Computer Indication	Known Condition
1	29MBRC12432	72316	IOS	IOS	IOS	IOS
2	29ABC12556	110830	IOS	IOS	IOS	IOS
3	29MBRC12423	72243	IOS	IOS	IOS	IOS
4	29MBRC12431	72315	IOS	IOS	IOS	IOS
5	29MBRC12407	71981	IOS	IOS	IOS	IOS
6	31MBRC60112	A2517	IOS	IOS	IOS	IOS
7	29ABC11608	83986	IOS	IOS	IOS	IOS
8	29ABC10934	73230	SLS	SLS	SLS	MSLS
9	31ABC10467	73021	SLS	SLS	SLS	SLS
10	31MBRC61089	A5023	SLS	SLS	SLS	XSLS
11	29ABC11607	83740	SLS	SLS	SLS	MSLS*
12	31ABCB10022	93894	SLS	SLS	SLS	XSLS
13	31MBRC10177	94382	SLS	SLS	SLS	XSLS
14	29MBRC12477	72330	SLS	SLS	SLS	MSLS
15	29MBRC15110	87384	IOS	IOS	IOS	IOS
16	29ABC10937	73234	SLS	SLS	SLS	MSLS*
17	29MBRC15994	90063	SLS	SLS	SLS	XSLS
18	29ABC40035	72393	IOS	IOS	IOS	IOS
19	29EMBRC10332	117432	SLS	SLS	SLS	MSLS
20	29MBC60029	A6628	IOS	IOS	IOS	IOS
21	31MBRC10029	85083	SLS	SLS	SLS	XSLS
22	31MBRC16369	113227	IOS	IOS	IOS	IOS
23	29MBRC12430	72310	IOS	IOS	IOS	IOS
24	S31MBRC10032	115573	SLS	SLS	SLS	MSLS
25	31MBRC12282	73225	SLS	SLS	SLS	MSLS
26	29MBRC12406	71903	IOS	IOS	IOS	IOS
27	29ABC10932	73180	SLS	SLS	SLS	MSLS
28	29MBRC14924	87161	IOS	IOS	IOS	IOS
29	31MBRC12926	76225	SLS	SLS	SLS	XSLS
30	29MBRC61636	A4865	SLS	SLS	SLS	XSLS
31	31MBRCB10006	84093	SLS	SLS	SLS	XSLS
32	29MBRC16797	102268	SLS	SLS	SLS	MSLS
33	31MBRC60939	A4567	SLS	SLS	SLS	XSLS
34	29ABC10925	73159	SLS	SLS	SLS	MSLS

*-Valves with MSLS mislabeled as IOS valves on shipping containers

8.7.4 Selection of the Computer Decision Threshold

The initial decision thresholds for the computer inspection software package were established experimentally during system development. A threshold was selected for each of the two gradiometers from measurements using the system prototype. A more rigorous approach for selecting the threshold involves examining the mean and standard deviation of the peak-to-peak θ variation for the valves with SLSs. Figure 8.45 shows the output θ variation for the test cases in Trial C. From these results (excluding the "no valve" case), the mean of the θ variation for all the SLS valves is $\mu = 1.5151^{o}$, and the standard deviation is $\sigma = 1.132^{o}$. The decision threshold may be selected as

$$Threshold = \mu + n\sigma \qquad n = 1, 2, 3... \tag{8.4}$$

Thresholds for n = 3 to 6 are plotted in Figure 8.45. Comparison with the output θ values show that only the thresholds at 4.911^{o} (n=3) and 6.042^{o} (n=4) are able to separate the two valve classes. Note that the threshold 6.042^{o} matches loosely the experimentally established threshold 6.081^{o}.

The data in Figure 8.45 show that the mean and standard deviation of θ have been influenced by two outlier SLS data points corresponding to Sample ID #12 and #17. If these data points are excluded, the adjusted mean and standard deviation become μ *(adjusted)* = 1.397^{o} and σ*(adjusted)* = 0.815^{o}. Applying these values to (8.4) yields the adjusted thresholds (n=3 to 6) in Figure 8.46. These results suggest that the threshold

7.175^{o} (n=5) or 8.307^{o} (n=6) may be used to distinguish between the two outlet strut classes. The mean, standard deviation and thresholds for the cases when all the SLS data are used and when the outliers (#12 and #17) are excluded are summarized in Table 8.9. The gradiometer-based examination system software employs a decision threshold of 8.307^{o} ($\mu + 6\sigma$, adjusted) when used with the 6 F gradiometer, and 1.20^{o} when used with the 9 F gradiometer.

Table 8.9 Summary of the mean, standard deviation, and decision thresholds for the cases when all SLS data are used and when the outlier data points are excluded.

	All SLS cases (^{o})	Excluded Outliers #12 & #17 (^{o})
μ	1.5151	1.3965
σ	1.132	0.81451
Threshold T3: $\mu + 3\sigma$	4.911	3.84
Threshold T4: $\mu + 4\sigma$	6.043	4.6545
Threshold T5: $\mu + 5\sigma$	7.175	5.4691
Threshold T6: $\mu + 6\sigma$	8.307	6.2836

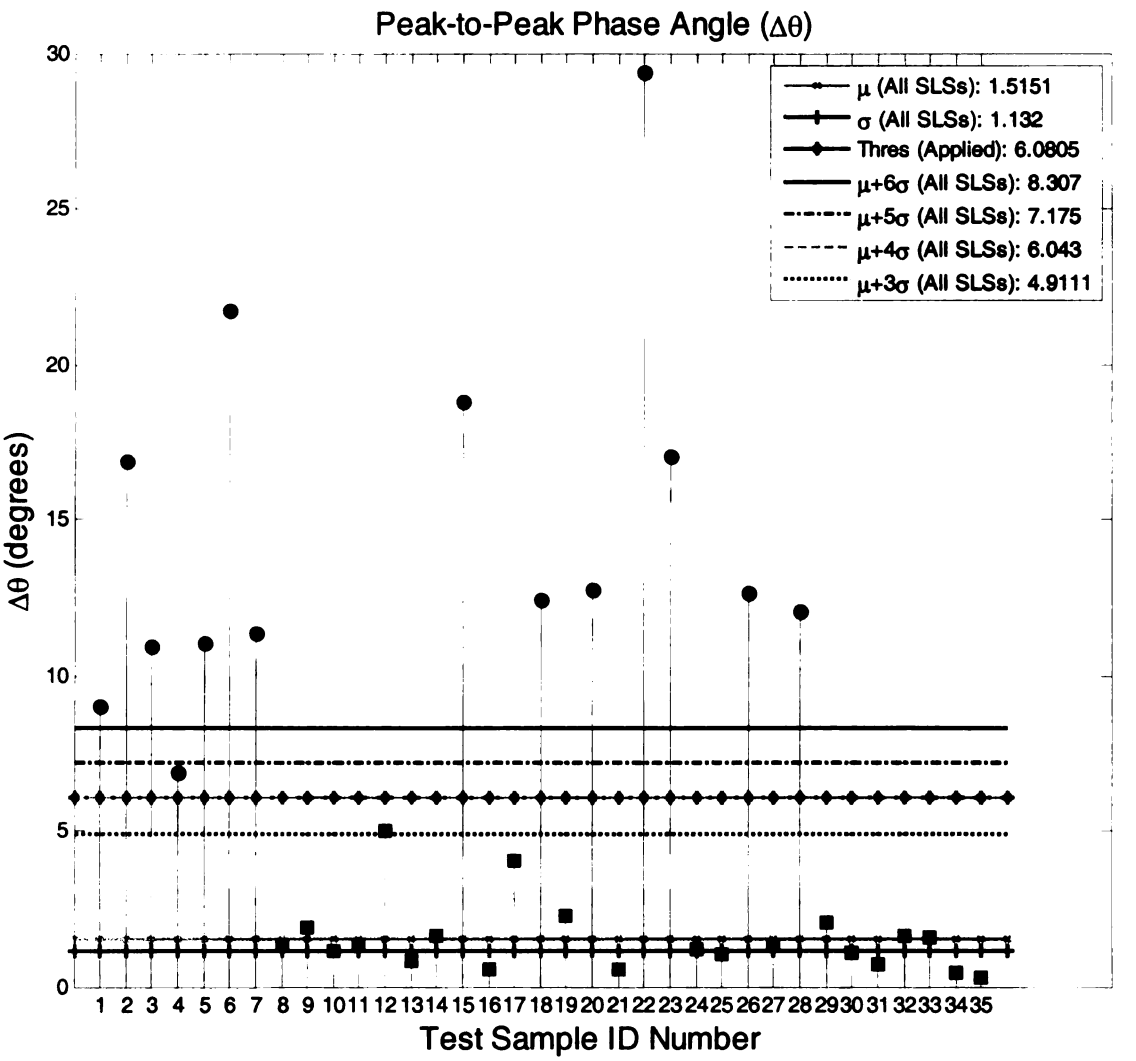

Figure 8.45 Peak-to-peak θ variation for the samples examined in Trial C. The mean, standard deviation, and various thresholds for θ are as indicated.

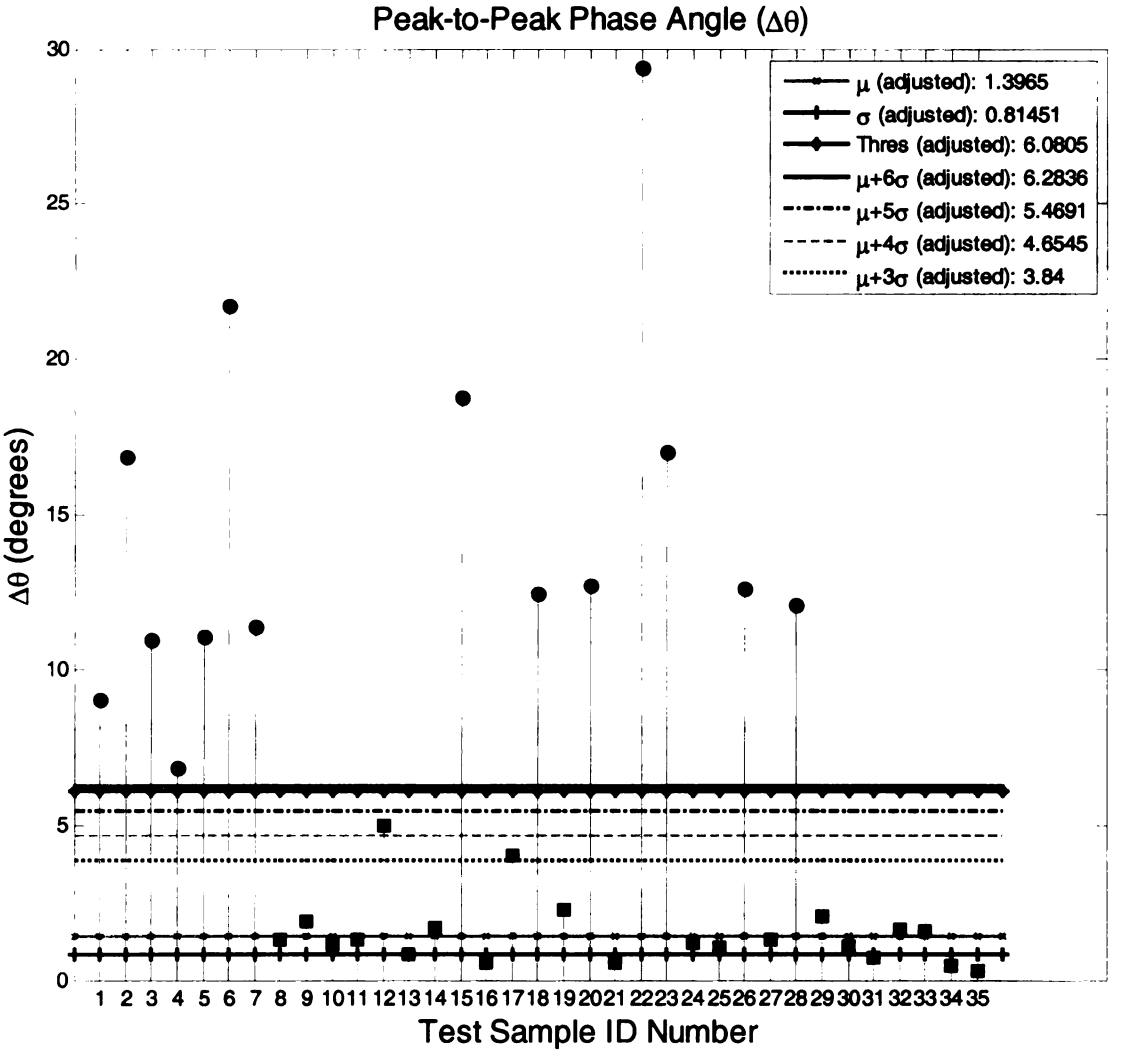

Figure 8.46 Peak-to-peak θ variation for the samples examined in Trial C. The adjusted mean, standard deviation, and thresholds for θ are as indicated.

8.7.5 Trial D: Threshold Verification, 11 BSCC Heart Valves, 6 F Gradiometer

A double-blind study with 11 randomly selected BSCC heart valves of various outlet strut conditions (2 XSLS, 4 MSLS, and 5 IOS) was conducted to verify the decision threshold established in the previous section. In this study, the excitation frequency was 63.02 kHz, applied magnetic field was 1.55×10^{-4} T (1.55 gauss), and a 6 F gradiometer (POT-9085, #2) was used. All other test conditions were identical to those employed in the previous trials. Figure 8.47-Figure 8.49 show the θ signals from the study, and Table 8.10 summarizes the decisions from the operators and computer software. These results demonstrate 100 % accuracy in indicating the valve conditions. Figure 8.50 shows the peak-to-peak θ values for the heart valves examined. The adjusted thresholds from Table 8.9 are also plotted in this figure for comparison. The results from this figure verify that the 6-sigma threshold 6.2836^{o} (the value employed by the gradiometer-based examination system) may be used to classify the outlet strut condition of the BSCC heart valves.

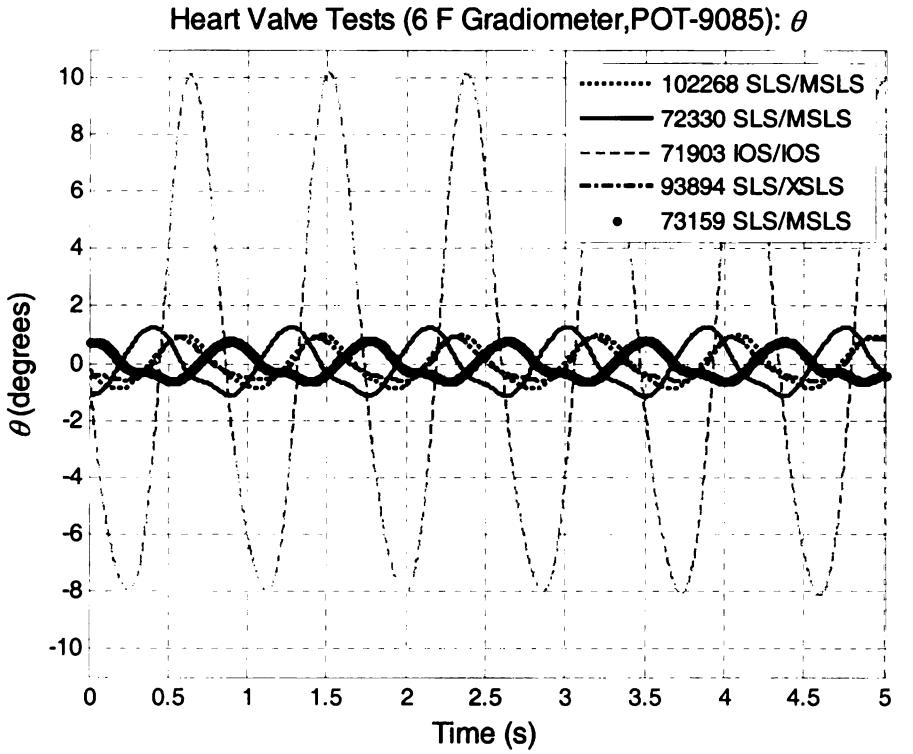

Figure 8.47 Output θ signals from the BSCC heart valve study (Trial D), part I

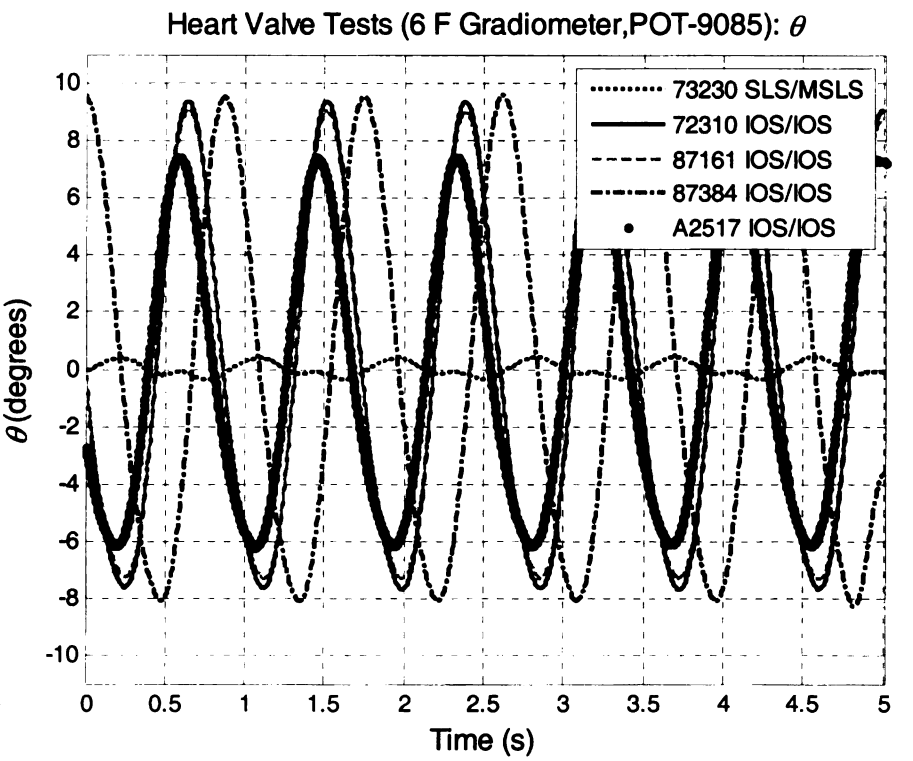

Figure 8.48 Output θ signals from the BSCC heart valve study (Trial D), part II

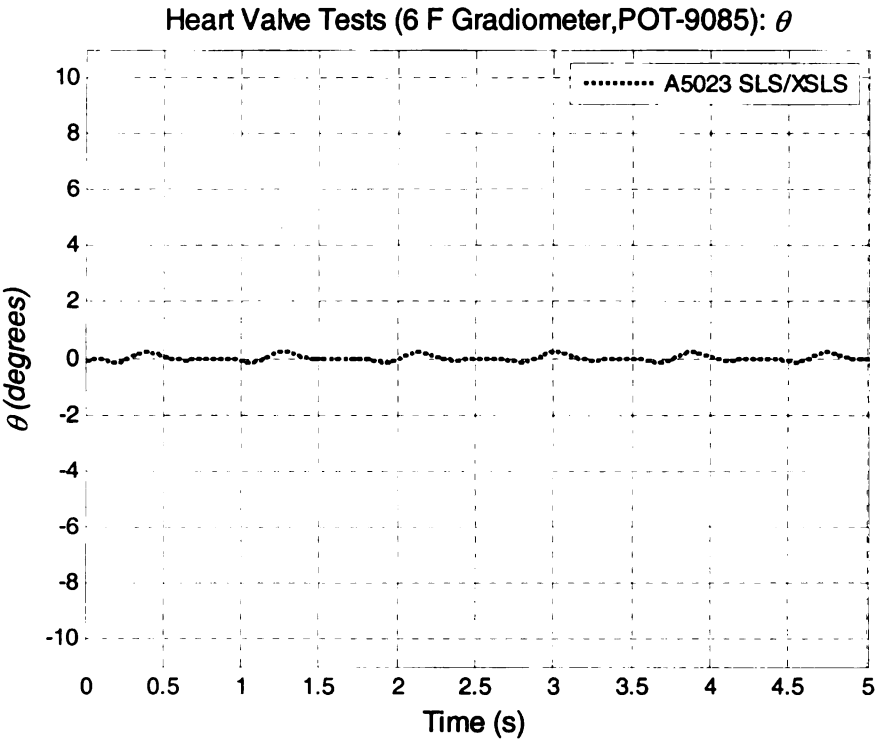

Figure 8.49 Output θ signals from the BSCC heart valve study (Trial D), part III

Table 8.10 Summary of *In Vitro* Double-Blinded Test Results of 11 BSCC Heart Valves with the 6 F gradiometer (Trial D)

Sample No	Serial No	Flange No	Operator1 Indication	Operator2 Indication	Computer Indication	Known Condition
1	29MBRC16797	102268	SLS	SLS	SLS	MSLS
2	29MBRC12477	72330	SLS	SLS	SLS	MSLS
3	29MBRC12406	71903	IOS	IOS	IOS	IOS
4	31ABCB10022	93894	SLS	SLS	SLS	XSLS
5	29ABC10925	73159	SLS	SLS	SLS	MSLS
6	29ABC10934	73230	SLS	SLS	SLS	MSLS
7	29MBRC12430	72310	IOS	IOS	IOS	IOS
8	29MBRC14924	87161	IOS	IOS	IOS	IOS
9	29MBRC15110	87384	IOS	IOS	IOS	IOS
10	31MBRC60112	A2517	IOS	IOS	IOS	IOS
11	31MBRC61089	A5023	SLS	SLS	SLS	XSLS

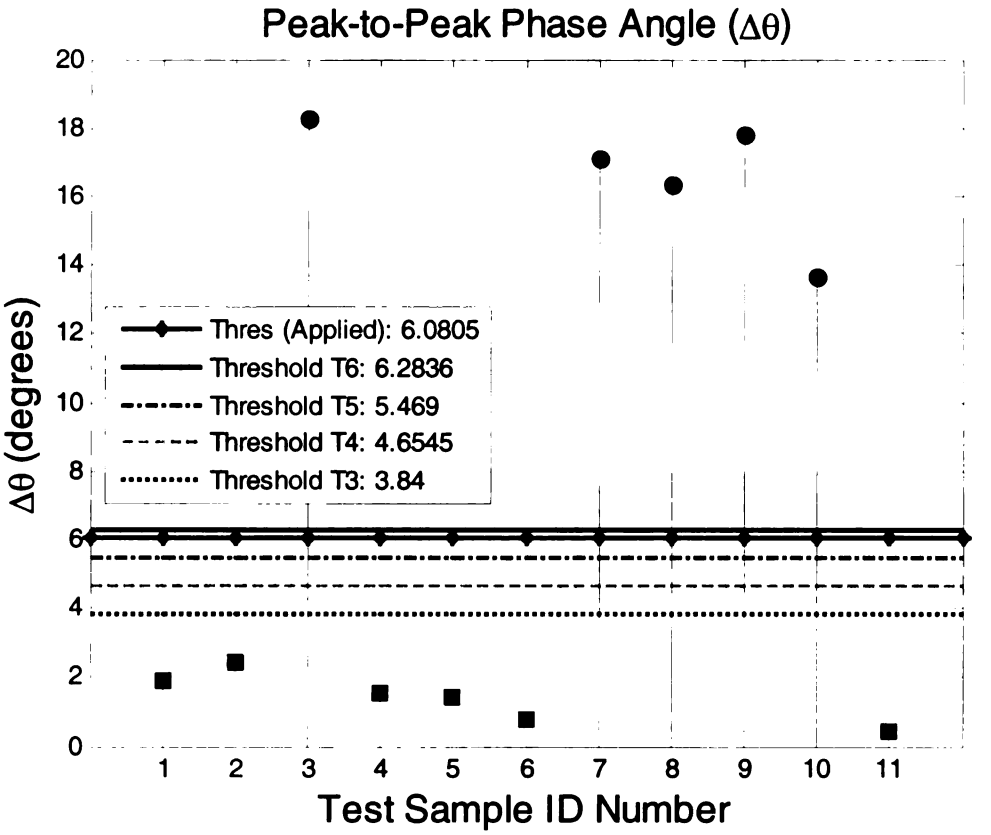

Figure 8.50 Peak-to-peak θ variation for the heart valves examined in Trial D. The adjusted thresholds from Table 8.9 are included for comparison.

The results presented in this chapter demonstrate the proof of concept of the gradiometer-based examination system in determining the outlet strut condition of a BSCC prosthetic heart valve. In the following chapter, a probability of detection model is developed to quantify the system performance when the gradiometer is placed away from the outlet strut plane.

CHAPTER 9. PROBABILITY OF DETECTION MODEL

The reliability of the gradiometer-based prosthetic heart valve evaluation system is influenced by several variables such as the alignment and distance of the gradiometer with respect to the heart valve outlet strut. To quantify the system performance, a probability of detection (POD) model that can predict the output signal in the presence of the measurement variabilities may be used. A POD model for the gradiometer-based system accounts for the uncertainties that affect the output signal by generating a distribution of this signal around its mean value to predict the variations. The development, analysis, and benefits of applying POD models for nondestructive evaluation techniques have been discussed extensively in [180]-[183]. This chapter presents a POD model for the gradiometer-based examination system. In particular, a POD model that takes variabilities in the gradiometer's initial position from the heart value outlet strut into account is presented. The initial position of the gradiometer is defined, in this context, as the closet distance of the gradiometer to the outlet strut during the cyclical movement. The concept described herein may be adapted to develop POD models accounting for other sources of variability in the examination system.

9.1 Sources of Variability

Figure 9.1 shows the optimal position of the gradiometer during a heart valve examination. The primary source of variability for the examination system is the deviation of the gradiometer from this optimal location. Figure 9.2 (a)-(c) show

examples of translational deviations and Figure 9.2 (d)-(e) show examples of alignment angle variations of the gradiometer. Other examples of variability include:

- Human factors (e.g., the skill set of the medical personnel);
- Variations in patient physiology such as the heart rate and cardiac output volume;
- Variations in the excitation source such as the input current value and the match between the excitation frequency and the resonant frequency of the load;
- Instrument noise.

The following sections present a POD model for the initial position of the gradiometer with respect to the outlet strut as shown in Figure 9.2(a). The technique employed is applicable for developing POD models for other parametric variabilities in the system.

9.2 POD Model

The probability of detecting a defect by an inspection system can be determined by generating conditional probability density functions (pdfs) for the output parameter of interest. Figure 9.3 shows examples of the output signal parameter distribution in the presence of a defect, $p(y|x_1)$, and without a defect, $p(y|x_0)$. In this figure, y is the output parameter and x_0 and x_1 represent the case where a defect is absent and present, respectively.

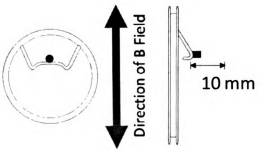

Figure 9.1 Optimal position and movement range for the gradiometer with respect to the outlet strut

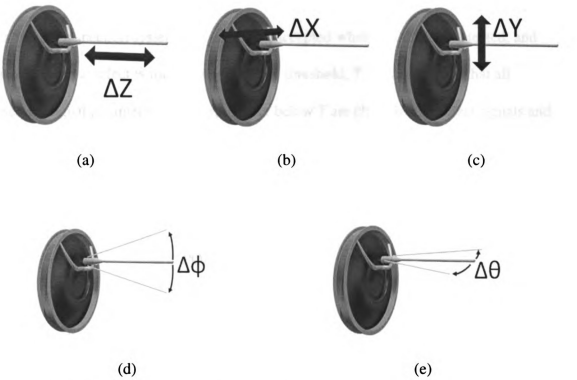

Figure 9.2 Examples of variations in the gradiometer position with respect to the heart value outlet strut: (a)-(c) translational, (e)-(f) alignment angle.

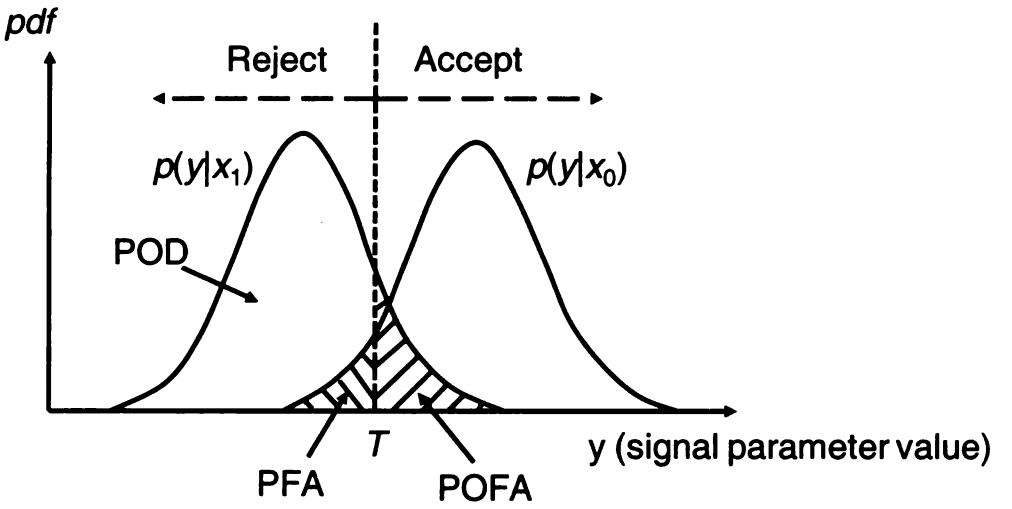

Figure 9.3 Probability density functions of the output signal parameter when a defect is present ($p(y|x_1)$), and without a defect ($p(y|x_0)$).

In a typical inspection system, a specimen is accepted when no defect is detected, and rejected when a defect is found. The decision threshold, T, is chosen such that all observed signal parameter values, y, that are below T are classified as defect signals and those exceeding the threshold are interpreted as absence of defect. The probability of detection is then given by

$$\text{POD} = \int_{-\infty}^{T} p\left(y \mid x_1\right) dy . \tag{9.1}$$

A *false alarm* occurs when a specimen without defect is rejected due to misinterpretation of the signal. The probability of false alarm (PFA) is given by

$$\text{PFA} = \int_{-\infty}^{T} p\left(y \mid x_0\right) dy \tag{9.2}$$

On the other hand, a *false acceptance* is the case when a specimen is accepted even when a defect is present. The probability of false acceptance (POFA) is related to the POD as

$$\text{POFA} = 1 - \text{POD} \tag{9.3}$$

The POFA can also be obtained from

$$\text{POFA} = \int_{T}^{\infty} p\left(y \mid x_1\right) dy \tag{9.4}$$

Figure 9.3 shows the regions under the two pdfs corresponding to the POD, PFA, and POFA for a given threshold, *T*. The degree of overlap between the defect and no-defect signal parameter distributions is typically a function of the defect characteristic such as geometry and dimensions. If the characteristic of the defect is not distinctive under the inspection modality, the overlap region between the two pdfs will be large, and the ability to detect a critical defect is low. In this case, the detection ability of the system becomes a function of *T*. The value of *T* may be selected based on one of the following three criteria [180]-[183]:

1. Set the probability of false alarm (PFA) to a constant value.
2. Set the probability of false acceptance (POFA) to a constant value.
3. Minimize the total signal classification error.

In the third criterion, the total signal classification error, *E(T)*, is a weighted sum of the PFA and the POFA [180]-[183], [191] given by:

$$E(T) = \alpha \cdot \text{POFA} + (1-\alpha) \cdot \text{PFA}$$
$$= \alpha \int_{T}^{\infty} p(y \mid x_1)\, dy + (1-\alpha) \int_{-\infty}^{T} p(y \mid x_0)\, dy \tag{9.5}$$

In (9.5), α is the prior probability of a defect being present in the specimen. The threshold T is then obtained by solving

$$\frac{\partial E(T)}{\partial T} = 0 \tag{9.6}$$

To calculate the POD, PFA, and POFA using (9.1)-(9.4), the signal pdf with and without a defect are needed. Several probabilistic models for obtaining these pdfs are described in details in [180]-[183] and [192]-[193]. These include the experimental, numerical, and functional models.

In the experimental model, a large number of measurements are taken on the output to generate the pdf for the signal. This approach is laborious, costly, and time consuming as it requires the generation of a large observation set to produce statistically significant estimates. To overcome this limitation, a numerical model may be used to predict the defect signal and effects of measurement variabilities. Although it is more cost effective than the experimental model, the numerical model is often computationally intensive since three dimensional numerical models must be simulated a large number of times to produce the probabilities. The functional model, on the other hand, does not require extensive human or computational resources. The following sections describe the

functional model and its application to POD evaluations for the gradiometer-based examination system.

9.2.1 Functional Model

The functional model [180], [181] uses a small set of system output values to establish a mathematical relationship between the output signal parameter, y, and a perturbed system parameter, r. Examples of r include liftoff, probe alignment, and excitation signal level, while examples of y include the maximum amplitude and largest phase angle of the output signal. The output signal parameter values may be obtained from either physical measurements or a numerical model. With a given perturbed system parameter value, r, two sets of y data are collected—one with the influence of a defect, and the other without. Two corresponding mathematical functions are then developed using simple curve fitting techniques. If the pdf of the system parameter perturbations is known, the conditional pdfs of the output signal parameter with ($p(y|x_1)$) and without ($p(y|x_0)$) a defect can be calculated using the proper functional model as shown in Figure 9.4. Once the conditional pdfs are known, equations (9.1) and (9.2) are used to obtain the POD and PFA, respectively.

9.3 Parametric Study

The outputs of the gradiometer-based prosthetic heart valve examination system represent the scaled amplitude, R, and phase angle, θ, of the gradiometer signal. The results in Chapter 8 show that the condition of the heart valve is related to the maximum value of θ. Hence, in the POD formulation, the maximum value of θ is the signal parameter of

interest, y. With a given threshold, T, the following sections describe a technique to develop a functional model and calculate the POD for the examination system with respect to the initial position between the gradiometer and the outlet strut. The technique presented may be used to develop the POD with respect to other sources of variabilities.

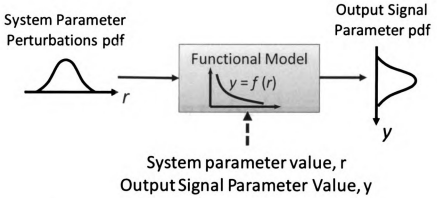

Figure 9.4 Application of the functional model to obtain the output signal parameter conditional pdf. Adapted from [180] and [181].

9.3.1 POD With Respect to the Gradiometer Distance from the Outlet Strut

Two BSCC heart valves, one with an IOS (flange no. 71981[1]) and the other an explanted valve with a SLS (flange no. A4865[2]), have been chosen randomly for the POD study. The objective of the study is to develop the POD for the examination system with respect to the initial position, z, between the gradiometer and the outlet strut. Figure 9.5 shows the output phase angle, θ, for the two valves over five cardiac cycles obtained from the *in vitro* test system (Chapter 8). Using the gradiometer movement data from Figure 8.16, the output phase angle for the two valves as a function of distance are shown in Figure

[1] Valve flange number: 71981, S/N: 29MBRC 12407, condition: IOS

[2] Valve flange number: A4865, S/N: 29MBRC 61636, condition: explanted SLS

9.6. For comparison, offsets have been added to the results in this figure such that the two curves intercept at z = 12 mm, corresponding to the maximum distance of the gradiometer from the outlet strut during a cardiac cycle. A functional model, f, is developed for each data set in Figure 9.6 to relate the input distance, z, to the output phase angle, θ. For the two outlet strut cases, the functional models are

$$\theta_{IOS} = f_{IOS}(z) \tag{9.7}$$

and

$$\theta_{SLS} = f_{SLS}(z) \tag{9.8}$$

In each case, a 7^{th} order polynomial is fitted to the data to produce a mathematical model. Comparisons of the original and model generated outputs for the IOS and SLS cases are shown in Figure 9.7 and Figure 9.8, respectively.

The perturbations of z is assumed to follow a Gaussian distribution with a selected mean and fixed variance of 0.4 mm^2. A fixed variance is used since, in practice, the gradiometer oscillates about a mean position with the same amplitude regardless of the distance between this position and the heart valve outlet strut. Figure 9.9 shows an input pdf with a mean distance z = 2.5 mm from the outlet strut and a positional variance of 0.4 mm^2. Applying this pdf to the functional models in (9.7) and (9.8) yields the pdf for the output phase angles θ_{IOS} and θ_{SLS} in Figure 9.10 and Figure 9.11, respectively. Figure 9.12 shows the locations of these two pdfs. In this figure, the pdf of θ_{SLS} (dashed line)

corresponds the conditional probability $p(y|x_1)$, and the pdf for θ_{IOS} (solid line) corresponds to the conditional pdf $p(y|x_0)$, of Figure 9.3.

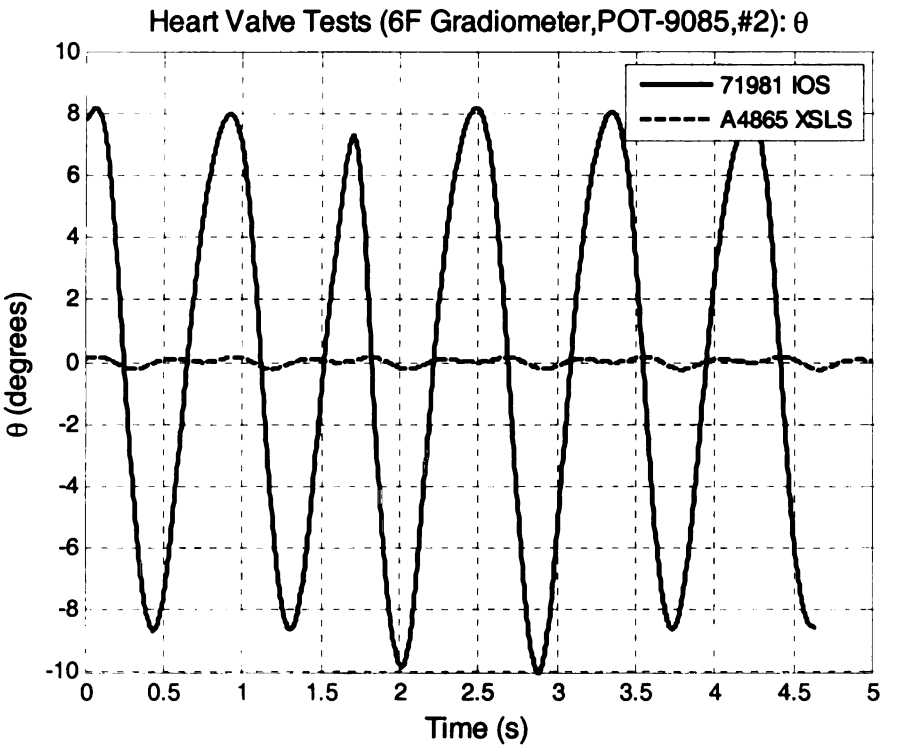

Figure 9.5 Output phase angle, θ, over time for a valve with an IOS (solid line), and one with a SLS (dashed line).

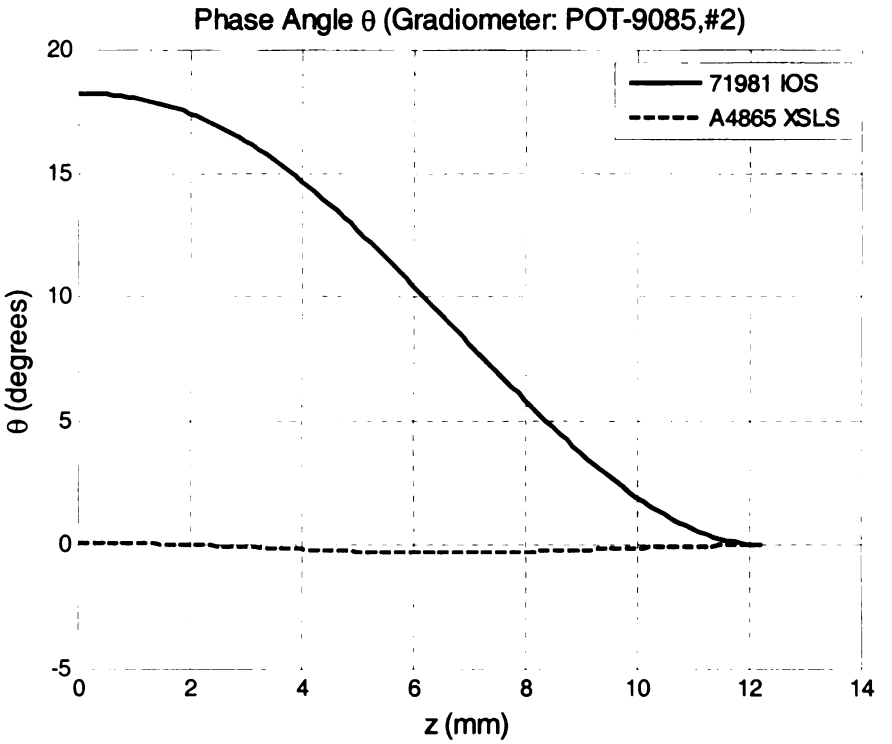

Figure 9.6 Output phase angle, θ, as a function of z, the distance between the gradiometer and outlet strut, for a valve with an IOS (solid line), and one with a SLS (dashed line).

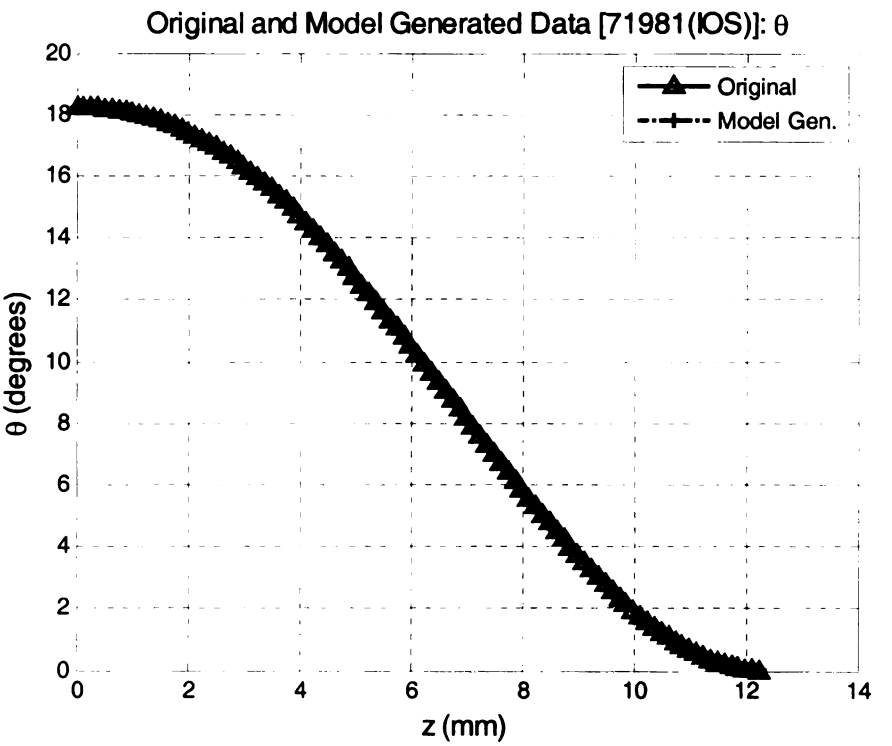

Figure 9.7 Original and model generated outputs for the IOS case

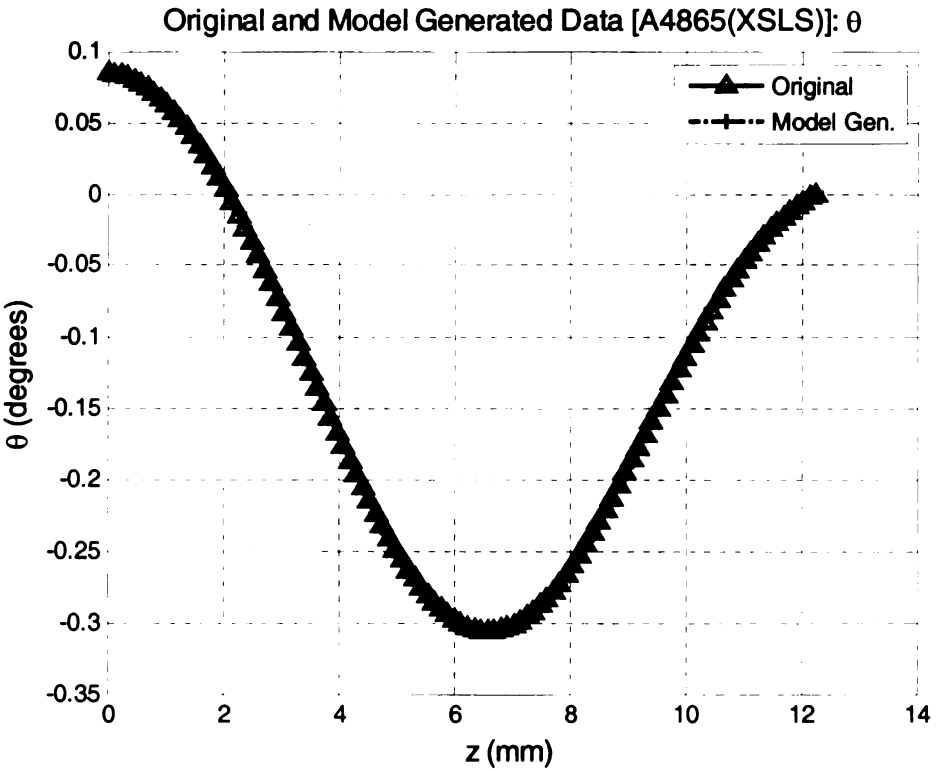

Figure 9.8 Original and model generated outputs for the SLS case

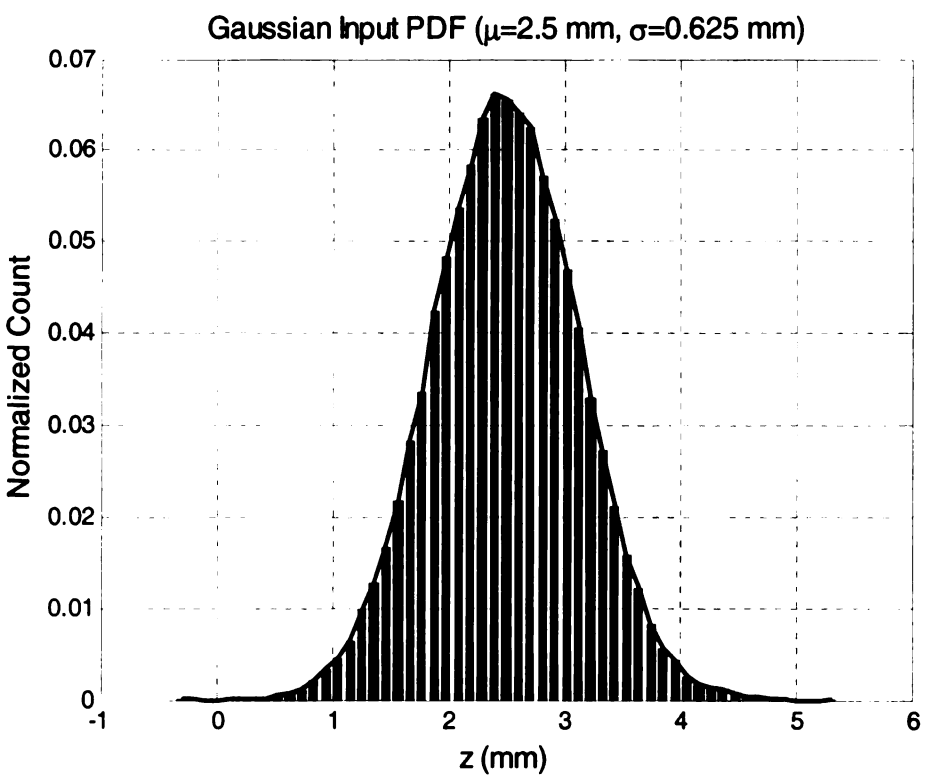

Figure 9.9 Example of a Gaussian distribution for the input pdf (z)

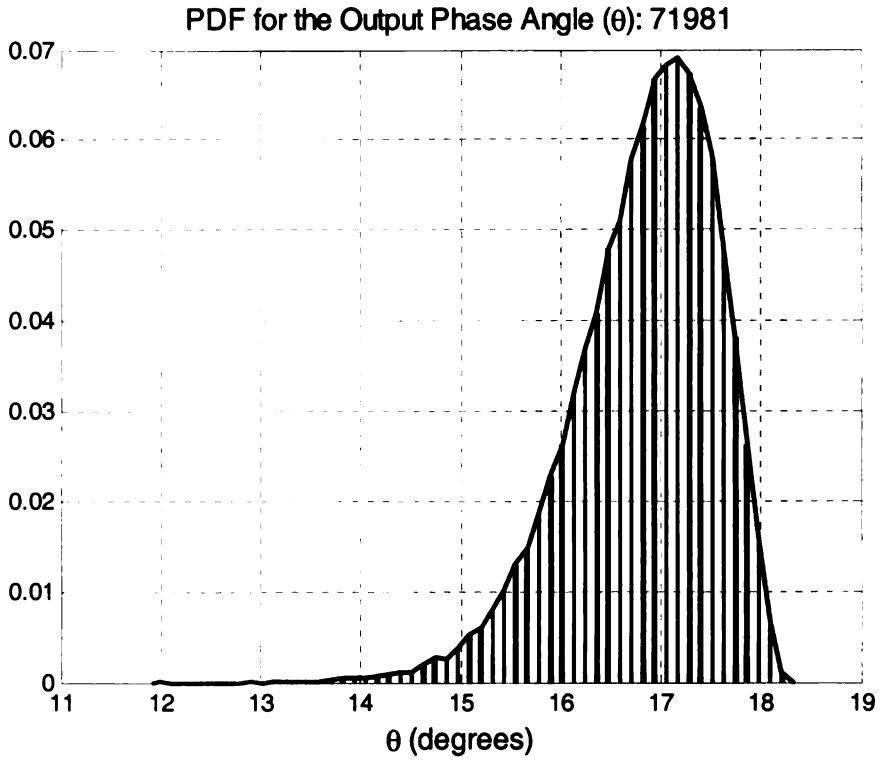

Figure 9.10 PDF of θ_{IOS} for heart valve 71981 with an IOS (z = 2.5 mm)

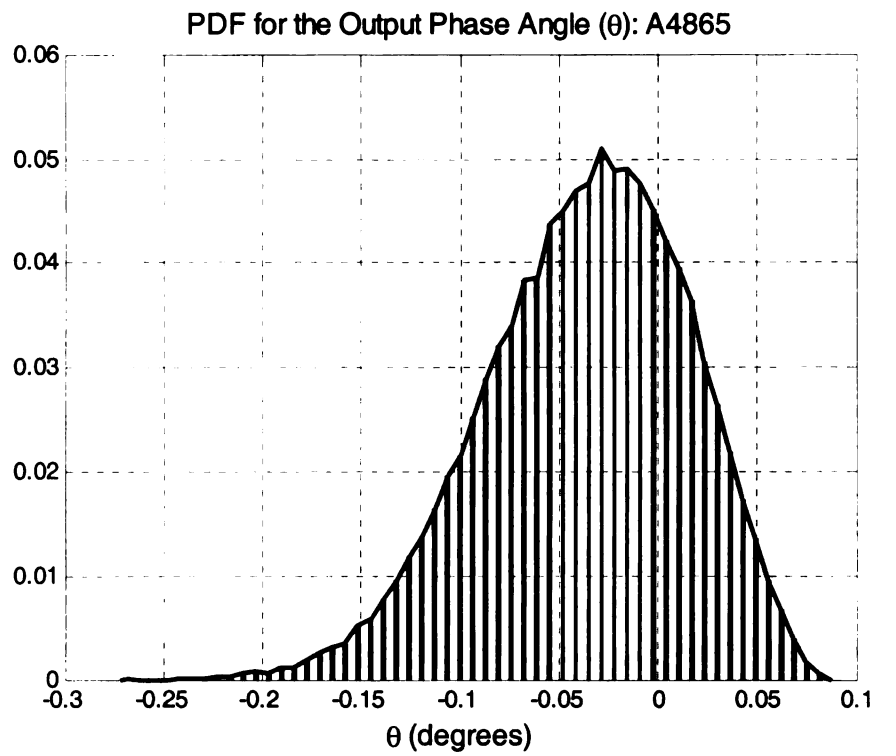

Figure 9.11 PDF of θ_{SLS} for heart valve A4865 with a SLS (z = 2.5 mm)

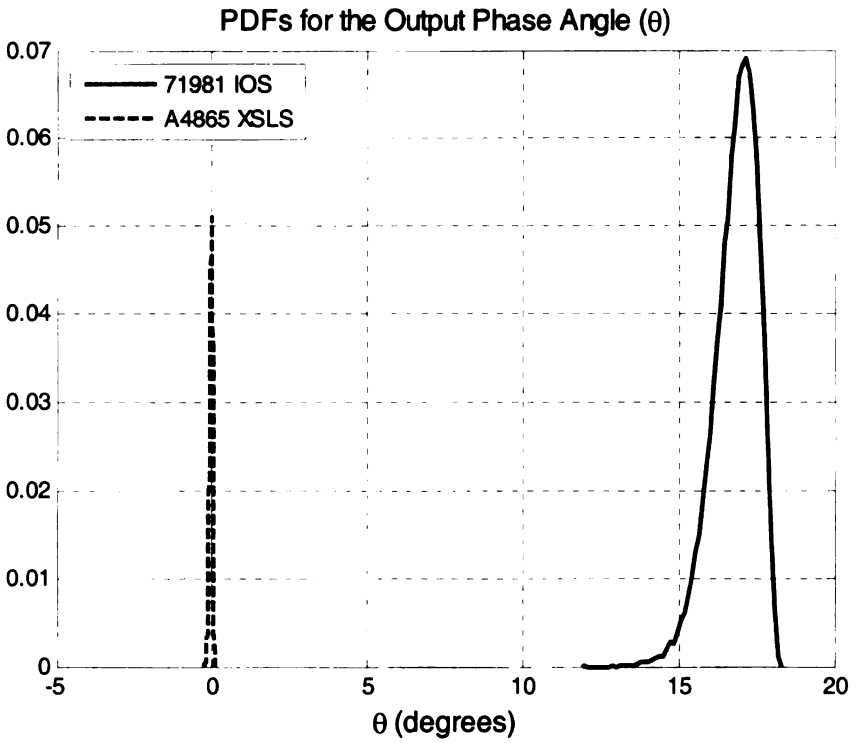

Figure 9.12 PDF for θ_{IOS} (solid line) and θ_{SLS} (dashed line), (z = 2.5 mm)

9.3.1.1 POD Curve

With the conditional probability for θ_{IOS} and θ_{SLS}, the corresponding POD and PFA are calculated using the integrals in (9.1) and (9.2) for the current the specific z. The threshold, T, obtained by fixing the PFA to 5 %, is 18.01 degrees. Note that since the two pdfs in Figure 9.12 do not overlap, the POD is 1. If the shortest distance between the gradiometer and the outlet strut plane is non-zero (i.e., an initial position of $z > 0$), the separation between the two pdfs decreases. Figure 9.13 shows the pdfs overlapping when z = 12 mm. Figure 9.14 shows a magnified view of the overlapped region between the two pdfs. In this case, T is 0.0188 degrees and the corresponding POD is 1.66×10^{-5}.

Figure 9.15 shows the POD curve with respect to the initial position (shortest distance) between the gradiometer and the outlet strut. In this figure, the POD remains unity until

the gradiometer is at a distance from the outlet strut. At z > 10 mm, the phase angle of the output signal between the IOS and SLS cases become indistinguishable and the POD decreases rapidly towards zero. These results agree with the mathematical (Section 4.10), numerical (Section 5.2), and experimental results (Section 8.4) in suggesting that the gradiometer be positioned within 5 mm of the outlet strut for a heart valve examination.

The POD curve for the gradiometer-based examination system with respect to the initial position between the gradiometer and the outlet strut has been developed. The POD curve shows that the examination system is reliable when the gradiometer is placed within 5-10 mm of the outlet strut. The technique presented may be used to develop POD curves for other sources of system parameter variabilities.

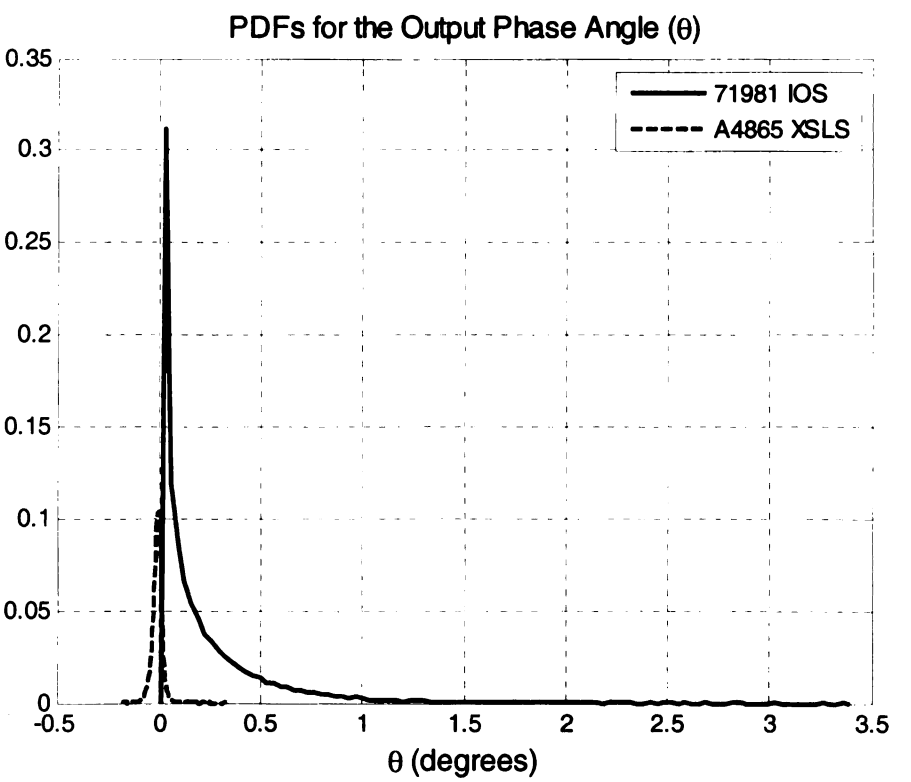

Figure 9.13 PDF for θ_{IOS} (solid line) and θ_{SLS} (dashed line), (z = 12 mm)

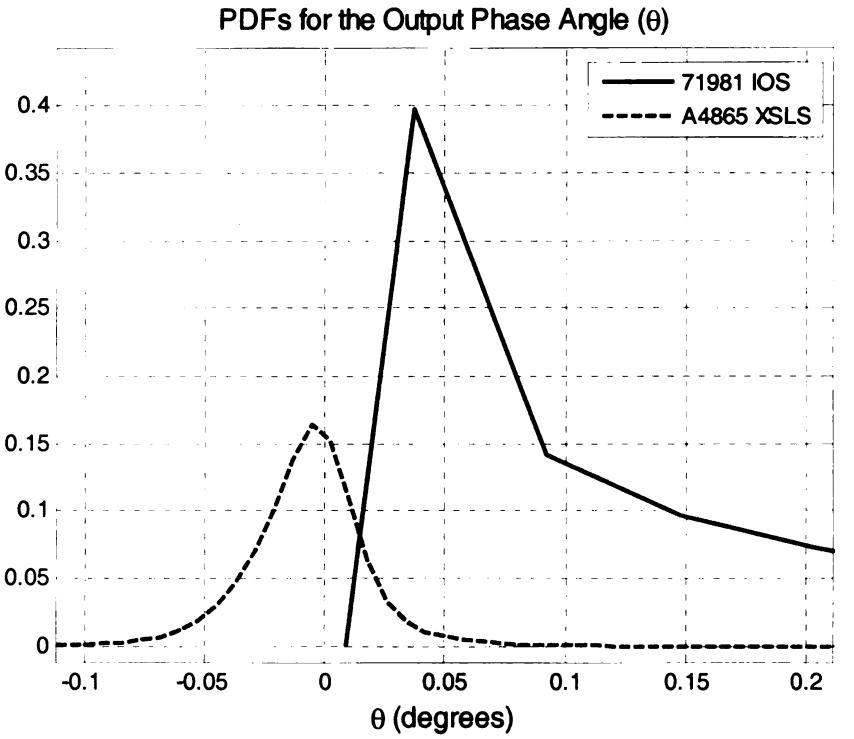

Figure 9.14 Magnified view of the overlapped region between the two output phase angle pdfs (z = 12 mm)

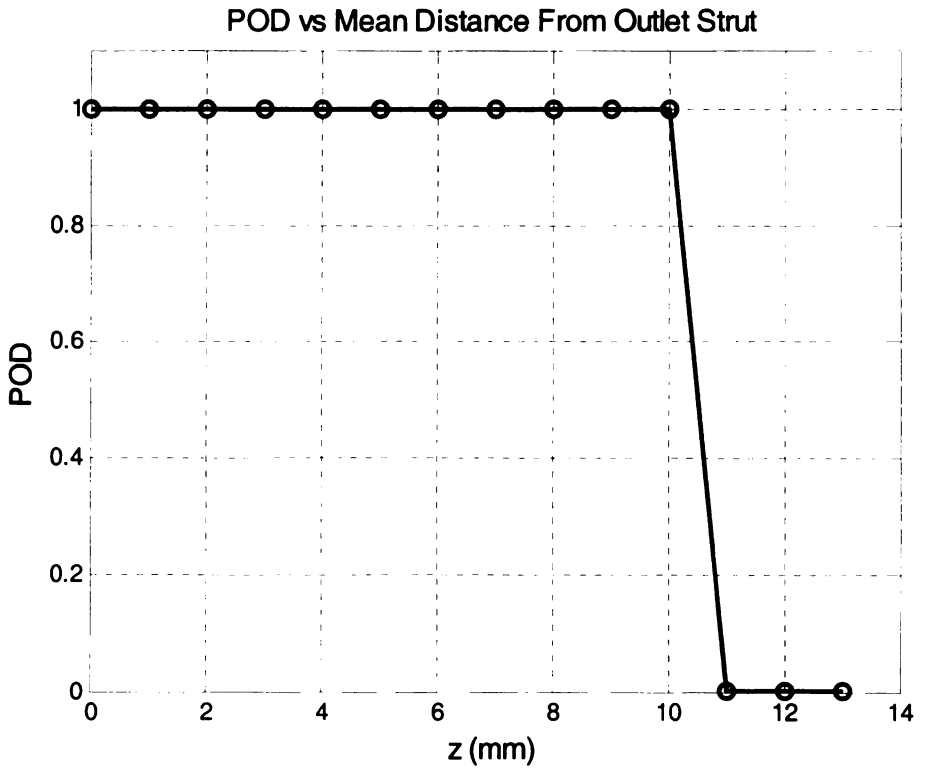

Figure 9.15 POD with respect to the distance between the gradiometer and outlet strut

CHAPTER 10. SIMULATION OF INDUCTIVE HEATING EFFECTS

A radio frequency (RF) radiation source induces electric charges or currents in nearby conducting objects. In the gradiometer-based method, the excitation field induces currents in the flange and struts of the BSCC heart valve, resulting in resistive (joule) heating of the metallic parts. This heating process is also known as inductive heating. The rise in the heart valve temperature and the surrounding environment such as the suture ring and the myocardium under RF tone-burst excitation was previously studied using finite element analysis and reported in [155]. In this chapter, we present a similar model to investigate the temperature rise under continuous wave excitation for the gradiometer-based method under two conditions. In the first case, the model takes into consideration the temperature-regulating effect of blood circulation around the prosthetic heart valve as well as the heat conduction from the heart valve into the suture ring and the myocardium. In the second case, the hypothetical situation where no convective or conductive heat loss occurs from the heart valve into its surrounding environment is examined. This scenario provides an estimate on the worst-case temperature rise of the prosthetic heart valve due to inductive heating. Effects of medium and long duration excitation (3 and 15 minutes, respectively) are also investigated. The results of these studies show that the temperature rise of the heart valve due to excitation by the gradiometer-based examination system is negligible, and that the system is safe for patient use.

10.1 Model Formulation

To determine the time-varying temperature, T, of the prosthetic heart valve, a variation of the Pennes' [156], [157] bioheat equation is used. In Pennes' formulation, the thermal energy balance for perfused tissue is expressed as:

$$\rho C_p \frac{\partial T}{\partial t} - k\nabla^2 T = Q + q_m + q_b \tag{10.1}$$

where

$$q_b = V\rho_b C_b (T_b - T) \tag{10.2}$$

and

ρ: density (kg/m^3),

C_p: specific heat capacity (J/(kg·°C)),

k: thermal conductivity (W/(m·°C)),

Q: power density from inductive heating (W/m^3),

q_m: metabolic heat production rate per unit volume (W/m^3),

q_b: arterial-tissue heat transfer rate per unit volume (W/m^3),

V: perfusion rate per unit volume (s^{-1}),

ρ_b: density of blood (kg/m^3),

C_b: specific heat capacity of blood (J/(kg·°C)),

T_b: arterial blood temperature (°C), assumed as core temperature (37 °C).

The power density from inductive heating, Q, is given by

$$Q = \frac{1}{2}\sigma|\mathbf{E}|^2 \tag{10.3}$$

where σ is the electrical conductivity (S/m). The electric field intensity, **E,** (V/m) is governed by the time-harmonic equation

$$\left(j\omega\sigma - \omega^2\varepsilon\right)\mathbf{E} + \nabla\times\left(\frac{1}{\mu}\nabla\times\mathbf{E}\right) = -j\omega\mathbf{J} \tag{10.4}$$

In (10.4), $\omega=2\pi f$ is the angular frequency (rad/s) associated with the excitation frequency, f (Hz), ε is the permittivity (F/m) and μ is the permeability (N/A^2). The external current density $\mathbf{J}$ (A/m^2) is related to the externally applied magnetic flux density, $\mathbf{B}$ (T), as $\mathbf{J} = \frac{1}{\mu}(\nabla\times\mathbf{B})$.

In the model formulation, the metabolic heat production process, q_m, in (10.1) is neglected as it is small compared to Q, the energy generated from inductive heating. The arterial-tissue heat transfer process, q_b, between the perfused blood and the myocardium and that with the body muscle are also neglected as the temperature regulation of the prosthetic heart valve and its surrounding tissues is dominated by the circulating blood in the atrial-ventricular chamber. By ignoring the contributions from q_m and q_b, the temperature effects due to Q are also more readily observed.

The convective heat exchange process with the circulating blood is described by:

$$k\frac{\partial T}{\partial \mathbf{n}} = h_b\left(T - T_b\right) \tag{10.5}$$

where $\mathbf{n}$ is the unit vector normal to the boundary and h_b ($W/(m^2\cdot°C)$) is the convective heat transfer coefficient, or film coefficient. The temperature, T_b, of the blood entering the atrium is at the core temperature (37 °C). By substituting different values for the

thermal conductivity, k, and the convective film coefficient, h_b, the heat flux at the blood-valve and blood-myocardium boundaries may be calculated. In the numerical model, convection film coefficients listed in Table 10.1 from swine study data [158] are used.

Table 10.1 Selected convective film coefficients. After [158]

Boundary	h_b (W/(m^2·°C))	
	Circulating Blood	Stagnant Blood
Blood—Left Atrium	5700	2430
Blood—Flange Ring	6830	2355
Blood—Left Ventricle	4480	2280

With the omission of the metabolic heat generation rate, q_m, and the tissue perfusion heat exchange, q_b, terms, equation (10.1) becomes the heat equation

$$\rho C_p \frac{\partial T}{\partial t} - k\nabla^2 T = Q \tag{10.6}$$

The governing equations (10.5) and (10.6) are solved numerically to simulate the heat exchange between the prosthetic heart valve and its surrounding environment.

10.2 Model Description

In the gradiometer-based examination system, the prosthetic heart valve is aligned such that the flange plane is parallel to the direction of the applied field. This orientation causes the currents induced in the outlet strut to dominate over those induced in the flange. In the worst-case scenario, the heart valve may be positioned such that the flange

plane is orthogonal to the direction of the applied field. In this orientation, the maximum amount of eddy current is induced in the flange, resulting in the largest temperature rise of the valve due to inductive heating. This worst-case scenario is investigated to ensure patient safety.

A two-dimensional axisymmetric finite element model of an implanted BSCC heart valve is shown in Figure 10.1. In this figure, the vertical line at the center is the axis of symmetry. The outer-most layer represents the (generic) body muscle. The middle layer is cardiac muscle, and the inner-most atrial-ventricular chamber is filled with "circulating" blood. Figure 10.2 shows the model of the heart and the BSCC heart valve flange ring. The inside surface of the flange is in contact with the atrial and ventricular blood in the respective chamber. The outside surface of the flange is in contact with the woven Teflon fabric suture ring, which in turn is in contact with the myocardium. The dimensions and configuration of the flange and suture rings are given in Figure 10.3. Note that the inlet and outlet struts, as well as the occluder disc, have been excluded from the model to reduce computational complexity.

A uniform magnetic field with peak-to-peak amplitude of B_0 and frequency f is applied along the vertical (z) direction. To apply this field, a circumferential surface current, $J_{S\varphi}$, is imposed along the outside boundary of the body muscle such that

$$-\mathbf{n}_S \times \mathbf{H} = J_{S\varphi} \tag{10.7}$$

where $\mathbf{n}_S$ is the unit vector normal to the surface of the body muscle.

The core temperature of the model is set at $T_0 = 310$ K (37 °C). The outer boundary of the body muscle is set at a constant temperature of $T = T_0$, as is the upper boundary of the atrium (where the blood "enters"). The systole and diastole durations are set at 0.3 s and 0.5 s, respectively, corresponding to a heart rate of 75 beats per minute. The material properties of the flange ring (HAYNES® 25 alloy) are obtained from [159], the suture ring (woven Teflon fabric) from [160], and those for the blood and cardiac and body muscles are from [161] and [162]. The data is summarized in Table 10.2. The material properties of interest are the density, specific heat coefficient, permeability and the electrical and thermal conductivities.

Table 10.2 Material properties used in the finite element model. After [159]-[162]

	$\rho\left(\frac{kg}{m^3}\right)$	$k\left(\frac{W}{m\cdot°C}\right)$	$C_p\left(\frac{J}{kg\cdot°C}\right)$	$\sigma\left(\frac{S}{m}\right)$	$\varepsilon\left(\frac{F}{m}\right)$
Flange Ring	9130	9.4	385	1123600	1
Suture Ring	2160	0.25	1400	0	2.1
Blood	1000	0.627	4178	0.67	2740
Cardiac Muscle (myocardium)	1070	0.59	3500	0.5	50000
Body Muscle (Generic)	1050	0.5	3600	0.575	26050

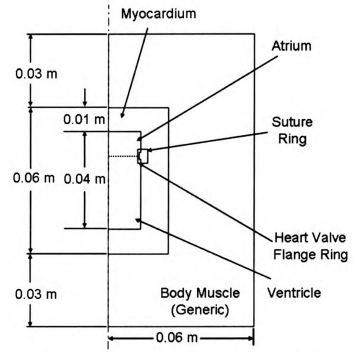

Figure 10.1 Geometry of the axisymmetric finite element model. The vertical line at the center is the axis of symmetry. (See Figure 10.2 and Figure 10.3 for more details.)

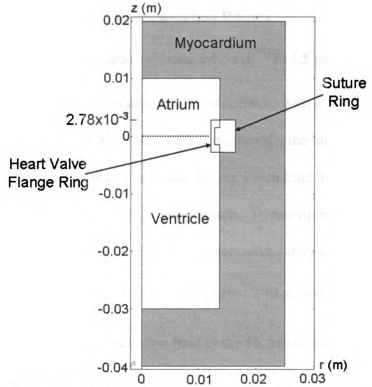

Figure 10.2 Configuration and dimensions of the heart and the heart valve flange ring at the center of the finite element model.

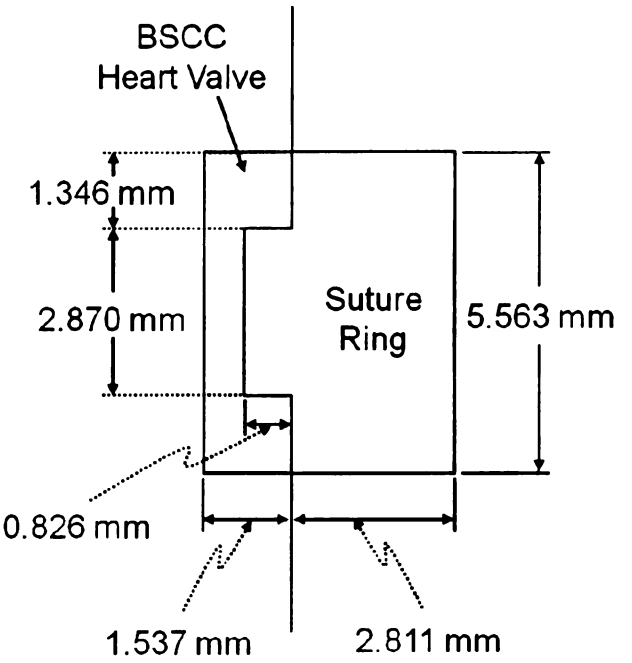

Figure 10.3 Cross-sectional dimensions of the flange and suture rings used in the finite element model.

10.3 Simulation Results

In the gradiometer-based examination system, a 1.5×10^{-4} T (1.5 gauss) excitation field is applied to the BSCC heart valve in intervals of 90 seconds, with a maximum of six intervals per examination. Between the excitation intervals, the magnetic field is removed for a period of more than 5 minutes, during which time the heart valve and the surrounding structures return to the core temperature. To determine the temperature variations of the prosthetic heart valve with a conservative safety margin, a sinusoidal magnetic field of frequency $f = 62.5$ kHz and a 2×10^{-4} T (2 gauss) peak-to-peak amplitude (B_0) is applied as the excitation field in the FE model simulation. The maximum temperature elevation over 3 and 15 minutes of continuous exposure are examined. Also, two special cases are investigated to study the heating effects of the

prosthetic heart valve and the surrounding structures: (1) Model with conduction and radiation; (2) Model with radiation but no convection or conduction. In the first case, blood circulation is stopped in the model and the blood in the atrial-ventricular chamber becomes stationary. This essentially removes the convection cooling of the prosthetic heart valve and myocardium. This arrangement allows the study of conduction and radiation heating of the tissue, as well as the heating of any stagnated blood within the heart. In the second case, both the convection and conduction cooling of the prosthetic heart valve and its neighboring structures are eliminated. This presents the worst case scenario in which the temperature of the prosthetic heart valve continues to rise due to inductive heating and the lack of heat dissipation except via thermal radiation to the surrounding structures. The results of these two studies are presented later in this chapter.

10.3.1 Maximum Temperature Increase After Three Minutes of Exposure

Figure 10.4 shows the spatial temperature elevation ($\Delta T = T - T_0$) profile of the model after 180 seconds of continuous excitation. The time step interval is 0.01 seconds and the measurement unit is Kelvin. The background "dark" areas of this figure represent regions with $\Delta T = 0$. The "highlighted" area around the heart valve shows the temperature elevation due to the heating of the prosthetic heart valve. A magnified view of this region is shown in Figure 10.5. In this figure, localized temperature elevations are visible around the outer "rims" of the flange ring. Figure 10.6 shows a close-up view of this heart valve region. In this figure, the location with the highest instantaneous

temperature (T_{max} = 310.002953 K) at t = 180 s is also indicated. The maximum temperature rise at this point is $\Delta T = 2.953 \times 10^{-3}$ degrees.

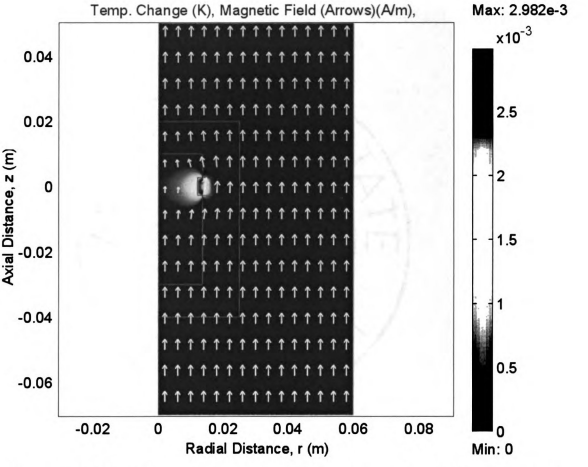

Figure 10.4 Finite element analysis results showing the spatial temperature elevation profile of the BSCC heart valve, suture ring and the surrounding biological materials after 180 seconds of continuous excitation.

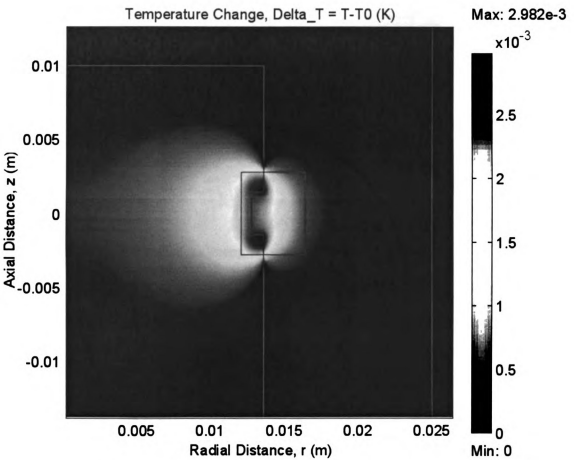

Figure 10.5 Finite element analysis results at t = 180 s showing localized temperature elevations around the outer "rim" of the flange ring.

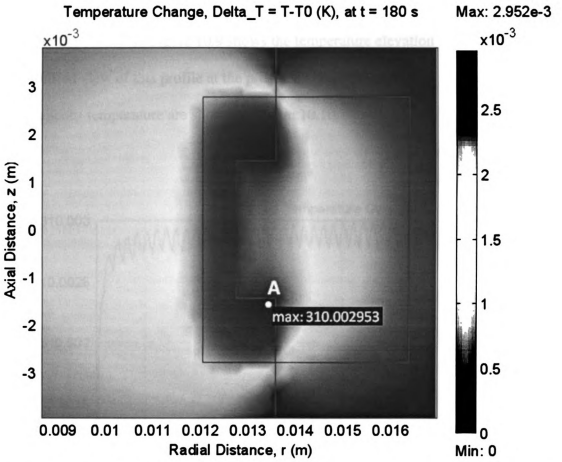

Figure 10.6 Magnified view of the temperature elevation profile on the BSCC heart valve at t = 180 s. The location of the peak instantaneous temperature (T_{max} = 310.002953 K) is as indicated.

Figure 10.7 shows the temperature variations of the heart valve over 180 seconds of exposure at point "A" of the peak instantaneous temperature as indicated in Figure 10.6. The results in this figure show that the valve temperature varies cyclically over time due to the effects of inductive heating and cooling from the perfusion of "cooler" blood into the atrial-ventricular chamber. The upper envelope of the temperature function peaks at a value just below 310.003 K. Figure 10.8 shows the temperature variations from t = 171-180 s. From this figure, the last temperature peak for the 180-second simulation occurs at t = 177 s, with a maximum temperature of T_{max} = 310.002983 K ($\Delta T = 2.983 \times 10^{-3}$ K).

This indicates that the maximum temperature elevation profile does not occur at t = 180 s, but rather, at t = 177 s. Figure 10.9 shows the temperature elevation profile at t = 177 s. A magnified view of this profile at the prosthetic heart valve and the point of highest instantaneous temperature are shown in Figure 10.10.

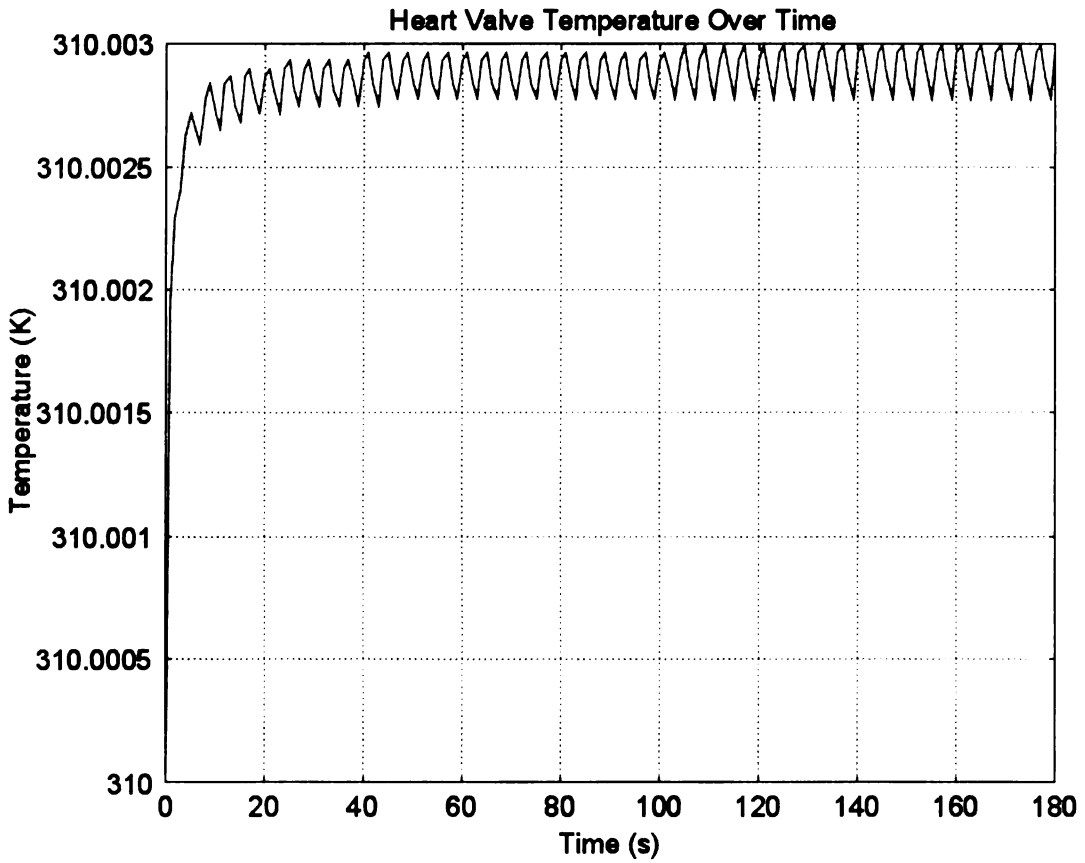

Figure 10.7 Finite element analysis results showing the BSCC heart valve temperature over 180 seconds of exposure to the gradiometer-based examination system (observed at the peak temperature point as indicated in Figure 10.6).

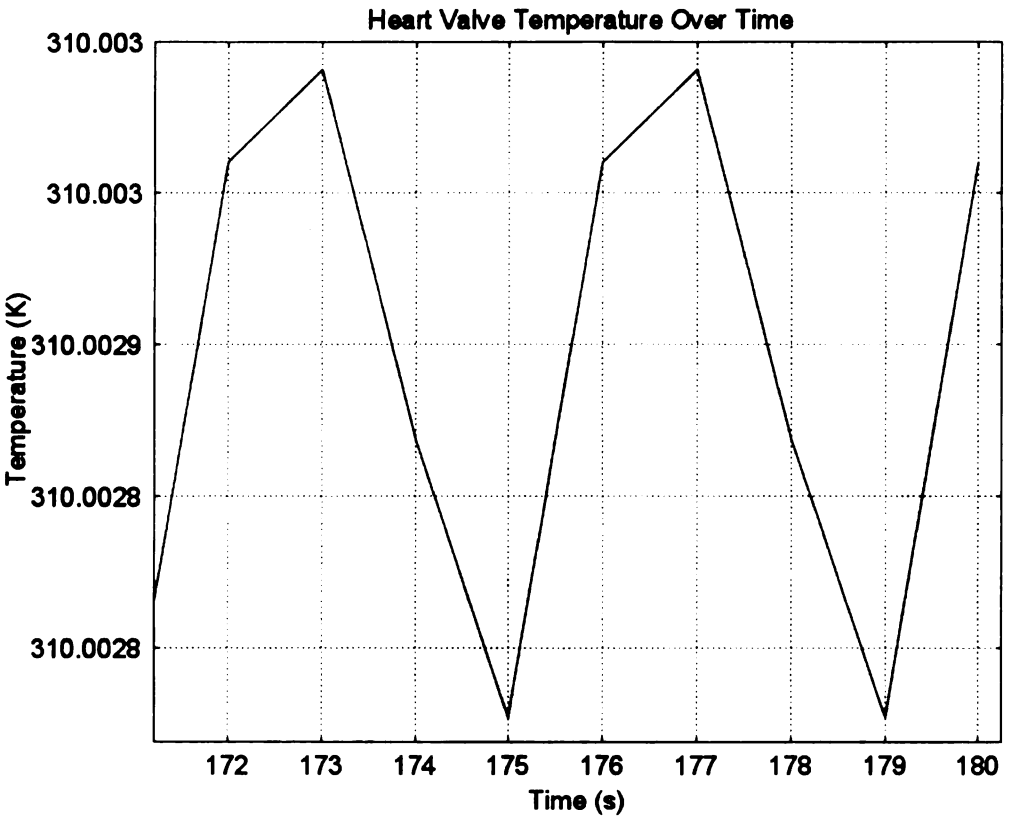

Figure 10.8 Finite element analysis results showing the last temperature peak in a 180-second simulation at t = 177 s, with T_{max} = 310.002983 K.

Results from Figure 10.4-Figure 10.10 show that the maximum temperature rise is limited to $\Delta T = 2.983 \times 10^{-3}$ K (T_{max} = 310.002983 K) after 3 minutes of exposure to the excitation field. Furthermore, there is no temperature rise in the tissue regions outside of the heart (myocardium).

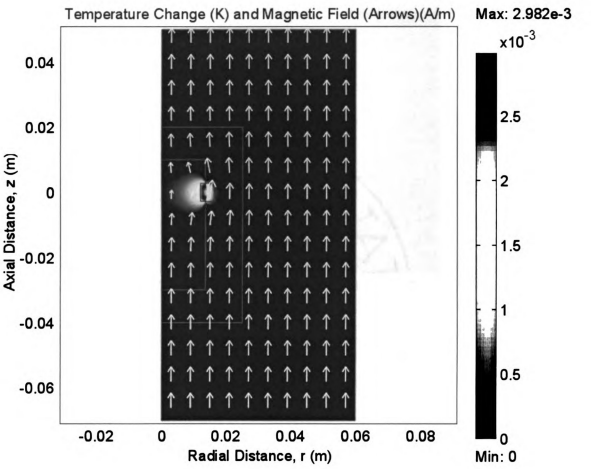

Figure 10.9 Spatial temperature elevation profile of the BSCC heart valve, suture ring and the surrounding biological materials after 177 seconds of continuous excitation.

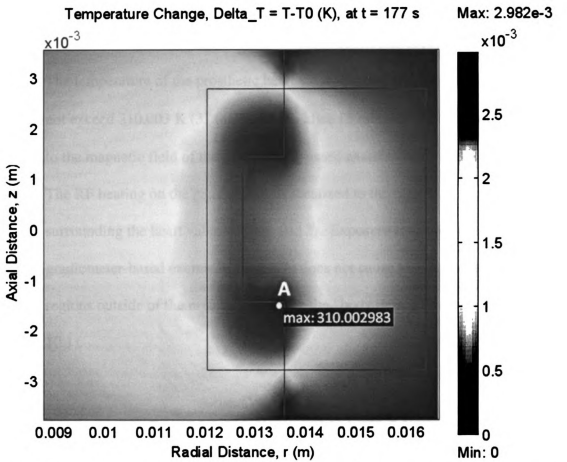

Figure 10.10 Magnified view of the spatial temperature elevation profile on the BSCC heart valve at t = 177 s. The point in the figure indicates the location of the peak instantaneous temperature (T_{max} = 310.002983 K).

10.3.2 Maximum Temperature Increase After Fifteen Minutes of Exposure

Figure 10.11 shows the temperature variation of the BSCC heart valve flange ring (observed at the peak temperature point indicated in Figure 10.6) over 15 minutes of exposure to the excitation field. In this case, the valve temperature reaches T_{max} = 310.00296 K ($\Delta T = 2.959 \times 10^{-3}$ K). The corresponding temperature elevation profile at t = 900 s is shown in Figure 10.12. A magnified view of this profile for the heart valve

and the neighboring structures is shown in Figure 10.13. The results from these figures suggest:

1. The temperature of the prosthetic heart valve and the surrounding structures do not exceed 310.003 K (37.003 °C) even after 15 minutes of continuous exposure to the magnetic field of the gradiometer-based examination system.
2. The RF heating on the patient body is localized to the regions immediately surrounding the heart valve (Figure 10.12). Exposure to the RF energy from the gradiometer-based examination system does not cause any temperature rise in regions outside of the myocardium (e.g., the "body muscle" region in Figure 10.1).

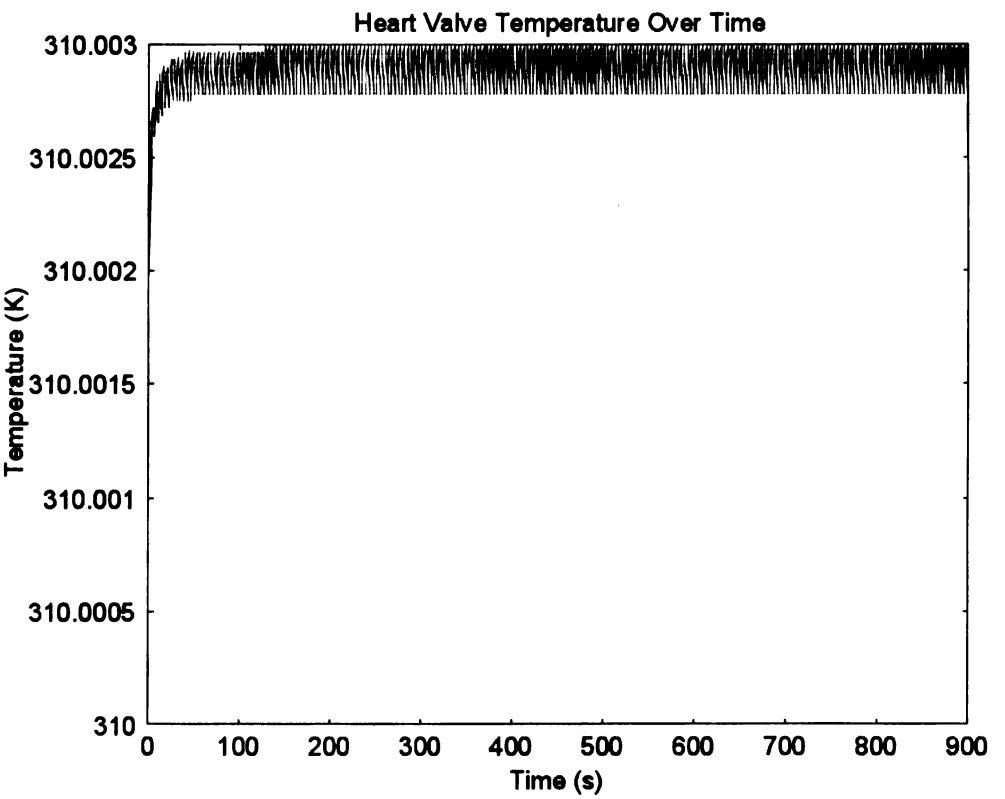

Figure 10.11 Finite element analysis results showing the BSCC heart valve temperature (observed at the peak temperature point indicated in Figure 10.6) over 15 minutes of exposure to the excitation magnetic field

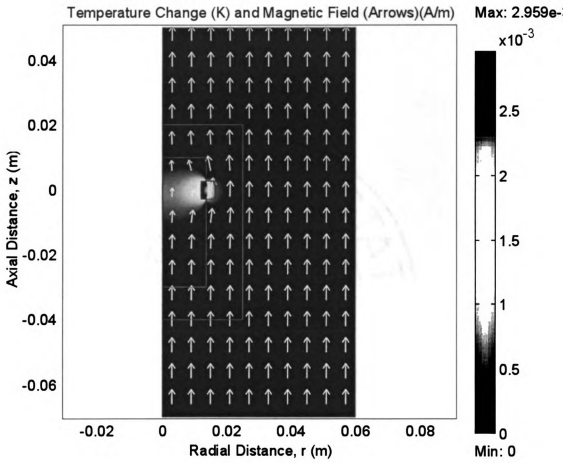

Figure 10.12 Spatial temperature elevation profile of the BSCC heart valve, suture ring and the surrounding biological materials after 900 s of continuous excitation. T_0 = 310 K.

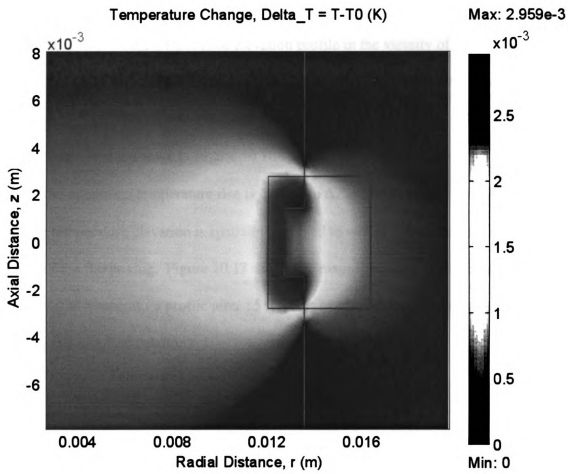

Figure 10.13 Magnified view of the spatial temperature elevation profile of the BSCC heart valve at t = 900 s. T_0 = 310 K.

10.3.3 Special Case I: Excitation Without Blood Circulation

To investigate the inductive heating of the prosthetic heart valve and the temperature increase in the neighboring regions in the absence of blood circulation, the convective film coefficients are set to zero in the finite element model (see Equation (10.5). This eliminates the convective cooling of the structures as well as the automatic blood temperature regulation in the heart. This model may also be used to describe the temperature rise of any stagnated blood pool in the heart when heated indirectly by the thermal radiation from the prosthetic heart valve which is, in turn, being induction heated.

Figure 10.14 shows the temperature elevation profile in the vicinity of the prosthetic heart valve after 15 minutes of continuous excitation. A three-dimensional view of this profile is shown in Figure 10.15, and a magnified view of the myocardium and the inner region of the body tissue is shown in Figure 10.16 . From the results in Figure 10.14-Figure 10.16, the maximum temperature rise is limited to $\Delta T = 0.0652$ K. The results also show that the temperature elevation is spatially localized to within a 4 cm-radius from the center of the flange ring. Figure 10.17 shows the magnified view of the prosthetic heart valve spatial temperature profile after 15 minutes of excitation without convection cooling (no blood circulation).

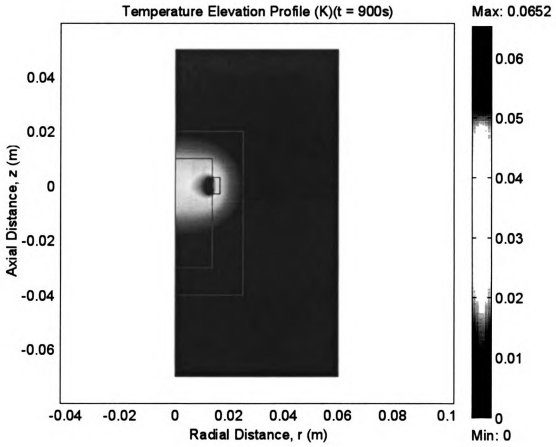

Figure 10.14 Spatial temperature elevation profile of the BSCC heart valve, suture ring and the surrounding biological materials after 15 minutes (t = 900 s) of continuous excitation without blood circulation (convective cooling).

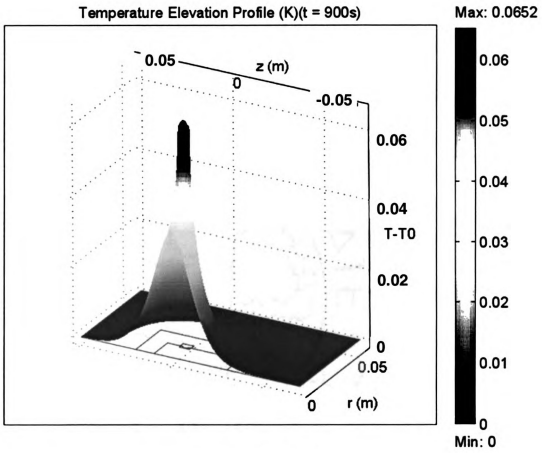

Figure 10.15 Three dimensional view of the profile from Figure 10.14.

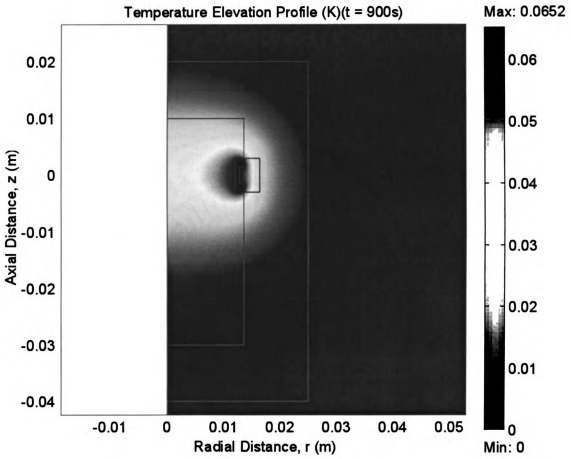

Figure 10.16 Temperature elevation from inductive heating (with no blood flow) is spatially localized to a region of 4 cm radius from the center of the flange ring.

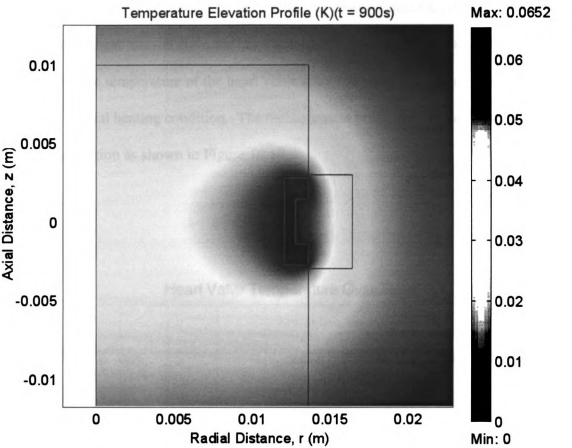

Figure 10.17 Magnified view of the spatial temperature elevation profile of the BSCC heart valve at $t = 900$ s with no convection cooling. The peak of the instantaneous temperature is located at the center of the heart valve cross-section. The maximum temperature rise is $\Delta T = 0.0652$ K. ($T_0 = 310$ K).

10.3.4 Special Case II: Excitation without Convection and Conduction Cooling

In this case, a hypothetical scenario was considered and the temperature rise of the heart valve and the body tissues from inductive heating in the absence of convective and conductive cooling was studied. The results from this study may serve as the theoretical upper bound for the temperature increase in the heart valve and the neighboring regions. In this study, the convective film coefficients for the *blood—flange ring* interface in Table 10.1 are set to zero in the finite element model. The thermal conductivity, k, values in Table 10.2 are also set to zero except that for the flange ring. This essentially

eliminates the convective cooling by the circulating blood (Equation (10.5)), as well as the conductive heat transfer from the heart valve to its surround environment. Figure 10.18 shows the temperature of the heart valve after 180 seconds of continuous excitation under this special heating condition. The measurement point, P, is at the center of the valve cross-section as shown in Figure 10.19.

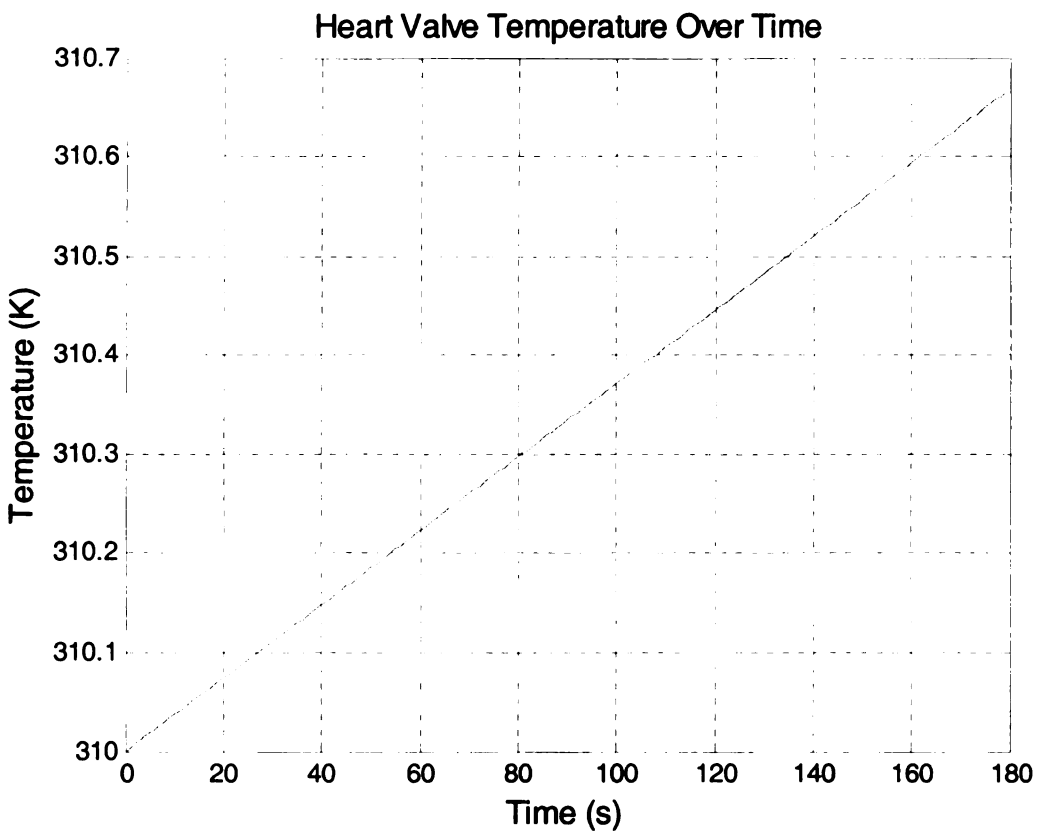

Figure 10.18 Finite element analysis results showing the BSCC heart valve temperature over 180 seconds without convective and conductive heat transfers.

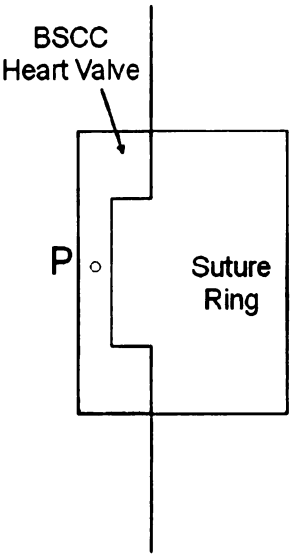

Figure 10.19 Measurement point, P, for the second special case (II) temperature study

In this figure, the valve temperature rises in an approximately linear fashion to T = 310.6682 K after 180 seconds of continuous excitation in the absence of convective and conductive cooling. Figure 10.20 shows the temperature of the heart valve after 15 minutes of exposure. In this case, the valve temperature reaches T = 313.34 K, showing an elevation of ΔT = 3.34 K. Figure 10.21 shows the temperature elevation profile of the heart valve and its surrounding structures at t = 900 s. This figure is then processed to produce Figure 10.22, which shows the temperature elevation profile for the heart valve alone. (The temperature scale to the right of this figure shows only markings of 3.341 degrees since the range variation is too small (less than 10^{-4} degrees) for proper labeling. Note that the "ripple" pattern around the flange ring in Figure 10.21 is due to the accumulation of numerical noise over 90000 calculation time steps (a 15-minute simulation duration with a time step size of 0.01 seconds). To better observe the numerical noise, the early time (t = 0.01 s) temperature profile from the finite element simulation is shown in Figure 10.23. In this figure, the temperature of the flange ring has

just begun to rise (maximum temperature rise, ΔT, is 4.21×10^{-5} degrees) and the effect of the numerical noise, though small in amplitude, is visible. Since there is no heat transfer into this region due to the lack of convection and conduction from the heart valve, the numerical noise becomes the dominant signal. The numerical noise is accumulated over time, and eventually manifests into the "ripples" seen in Figure 10.21. This numerical noise does not affect the accuracy of the simulation results for the most part, especially in the cases where heat transfer exists between the heart valve and the neighboring regions.

Figure 10.21 and Figure 10.22 show that the temperature elevations are highly localized to the prosthetic heart valve under no conduction or convection cooling. Regions outside of the heart valve show no temperature rise after 15 minutes of continuous exposure to the RF energy from the gradiometer-based examination system. This result is expected as the generated heat is mostly retained and not dissipated by conduction or conduction into the neighboring structure.

Figure 10.24 combines the results from Figure 10.11 and Figure 10.20 to show the heart valve temperature elevation over 900 seconds of continuous excitation for the normal and special (no convection and conduction) cooling cases.

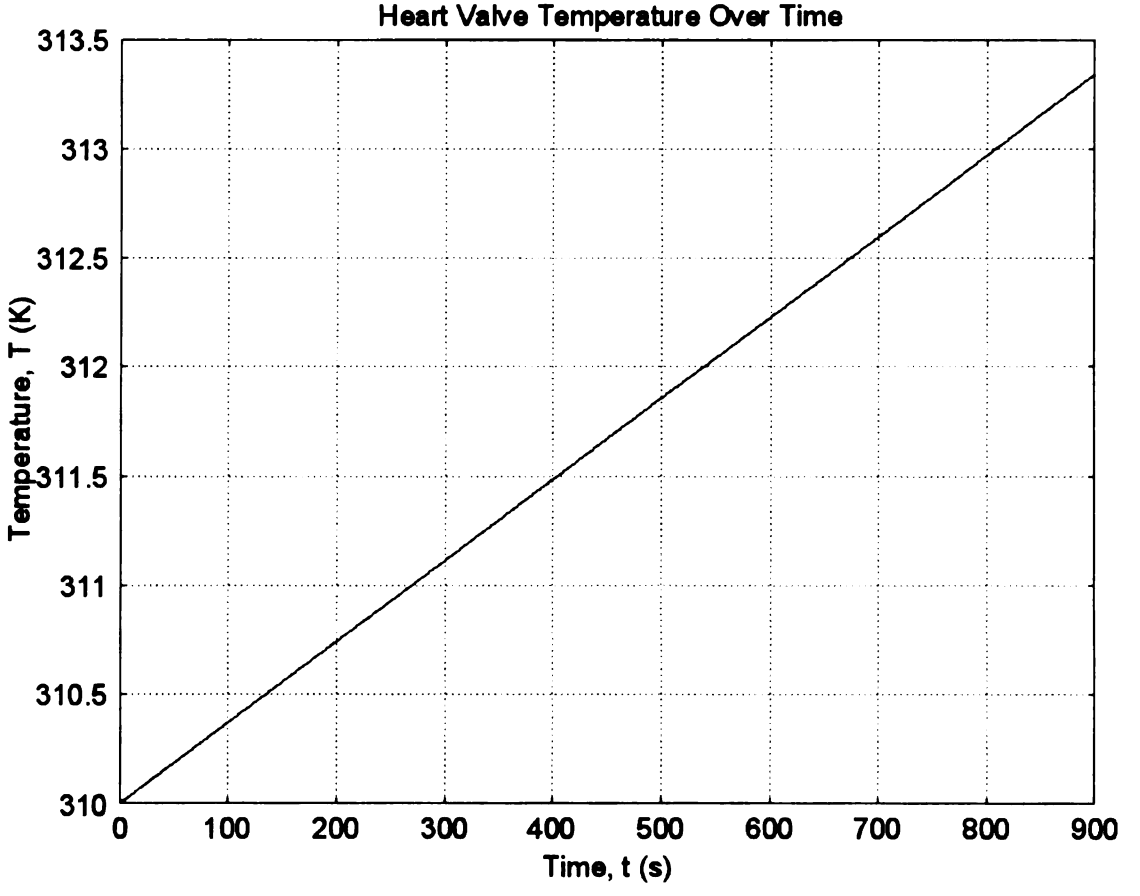

Figure 10.20 Finite element analysis results showing the BSCC heart valve temperature without convection and conduction cooling over 900 seconds of continuous exposure to the excitation magnetic field.

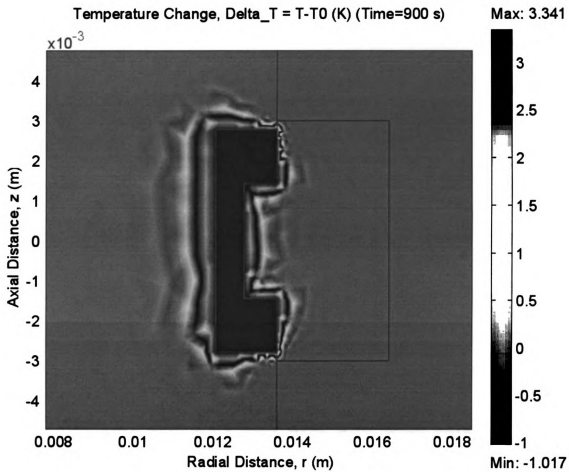

Figure 10.21 Magnified view of the spatial temperature elevation profile of the BSCC heart valve without convection and conduction cooling at $t = 900$ s. $T_0 = 310$ K.

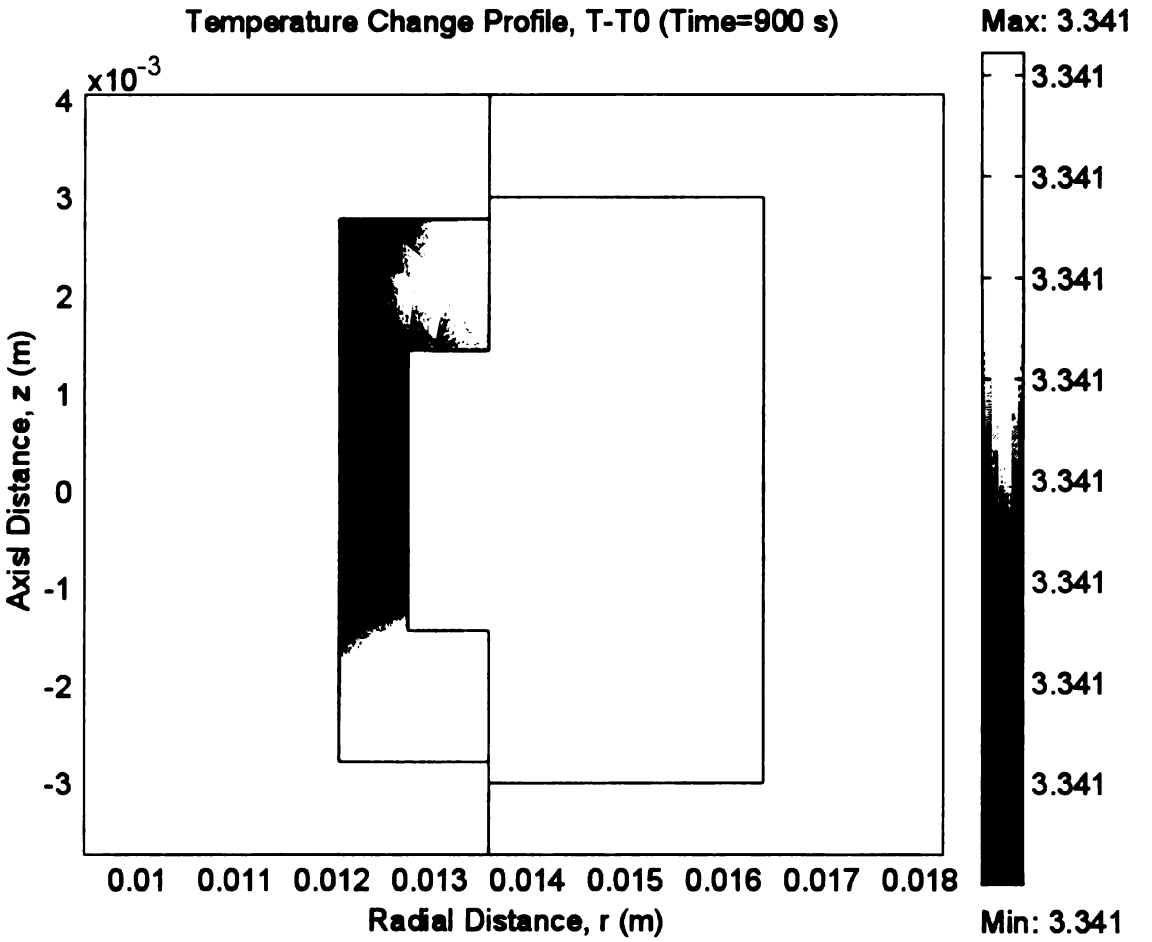

Figure 10.22 Temperature profile inside the heart valve at t = 900 s after a continuous exposure to the excitation signal without conductive and convective cooling. T_0 = 310 K. (Note that the temperature variation is too small, < 10e-4 degrees, for proper labeling of the temperature scale)

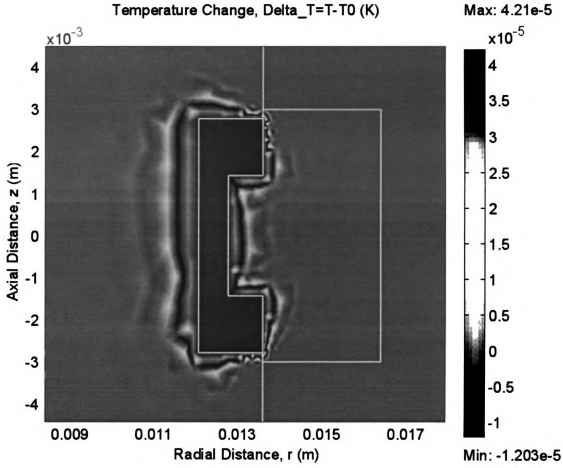

Figure 10.23 Temperature elevation profile at the beginning of the simulation ($t = 0.01$ s) showing the effects of numerical noise. The maximum temperature rise at this instance is $\Delta T = 4.21 \times 10^{-5}$ K.

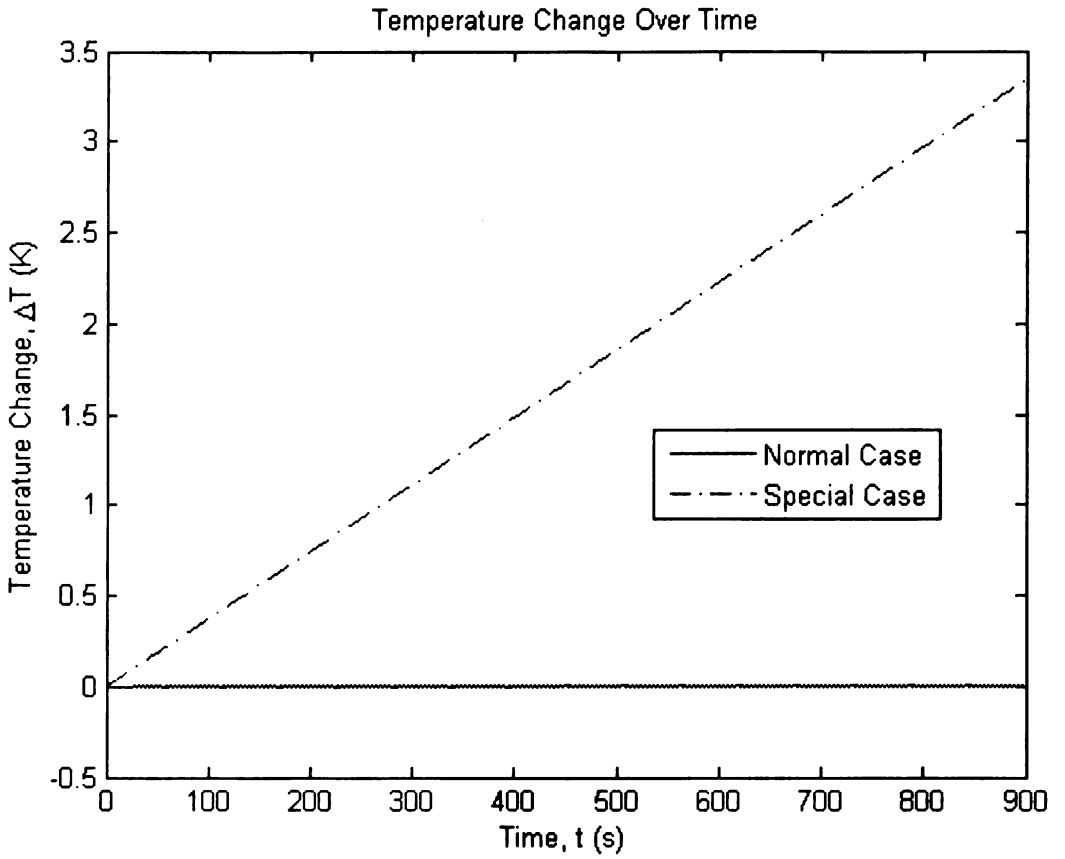

Figure 10.24 Temperature of the BSCC heart valve with normal (solid line) and special/worst case (broken line) cooling conditions over 15 minutes. $T_0 = 310$ K.

The results from Figure 10.18 and Figure 10.24 are summarized in Table 10.3. The data from this table show that, for the hypothetical worst-case scenario without convective and conductive cooling, the maximum temperature rise of the prosthetic heart valve is approximately $\Delta T = 3.3408$ degrees for 15 minutes of exposure. These results show that even in the hypothetical worst-case scenario, the maximum temperature rise after 15 minutes of exposure does not exceed 3.5 degrees. Moreover, the results from Figure 10.12 and Figure 10.21 show that there is no temperature rise in the tissues outside of the

myocardium under both normal and near-adiabatic (no convection or conduction cooling) conditions.

The data in Table 10.3 also shows that the temperature of the BSCC heart valve does not rise beyond $\Delta T = 0.003$ degrees after 15 minutes of exposure under normal heat transfer conditions. In practice, a temperature rise prediction of 0.003 degrees is close to the accuracy limit of the numerical model and should be considered negligible for all practical purposes. Moreover, in a biological system such as the human body, a temperature rise of such small magnitude is not perceivable and we do not expect any adverse effect.

The finite element analysis results presented in Table 10.3 show that induction heating of the BSCC heart valve from exposure to the excitation field of the gradiometer-based examination is negligible, and that the system is safe for patient use.

Table 10.3 Summary of maximum temperature elevations of the heart valve after 180 and 900 seconds of continuous exposure, respectively, for the normal and worst-case heat transfer scenarios.

($T_0 = 310$ K)	180 seconds (3 minutes)	900 seconds (15 minutes)
Normal cooling	0.002983 degrees	0.002959 degrees
Worst-case: without convection and conduction cooling	0.6682 degrees	3.34080 degrees

CHAPTER 11. PATIENT SAFETY AND REGULATORY COMPLIANCE

The gradiometer-based prosthetic heart valve evaluation system is an electromagnetic (EM) diagnostic system that subjects the patient to a low-level radio frequency (RF) magnetic field during the examination. To ensure patient and medical personnel safety, the operating conditions of the system had been assessed against United States and international regulatory standards and safety guidelines. This chapter describes the assessment results and demonstrates compliance of the examination system with the international health standards. The results also show that exposure to the system's EM field will not result in any adverse health effects or discomfort to the patient and the medical staff.

11.1 Health Effects of Radio Frequency EM Field Exposure

In a RF non-ionizing radiation system such as the gradiometer-based examination system, three principal effects from electric and magnetic field exposure may potentially lead to adverse effects in humans: (1) electrostimulation, (2) RF heating of the biological tissues, and (3) induction heating of metallic implants. Electrostimulation is the induction of a nerve pulse (an action potential) in excitable tissues such as nerves and muscles by an externally applied electrical stimulus. Depending on the amount of excitation, the biological effects of electrostimulation may range from minor patient annoyance to detectable impairment of normal physiological functions (e.g., the cardiac rhythm).

Radio frequency heating, or induction heating, includes the heating of the biological tissue and metallic implant due to exposure to a time-varying EM field. Such exposure induces electric fields and currents in the tissue and the metallic parts of the implant according to *Faraday's Law*. The magnitudes of the induced field and current density are proportional to the frequency of the field, rate of change of the applied magnetic flux density, $\frac{dB}{dt}$, and conductivity, σ, of the medium. The induced electric field, **E**, and current density, **J**, are related by *Ohm's Law*:

$$\mathbf{J} = \sigma \mathbf{E} \tag{11.1}$$

The flow of the induced currents causes heating of the affected region. The amount of temperature rise may be obtained by either an *in situ* measurement (if the location of interest is accessible) or solving the bioheat transfer equation (10.1) [156] for the region of interest as demonstrated in the Chapter 10.

In general, exposure to EM fields may result in an increase in body temperature due to absorption of energy. The transmitted power and signal frequency are two of the most important factors affecting absorption as they relate to the penetration depth and absorption of the RF energy below the skin surface [163]. It is, therefore, important to ensure patient safety by characterizing, monitoring and, if necessary, limiting the electromagnetic energy absorption when using a medical diagnostic device such as the gradiometer-base examination system.

11.2 Nature and Duration of EM Field Exposure in the Gradiometer-Based Examination System

During the heart valve examination, the patient assumes a supine position with the long axis of the body resting on the plane centered between the excitation coils of a Helmholtz system. The magnetic field is uniform and at its maximum value within an approximately 40 cm-diameter circular region at the center of this plane. Outside of this region, the field decreases dramatically with increasing distance as shown in Figure 11.1. This field distribution exposes a patient to a non-uniform magnetic field with a maximum exposure per unit volume at the center (around the chest area). For a worst-case approximation, an uniform magnetic field distribution is assumed throughout the entire Helmholtz coil volume (the compliance volume) with a field strength equal to the maximum value obtained at center of the coils. Note that the actual patient exposure to the magnetic field is significantly less that this conservatively estimated value.

The gradiometer-based examination system produces a maximum peak-to-peak magnetic flux density of approximately 1.5 gauss at an excitation frequency of approximately 65 kHz. During the examination, the excitation field is first applied when the gradiometer is placed approximately 10 cm away from the heart valve. At this location, a reference signal is recorded for approximately 30 seconds. The field is then removed and the gradiometer is advanced into the mitral annulus and placed in front of the outlet strut.

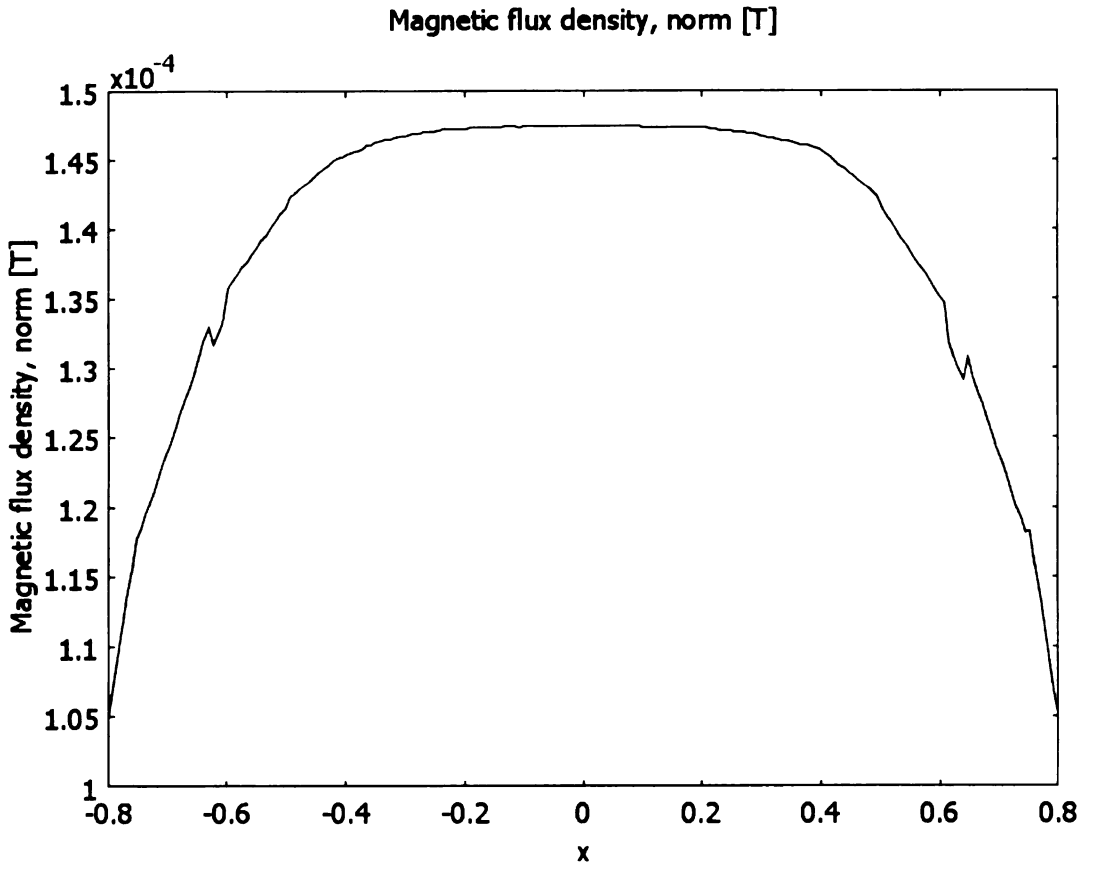

Figure 11.1 Amplitude of the magnetic flux density is the largest at the center of the plane positioned mid-way between the two excitation coils.

After the gradiometer is properly-positioned, the excitation field is re-applied. The gradiometer signal is then recorded for 60-90 seconds before the field is once again removed. Depending on the fidelity of the recorded signal, the gradiometer may be repositioned (and its signal recorded) up to five times during the examination. Each gradiometer repositioning may take up to 5 minutes.

11.3 Specific Absorption Rate

The specific absorption rate, SAR (W/kg), is the radio frequency power absorbed per unit mass of an object:

$$SAR = \frac{d}{dt}\left(\frac{dW}{dm}\right) = \frac{d}{dt}\left(\frac{dW}{\rho dV}\right) \tag{11.2}$$

where W (J) is the energy absorbed, m (kg) is the mass, V (m^3) is the volume, and ρ (kg/m^3) is the density of the object. When applying to human, the SAR describes the amount of energy absorbed per unit mass of the affected tissue, organ, or body region.

The SAR can also be related to the electric field at a point by

$$SAR = \frac{\sigma |E_{RMS}|^2}{\rho} \tag{11.3}$$

where σ is the conductivity (S/m) and E_{RMS} is the RMS electric field strength (V/m) of the tissue.

Alternatively, the SAR can be related to the increase in temperature at a point by

$$SAR = \frac{c\Delta T}{\Delta t}\Big|_{t=0} \tag{11.4}$$

where ΔT is the change in temperature (°C), Δt is the duration of exposure (s), and c is the specific heart capacity (J/(kg °C)). Note that (11.4) is valid only under adiabatic conditions (non-thermodynamic circumstances) with no heat loss by thermal diffusion, radiation, convection, or other natural bio-thermoregulation processes (blood flow, sweating, etc.).

11.4 Specific Absorption Rate Calculation

The SAR of the RF energy from the gradiometer-based examination system by the various body parts had been evaluated to assure patient safety. The induction heating finite element analysis (FEA) results from Chapter 9 were used to calculate the myocardial, whole body and local SARs. Additionally, the whole body average (WBA) SAR had been estimated using two different approaches. In the first approach, the induced electric field due to the RF exposure was obtained from the finite element model and applied to (11.3). In the second approach, the WBA SAR was calculated directly from the FEA results. These SARs were then compared against the regulatory standards and guidelines to assess compliance.

11.4.1 SAR Inference from Derived Electric Field Strength

Equation (11.3) may be used for estimating the SAR in cases where other, perhaps more direct, means of obtaining this value do not exist [166]. When applying this equation to estimate the WBA SAR, a homogenous body conductivity of 0.2 S/m [172] and density of 1000 kg/m^3 may be used. The IEEE standard recommends averaging over a distance of 5 mm to obtain the magnitude of the RMS electric field strength, $|E_{RMS}|$. For compliance determination, the SAR value is averaged over 6 minutes [166], [172] of exposure.

To obtain the 5-mm average of the electric field in the vicinity of the prosthetic heart valve, the magnitude of the field is averaged over 6 minutes[1] along a radial path, L_E, near the outer boundary of the myocardium (from r = 0.0549 to 0.0599 m, at z = 0 m) as shown in Figure 11.2. The magnitude of the electric field along this path is shown in Figure 11.3. The data in this figure shows that the induced electric field is stronger towards the exterior of the body muscle (perimeter of the body). This observation may be extended to the full-body exposure case where the near-surface regions of the body experience most exposure to the EM energy. As a result, more heat is generated in the perimeter than the core regions of the body. In general, the RF energy penetration below the skin surface is a function of frequency and the characteristics of the skin and underlying tissues.

From the FEA results, the average value of the electric field along L_E was $E_{avg} = 1.12$ V/m, and the corresponding RMS value was $E_{RMS} = 0.792$ V/m. Substituting E_{RMS} into (11.3) yields

$$SAR_{\mathrm{WBA}} = \frac{0.2(0.792)^2}{1000} = 1.24\times10^{-4} \quad \text{(W/kg)} \tag{11.5}$$

The IEEE standard [163] accepts the WBA SAR estimate obtained using equation (11.5) for the purpose of compliance assessment. To obtain region-specific SARs, the finite

[1] For the SAR calculations, the 6-minute time-average window is selected from t = 540-900 s from the finite element analysis results.

element analysis results from Chapter 10 are used. These SAR calculations are described in the following sections.

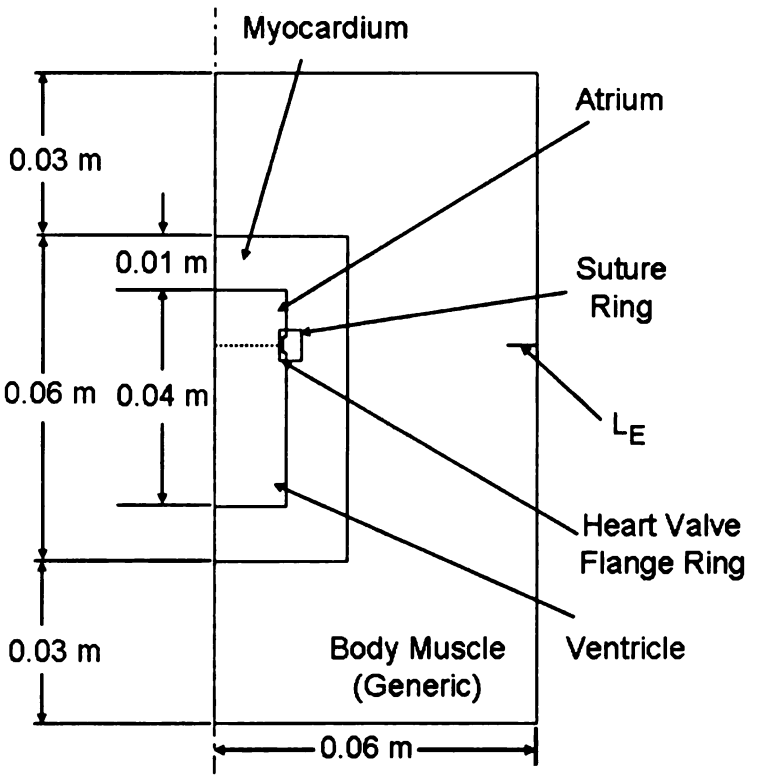

Figure 11.2 The average value of the electric field intensity, E, along path L_E is used for SAR calculation.

11.4.2 Region-Specific SAR Calculations

11.4.2.1 SAR for the myocardium

To calculate the 6-minute average of the total power absorbed by the myocardium, the inductive heating power density, Q, is integrated over the volume of the myocardium and averaged over time.

Table 11.1 lists the FE model parameters that are pertinent to the SAR calculations.

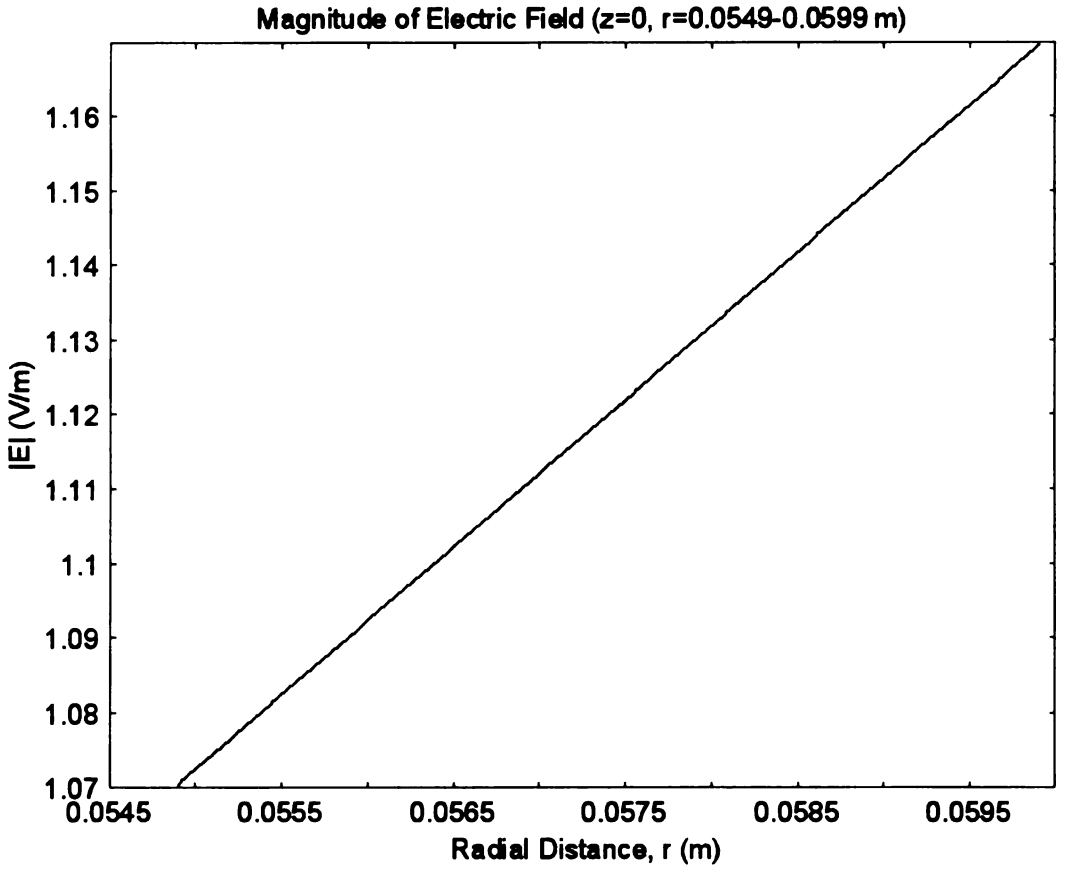

Figure 11.3 The magnitude of the electric field, $|E|$, along path L_E (z=0, r= 0.0549-0.0599 m) for the finite element model in Figure 11.2.

From the FEA results, the total power absorbed is $P_{my} = Q(\text{myocardium}) = 2.9654\times10^{-6}$ W. The volume of the myocardium is approximately $V_{my} = 9.31\times10^{-5}$ m^3, with a density $\rho_{my} = 1070$ kg/m^3 (Table 10.2). Using (11.2), the SAR for the myocardium is

$$SAR_{my} = \frac{P_{my}}{\rho_{my} V_{my}}$$
$$= \frac{2.9654\times10^{-6}}{(1070)(9.31\times10^{-5})}$$
$$= 2.9768\times10^{-5} \quad \text{(W/kg)} \qquad (11.6)$$

Table 11.1 Selected results from the RF inductive heating FEA from Chapter 9

Quantity	Myocardium	Body muscle
Volume, V	9.3131×10^{-5} m^3	1.239×10^{-3} m^3
Total power absorbed, Q	2.9654×10^{-6} W	2.6307×10^{-4} W
Total current density, J	0.144898×10^{-3} A/m^2	2.235×10^{-3} A/m^2

11.4.2.2 Whole Body Average SAR

To obtain the whole body average (WBA) SAR, the total power dissipated in the "body muscle" region of the finite element model was calculated. From Table 11.1, the total power is $P_{bm} = Q$(body muscle) $= 2.6307\times10^{-4}$ W, and the volume of the region was $V_{bm} = 0.001239$ m^3. The power density dissipated in, or absorbed by, the "body muscle" region is then given by:

$$\begin{aligned} Q_{body} &= \frac{P_{bm}}{V_{bm}} \\ &= \frac{2.6307\times10^{-4}}{0.001239} \\ &= 0.21233 \quad (\text{W/ m}^3) \end{aligned} \tag{11.7}$$

For the worst-case scenario where the entire body is exposed to this power density, with an average body density [172] of $\rho_{body} = W_{body} / V_{body} = 1025$ kg/ m^3, the worst-case WBA SAR is given by:

$$SAR_{\mathrm{WBA}} = \frac{P_{bm}}{V_{bm}} \cdot V_{body} \cdot \frac{1}{W_{body}}$$
$$= \frac{Q_{body}}{\rho_{body}}$$
$$= \frac{0.21233}{1025}$$
$$= 2.0715 \times 10^{-4} \qquad \text{(W/ kg)} \qquad (11.8)$$

where W_{body} is the full body weight of the patient. The WBA SARs from equations (11.5) and (11.8) agree in their orders of magnitude, with the later value approximately 1.6 times the former. These results show that equation (11.5), when used with the whole body averaged conductivity and density values, provides a convenient estimate of the SAR and is sufficient for compliancy assessment.

11.4.2.3 Local SAR

The IEEE and IEC standards specify that the power dissipated in a 10-gram mass (defined as a tissue volume of 10 cm^3 in the shape of a cube) is to be used for calculating the local SAR. From (11.7), the power density dissipated in the "body muscle" region is $Q_{body} = 0.21233$ W/m^3. If $V_{local} = 10\ \mathrm{cm}^3 = 10 \times 10^{-6}\ \mathrm{m}^3$, $W_{local} = 10$ g $= 0.01$ kg, the local SAR is then given by

$$SAR_{local} = Q_{body} \cdot V_{local} \cdot \frac{1}{W_{local}}$$
$$= (0.21233)\left(10 \times 10^{-6}\right)\frac{1}{0.01}$$
$$= 2.1233 \times 10^{-4} \qquad \text{(W/ kg)} \qquad (11.9)$$

The myocardial, whole body, and local SARs from (11.6), (11.8), and (11.9), respectively, are used to access the safety of the examination system in the following sections.

11.5 Applicable Regulatory Standards and Guidelines

The excitation energy level and patient exposure conditions of the gradiometer-based examination system had been assessed against the IEEE[1] ([163]-[166]) and IEC[2] ([167]-171]) standards, as well as the ICNIRP[3] ([172]) and FDA[4] ([173]-[175]) guidelines, to ensure patient and medical personnel safety.

11.5.1 The IEEE Standard (IEEE Std C95.1-2005)

The IEEE Std C95.1-2005 [163] standard recognizes that exposure to different frequency RF energies result in differing impacts. Therefore, it provides exposure restrictions called *basic restrictions* (BRs) to address three distinct frequency bands. The BRs are expressed in terms of the *in situ* electric field (3 kHz to 5 MHz), specific absorption rate (100 kHz to 3 GHz), or the incident power density (3 GHz to 300 GHz). In cases where values of the physical quantities are difficult or impossible to ascertain, the standard also

---

[1] IEEE: Institute of Electrical and Electronics Engineers, Incorporated (www.ieee.org).

[2] IEC: Commission Electrotechnique Internationale (International Electrotechnical Commission) (www.iec.org).

[3] ICNIRP: International Commission on Non-Ionizing Radiation Protection (www.icnirp.org).

[4] FDA: United States Food and Drug Administration (www.fda.gov).

recommends *maximum permissible exposure*[1] (MPE) values. The MPEs are derived or estimated from the basic restrictions. When comparing with the respective MPEs and BRs, compliance with the MPEs automatically ensures compliance with the underlying BRs.

In the following sections, four criteria are used to demonstrate compliance of the gradiometer-based examination system with the IEEE standard: basic restrictions for the *in situ* electric field, MPE for the magnetic field, peak *in situ* electric field, and peak external magnetic field.

11.5.1.1 Basic restrictions for the in situ electric field

Table 11.2 lists the basic restrictions for the *in situ* electric field for various body regions according to IEEE Std C95.1-2006 [166]. In this table, E_0 is the rheobase *in situ* electric field and f_e is a strength-frequency parameter. The maximum allowed induced *in situ* electric field, E_i, for each body region is determined from this table according to:

$$\begin{aligned} E_i &= E_0 && f \le f_e \\ E_i &= E_0\left(\frac{f}{f_e}\right) && f \ge f_e \end{aligned} \tag{11.10}$$

[1] Maximum Permissible Exposure (MPE): The highest level of exposure, with an additional margin of safety, to which a person may experience without incurring any established adverse health effects. The MPEs are sometimes referred to as the reference levels, derived limits, or investigation levels in literatures.

Table 11.2 Basic restrictions on exposure for the various regions of the body (after [163], Table 1), with limits for the gradiometer-based examination system.

		IEEE Std C95.1-2006		Limits for the gradiometer-based examination system (f = 65 kHz)		
		Action level[1]	Persons in controlled environments		Action level[1]	Persons in controlled Environ.
Exposed tissue	f_e (Hz)	E_0 (RMS) (V/m)	E_0 (RMS) (V/m)	$\frac{f}{f_e}$	E_i (RMS) (V/m)	E_i (RMS) (V/m)
Brain	20	5.89×10^{-3}	1.77×10^{-2}	3250	19.1425	57.525
Heart	167	0.943	0.943	389.222	367.0359	367.0359
Extremities	3350	2.10	2.10	19.4029	40.7463	40.7463
Other tissues	3350	0.701	2.10	19.4029	13.6015	40.7463

Substituting the operating frequency f = 65 kHz into (11.10) and applying values from the left half of Table 11.2 yield the limits for the gradiometer-based examination system. These limits are expressed as E_i's on the right half of Table 11.2.

In the gradiometer-based examination system, the excitation magnetic field is the strongest at the center of the Helmholtz coil. As a result, the induced currents are also the largest when objects or body parts are submerged in this uniform field. In the worst-case scenario, if the region of uniform magnetic field was extended to the entire compliance volume, the maximum electric field induction volume would also expand accordingly. For a patient positioned between the excitation coils, the majority of the induced currents are confined near the body surface as described in Section 11.4.1. Therefore, the RMS electric field value, E_{RMS} = 0.792 V/m, obtained from Section 11.4.1 for the body muscle is suitable for use as an upper bound for the induced *in situ* electric field for all exposed regions of the body. Comparing E_{RMS} with the E_i values in the right half of is

show that the gradiometer-based examination system is compliant with the basic restrictions for induced *in situ* electric field.

11.5.1.2 MPE for the magnetic field

The peak-to-peak magnetic flux density at the center of the gradiometer-based examination system excitation coils is approximately 0.15 mT (1.5 gauss). The RMS value of this field is

$$B_{\mathrm{RMS}} = 1.5\times10^{-4}\left(\frac{1}{2}\right)\left(\frac{1}{\sqrt{2}}\right) \quad \text{(T)}$$

$$= 0.5303\times10^{-4} \quad \text{(T)} \qquad (11.11)$$

The corresponding magnetic field strength, H_{RMS}, is

$$H_{\mathrm{RMS}} = \frac{1}{\mu}B_{\mathrm{RMS}}$$

$$= \frac{0.5303\times10^{-4}}{4\pi\times10^{-7}}$$

$$= 42.202 \quad \text{(A/m)} \qquad (11.12)$$

If the uniform magnetic field at the center of the Helmholtz coil was expanded to the entire coil volume, the head, torso and limbs of the patient will also be exposed to B_{RMS}. Table 11.3 lists the RMS MPEs limits for B_{RMS} and the magnetic field, H_{RMS}, for exposure to the head, torso, and limbs (arms and legs) from the IEEE standard[1]. A comparison of the results from (11.11) and (11.12) with those from Table 11.3 show that

[1] IEEE Std C95.1-2006 Section 4.1: Basic restrictions (BRs) and maximum permissible exposures (MPEs) for frequencies between 3 kHz and 5 MHz

the B_{RMS} and H_{RMS} levels for the gradiometer-based examination system are within the thresholds recommended by the IEEE standard.

Table 11.3 MPE for the head, torso and limbs: f = 3.35 kHz to 5 MHz (after [166], Tables 2 and 3)

Body part	Action level[1]		Persons in controlled environments	
	B_{RMS} (mT)	H_{RMS} (A/m)	B_{RMS} (mT)	H_{RMS} (A/m)
Head and torso	0.205	163	0.615	490
Limbs	1.13	900	1.13	900

11.5.1.3 Peak in situ electric field

The IEEE standard states that the temporal peak value of the *in situ* electric field must not exceed that obtained by multiplying the RMS values in Table 11.2 by $\sqrt{2}$. From the induction heating FEA results, the peak *in situ* electric field for the model in Figure 11.3 is E_{peak} = 1.169422 V/m. From Table 11.2, the minimal RMS E_i value is the exposure limit for "Other tissues" (E_i = 13.6015 V/m), and the corresponding peak value is $E_{i,peak} = \sqrt{2}(13.6015) = 19.2354$ V/m. Comparison of these electric field values show that the peak *in situ* induced electric field, E_{peak}, is less than the lowest peak restriction level, $E_{i,peak}$, from Table 11.2. These results show that the gradiometer-based

[1] IEEE Std C95.1-2006 Section 4.1: Basic restrictions (BRs) and maximum permissible exposures (MPEs) for frequencies between 3 kHz and 5 MHz

examination system satisfies the peak *in situ* electric field restriction recommended by the IEEE standard.

11.5.1.4 Peak external magnetic field

The peak-to-peak magnetic flux density for the gradiometer-based examination system is approximately 1.5×10^{-4} T (1.5 gauss). This excitation magnetic flux density may be expressed as $B = B_0 \sin(2\pi f t)$ (T), where $B_0 = 0.75\times10^{-4}$ T and $f = 65$ kHz. The time derivative of this external field is $\dot{B} = \frac{dB}{dt} = 2\pi f B_0 \cos(2\pi f t)$. The peak value of $\dot{B}$ is

$$\begin{aligned} |\dot{B}| &= 2\pi f B_0 \qquad (\mathrm{T}) \\ &= 0.471 f \qquad (\mathrm{mT}) \end{aligned} \tag{11.13}$$

and the phase duration[1], t_p, is $t_p = \frac{1}{2f}$. For compliance assessment, $|\dot{B}|$ is to be compared with the allowable peak limit on B, denoted as $\dot{B}_p$, given by

$$\dot{B}_p = \sqrt{2} MPE_{\mathrm{B}}(2\pi f) \tag{11.14}$$

The values for MPE_{B} are obtained from the MPEs in Table 11.3. Table 11.4 lists the $\dot{B}_p$ values for the head, torso and limbs. Comparisons of the values from (11.13) and Table 11.4 show that the peak external magnetic field value in the gradiometer-based examination system falls well below the limits recommended by the IEEE standard.

---

[1] For a periodic waveform, the phase duration is defined as the time between zero crossings

Table 11.4 Maximum permissible values, $\dot{B}_p$, of the time derivative of the external magnetic field for the head, torso and limbs ($f = 65$ kHz).

Body part	Action level (mT)	Persons in controlled environments (mT)	Gradiometer-based system values
Head and torso	0.2899 ($2\pi f$)	0.8698 ($2\pi f$)	0.075 ($2\pi f$)
Limbs	1.5981 ($2\pi f$)	1.5981 ($2\pi f$)	

The assessment of the gradiometer-based examination system with regard to the basic restrictions for the *in situ* electric field, MPE for the magnetic field, peak *in situ* electric field and the peak external magnetic field demonstrate that the system is compliant with the IEEE Std C95.1-2005 standard, and that exposure to RF energy levels generated by the system is safe for patients and medical personnel.

11.5.2 The IEC Standard (IEC 60601-2-33)

The IEC standards ([167]-[171]) establish the general requirements for basic safety and essential performance of medical electrical equipments, with IEC 60601-2-33 ([167], [168]) providing particular requirements for the safety of magnetic resonance (MR) medical diagnostic equipment. Although originally intended for medical MR systems, the standard nevertheless provides SAR limits that are applicable to the gradiometer-based examination system. These limits intend to provide protection against:

1. Excessive low frequency field variations produced by the gradient system;
2. Excessive radio frequency energy;

A third objective, *protection against exposure to static magnetic fields*, does not apply to the gradiometer-based examination system as it does not utilize any static magnetic fields.

11.5.2.1 Protection against excessive low frequency field variations

The IEC standard establishes limits for a RF system's gradient output. The objective of the limits is to prevent cardiac or peripheral nerve stimulation (PNS) due to exposure to excessive low frequency variations. The limits are expressed in terms of either the induced electric field, *E*, in the patient, or the time rate of change of the magnetic flux density, *dB/dt* (T/s). The limits are functions of the effective stimulus duration, $t_{s,eff}$ (ms), defined as the ratio of the peak-to-peak field variation to the maximum value of the time derivative of the gradient [168]. From equation (11.13), $t_{s,eff}$ may be written as:

$$t_{s,eff} = \frac{2B_0}{\left(\frac{dB}{dt}\right)_{\max}} = \frac{2B_0}{|\dot{B}|} = \frac{1}{\pi f} \tag{11.15}$$

For a sinusoidal excitation with frequency f = 65 kHz, the effective stimulus duration is $t_{s,eff} = 4.897 \times 10^{-3}$ ms.

11.5.2.1.1 Limits for prevention of cardiac stimulation

To protect against cardiac stimulation, the induced electric field due to the gradient output of the system must satisfy:

$$E < \frac{2}{\left\{1 - \exp\left(-\frac{t_{s,eff}}{3}\right)\right\}} \tag{11.16}$$

Substituting (11.15) into (11.16) yields

$$E < \frac{2}{\left\{1 - \exp\left(-\frac{4.897 \times 10^{-3}}{3}\right)\right\}}$$

$$< \frac{2}{1.631 \times 10^{-3}}$$

$$E < 1226.221 \qquad \text{(V/m)} \tag{11.17}$$

From the inductive heating finite element analysis results discussed in Section 11.4.1, the average induced electric field in the patient by the gradiometer-based examination system is E_{avg} = 1.12 V/m. This value is well below the IEC limit given by (11.17).

Alternatively, the IEC standard [168] states that for a whole body gradient system such as the gradiometer-based examination system, equation (11.16) may be replaced by

$$\frac{dB}{dt} < \frac{20}{\left\{1 - \exp\left(-\frac{t_{s,eff}}{3}\right)\right\}} \tag{11.18}$$

Applying the results from (11.15) to equation (11.18) gives

$$\frac{dB}{dt} < \frac{20}{\left\{1 - \exp\left(-\frac{4.897 \times 10^{-3}}{3}\right)\right\}}$$

$$< \frac{20}{1.631 \times 10^{-3}}$$

$$\frac{dB}{dt} < 12262.214 \qquad \text{(T/s)} \tag{11.19}$$

For the gradiometer-based examination system, substituting f = 65 kHz into (11.13) gives $|\dot{B}| = \left|\frac{dB}{dt}\right|$ = 61.261 T/s. This value is below the limit specified by (11.19).

Comparisons of the induced electric field, E, and the time rate of change of the magnetic flux density, dB/dt, against the limits given by (11.17) and (11.19), respectively, demonstrate that the gradient output of the gradiometer-based examination system are within the safety limits set forth by the IEC for the prevention of cardiac stimulation.

11.5.2.1.2 Limits for prevention of peripheral nerve stimulation

To prevent peripheral nerve stimulation, the IEC establishes output limits for the two types of gradient systems: the whole body and special purpose systems. For each system, the limits for two operating modes are specified: the normal operating mode[1] ($L01$) and the first level controlled operating mode[2] ($L12$):

$$L12 = 1.0\, r_b \left(1 + \frac{0.36}{t_{s,eff}}\right)$$
$$L01 = 0.8\, r_b \left(1 + \frac{0.36}{t_{s,eff}}\right) \qquad (11.20)$$

[1] In this operational mode, none of the system outputs may cause physiological stress to patients.

[2] The operational mode in which the system must be controlled under medical supervision as one or more output levels may cause physiological stress to patients

In (11.20), r_b (T/s) is the rheobase given in Table 11.5. Note that $L01$, $L12$ and r_b may be expressed in terms of the induced electric field, E (V/m), or the time rate of change of the magnetic field, dB/dt (T/s). From Section 11.5.2.1, the $t_{s,eff}$ for the gradiometer-based examination system was found to be $t_{s,eff} = 4.897\times10^{-3}$ ms. Substituting this value in (11.20) yields the $L01$ and $L12$ limits in Table 11.5.

From the results in Section 11.4.1, the average induced electric field in the patient by the gradiometer-based examination system is E_{avg} = 1.12 V/m, and the maximum time rate of change of the magnetic flux density is $\frac{dB}{dt}$ = 61.261 T/s. Comparison of E_{avg} and $\frac{dB}{dt}$ with the limits in Table 11.5 show that the gradient output of the gradiometer-based examination system satisfies the safety limits set forth by the IEC for the prevention of peripheral nerve stimulation.

11.5.2.2 Protection against excessive RF energy

To protect against the effects of excessive RF energy, the IEC standard provides limits for core and spatially localized temperature elevations and SARs due to exposure to RF energy. The temperature limits are shown in Table 11.6 and the SAR limits are shown in Table 11.7.

Table 11.5 Gradient output limits for the gradiometer-based examination system at the operating frequency of $f = 65$ kHz. (The r_b values are obtained from [168].)

Type of gradient system	*E* (V/m)			*dB/dt* (T/s)		
	r_b	*L*12	*L*01	r_b	*L*12	*L*01
Whole body	2.2	163.929	131.143	20	1490.265	1192.212
Special purpose	2.2	163.929	131.143	N/A	-	-

From the finite element analysis results presented in Section 10.3.2, the temperature elevation of the prosthetic heart valve and the surrounding regions is no more than 0.003 °C after 15 minutes of continuous exposure to the RF energy from the gradiometer-based examination system. The results also show that there is no RF exposure-related temperature rise in any other regions of the body. Therefore, the core and spatially localized temperature elevations are well below the limits prescribed by the IEC as shown in Table 11.6.

The results from Sections 11.4.1 and 11.4.2 show the whole body SARs from equations (11.5) and (11.8) are 1.24×10^{-4} and 2.0715×10^{-4} W/kg, respectively. The partial body SAR is 2.1233×10^{-4} W/kg (11.9). These values satisfy the IEC limits listed in Table 11.7.

To assess the head and local SARs of the examination system, the limits in Table 11.7 are expressed in terms of temperature elevations [173] in the affected region. Specifically, in the normal mode, a head SAR of 3.2 W/kg corresponds to a 1-degree rise in the cranial temperature [175].

Table 11.6 IEC temperature limits for RF exposure (after [169], Table 104)

Operating Mode	Core Temperature Rise, °C	Spatially localized temperature limits		
		Head, °C	Torso, °C	Extremities, °C
Normal	0.5	38	39	40
First level controlled	1	38	39	40
Second level controlled [1]	>1	>38	>39	>40

Table 11.7 SAR limits (after [167], Table 105)

Averaging time	6 min					
	WHOLE BODY SAR	PARTIAL BODY SAR	HEAD SAR	LOCAL SAR		
Body region →	Whole body	Exposed body part	Head	Head	Trunk	Extremities
Operating mode ↓	(W/kg)	(W/kg)	(W/kg)	(W/kg)	(W/kg)	(W/kg)
NORMAL	2	2-10[a]	3.2	10[b]	10	20
FIRST LEVEL CONTROLLED	4	4-10[a]	3.2	10[b]	10	20
SECOND LEVEL CONTROLLED	>4	>(4-10)[a]	>3.2	>10[b]	>10	>20
SHORT TERM SAR	The SAR limits over any 10 s period shall not exceed three times the stated values					

[a] The limit scales dynamically with the ratio "exposed patient mass / patient mass":
Normal Operating Mode:
Partial Body SAR = 10 W/kg – (8 W/kg * exposed patient mass / patient mass)
First Level Controlled Operating Mode:
Partial Body SAR = 10 W/kg – (6 W/kg * exposed patient mass / patient mass)
[b] In cases where the orbit is in the field of a small local RF transmit coil, care should be taken to ensure that the temperature rise is limited to 1 °C.

In Table 11.7, a torso SAR of 10 W/kg, averaged over any 10 grams of trunk tissue, corresponds to a temperature rise of 2 degrees [173]-[175]. For extremities, a SAR limit

[1] The output limit beyond which a formal human studies protocol and internal review board approval are required.

of 10 W/kg, averaged over any 10 grams of tissue in the exposed region, corresponds to a temperature rise of 3 degrees [175]. Since the results in Section 10.3.2 show that the temperature rise in the regions outside of the myocardium is negligible, it can be concluded that the gradiometer-based examination system satisfies the head and local SAR limits for all three operation modes in Table 11.7.

The results from Sections 11.5.2.1 and 11.5.2.2 show that the gradiometer-based examination system is compliant with the IEC standard for RF medical equipment safety.

11.5.3 The ICNIRP Guidelines

Similar to the IEEE standard [166], the ICNIRP guidelines [172] also provide *basic restrictions* for exposure to EM fields. However, in the ICNIRP guidelines, the physical quantities used to specify the basic restrictions are the current density, SAR, and power density. Application of these quantities is based on the frequency range of the EM field. Specifically, between 1 Hz and 10 MHz, induced current density basic restrictions are provided for preventing nervous system stimulation and adverse effects. From 100 kHz to 10 GHz, SAR basic restrictions are stated to prevent whole body heat stress and excessive localized tissue heating. Within the overlapped frequency range of 100 kHz to 10 MHz, both the current density and SAR restrictions must be satisfied. Finally, between 10 and 300 GHz, power density basic restrictions are provided to prevent excessive local tissue heating at or near the surface of the body.

The ICNIRP basic restrictions applicable to the gradiometer-based examination system are those in the 1-100 kHz frequency range. These restrictions specify the maximum allowable induced current in the exposed region. For an operating frequency of $f = 65$ kHz, the basic restrictions are listed in Table 11.8.

Table 11.8 ICNIRP basic restrictions for a time-varying EM field at $f = 65$ kHz

Exposure characteristics	Current density for head and trunk (mA m^{-2})(RMS)
Occupational	650
General public	130

From Table 11.1, the RMS current density in the myocardium is $J_{my,\mathrm{RMS}} = 0.1448978\times10^{-3} \times 0.7071 = 0.1236$ mA/m^2, and that in the body muscle region is $J_{bm,\mathrm{RMS}} = 2.235\times10^{-3} \times 0.7071 = 1.5804$ mA/m^2. Comparing these values with the levels in Table 11.8, the highest RMS current density induced in the patient body (1.5804 mA/m^2) is below the 130 mA/m^2 basic restriction value for general public exposure. Therefore, these results demonstrate that the gradiometer-based examination system is compliant with the ICNIRP standards.

11.5.4 The FDA Guidelines

The FDA guidelines ([173]-[175]) align closely with the IEC standard IEC 60601-2-33 ([167]-[171]). They share the same operating mode definitions, as well as limits for whole body and localized heating, SARs, gradient output, and induced electric field levels [169]. The FDA guidelines, however, imposes additional limits on the RF heating

of the implanted medical devices. Compliance of the gradiometer-based examination system with the IEC standard has already been demonstrated in Section 11.5.2. The remaining FDA requirements are examined here for safety assessment.

11.5.4.1 FDA Limits on Implant Heating

Implant heating can occur in two ways. First, as eddy currents are induced in the human body by a RF magnetic field, a conductor may concentrates these currents and produce intense localized heating at any exposed "corners" or "points" such as the tip of a wire. Second, induced eddy currents may result in inductive heating of the conductor itself. The FDA guidelines require that the temperature rise of the medical device, without convective heat transfer, shall not exceed 3 degrees over 15 minutes of exposure [175].

In the gradiometer-based examination system, the flange ring, and the inlet and outlet struts of the prosthetic heart valve form multiple metallic closed loops. During a heart valve examination, the heart valve is aligned such that the flange ring is parallel to the applied magnetic field. In this orientation, there is no current induced in the inlet strut loop, and only minimal eddy currents are induced in the portion of the flange that intercepts the applied magnetic field. In the worst-case scenario when the prosthetic heart valve is oriented such that the flange ring is orthogonal to the applied magnetic field, a maximum amount of eddy currents will be induced in the flange, resulting in a maximum temperature rise of the heart valve. This scenario has been investigated in Chapter 9 for various cooling scenarios. The results in Section 10.3.2 show that, for 15 minutes of exposure with normal temperature regulation, the temperature of the prosthetic heart valve does not rise beyond 37.003 °C (a temperature rise of 0.003

degrees). In the case when there is no convection cooling (no blood flow), the results in Section 10.3.3 show that the maximum temperature rise of the prosthetic heart valve is 0.0652 °C after 15 minutes of exposure. These temperature elevations are less than the 3 °C limit set forth in the FDA guidelines.

The inductive implant heating FEA results showing compliance with the IEC standard affirms that the gradiometer-based examination system is compliant with the FDA guidelines for RF medical equipment safety. It must be mentioned that the system cannot be employed for examining patients with cardiac pacemakers and other implanted devices containing metal.

11.6 Compliancy Statement

The results presented in this chapter demonstrate that the gradiometer-based examination system is compliant with the IEEE Std C95.1-2005 [166] and IEC 60601-2-33 [168] standards, as well as the ICNIRP [172] and FDA [175] guidelines. The RF energy emission level from the examination system is safe for patients and medical personnel.

CHAPTER 12. CONCLUSIONS AND FUTURE WORK

A novel minimally invasive gradiometer-based prosthetic heart valve examination system has been developed. The system is capable of detecting single-leg separation (SLS) failures in BSCC heart valves with a reasonable degree of confidence. A clinical-scale prototype of the system has been constructed, and two gradiometer designs have been built for use with different patient physical conditions and physiques. An *in vitro* test system that can simulate the movement of the heart valve during the cardiac cycle has also been constructed. Double-blind *in vitro* studies with the examination system prototype on 34 BSCC heart valves with various outlet strut conditions have repeatedly achieved 100 % accuracy in detecting the SLS cases.

During the development of the examination system, finite element (FE) techniques were used to characterize and optimize various system components such as the magnetic field distribution generated by the excitation coils, design of the gradiometer, as well as to demonstrate the detection feasibility of the magnetic field perturbations in the vicinity of the outlet strut. Based on these results, the components of the examination system were designed.

Since the excitation field of the gradiometer-based method induces currents in the flange and struts of the BSCC heart valve, a FE analysis has also been performed to investigate the potential temperature rise of the heart valve due to inductive heating effects. Analysis results show that inductive heating of the prosthetic heart valve and the neighboring

tissues from exposure to the excitation field of the gradiometer-based examination system is negligible, and that the system is safe for patient use.

The FE analysis results also show that the low-level and low frequency magnetic field ($< 1.5\times10^{-4}$ T at $\approx$ 65 kHz) employed by the examination system is compliant with all key international health and safety standards established by organizations such as the IEEE, IEC, ICNIRP, and the US FDA. The RF energy emission level from the system is safe for patients and medical personnel, and will not cause any adverse health effects.

To quantify the reliability of the examination approach when under the influence of system parameter variabilities, a technique for developing the probability of detection (POD) model for the examination system has been presented. Application of this model shows that the examination system is highly robust against parameter variability such as the deviation in the gradiometer initial position from the specified target location during an examination. The procedures presented may be adapted for developing PODs for other sources of system variabilities.

The clinical-scale system prototype is portable. It is suitable for transportation over long distances as well as relocation from one operating room to another. A custom surgery table has also been prepared for use with the examination system. The top of this table has been replaced with one made from high-strength non-metallic materials so that it will not interfere with the excitation magnetic field. The examination system prototype, with the supporting equipment, is ready for animal studies.

In conclusion, a minimally invasive, highly accurate gradiometer-based examination system for detecting SLS failures in BSCC prosthetic heart valve has been developed. The system is highly reliable and safe for patients and medical personnel.

12.1 Future Work

The gradiometer-based examination system is ready for animal studies. The system needs to be evaluated in a suitable animal clinic or hospital. An animal use protocol must be submitted for approval and BSCC heart valves with various outlet strut conditions need to be implanted into either ovine or bovine models. The cardiac surgeon responsible for catheterizing the animal subject and conducting the examination should be familiar with the recommended animal study examination procedures provided in Appendix B of this thesis. It is crucial that the surgeon understands the principal of the examination technique, and be able to position the gradiometer to the prescribed target location in front of the outlet strut. If feasible, double-blind tests should be performed for the animal studies.

Upon the successful completion of the animal studies, human trials should commence immediately. The gradiometer-based examination system may be relocated to a national test center and BSCC heart valve patients are to be transported to the center for examinations. A successful human trial will provide BSCC patients with an early detection mechanism for SLS failures.

APPENDIX

APPENDIX A. BIOLOGY OF THE HEART AND HEART VALVE DISORDERS

A.1 The Heart

The cardiovascular system consists of the heart and the circulatory system. The heart works as a pump that pushes blood to the organs, tissues, and cells of the body through a complex network of arteries, arterioles, and capillaries. Blood delivers oxygen and nutrients to every cell and removes the carbon dioxide and waste products produces by the cells. The blood is then returned to the heart through venules and veins. If all the blood vessels in the human body were laid end-to-end, they would extend for almost 60,000 miles (more than 96,500 kilometers), which is twice the circumference of the earth.

The heart weighs between 7 and 15 ounces and is approximately the size of two clenched fists. On average, the heart beats approximately 100,000 times a day, pumping more than 2,000 gallons of blood. This amounts to nearly 38 million heart beats a year, circulating more than 730000 gallons of blood. In an average lifetime of a person, the heart pumps about 1 million barrels of blood, enough to fill 3.3 supertankers [190].

The heart is located between the lungs in the middle of thorax (chest), behind and slightly to the left of the sternum (breastbone). It is a muscular organ enclosed in a double-layered fibrous sac called the pericardium. The outer layer of the pericardium surrounds the roots of the heart's major blood vessels and is attached by ligaments to the spinal

column, diaphragm, and other parts of the body. The inner layer of the pericardium is attached to the heart muscle. The extremely narrow space between the pericardium and the heart is filled with a watery fluid that serves as a lubricant as the heart moves within the sac. The walls of the heart are called the myocardium. It is composed primarily of cardiac muscle cells. The inner surface of the walls that is in contact with the blood within the cardiac chambers is lined by a thin layer of cells known as endothelial cells, or endothelium.

The human heart (Figure 12.1) is divided into left and right halves, each consisting of an upper chamber called the atrium and a lower chamber called the ventricle. A wall of muscle called the septum separates the two halves of the heart. Located between the atrium and ventricle in each half of the heart is an atrioventricular (AV) valve that prevents retrograde flow of the blood from the atrium to ventricle. The left AV valve is called the mitral valve, and the right is called the tricuspid valve. In addition to the AV valves, two semilunar valves ensure the directional flow of blood exiting the heart from the ventricles: The pulmonary valve located at the entrance to the pulmonary trunk, and the aorta valve located at the entrance to the aorta. These valves permit blood to flow into the arteries during ventricular contraction but prevent blood from moving in the opposite direction during ventricular relaxation. Like the AV valves, the semilunar valves operate passively accordingly to the pressure differences across them.

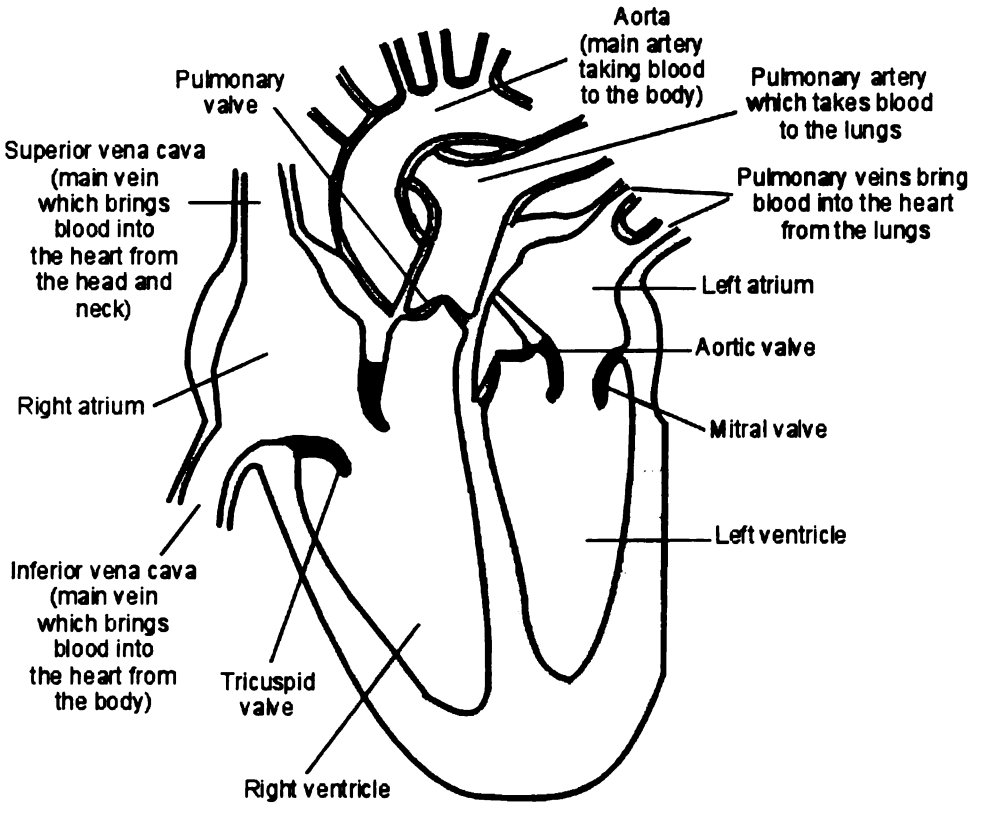

Figure 12.1 A simplified cross-section view of the human heart. After [135]

The pumping of blood by the heart is due to the orderly atrial and ventricular contractions and relaxations known as the cardiac cycle. The cardiac cycle consists of two major phases: The period of ventricular contraction and blood ejection called systole (Figure 12.2), and the period of ventricular relaxation and blood filling called diastole (Figure 12.3). The opening and closing of the AV valves is a passive process resulting from pressure differences across the valves during the cardiac cycle. During diastole, the ventricle relaxes and the blood pressure in the atrium is greater than that in the adjacent ventricle. The connecting AV valve is pushed open and blood flows from the atrium to the ventricle. In contrast, during systole when a contracting ventricle achieves an internal pressure greater than that in the adjacent atrium, the connecting AV valve is forced closed. Consequently, blood in the right ventricle is forced into the pulmonary trunk and

blood in the left ventricle is forced into the aorta. At an average heart rate of 72 beats per minute, each cardiac cycle last approximately 0.8s, with 0.3s in systole and 0.5s in diastole.

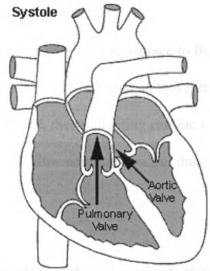

Figure 12.2 During systole, the ventricles contract. The AV vales are closed and blood in the right ventricle is forced into the pulmonary trunk while blood in the left ventricle is forced into the aorta. After [136]

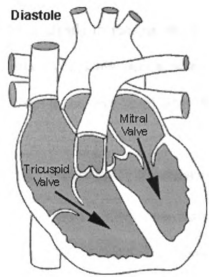

Figure 12.3 During diastole, the ventricles relax. The AV valves are pushed open and blood flows from the atria to the ventricles. After [136]

To prevent the AV valves from being pushed up into the atrium, the valves are fastened to muscular projections (papillary muscles) of the ventricular walls by fibrous strands (chordae tendinae). They act only to limit the valves' movements and prevent them from being everted.

When opened, a heart valve offers very little resistance to flow. In disease states, however, a valve opening may become narrowed so that it imposes a high flow resistance even when opened. In such a state, the contracting cardiac chamber must produce an unusually high pressure to cause flow across the valve, thus increasing the stress on the cardiac muscles.

There are no valves at the entrances of the superior and inferior vanae cavae into the right atrium, and of the pulmonary veins into the left atrium. However, atrial contraction pumps very little blood back into the veins because the contraction compresses the veins at their sites of entry into the atria, greatly increasing the resistance to backflow. (Accordingly, a little blood is ejected back into the veins, and this accounts for the venous pulse that can often be seen in the neck veins when the atria are contracting.)

A.2 Heart Valve Disorders

The heart valves can be malformed (due to prolapse) or malfunctioned either in the form of leaking (causing regurgitation) or by not opening adequately and thus partially obstructing the flow of blood through the valve (causing stenosis). While valve prolapse is unique to the mitral valve, stenosis and regurgitation can affect any of the heart valves,

sometimes simultaneously. These three disorders are described below with respect to the mitral valve.

A.2.1 Mitral Valve Prolapse

Mitral valve prolapse occurs when the valve cusps (flaps) are abnormally long, floppy, billows out into the left atrium and does not close properly when the left ventricle contracts. In most cases, mitral valve prolapse is harmless, asymptomatic and does not need to be treated. In a small number of instances, it can cause severe mitral regurgitation (leakage of blood back through the valve) and requires extensive treatment.

A.2.2 Mitral Stenosis or Obstruction

Mitral stenosis, also known as mitral valve obstruction, is a narrowing of the mitral valve opening. This prevents adequate blood flow from the left atrium into ventricle during diastole (Figure 12.4).

A.2.3 Mitral Regurgitation or Insufficiency

Mitral regurgitation, or mitral valve insufficiency, is a disorder in which the mitral valve does not close properly. This causes blood to leak (backflow, or regurgitation) into the left atrium from the left ventricle during systole (Figure 12.5).

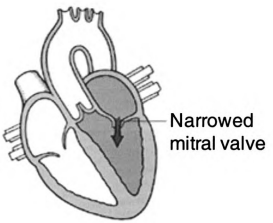

Figure 12.4 Mitral stenosis is the narrowing of the valve opening that reduces blood flow from the atrium to the ventricle. After [137]

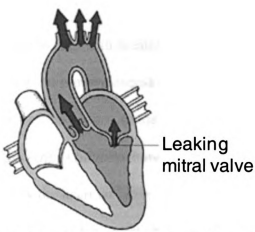

Figure 12.5 In mitral regurgitation, the improper closing of the valve causes blood to leak back into the atrium from the ventricle during systole. After [137]

A.3 Treatments of Heart Valve Disorders

Treatments of mitral valve prolapse, stenosis, and regurgitation can range from monitoring, medications, to surgical repair and replacement of the diseased valve, depending on the severity of the case.

A.3.1 Observations and Monitoring

Most cases of mitral valve prolapse and mild, asymptomatic cases of stenosis and regurgitation do not require treatment. In case of mitral valve prolapse or regurgitation, echocardiograms are recorded periodically to monitor the enlargement of the left ventricle.

A.3.2 Medications

In more moderate cases of heart valve disorders, medications may be advised to relief the symptoms and to prevent complications. Some of these medications include:

- *Diuretics* (water tablets) to help with breathlessness. They facilitate urine production in the kidneys to remove excess blood and fluid which may build up in the lungs or other parts of the body with the "back pressure" from the heart.
- *ACE (angiotensin-converting) Inhibitors* are medicines which help to reduce the amount of work done by the heart and ease symptoms of heart failure.
- *Anti-arrhythmic medication* such as a beta-blocker helps to control and lower the heart rate in case of atrial fibrillation, as well as to reduce palpitations (heartbeat sensations that feel like pounding or racing, with either normal or abnormal rhythms).
- *Warfarin (anticoagulation)* is also advised in cases of atrial fibrillation to prevent blood clots from forming.
- *Antibiotics* to prevent endocarditis. Damaged, abnormal, or artificial heart valves are susceptible to a serious bacteria infection called infective endocarditis. A

patient should take antibiotics before surgical, dental, or medical procedures to reduce the risk of an infection on a valve, even though this risk is small.

A.3.3 Surgical Repair

If medications do not reduce the symptoms satisfactorily, a surgical procedure may be performed in attempt to correct the heart valve disorder. During valve repair, parts of a valve are reshaped or removed to make the valve function more efficiently. Certain valve problems can be repaired. For insufficiency, extra tissue is removed, or parts of the valve are strengthened to help it close more tightly. This may be accomplished by sewing a ring around the opening of the valve. For stenosis, an obstructing valve can be stretched open using a procedure called balloon valvuloplasty. In this procedure, a balloon-tipped catheter is threaded through a vein into the heart. Once inside the valve, the balloon is inflated, separating the valve leaflets. Alternatively, a heart surgery may be performed to separate the fused cusps. One advantage of a heart valve repair operation is that only the patient's own valve tissues are used. If a valve is too badly damaged, surgical replacement with an artificial valve maybe the only option.

A.3.4 Heart Valve Replacement

Heart valves that are seriously deformed or degenerated cannot be repaired. In this case, the old valve is removed and replaced with a new valve mechanism. The new valve is attached by suture to a rim of tissue kept from the original valve. The replacement valve is either a mechanical valve made of plastic and metal or a biologic valve made of tissue,

usually from pigs, cows or humans, placed in a synthetic ring. The various types of prosthetic valves are summarized in the following sections.

Choice of a valve depends on many factors, including characteristics of the valve. A mechanical valve lasts longer than a biologic valve but a lifetime therapy with an anticoagulant (blood thinner) is needed to prevent the formation of blood clots on the valve. A biologic valve does not last as long as a mechanical valve, but anticoagulants are rarely required for the patient. Therefore, a patient's suitability to take anticoagulants is an important deciding factor. For instance, anticoagulants may not be appropriate for women of childbearing age because anticoagulants cross the placenta and may affect the fetus. The patient's age, activity level, the condition of the heart as well as the location of the damaged valve are all important factors affecting the choice of the replacement valve. Typically, mechanical valves are preferred in younger and more active patients.

Heart valve replacement surgery requires general anesthesia of the patient. The heart is stopped and a heart-lung machine is used to by-pass the heart. The damaged valve is removed, and the replacement valve is sewn in place. The incisions are closed, the heart-lung machine is disconnected, and the heart is restarted. The operation may take between 2 to 5 hours. After surgery, the patient is monitored in an intensive care unit for one or two days before being moved to an in-patient care unit. Full recovery may take anywhere from 6 to 8 weeks.

A.4 Types of Prosthetic Heart Valves

Prosthetic heart valves are either mechanical or tissue valves. The following sections described the structures and provide examples of each type of these valves.

A.4.1 Mechanical Valves

Mechanical heart valves include the ball valves and disc valves. The disc valves include the single leaflet and bileaflet disc valves. The single disc valves can be further divided into caged disc or tilting disc valves. Examples of these mechanical prosthetic heart valves are given below.

A.4.2 Ball Valves

Ball valves, also known as ball-in-a-cage valves, were the earliest prosthetic heart valves implanted in humans. They remain one of the most reliable and durable designs available. Designed by engineer Lowell Edwards and Dr. Albert Starr, the Starr-Edwards silastic ball valve was the world's first commercially available replacement mitral valve The Starr-Edwards model 1260 aortic valve (European model: 1200) and the mitral model 6120 are shown in Figure 12.6.

The original Starr-Edwards valve suffered from a suboptimal hemodynamics design. Since the ball had to be larger than the valve opening to stop the back-flow of blood when the valve was closed, this left a large ball in the middle of the blood stream that partially obstructed blood flow. Design improvements were made in later models to

reduce the relative size of the occluder ball. The last available models, 1200, 1260 and 6120, discontinued in 2004, had been unchanged since 1968.

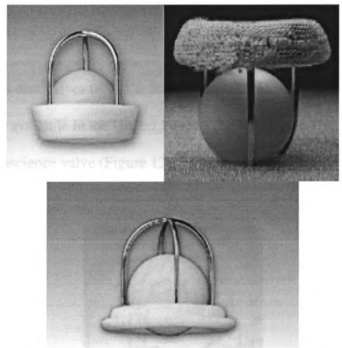

Figure 12.6 Starr-Edwards Silastic Ball Valves. Top: Mitral Model 1260. Bottom: Aortic Model 6120.

A.4.3 Disc Valves

There are two kinds of disc valves: Single leaflet and bileaflet valves. A single leaflet valve can be either a caged disc or tilting disc valve. The earliest disc valves implanted were single leaflet valves and they were very successful. Although the development of the bileaflet valve did not begin until later, as of 1997 bileaflet valves dominated the mechanical valve market in the United States with a 90% market share [138]

Single leaflet disc valves. The original Björk-Shiley single leaflet valve (Figure 12.7) had a very successful and durable design. Although this valve is no longer sold in the United States, it is arguably the most controversial single leaflet tilting disc valve. Issues with the Björk-Shiley single leaflet valve are discussed in Chapter 3.

Single leaflet caged disc valves (e.g., the Kay-Shiley TGCD series valve shown in Figure 12.8) are no longer available in the United States. The Medtronic-Hall valve (Figure 12.9) and the Omniscience valve (Figure 12.10) are the two single tilting disc valves still being used in the U.S.

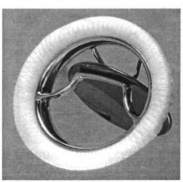

Figure 12.7 Björk-Shiley titling disc valve

Figure 12.8 Kay-Shiley TGCD series single leaflet caged disc valve.

Bileaflet disc valves. The most successful bileaflet disc valve is the St. Jude valve (Figure 12.11) and it is the leading choice for mechanical valve implantations in the

United States [138]. Other bileaflet valves available in the U.S. include the Carbomedics valve (Figure 12.12) and the On-X valve (Figure 12.13).

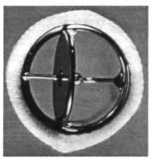

Figure 12.9 Medtronic-Hall single tilting disc valve.

Figure 12.10 Omniscience single tilting disc valve.

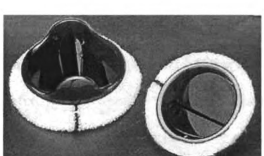

Figure 12.11 St. Jude standard bileaflet valve.

Figure 12.12 Carbomedics CPHV standard bileaflet valve.

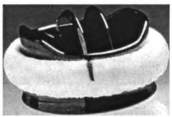

Figure 12.13 On-X bileaflet valve.

A.4.4 Tissue Valves

Tissue valves are also called bioprosthetic valves. There are three types of tissue valves: Animal tissue valves, human tissue valves and Synergraft (synthetic tissue valves).

A.4.4.1 Animal Tissue Valves (xenografts, heterografts)

Animal tissue valves are called xenografts (from the Latin prefix "xeno-," for foreign) or heterografts (where the prefix "hetero-" means "different"). The most commonly used xenografts can either be of valve tissue, typically porcine or pig valve tissue, or of non-valve pericardial tissue from bovine or cow. Four examples of the porcine valves are the Hancock (standard and modified orifice) valves (Figure 12.14), the Carpentier-Edwards Porcine valve (Figure 12.15), the St. Jude Toronto Stentless Porcine valve (Figure 12.16), and the Medtronic Freestyle Aortic Root Bioprosthesis (Figure 12.17). The later two employ stentless designs intended to improve the hemodynamics of the valves. The only

pericardial valve currently available is the Carpentier-Edwards Pericardial valve (Figure 12.18) and its variants.

Figure 12.14 Hancock porcine valve.

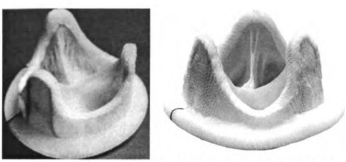

Figure 12.15 Carpentier-Edwards porcine valve (two views).

Figure 12.16 St. Jude Toronto Stentless Porcine Valve (SPV).

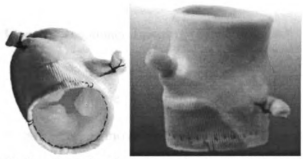

Figure 12.17 Freestyle Stentless Aortic Bioprosthesis: End view (left) and lateral view (right).

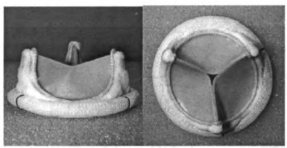

Figure 12.18 Carpentier-Edwards pericardial valve: Lateral view (left) and top view (right).

A.4.4.2 Human Tissue Valves (homografts, autografts) and the Ross Procedure

A human tissue valve transplant from a donor person is called a homograft valve. Homograft valves tend to be durable and have good hemodynamics, although it is uncertain at the time of this writing whether these characteristics are significantly better than ordinary tissue valves. There are generally no rejection issues and immunosuppressive therapy is typically no required. One drawback of the homograft valves is that they are more technically challenging to implant than standard tissue valves. In addition, homograft availability is limited by donor availability. Also, since the valve is typically cryopreserved in liquid nitrogen until it is used, the valve must be thawed overnight before the surgery. This means that the patient's valve size must be

known beforehand. This information may be ascertained through the use of either echocardiograms or Magnetic Resonance Imaging (MRI) images.

An autograft is a valve moved from one position to another within the same patient. The most common autograft procedure is moving the pulmonary valve to the aortic position, also known as the Ross procedure [139]. Figure 12.19 explains the Ross procedure.

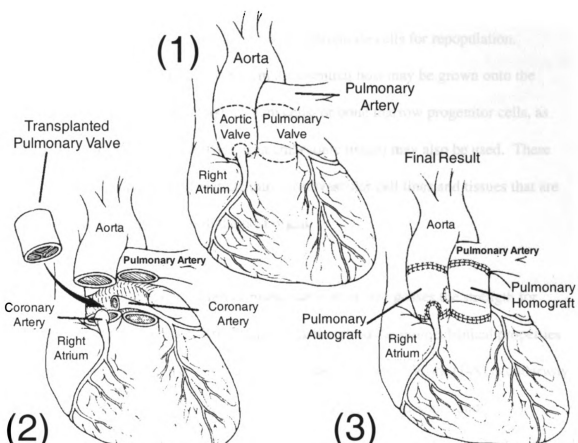

Figure 12.19 The Ross procedure. The numbers depict the surgery sequence. After [143]

A.4.4.3 Decellularized homograft and xenograft aortic prosthesis (Synergraft)

Although still in its infancy and highly experimental, Synergraft [144]-[146] is intended to be the ideal replacement valve of the future. Synergraft is a tissue-engineered valve

made from either synthetic materials, stem cells, or a mixture of both. To create the valve, a suitable immunologically inert scaffold is used as a matrix for cellular population. The scaffold is biodegradable and is eventually replaced by autologous tissue growth. Some choices of biological scaffold material include fibrin gel and extracellular matrix, while synthetic matrices include glactin polymers, glycolic acid and polyurethane [147].

After the scaffold is in place, it is seeded with appropriate cells for repopulation. Endothelial cells and myofibroblasts from the eventual host may be grown onto the scaffold. Alternatively, mesenchymal stem cells, or bone marrow progenitor cells, as well as allogenic stem cells (derived from embryonic tissue) may also be used. These stem cells can potentially differentiate into cardiovascular cell lines and tissues that are morphologically compatible with the host organ.

A completely tissue-engineered replacement valve must also posses the strength for attachment to the recipient's existing valve apparatus, and the biomechanical properties to sustain the hemodynamical stress and strain inside the heart. Work [148] is underway to characterize and develop numerical models for the cellular structure and biomechanical properties of the mitral valve (leaflet), as well as to develop biological and synthetic materials [149] for the scaffold and valve repopulation.

APPENDIX B. ANIMAL STUDY EXAMINATION PROCEDURE

This chapter describes the animal study procedure, provides a list of critical considerations and recommends several data events to be captured for the gradiometer-based BSCC heart valve examination system. To ensure success, the animal study must be conducted by qualified and experienced medical and engineering personnel to ensure that the listed critical considerations are addressed and observed. The list of recommended data collection events should be followed whenever a listed data source is available. Minimally, the gradiometer-based examination system outputs must be recorded.

B.1 The Animal Study Procedure

B.1.1 Animal Support

During the heart valve examination, the animal is supported by a custom surgery table (Figure 12.20) which provides height, roll, pitch, and yaw angle adjustments. With the animal secured in the supine (or lateral decubitus, depending on the surgeon's preference) position, the table top of the surgery bed is inserted into the region between the excitation coils (see Figure 12.21). Note that the table top is custom constructed from non-metallic components that do not interfere with the magnetic excitation field.

B.1.2 Position and Orientation of the Test Animal

With the aid of a mobile fluoroscope, identify the position and orientation of the heart valve. Adjust the surgery bed to the proper height to ensure that the heart valve is located

at the center of the excitation coils. Orient the animal (by adjusting the surgery bed) to align the heart valve flange with the axis of the portable excitation coils. Note that the proper orientation of the heart valve within the excitation coils is critical to the success of this examination technique. The cardiologist must provide accurate orientation information and supervise the alignment of the heart valve with the coils.

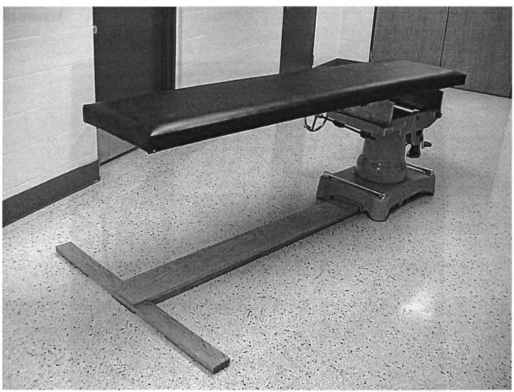

Figure 12.20 The custom surgery table for the gradiometer-based heart valve examination system

B.1.3 Calibration and Zeroing of Measurement Instruments

Prior to inserting the animal between the excitation coils, position a guide catheter into the left ventricle under fluoroscopy. Advance a gradiometer via the catheter lumen to a position approximately 10 cm away from the outlet strut. Remove the fluoroscope and

position the mobile excitation coils to surround the animal such that the heart valve is at the center of the coils. (It is recommended to move the excitation coils rather than the surgery bed as the animal will be attached with life-support and anesthesia equipment at this point.) Energize the excitation coils and calibrate the test equipment at this gradiometer location to remove the effects of background noise from the operating room. Switch off and remove the excitation coils, and reposition the portable fluoroscope over the test animal.

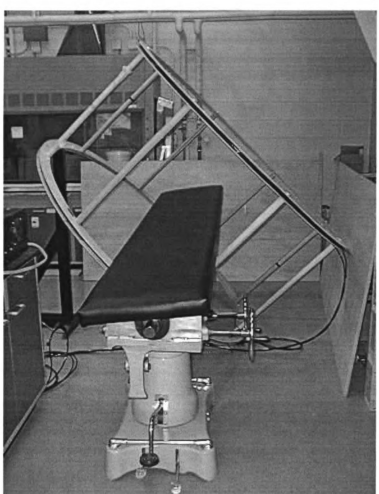

Figure 12.21 Table top of the custom surgery bed is positioned between the excitation coils through a side opening during examination

B.1.4 Positioning of the Gradiometer

Under fluoroscopy, advance the gradiometer into the left ventricle and position the distal end in the mitral annulus. Due to cardiac activities, the relative distance between the gradiometer and the outlet strut will change in an oscillatory fashion. At its closest point, the gradiometer should be inside the outlet strut loop (Figure 12.22) and as close to the strut plane as possible without crossing the plane (Figure 12.23). Figure 12.24 shows the optimal location of the gradiometer in relation to the outlet strut.

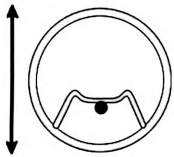

Figure 12.22 Optimal position of the gradiometer inside the outlet strut loop

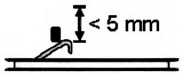

Figure 12.23 The gradiometer should be placed as close to the outlet strut loop as possible without crossing the plane of the loop

Figure 12.24 Optimal position of the gradiometer in relation to the outlet strut

B.1.5 Examination and Data Acquisition

After the gradiometer is properly positioned, remove the fluoroscope and energize the external low-field excitation coils. Record the gradiometer output signals for 10 or more cardiac cycles. Switch off and remove the excitation coils and readjust the position of the gradiometer under fluoroscopy. Reposition the excitation coils over the animal and reenergize the system. Record the gradiometer system output signals again. Repeat the gradiometer position adjustment three to five times, depending on signal quality, and record the gradiometer system outputs at each position.

B.1.6 Animal Recovery

After the tests, remove the sensor and the sheath and repair the arterial incision site. Extubate and recover the animal.

B.2 Critical Considerations

There are a few important considerations that must be satisfied to ensure the success the of gradiometer-based examination technique:

(a) The heart valve flange must be aligned with the center (z-) axis of the excitation coils

(b) The outlet strut is to be positioned at either the due north or due south direction with respect to the center axis of the excitation coils

(c) The gradiometer must be positioned inside the outlet strut loop at the location shown in Figure 12.22 and Figure 12.24

(d) The gradiometer must be placed as close to (within 3 mm) the plane of the outlet strut loop as possible without crossing the plane.

The lead cardiologist is expected to provide accurate information regarding the orientation and location of the valve in relation to the distal end of the catheter. He or she is also expected to position the gradiometer at the desired location.

B.3 Recommended Data Capture Events

The following is a list of recommended data capture events and items for both record keeping and analyses purposes. These items should be recorded whenever the data source is accessible and a mean of recording is available. At a minimum, the inspection system outputs must be recorded.

(a) Date, time, and location of the animal study

(b) Names and ranks or titles of the investigating personnel

(c) Digital photos of the operating room and instruments

(d) Digital photos of the test animal before the study

(e) Digital photos of the test animal after catherization

(f) Digital photos of test animal on the custom examination bed, surrounded by the excitation coils

(g) Video recording of the fluoroscope cinegram during the entire procedure

(h) Recording of the test animal ECG

(i) Capture of fluoroscope image at each gradiometer position

(j) Settings of the gradiometer-based system instruments (both the excitation and measurement systems)

(k) Inspection system outputs for 10 or more cardiac cycles

(l) A second measurement of the system outputs in part (k), if necessary

(m) Repeat part (k) as the gradiometer position is readjusted (three to five times, depending on the signal quality)

BIBLIOGRAPHY

BIBLIOGRAPHY

[1] Kraus, John Daniel, *Electromagnetics*, New York, New York: McGraw-Hill, 1973.

[2] Sadiku, Mathew N.O., *Elements of Electromagnetics, 2nd Edition,* New York, New York: Saunders College Publishing/Harcourt Brace College Publishers, 1994, p 412.

[3] Balanis, Constantine A., *Advanced Engineering Electromagnetics*, New York, New York: John Wiley & Sons, 1989.

[4] Björk, Viking O., "A new tilting disc valve prosthesis," *Scandinavian Journal of Thoracic and Cardiovascular Surgery*, Vol. 3, 1969, pp. 1-10.

[5] Moulton, A.L., Lincoln, S., Attar, S., Green, D. C., Sequeira, A., and McLaughlin, J. S., "The convexo-concave modification of the Björk-Shiley prosthesis: significant reduction of thromboembolism (abstract)," *Journal of American College of Cardiology*, Vol. 5, 1985, p 391.

[6] Kuntze, C. E., Eijgelaar, A., Ebels, T., and Homan Van Der Heide, J.N., "Rates of Thromboembolism with Difficerent Mechanical Heart Valve Prostheses: Randomised Study," *The Lancet*, Vol. 333, Issue 8637, March 11, 1989, pp. 514-517.

[7] Björk, Viking O., Henze, A., and Hindmarsh, T., "Radiopaque marker in the tilting disc of the Björk-Shiley heart valve. Evaluation of in vivo prosthetic valve function by cineradiography," *Journal of Thoracic and Cardiovascular Surgery*, Vol. 73, 1977, pp. 563-569.

[8] Björk, Viking O., "The improved Björk-Shiley tilting disc valve prosthesis," *Scandinavian Journal of Thoracic and Cardiovascular Surgery*, Vol. 12, 1978, pp. 81-84.

[9] *Chronology of the Björk-Shiley Cardiac Prostheses*, Shiley, Incorporated, Irvine, CA, 1986.

[10] Shiley, Inc., presentation in *FDA and the Medical Device Industry*, Hearing Before the Subcommittee on Oversight and Investigations of the Committee on Energy and Commerce, U.S. House of Representatives, One Hundred First Congress, Second Session, Ser. No. 101-127, Feb. 26, 1990, p 175.

[11] Brubakk, O., Simonsen, S., Kallman, L., and Fredriksen, A., "Strut fracture in the new Björk-Shiley mitral valve prosthesis," *The Thoracic Cardiovascular Surgeon*, Vol. 29, 1981, pp. 108-109.

[12] Lindblom, D., Björk, V.O., and Semb, B.K.H., "Mechanical failures of the Björk-Shiley valve: incidence, clinical presentation, and management," *Journal of Thoracic and Cardiovascular Surgery*, Vol. 92, 1986, pp. 894-907.

[13] Fielder, John H., "Ethical Issues in Biomedical Engineering: The Björk-Shiley Heart Valve," *IEEE Engineering in Medicine and Biology*, March 1991, pp. 76-78.

[14] Chandler, J., Knight, R., and Strom, J., "Broken Heart Valves," *Emergency Medicine*, Cahners Publishing Co.: Highlands Ranch, CO, Vol. 24, June 15, 1992.

[15] Hedger, Philip, "Single-leg separations In explanted Bjork-Shiley convexo-concave heart valves," *Lancet*, Vol. 343, No. 8892, January 29, 1994, pp. 294-295.

[16] Fielder, J. H., "Defects and Deceptions—The Björk-Shiley Heart Valve," *IEEE Technology and Society Magazine*, Fall 1995, pp. 17-22.

[17] Wieting, David. W., Eberhardt, Allen. C., Reul, H., Breznock, E. M., Schreck, S. G., and Chandler, J. G., "Strut fracture mechanisms of the Bjork-Shiley convexo-concave heart valve," *Journal of Heart Valve Diseases*, Vol. 8, No. 2, March 1999, pp. 206-217.

[18] Guo, G. X., Xu, C. C., and Hwang, N. H. C., "The closing velocity of Baxter-Duromedics heart valve prostheses," *American Society for Artificial Internal Organs (ASAIO) Transactions*, Vol. 36, No. 3, 1990, pp. 529-532.

[19] Eberhardt, Allen C., Ward, Mark A., Lewandowski, Simon J., Inderbitzen, Rebecca, Wieting, David W., "Relationships between closure delay, pressure, velocity, and outlet strut forces of the Björk-Shiley heart valve," *Advances in Bioengineering*, ASME, Vol. 26, 1993, pp. 547-550.

[20] Rau, Günter, Reul, Helmut, Eichler, Michael, Schreck, Stefan, and Wieting, David W., "The Effect of Left Ventricular dP/dt on the In Vitro Dynamics of the Björk-Shiley Convexo-Concave Mitral Valve," *The Journal of Heart Valve Disease*, Vol. 4, Suppl. I, 1995, pp. S17-S20.

[21] Schreck, S., Inderbitzen, Rebecca, Chin, H., Wieting, David W., Smilor, M., Breznock, E., and Pendray, D., "Dynamics of Björk-Shiley Convexo-Concave Mitral Valves in Sheep," *The Journal of Heart Valve Disease*, Vol. 4, Suppl. I, 1995, pp. S21-S25.

[22] Chandran, Krishnan B., Lee, Chong-sun, Aluri, Srinivas, and Dellsperger, Kevin C., "Pressure Distribution Near the Occluders and Impact Forces on the Outlet Structs of Björk-Shiley Convexo-Concave Valves during Closing," *The Journal of Heart Valve Disease*, Vol. 5, No. 2, Mar 1996, pp. 199-206.

[23] Structural Acoustics, Incorporated, *Acoustic Characterization of Outlet Strut Condition and Loading*, a research proposal submitted to the Bowling-Pfizer Supervisory Panel, July 26, 1994, p. 20 (access through the Bowling-Pfizer

Document Repository web site: www.bowling-pfizer.com/repository. Title=030011.).

[24] Björk, Viking O., "Metallurgic and design development in response to mechanical dysfunction of Björk-Shiley heart valves," *Scandinavian Journal of Thoracic and Cardiovascular Surgery*, Vol. 19, 1985, pp. 1-12.

[25] Sacks, S. H., Harrison, M., Bischler, P. J., Martin, J. W., Watkins, J., and Gunning, A., "Metallurgical analysis of failed Björk-Shiley cardiac valve prostheses," *Thorax*, Vol. 41, Feb 1986, pp. 142-147.

[26] Röckelein, G., Breme, J., and van der Emde, J., "Lethal blockage of a Björk-Shiley artifical heart valve caused by strut failure – The metallurgical aspect," *The Thoracic Cardiovascular Surgeon*, Vol. 37, 1989, pp. 47-51.

[27] Swieten, van H. A., Mol, de B. A., Defauw, J. J., Overkamp, P. J., and Vermeulen, F. E. E., "Metallurgical analysis of the Björk-Shiley convexo-concave valve prosthesis to assess the case of late outlet strut fracture," *Surgery for Heart Valve Disease*," Bodnar, E., editor, ICR Publishers: London, 1990, pp. 616-627.

[28] Xiao, K., and Appleby, A. J., "Stress Corrosion Cracking in Björk-Shiley Convexo-Concave Prosthetic Heart Valves Due to Random *In Vivo* Electrochemical Pulsing," *International Journal of Artificial Organs*, Vol. 19, No. 8, August 1996, pp. 477-486. (Center for Electrochemical Systems and Hydrogen Research, Texas Engineering Experiment Station/Texas A & M University, College Station, USA)

[29] Wenzel, Thomas C., Manning, Charles R., Chandler, James G., and Williams David F., "Welding Metallurgy's Putative Influence on Björk-Shiley Convexo-Concave Valve Outlet Strut Failures," *Journal of Heart Valve Diseases*, Vol. 8, No. 2, March 1999, pp. 218-231.

[30] Sethia B., Quin R. O., and Bain, W.H., "Disc embolization after minor strut fracture in a Björk-Shiley mitral valve prosthesis," *Thorax*, Vol. 38, 1983, pp. 390-391.

[31] Ibarra F., Gutierrez, A., Martinez, F., Carreras, L., Lopez, C., and Alonso-Lej, F., "Fracture of the outlet strut of a Björk-Shiley mitral prosthesis: emergency operation with survival," *Journal of Thoracic and Cardiovascular Surgery*, Vol. 87, 1984, pp. 315-318.

[32] Garcia-De-Castillo, H., Larrousse-Perez, E., Murtra-Ferre, M., and Soler-Soler, J., "Strut fracture and disc embolization of a Björk-Shiley mitral valve prosthesis," *American Journal of Cardiology*, Vol. 55, 1985, pp. 597-598.

[33] Davis, P. K., Myers, J. L., Pennock, J. L., and Thiele, B. L., "Strut fracture and disc embolization in Björk-Shiley mitral valve prostheses: diagnosis and management," *The Annul of Thoracic Surgery*, Vol. 40, 1985, pp. 65-69.

[34] Miccolo M. L., Lemole, G. M., and Spagna, P. M., "Late strut fracture and disc 23 in a 27mm Björk-Shiley mitral prosthesis," *American Heart Journal*, Vol. 110, 1985, pp. 898-899.

[35] Khalil, Y., Sethia, B., Quin, R. O., and Bain, W. H., "Disc and strut embolization after minor strut fracture in a Björk-Shiley mitral valve prosthesis," *Thorax*, Vol. 40, 1985, pp. 158-159.

[36] Hendel, P. N., "Björk-Shiley strut fracture and disc escape: literature review and a method of disc retrieval," *The Annals of Thoracic Surgery*, Vol. 47, 1989, pp. 436-440.

[37] Mass, A. H. E. M., van Swieten, H. A., Knaepen, P. J., Defauw, J. J., Brutel, de la Riviere A., and van Herpen, G., "Successful emergency surgery after strut fracture of Björk-Shiley mitral heart valve," *Ned Tijdschr Geneeskd*, Vol. 130, 1986, pp. 835-838.

[38] Tanaka, M., Abe, T., Takeuchi, E., Watanabe, T., and Tamaki, S., "Intraoperative echocardiography of a dislodged Bjork-Shiley mitral valve disc," *The Annals of Thoracic Surgery*, Vol. 51, 1991, pp. 315-316.

[39] Personal electronic mail correspondence with David E. Miller, Chairman of the Bowling-Pfizer Supervisory Panel, Nov 2004 and March 2005.

[40] Kallewaard, Marjon, Algra, Ale, and van der Graaf, Yolanda, "Welder identity, weld date, and the risk of outlet strut fracture in Björk-Shiley convexo-concave valves: the Dutch cohort study," *Heart*, Vol. 76, 1996, pp. 510-512.

[41] Walker, Alexander M., Funch, Donnie P., Sulsky, Sandra I., and Dreyer, Nancy A., "Manufacturing Characteristics Associated with Strut Fracture in Björk-Shiley 60° Convexo-Concave Heart Valves," *Journal of Heart Valve Diseases*, Vol. 4, No. 6, November 1995, pp. 640-648.

[42] Walker, Alexander M., Funch, Donnie P., Sulsky, Sandra I., and Dreyer, Nancy A., "Shop order fracture rate as a risk factor for strut fracture in Björk-Shiley CC 60 degrees heart valves," *Journal of Heart Valve Diseases*, Vol. 6, No. 3, May 1997, pp. 264-267.

[43] Kallewaard, Marjon, Algra, Ale, Defauw, Jo, and van der Graaf, Yolanda, "Which Manufacturing Characteristics are Predictors of Outlet Strut Fracture in Large Sixty-Degree Björk-Shiley Convexo-Concave Mitral Valves? " The Björk-Shiley Study Group, *Journal of Thoracic and Cardiovascular Surgery*, Vol. 117, 1999, pp. 766-775.

[44] Omar, Rumana Z., Morton, Linda S., Beirne, Mairead, Blot, William J., Lawford, Patricia V., Hose, Rodney, and Taylor, Kenneth M., "Outlet strut fracture of Björk-Shiley convexo-concave valves: Can valve-manufacturing characteristics explain the risk?" *Journal of Thoracic and Cardiovascular Surgery*, Vol. 121, No. 6, 2001, pp. 1143-1149.

[45] Omar, Rumana Z., Morton, Linda S., Murad, Shahed, and Taylor, Kenneth M., "Use of flexibility tests in the manufacturing process of 60° Björk-Shiley convexo-concave valves and the risk of outlet strut fracture," *Journal of Thoracic and Cardiovascular Surgery*, Vol. 126, 2003, pp. 832-836.

[46] Advanced Computational and Engineering Services (ACES, Columbus, Ohio), *Evaluation of Hook to Well Separation on Tip Loading*, a research proposal approved by the Bowling-Pfizer Supervisory Panel, May 2004. (Available from the Bowling-Pfizer Document Repository: http://www.bowling-pfizer.com/repository.)

[47] van Der Graaf, Y., Waard, F. D., van Herwerden, L. A., and Defauw, J., "Risk of strut fracture of Björk-Shiley valves," *The Lancet*, Vol. 339, No. 8788, February 1992, pp. 257-61.

[48] Ericsson, A., Lindblom, D., Huysmans, H. A., Thulin, L. I., Scully, H. E., Bennett, J. G., Ostermeyer, J., and Grunkemeier, G. L., "Strut fracture with Björk-Shiley 70° convexo-concave valve: An international multi-institutional follow-up study," *European Journal of Cardio-thoracic Surgery*, Vol. 6, 1992, pp. 339-346.

[49] Grunkemeier, J. D., Chandler, J. G., Miller, C., Jamieson, W. R. E., and Starr, A., "Utilization of manufacturer's implant card data to estimate heart valve failure," *Journal of Heart Valve Diseases*, Vol. 2, 1993, pp. 493-503.

[50] Walker, Alexander M., Funch, Donnie P., Sulsky, Sandra I., and Dreyer, Nancy A., "Patient Factors Associated With Strut Fracture in Björk-Shiley 60° Convexo-Concave Heart Valves," *Circulation*, Vol. 92, No. 11, December 1995, pp 3235-3239.

[51] Piehler, Jeffery M., Blackstone, Eugene H., Bailey, Kent R., Sullivan, Michael E., Pluth, James, R., Weiss, Noel S., Brookmeyer, Ron S., and Chandler, James G., "Reoperation on prosthetic heart valves: Patient-specific estimates of in-hospital events," *European Journal of Thoracic and Cardiovascular Surgery*, Vol. 109, No. 1, 1995, pp. 30-48.

[52] de Mol, Bas A. J. M., Overkamp, Peter J., van Gaalen, Geerda L., and Becker, Anton E., "Non-destructive assessment of 62 Dutch Björk-Shiley convexo-concave heart valves," *European Journal of Thoracic and Cardiovascular Surgery*, Vol. 11, 1997, pp. 703-709.

[53] Omar, Rumana Z., Morton, Linda S., Halliday, D. A., Danns, E. M., Beirne, M. T., Blot, W. J., and Taylor K. M., "Outlet strut fracture of Björk-Shiley convexo-concave heart valves: the UK cohort study," *Heart*, Vol. 86, 2001, pp. 57-62.

[54] UK Cohort, *Patient Follow-up to Improve Estimation of Risk of Strut Fracture, 2002-2003,* sponsored by the Bowling-Pfizer Supervisory Panel, 2003.

[55] Lindblom, D., Rodriguez, L., and Björk, V.O., "Mechanical failure of the Björk-Shiley valve: updated follow-up and considerations on prophylactic rereplacement," *Journal of Thoracic and Cardiovascular Surgery*, Vol. 97, 1989, pp. 95-97.

[56] Birkmeyer, J. D., Marrin, C. A., and O'Connor, G. T., "Should patients with Björk-Shiley valves undergo prophylactic replacement?" *Lancet*, Vol. 340, 1992, pp. 520-523.

[57] Marrin, C. A., Birkmeyer, J. D., and O'Connor, G. T., "The Björk-Shiley dilemma," *Annal of Thoracic Surgery*, Vol. 55, 1993, pp. 1361-1364.

[58] van der Meulen, Jan H. P., Steyerberg, Ewout W, van der Graaf, Y., et al., "Age thresholds for prophylactic replacement of Björk-Shiley convexo-concave heart valves: a clinical and economic evaluation," *Circulation*, Vol. 88, 1993, pp. 156-164.

[59] de Mol, Bass A., Kallewaard, M., McLellan, R. B., van Herwerden, L. A., Defauw, J. J., and van der Graaf, Y., "Single-leg strut fractures in explanted Björk-Shiley valves," *Lancet*, Vol. 343, January 1994, pp 9-12.

[60] Steyerberg, Ewout W, van der Meulen, Jan H. P., van Herwerden, L. A., et al. "Prophylactic replacement of Björk-Shiley convexo-concave heart valves: an easy-to-use tool to aid decision-making in individual patients," *Heart*, Vol. 76, 1996, pp. 264-268.

[61] Kallewaard, Marjon, Defauw, Jo, and van der Graaf, Yolanda, "Psychological distress among recipients of Björk-Shiley convexo-concave valves: the impact of information," *Heart*, Vol. 78, 1997, pp. 577-580.

[62] van Gorp, M. J., Steyerberg, E.W., Kallewaard, Marjon, and van der Graaf, Yolanda, "Clinical prediction rule for 30-day mortality in Björk-Shiley convexo-concave valve replacement," *Journal of Clinical Epidemiology*, Vol. 56, No. 10, 2003, pp. 1006-1012.

[63] van Gorp, M. J., Steyerberg, E.W., and van der Graaf, Yolanda, "Decision Guidelines for Prophylactic Replacement of Björk-Shiley Convexo-Concave Heart Valves: Impact on Clinical Practice," *Circulation*, Vol. 109, No. 17, May 4, 2004, pp. 2092-2096.

[64] Lindblom, D., "Management of patients with Björk-Shiley prosthetic valves," *British Heart Journal*, Vol. 68, 1992, p. 249.

[65] Hiratzka, Loren F., Kouchoukos, Nicholas T., Grunkemeier, Gary L., Miller, D. Craig, and Scully, Hugh E., "Outlet Strut Fracture of the Björk-Shiley 60° Convexo-Concave Valve: Current Information and Recommendations for Patient Care," *Journal of American College of Cardiology*, Vol. 11, 1988, pp. 1130-1137.

[66] Bowling-Pfizer Supervisory Panel, "Guidelines to Assess Patients with Björk-Shiley Convexo-Concave Heart Valves for Elective Explantation," sent as an attachment to a "Dear Doctor" letter, August 1997 (http://www.bowling-pfizer.com/guidelines.htm).

[67] Bowling-Pfizer Supervisory Panel, "Amended Guidelines to Assess Patients with Björk-Shiley Convexo-Concave Heart Valves for Elective Explantation," sent as an attachment to a "Dear Doctor" letter, March 2000 (http://www.bowling-pfizer.com/guidelines.htm).

[68] Bowling-Pfizer Supervisory Panel, "The 2003 Amended Guidelines to Assess Patients with Björk-Shiley Convexo-Concave Heart Valves for Elective Explantation," sent as an attachment to a "Dear Doctor" letter, October 2003 (http://www.bowling-pfizer.com/guidelines.htm).

[69] Eberhardt, A., "Finite Element Stress Analysis," Accident Reconstruction Analysis, Inc., 5801 Lease Lane, Raleigh, NC 27613, Oct, 1989.

[70] Chia, Raymond, "Finite Element Analysis of Vibrations of the Björk-Shiley Convexo-Concave Heart Valve," *Proceedings of the 1994 IEEE Seventh Symposium on Computer-Based Medical Systems*, June 1994, pp. 48-52.

[71] Goldstein, J. A., Zucker, R. P., and Lee, B. Y., "Echocardiographic demonstration of outlet strut fracture of a Björk-Shiley mitral prosthesis," *Journal of the American College of Cardiology*, Vol. 7, 1986, pp. 949-952.

[72] Chandra, Rajiv, Bilsker, Martin, Myerburg, Robert J., and Kessler, Kenneth M., "Echocardiographic diagnosis of outlet strut fracture of a Björk-Shiley prosthesis in the mitral position," *The American Journal of Cardiology*, Vol. 58, Issue 11, 1986, pp. 1117-1118.

[73] Assanelli, D., Aquilina, M., Marangoni, S., MOrgagni, G. L., and Visioli, O., "Echophonocardiographic evaluation of the Björk-Shiley mitral prosthesis," *American Journal of Cardiology*, Vol. 57, 1986, pp. 165-170.

[74] Min, Pu, Vandervoort, Pieter M., Greenberg, Neil L., Bibawy, George A., Eberhardt, Allen C., Schreck, Stefan, and Thomas, James, D., "Assessment of The Closing

Dynamics In Björk-Shiley Mitral Prosthesis By Digital Echocardiography: In Vitro Validation," *Computers in Cardiology 1994*, Sept. 1994, pp. 349-352.

[75] Mehlman, D. J. and Resnekov, L., "A guide to radiographic identification of prosthetic heart valves," *Circulation*, Vol. 57, 1978, pp. 613-23.

[76] Mehlman, D. J., "A guide to radiographic identification of prosthetic heart valves: an addendum," *Circulation*, Vol. 69, 1984, pp. 102-105.

[77] Cesmeli, Erdogan, Powell, Kimberly A., Greenberg, Neil L., and Cornhill, Fredrick, "An Automated Temporal Alignment Technique for the Translational and Rotational Correction of Digital Radiographic Images of Björk-Shiley Heart Valves," *Proceedings of Computers in Cardiology 1993*, Sept 1993, pp. 619-622.

[78] Powell, K. A., Cornhill, J. F., Nissen, S. N., Chandler, J. G., Abolfathi, A. H., LaPresto, E. L., Herderick, E. E., Mueller, K., Cesmeli, E., and Chandra, S., "Digital radiographic analysis of single-leg separations (SLS) in the outlet struts of Björk-Shiley convexo-concave valves," *Computer Assisted Radiology*, Lemke, H. U., Inamura, K., Vannier, M. W., Editors, Springer-Verlag: Berlin, Germany: 1993.

[79] Abolfathi, Amir H., Hirsch, Jamie Lee, Nissen, Steven E., Wieting, David W., and Chandler, James G., "Effect of Valve Profiling and Increasing kVp on In Situ Radiographic Detection of Single Leg Separations of the Björk-Shiley Convexo-Concave Heart Valve," *Engineering in Medicine and Biology Society, 1994. Engineering Advances: New Opportunities for Biomedical Engineers. Proceedings of the 16th Annual International Conference of the IEEE*, Vol. 1, Nov 1994, pp. 528-529.

[80] Cesmeli, E., Powell, Kimerly A., and Cornhill, J. Fredrick, "An Automated Method To Detect Single-Leg Separation In Radiographic Images Of Björk-Shiley 60° And 70° Convexo-Concave Heart Valves," *Proceedings of the EMBC'95*, 1995 Annual Conference of IEEE Engineering in Medicine and Biology Society, Vol. 1, 1995, pp. 427-428.

[81] O'Neill, William, W., Chandler, James G., Gordon, Richard E., Bakalyar, Donovan M., Abolfathi, Amir H., Castellani, Mark D., Hirsch, Jamie Lee, Wieting, David W., Bassett, Joseph S., Beatty, Karen C., Soltis, Mary Ann, Timmis, Gerald C., and Grines, Cindy L, "Radiographic Detection of Strut Separations in Björk-Shiley Convexo-Concave Mitral Valves," *The New England Journal of Medicine*, Vol. 333, No. 7, Aug 1995, pp. 414-419.

[82] Chandler, James G., Hirsch, Jamie Lee, O'Neill, William, W., Oesterle, Stephen N., Miller, D. Craig, Kennedy, John A., and Faichney, Alan, "Radiographic Detection of Single Strut Leg Separations as a Putative Basis for Prophylactic Explantation of Björk-Shiley Convexo-Concave Heart Valves," *World Journal of Surgery*, Vol. 20, No. 8, Oct 1996, pp. 953-960.

[83] Powell, Kimerly A., Obuchowski, Nancy A., Mueller, Klaus D., LaPresto, Eric, Hwang, Charles G., Hirsch, Jamie Lee, Nissen, Steven E., and Cornhill, J. Fredrick, "Quantitative Detection of Outlet Strut Separations in Björk-Shiley Convexo-concave Mitral Valves," *Circulation*, Vol. 94, 1996, pp. 32510-3256.

[84] Gilchrist, Ian C., Cardella, John F., Fox, Preston S., Pae, Walter E., Sabe, Ahmed R. Kunselman, and Hopper, Kenneth D., "Radiographic detection of single-leg fracture in Björk-Shiley Convexo-Concave prosthetic valves: A phantom model study," *American Heart Journal*, Vol. 133, 1997, pp. 197-202.

[85] Vrooman, Henri A., Maliepaard, Chris, Van der Linden, Leo, Jessurun, Emil R., Ludwig, J. Werner, Plokker, H. W. Thijs, Schalij, Martin J., Weeda, Hans W. H., Laufer, Jaap L., Huysmans, Hans A., and Reiber, Johan H. C., "Quantitative Assessment of the Presence of a Single Leg Separation in Björk-Shiley Convexoconcave Prosthetic Heart Valves," *Investigative Radiology,* Vol. 32, No. 9, September 1997, pp. 540-549.

[86] Hopper, Kenneth D., Gilchrist, Ian C., Landis, J. Richard, Abolfathi, Amir H., Localio, A. Russell, Wilson, Ronald P., Pae, Walter E., Jr., Kunselman, Allen R., Wieting, David W., Griffith, James W., Pierce, William S., Potok, Paul S., TenHave, Thomas R., and Chandler, James G., "In Vivo Accuracy Of Two Radiographic Systems In The Detection Of Björk-Shiley Convexo-Concave Heart Valve Outlet Strut Single Leg Separations," *Journal of Thoracic and Cardiovascular Surgery*, Vol. 115, Mar 1998, pp. 582-586.

[87] Brendzel, A., Rambod, E., Jorgensen, S. M., Reyes, D. A., Chmelik, M. S., and Ritman, E. L., "Three-Dimensional Imaging of Fractures in Outlet Struts of Björk-Shiley Convexo-Concave Heart Valves by Micro-Computed Tomography In-Vitro," *Journal of Heart Valve Diseases*, Vol. 11, 2002, pp. 114-120.

[88] Leilyn Perri, "Hershey Is The Primary Site In The Country To Test Heart Valves," Office of University Relations, Pennsylvania State University, November 7, 2000 (http://www.psu.edu/ur/2000/heartvalveshmc.html).

[89] Weber, Herman J. "Twenty-First Report of the Special Masters/Trustees," Bowling-Pfizer Litigation (case no. C-1-91-256), United States District Court, Southern District of Ohio, Western Division, Nov 1, 2004, Appendix 2.

[90] Stein, P. D., Sabbah, H. N., Albert, D. E., and Snyder, J. E., "Spectral Signature of the Opening Sound of the Björk-Shiley Convexo-Concave Valve as a Potential Indicator of Strut Fracture," *American Journal of Noninvasive Cardiology*, Vol. 1, 1987, pp. 369-372.

[91] Koymen, H., Altay, B. K., and Ider, Y. Z., "A study of prosthetic heart valve sounds," *IEEE Transaction on Biomedical Engineering*, Vol. 34, No. 11, 1987, pp. 853-863.

[92] Walker, David. K., Scotten, Lawrence N., "Discrimination *in vitro* between the acoustic emissions from Björk-Shiley Convexo-Concave valves with and without a broken minor strut," *Medical & Biological Engineering and Computing*, Vol. 29, 1991, pp. 457-464.

[93] Walker, David K., and Scotten, Lawrence N., "Discriminant Analysis Of Acoustic Emissions From Bjork-Shiley Heart Valves With And Without Broken Minor Struts," *Proceedings of the Annual International Conference of the IEEE Engineering in Medicine and Biology Society, 1991*, Vol. 13, Nov 1991, pp. 2107-2108.

[94] Plemons, Terry D., Hovenga, M., Reeder, H., Dow, J. J., Inderbitzen, Rebecca, Chia, Raymond, Wieting, David W., "Classification of Bjork-Shiley convexo-concave valve status by detection of the intact outlet strut resonant frequency," *Proceedings of the 15th Annual International Conference of the IEEE Engineering in Medicine and Biology Society*, Oct 1993, pp. 389–390.

[95] Nygaard, Hans, Inderbitzen, Rebecca, Hasenkam, J. Michael, Wieting, David W., Paulsen, P. K., "Measurement of sounds generated by mechanical aortic and mitral heart valve prostheses," *Proceedings of the 1994 IEEE Seventh Symposium on Computer-Based Medical Systems*, June 1994, pp. 55-60.

[96] Durand, Louis-Gilles, Stein, Paul D., Grenier, Marie-Claude, Henry, J. W., Inderbitzen, Rebecca S., and Wieting, David W., "In vitro and in vivo low frequency acoustic analysis of Björk-Shiley convexo-concave heart valve opening sounds," *Proceedings of the 1994 IEEE Seventh Symposium on Computer-Based Medical Systems*, June 1994, pp. 61-66.

[97] Eberhardt, Allen C., Chassaing, Charles E., Inderbitzen, Rebecca S., Wieting, David W., "Acoustic evaluation of progressive failure in BSCC heart valves," *Proceedings of the 1994 IEEE Seventh Symposium on Computer-Based Medical Systems*, June 1994, pp. 112-118.

[98] Plemons, Terry, Schreck, Stefan G., and Inderbitzen, Rebecca S., "Stability of the BSCC Heart Valve Outlet Strut Resonant Frequency Under Changing Physiological Conditions and Observation Times," *Proceedings of the 1994 IEEE Seventh Symposium on Computer-Based Medical Systems*, June 1994, pp. 119-124.

[99] Plemons, Terry, Dow, J. J., Wieting, David W., and Chandler, James, G., "Multiple Feature Acoustic Classification of BSCC Artificial Heart Valves," *Proceedings of the 1994 IEEE Seventh Symposium on Computer-Based Medical Systems*, June 1994, pp. 125-130.

[100] Scarbrough, Kent, and Inderbitzen, Rebecca S., "Application of Time-Frequency Analysis to the Classification of Björk-Shiley Conxevo-Concave Heart Valve Condition," *Proceedings of the 1994 IEEE Seventh Symposium on Computer-Based Medical Systems*, June 1994, pp. 131-138.

[101] Candy, J. V., and Jones, H. E., "Processing of prosthetic heart valve sounds for single leg separation classification," *Journal of the Acoustical Society of America*, Vol. 97, No. 6, June 1995, pp. 3663-3673.

[102] Candy, J. V., and Jones, H. E., "Classification of prosthetic heart valve sounds: A parametric approach," *Journal of the Acoustical Society of America*, Vol. 97, No. 6, June 1995, pp. 3675-3687.

[103] Sava, H. P., McDonnell, J. T. E., and Grant, P. M., "Spectral composition of closing sounds produced by mechanical prosthetic heart valves," *Proceedings of the 17th Annual Conference of the IEEE Engineering in Medicine and Biology Society, 1995*, Vol. 1, Sept 1995, pp. 125–126.

[104] Eberhardt, Allen C., Chassaing, Charles E., Ward, Mark A., and Lewandowski, Simon J., "Acoustic Characterization of Mechanical Valve Condition and Loading," *Journal of Heart Valve Diseases*, Vol. 4, No. 6, Nov 1995, pp. 649-659.

[105] Durand, Louis-Gilles, Grenier, Marie-Claude, Inderbitzen, Rebecca S., Wieting, David W., and Stein, Paul D., "Low Frequency Analysis of Opening Sound for Detection of Single Leg Separation of Björk-Shiley Convexo-Concave Heart Valves," *Journal of Heart Valve Diseases*, Vol. 4, Suppl. I, 1995, pp. S32-S37.

[106] Dow, J. J., Plemons, Terry D., Scarbrough, Kent, Reeder, Hugh, Hovenga, Mike, Wieting, David W., Chandler, James G., "Acoustic Assessment of the Physical Integrity of Bjork-Shiley Convexo-Concave Heart Valves," *Circulation*, Vol. 95, 1997, pp. 905-909.

[107] de Mol, Bas A., Cromheecke, Manon E., Groen, Janny G., Faber, Gerard, van der Heiden, Maurits S. and Ongkiehong, Leo, "The Complexity of External Acoustic Detection of Defects in Björk-Shiley Convexoconcave Heart Valves," *Artificial Organs*, Vol. 25, No. 1, Jan 2001, pp. 63-67.

[108] Shawkat, S., Petersen, S. A., and Bailey, J. S., "A new technique for the assessment of mechanical prosthetic heart valves: Analysis of their ultrasonic clicks," in *Surgery for heart valve disease*, Bodnar, E., editor, ICR Publishers, London, 1989, pp. 96-104.

[109] Rambod, Edmond, Fatemi, M., Sahn, David J., and Greenleaf, J. F., "An Innovative Technique to Detect the Single Leg Separation (SLS) in the Björk-Shiley Convexo-

concave (BSCC) Mechanical Heart Valve," *Journal of the American College of Cardiology*, Vol. 37, 2001, p. 136.

[110] Rambod, Edmond, "Application of Novel Technologies in Detection of SLS in the BSCC Heart Valves: Vibro-acoustography, X-Ray Micro-CT and Numerical Modeling," Report: *BioQ*uantetics, Inc., Signal, CA, Nov 12, 2001. (Available from the Bowling-Pfizer Document Repository: http://www.bowling-pfizer.com/repository. Title = 020001.)

[111] Rambod, Edmond, "Step towards clinical implementation of an ultrasound burst-spectrography technique for detection of single leg separation (SLS) in cycling Björk-Shiley Convexo-Concave (BSCC) Heart Valves," a research proposal submitted to the Bowling-Pfizer Supervisory Panel, Jan 21, 2003. (Available from the Bowling-Pfizer Document Repository: http://www.bowling-pfizer.com/repository. Title=240008.)

[112] van Neer, P. L. M. J., Bouakaz, A., Vlaanderen, E., de Hart, J., van de Vosse, F. N., van der Steen, A. F. W., de Jong, N., "In-vitro development of a novel method to noninvasively establish BScc valve integrity," *Proceedings of the 2005 IEEE International Ultrasonic Symposium*, Rotterdam, The Netherlands, Sept 18-21, 2005.

[113] Lepelaars, Eugène S. A. M., van Ooijen, Willem D. R., Tijhuis, Anton G., and de Mol, Bas A. J. M., "Detecting Fractures in Thin-Wire Structures," *Proceedings of the 18th Annual International Conference of the IEEE Engineering in Medicine and Biology Society, Amsterdam*, 1996, pp. 159-160.

[114] Lepelaars, Eugène S. A. M., van Ooijen, Willem D. R., Tijhuis, Anton G., and de Mol, Bas A. J. M., "Detecting fractures in artificial heart valves," *Digest of the IEEE Antennas and Propagation Society International Symposium, 1997*, Vol. 2, July 1997, pp. 1198-1201.

[115] Lepelaars, Eugène S. A. M., "Transient Electromagnetic Excitation of Biological Media by Circular Loop Antennas," Ph.D. Thesis, Eindhoven University of Technology, Eindhoven, The Netherlands, 1997, Ch. 8.

[116] Lepelaars, Eugène S. A. M., van Ooijen, Willem D. R., and Tijhuis, Anton G., "On the Feasibility of Detecting Flaws in Artificial Heart Valves," *IEEE Transactions on Microwave Theory and Techniques*, Vol. 48, Issue 11, Nov 2000, pp. 2165-2171.

[117] Tijhuis, Anton G. and Visser, Hubrecht J., "Development of a Catheter-Based Antenna for Detecting Flaws in Björk-Shiley Artificial Heart Valves," a research proposal submitted to the Bowling-Pfizer Supervisory Panel, Feb 27, 2003, Schedule A. (Available from the Bowling-Pfizer Document Repository: http://www.bowling-pfizer.com/repository. Title = 240001.)

[118] Amin, Viren, "Development and Evaluation of Differential Eddy Current Method for Detection of Outlet Strut Fracture in Björk-Shiley Valves. Progress Report: First animal test using differential eddy current approach," a report submitted to the Bowling-Pfizer Supervisory Panel, March 3, 2004. (Available from the Bowling-Pfizer Document Repository: *http://www.bowling-pfizer.com/repository*. Title = 290039.)

[119] Udpa, Satish S., "New Electromagnetic Methods for the Evaluation of Prosthetic Heart Valves," *Journal of Applied Physics*, Vol. 91, No. 10, 2002, pp. 1-5.

[120] Nair, Naveen V., Ramakrishnan, Sridhar, Clifford, Robert, Li, Yue, Majumdar, Shantanu, Chan, Shiu C., Ramuhalli, Pradeep, Udpa, Lalita, and Udpa, Satish S., "A Beat Frequency Electromagnetic Acoustic Transduction Technique for Detecting Strut Fractures in Prosthetic Heart Valves," (Proceedings of the 10th International Workshop on Electromagnetic Nondestructive Evaluation, East Lansing, Michigan, June 1-2 2004), Electromagnetic Nondestructive Evaluation (IX), Burke, VA: IOS Press, Inc., 2004.

[121] Ramakrishnan, Sridhar, Nair, Naveen V., Clifford, Robert, Majumdar, Shantanu, Chan, Shiu C., Li, Yue, Ramuhalli, Pradeep, Udpa, Lalita and Udpa, Satish S., "An Electromagnetic Acoustic Transduction Technique for Detecting Strut Fractures in Artificial Heart Valves," *Proceedings of the IEEE Electro/Information Technology (EIT) Conference 2005*, Lincoln, NE, May 22-25, 2005.

[122] Chan, Shiu C., Li, Yue, Udpa, Lalita, and Udpa, Satish S., "Electromagnetic Techniques for Detecting Failures in Artificial Heart Valves" *(Proceedings of the 8th International Workshop on Electromagnetic Nondestructive Evaluation, Saarbrücken, Germany, 2002), Electromagnetic Nondestructive Evaluation (VII)*, Kojima, F., Takagi, T., Udpa, Satish S., and Pavo, J., Editors, Burke, VA: IOS Press, Inc., 2003.

[123] Chan, Shiu C., Clifford, Robert, Majumdar, Shantanu, Nair, Naveen V., Ramakrishnan, Sridhar, Li, Yue, Ramuhalli, Pradeep, Udpa, Lalita, and Udpa, Satish S., "Novel methods for detecting fractures in prosthetic heart valves," *Insight (Journal of the British Institute of Non-Destructive Testing)*, Vol. 47, No. 1, Jan 2005, pp. 15-19. (Paper was also presented at the 16th World Conference on Nondestructive Testing, Montreal, Canada, Aug 30-Sep 3, 2004.)

[124] Chan, Shiu C., Oka, Mohachiro, Downey, Adam, and Udpa, Satish S., "Minimally Invasive System for the Evaluation of Prosthetic Heart Valves" *(Proceedings of the 9th International Workshop on Electromagnetic Nondestructive Evaluation, Saclay, Paris, France, May 2003), Electromagnetic Nondestructive Evaluation (VIII)*, Sollier, Thierry, Prémel, Denis, and Lesselier, Dominique, Editors, Burke, VA: IOS Press, Inc., 2004, pp. 247-254.

[125] *Nondestructive Testing Handbook, 3rd Edition, Volume 5: Electromagnetic Testing*, Satish S. Udpa (technical editor) and Patrick O. Moore (editor), American Society for Nondestructive Testing: Columbus, OH, 2004.

[126] Blitz, Jack, *Electrical and Magnetic Methods of Nondestructive Testing, 2nd Edition*, Springer-Verlag: New York, Nov 1997.

[127] Wieting, D. W., Breznock, E. M., Kafesjian, R., and Stobie, R., "Exercising sheep: An in vivo model for assessing the durability of pyrolytic carbon heart valves," *The International Journal of Artificial Organs*, Vol. 13, No. 9, 1990, p. 608.

[128] Breznock, E., Pendray, D., Kinoshita, G., Wieting, D., Kafesjian, R., and Litzman, R., "The Ovine Model for In Vivo Chronic Mitral/Tricuspid Valve Studies," *Journal of the American Society for Artificial Internal Organs (ASAIO)*, Vol. 42, 1997, p. 27.

[129] Nave, C. Rod, *HyperPhysics*, Georgia State University, 2005, *http://hyperphysics.phy-astr.gsu.edu/hbase/magnetic/helmholtz.html*

[130] Biddlecombe, C., Heighwar, E., Simkin, J. and Trowbridge, C., "Methods For Eddy Current Computation in Three Dimensions," *IEEE Transactions on Magnetics*, Vol. 18, No. 2, 1982, pp. 492-497.

[131] Salon, S. and Peng, J., "3-D Eddy Current Using a Four Component Finite Element Formulation," *IEEE Transactions on Magnetics*, Vol. 20, No. 5, Sept., 1984, pp. 1992-1994.

[132] Bardeen, James M. and Press, William H., "Radiation fields in the Schwarzschild background," *Journal of Mathematical Physics*, Vol. 14, No. 7, 1973 pp. 7-19.

[133] Fleiss, Joseph L., *Statistical Methods for Rates and Proportions, 2nd Edition*, New York: John Wiley & Sons, 1981, pp. 1-18.

[134] Woolson, Robert F., and Clarke, William R., *Statistical Methods for the Analysis of Biomedical Data, 2nd Edition*, New York: John Wiley & Sons, 2002.

[135] Patient UK, *Understanding the heart*, *http://www.patient.co.uk/showdoc/27000350/.*

[136] Texas Heart Institute at St. Luke's Episcopal Hospital, *Heart Information*, *http://www.tmc.edu/thi/valves.html.*

[137] Merck & Co., Inc., *The Merck Manual of Medical Information, 2nd Home Edition*, Ch. 28 (Online version: *http://www.merck.com/mmhe/sec03/ch028/ch028a.html*).

[138] Cedars-Sinai Medical Center Division of Cardiology, *Cedars-Sinai Medical Center Prosthetic Heart Valve Information. (http://www.csmc.edu/pdf/Heart_Valves.pdf)*

[139] Morse, D., Steiner, R.M., Fernandez, J., *Guide to Prosthetic Valves*, Springer-Verlag, New York, 1985.

[140] Baxter-Edwards Museum of Heart Valve Design.

[141] Evansville Heart Center, Evansville, IN, *Image gallery/Prosthetic Heart Valve Gallery, http://www.evansvilleheartcenter.com*

[142] St. Jude Medical, Inc., *Toronto SPV® Valve, http://www.sjm.com/devices/device.aspx?name=Toronto+SPV%26%23174%3b+Valve&location=us&type=19.*

[143] Kouchoukos, N.T., Davila-Roman, V.G., Spray, T.L., Murphy, S.F., and Perrillo, J.B., "Replacement of the Aortic Root with a Pulmonary Autograft in Children and Young Adults with Aortic-Valve Disease," *New England Journal of Medicine*, Vol. 330, No. 1, Jan 6, 1994, pp. 1-6.

[144] Kincaid, Edward H., Atala, Anthony, and Kon, Neal D., "Tissue Engineered Heart Valves: A Potential Cure for Valvular Heart Disease," Cardiothoracic Surgery Network (http://www.ctsnet.org/sections/innovation/valvetechnology/articles/article-12.html).

[145] Elkins, Ronald C., Dawson, Patti E., Goldstein, Steven, Walsh, Steven P., Black, Kirby S., "Decellularized human valve allografts," *The Annuals of Thoracic Surgery*, No. 71, 2001, pp. s428-s432.

[146] Bechtel, J. F., Muller-Steinhardt, M., Schmidtke, C., Brunswik, A., Stierle, U., Sievers, H. H., "Evaluation of the decellularized pulmonary valve homograft (SynerGraft)," *Journal of Heart Valve Diseases*, No. 12, 2003, pp. 734-739.

[147] Guan, J., Fujimoto, K. L., Sacks, M. S., Wagner, W. R., "Preparation and characterization of highly porous, biodegradable polyurethane scaffolds for soft tissue applications," *Biomaterials*, Vol. 26, 2005, pp. 3961-3971.

[148] Connolly, J. M., Alferiev, I., Clark, J. N., Eidelman, N., Sacks, M. S., Palmatory, E., Lu, Z., Kronsteiner, A., DeFelice, S., Xu, J., Ohri, R., Narula, N., Vyavahare, N. and Levy, R. J., "Triglycidyl amine crosslinking of porcine aortic valve cusps or bovine pericardium results in improved biocompatibility, biomechanics, and calcification resistance: Chemical and Biological mechanisms," *American Journal of Pathology*, Vol. 166, No. 1, 2005, pp. 1-13.

[149] Engelmayr, G. C., Jr., Rabkin, E., Sutherland, F. W. H., Schoen, F. J., Mayer, J. E., Jr. and Sacks, M. S., "The independent role of cyclic flexure in the early in vitro development of engineered heart valve tissue," *Biomaterials*, Vol. 26, No. 2, 2005, pp 175-187.

[150] Personal conversations with Dr. Donald C. Harrison of the Bowling-Pfizer Supervisory Panel (summer, 2003) (*http://www.bowling-pfizer.com/supervisor.htm*).

[151] Pfizer Incorporated (formerly Shiley Laboratories, Incorporated), *Björk-Shiley Convexo-Concave Prosthetic Heart Valve Technical Schematics*, New York: NY, drawing no.: Dp02-0119, Rev. E. document no.: 809018449.

[152] Pfizer Incorporated (formerly Shiley Laboratories, Incorporated), *Björk-Shiley Convexo-Concave Prosthetic Heart Valve Technical Schematics*, New York: NY, drawing no.: Dp02-0120, Rev. K. document no.: 809018497.

[153] Pfizer Incorporated (formerly Shiley Laboratories, Incorporated), *Björk-Shiley Convexo-Concave Prosthetic Heart Valve Technical Schematics*, New York: NY, drawing no.: Dp02-0121, Rev. D. document no.: 809018566.

[154] Cardima, Incorporated, On-line Product Catalog, *Naviport®* guide catheter product web page (*http://www.cardima.com/company/products/products_naviport.html*)

[155] Tian, Yong, Udpa, Satish S., Nair, Naveen, and Ramakrishnan, Sridhar, "Modeling of Electromagnetic Heating Effects During *In Vivo* Testing of Prosthetic Heart Valves," *Proceedings of the 2006 IEEE International Magnetics Conference (INTERMAG 2006)*, San Diego, CA., May 8-12, 2006.

[156] Pennes, Harry H., "Analysis of Tissue and Arterial Blood Temperatures in the Resting Human Forearm," *Journal of Applied Physiology*, Vol. 1, 1948, pp. 93-122.

[157] Wissler, Eugene H., "Pennes' 1948 paper revisited," *Journal of Applied Physiology*, Vol. 85, 1998, pp. 35-41.

[158] Tangwongsan, C., Will, J. A., Webster, J. G., Meredith, K. L. Jr., and Mahvi, D. M., "*In Vivo* Measurement of Swine Endocardial Convective Heart Transfer Coefficient," *IEEE Transactions on Biomedical Engineering*, Vol. 51, 2004, pp. 1478-1486.

[159] Haynes International, Inc., *HAYNES® 25 Alloy (h3057)*, 2004.

[160] MatWeb Material Property Data website, http://www.matweb.com.

[161] Bronzino, Joseph D., editor-in-chief, *The Biomedical Engineering Handbook, 2nd ed.*, Vol. II, CRC Press: Boca Raton, FL, 2000.

[162] Bronzino, Joseph D., editor, *The Biomedical Engineering Handbook, 3rd ed., Tissue Engineering and Artificial Organs*, CRC Press: Boca Raton, FL, 2006.

[163] IEEE Std C95.1-1982, ANSI Standard for Safety Levels with Respect to Human Exposure to Radio Frequency Electromagnetic Fields, 3 kHz to 100 GHz.

[164] IEEE Std C95.1, 1999 Edition, IEEE Standard for Safety Levels with Respect to Human Exposure to Radio Frequency Electromagnetic Fields, 3 kHz to 300 GHz.

[165] IEEE Std C95.1b-2004, IEEE Standard for Safety Levels with Respect to Human Exposure to Radio Frequency Electromagnetic Fields, 3 kHz to 300 GHz—Amendment 2: Specific Absorption Rate (SAR) Limits for the Pinna.

[166] IEEE Std C95.1-2005, IEEE Standard for Safety Levels with Respect to Human Exposure to Radio Frequency Electromagnetic Fields, 3 kHz to 300 GHz.

[167] IEC 60601-2-33, IEC Standard Medical Electrical Equipment—Part 2-33: Particular Requirements for the Safety of Magnetic Resonance Equipment for Medical Diagnosis, Second Edition, 2002.

[168] IEC 60601-2-33, IEC Standard Medical Electrical Equipment—Part 2-33: Particular Requirements for the Safety of Magnetic Resonance Equipment for Medical Diagnosis (including Amendment 1), Consolidated Edition 2.1, 2006.

[169] IEC 60601-1, IEC International Standard Medical Electrical Equipment—Part 1: General Requirements for Basic Safety and Essential Performance, Edition 3.0, 2005.

[170] IEC 60601-1-2, IEC International Standard Medical Electrical Equipment—Part 1-2: General Requirements for Safety—Collateral Standard: Electromagnetic Compatibility—Requirements and Tests (include Amendment 1), Edition 2.1, 2005.

[171] IEC 60601-1-SER, IEC International Standard Medical Electrical Equipment—All Parts, Edition 1.0, 2006.

[172] ICNIRP (International Commission on Non-Ionizing Radiation Protection), "Guidelines for Limiting Exposure to Time-Varying Electric, Magnetic, and Electromagnetic Fields (Up to 300 GHz)," *Health Physics*, Vol. 74, No. 4, April, 1998, pp. 494-522.

[173] Zaremba, Loren A., "FDA Guidelines for Magnetic Resonance Equipment Safety," 44th Annual Meeting of the American Association of Physicists in Medicine (AAPM), Montreal, Quebec, Canada, July 14-18, 2002.

[174] Zaremba, Loren A., "(Abstract) FDA Guidelines for Magnetic Resonance Equipment Safety," *Medical Physics*, Vol. 29, No. 6, June 2002, pp. 1302.

[175] Zaremba, Loren A., "Criteria for Significant Risk Investigations of Magnetic Resonance Diagnostic Devices," U.S. Food and Drug Administration, Rockville, MD, July 14, 2003.

[176] Javor, Edware R. and Anderson, Theodore, "Design of a Helmholtz Coil for Low Frequency Susceptibility Testing," *1998 IEEE International Symposium on Electromagnetic Compatibility*, Vol. 2, Aug 1998, pp. 912-917.

[177] Anderson, Theodore, "Design of a Helmholtz coil for susceptibility testing using variational calculus and experimental verification," *1999 IEEE International Symposium on Electromagnetic Compatibility*, Vol. 2, Aug 2-6, 1999, pp. 601-604.

[178] see [129]

[179] Chan, Shiu C., Oka, Mohachiro, and Udpa, Satish S., "A Minimally Invasive Electromagnetic Technique for the Evaluation of Prosthetic Heart Valves," *Paper Summaries of the ASNT 16th Annual Research Symposium*, The American Society for Nondestructive Testing, Wyndham Orlando Resort, Orlando, FL, March 26-30, 2007.

[180] Zeng Z., Xuan L., Sun Y., Udpa L., and Udpa S., "Probability of detection model for gas transmission pipeline inspection," *Research in Nondestructive Evaluation*, Vol. 15, No. 3, July-Sep. 2004, pp. 99-110

[181] Zeng, Zhiwei, *Applications of POD Studies and Robust Design to Electromagnetic NDE*, Ph. D. Dissertation, Iowa State University, Ames, IA, 2003.

[182] Rajesh, S. N., Udpa, L., and Udpa, S.S., "Numerical Model Based Approach for Estimating Probability of Detection in NDE Applications," *IEEE Transactions on Magnetics*, Vol. 29, No. 2., March 1993, pp. 1857-1860.

[183] Lawless, J. F., *Statistical Models and Methods for Lifetime Data*, New York, New York: John-Wiley and sons, 1982.

[184] Grivich, Matthew, I., and Jackson, David P., "The Magnetic Field of Current-Carrying Polygons: An Application of Vector Field Rotations," *American Journal of Physics*, Vol. 68, No. 5, May 2000, pp. 469-474.

[185] Bladel, J. Van, *Electromagnetic Fields*, New York, New York: McGraw-Hill Book Company, 1964, Chapter 6.

[186] MAGNET FORMULAS web site
(http://www.netdenizen.com/emagnet/offaxis/iloopoffaxis.htm)

[187] Montgomery, D. Bruce, and Terrell, J., "Some Useful Information for the Design of Air-Core Solenoids," published under Air Force Contract AF19(604)-7344.

[188] Abramowitz, Milton, and Stegun, Irene, *Handbook of Mathematical Functions*, New York, New York: Dover Publications, 1964, Chapter 17.

[189] Hancock, Harris, *Lectures on the Theory of Elliptic Functions*, New York, New York: J. Wiley and sons, 1910.

[190] eHealthMD.com web site
(http://www.ehealthmd.com/library/heartattack/HA_whatis.html).

[191] Rafael, C. Gonzalez, and Wintz, Paul, *Digital Image Processing*, 2nd Ed., Addison Wesley publishing, 1987, pp. 360-361.

[192] Mandayam, S., Udpa, L., Udpa, S. S., and Lord, W., "Monte Carlo Methods for Modeling Magnetostatic NDE Phenomena: A Feasibility Study," *IEEE Transactions on Magnetics*, Vol. 32, No. 3, May 1996, pp. 1425-1428

[193] Zhang, Y., Zhang, Y., Udpa, L., and Udpa, S. S., "Probability of detection model for Pipeline inspection," *Review of Progress in Quantitative Nondestructive Evaluation*, Vol. 16, pp. 1307-1314, 1997

[194] Personal meeting with Dr. James Thomas, Section Head, Cardiovascular Imaging, Heart and Vascular Institute, Cleveland Clinic, on October 16, 2003.

[195] Personal correspondence with Dr. Donald Moore, Division of Pediatric Cardiology, Vanderbilt University School of Medicine, Nashville, TN, on March, 2004.